

UNIVERSITY OF OKLAHOMA  
GRADUATE COLLEGE

THREE DIMENSIONAL THERMO-POROELASTIC MODELING OF FLUID INJECTION  
AND INDUCED MICROSEISMICITY IN NATURALLY FRACTURED RESERVOIRS

A DISSERTATION  
SUBMITTED TO THE GRADUATE FACULTY  
in partial fulfillment of the requirements for the  
Degree of  
DOCTOR OF PHILOSOPHY

By  
QINGLU CHENG  
Norman, Oklahoma  
2018

THREE DIMENSIONAL THERMO-POROELASTIC MODELING OF FLUID INJECTION  
AND INDUCED MICROSEISMICITY IN NATURALLY FRACTURED RESERVOIRS

A DISSERTATION APPROVED FOR THE  
MEWBOURNE SCHOOL OF PETROLEUM AND GEOLOGICAL ENGINEERING

BY

Dr. Ahmad Ghassemi, Chair

Dr. Mrinal Saha

Dr. Deepak Devegowda

Dr. Mashhad Fahes

Dr. Xingru Wu

© Copyright by QINGLU CHENG 2018  
All Rights Reserved.

## **Dedication**

To my family

## **Acknowledgements**

First of all, I would like to express my sincerest appreciation to my advisor, Dr. Ahmad Ghassemi. I feel honored to have had a chance to work with him and learn from him. His knowledge and expertise in geomechanics guided me through the challenges of accomplishing my research. I am thankful for his generous time and efforts invested in my Ph.D. study. Despite his busy schedule, the door to Dr. Ghassemi's office was always open whenever I need a discussion on my research. I am also thankful for his patience in proofreading draft after draft of every report and paper I wrote. This dissertation would not have been possible without his constant guidance and support over the years.

I would also like to thank my committee members, Dr. Mrinal Saha, Dr. Deepak Devegowda, Dr. Mashhad Fahes, and Dr. Xingru Wu, and my former committee members, Dr. Ahmad Jamili and Dr. Ahmad Sakhaee-Pour, for their contributions and time through serving on my committee. I have benefitted greatly from their valuable comments and suggestions. Special thanks are due to Dr. Jean-Claude Roegiers for numerous insightful technical discussions and his encouragement during various stages of my Ph.D. study.

I would also want to extend my appreciation to my colleagues in our Reservoir Geomechanics and Seismicity Research Group. I am thankful to all of them for their friendship and support, and for providing such a pleasurable working atmosphere.

Finally, I sincerely thank my parents, Hao Cheng and Hui Zhang, for their continuous and unconditional love. Also, I would like to thank my husband, Jie Qi, for his support and encouragement over the years. My dear daughter, Mo Qi, thank you for all the joy and happiness you bring to my life.

# Table of Contents

Dedication .....	iv
Acknowledgements.....	v
List of Tables .....	viii
List of Figures .....	ix
Abstract.....	xxii
1. Introduction.....	1
1.1 Naturally Fractured Reservoirs .....	1
1.2 Motivation and Objectives .....	5
1.3 Dissertation outline .....	5
2. Thermo-poroelasticity.....	8
2.1 Coupling in Thermo-poroelasticity.....	9
2.2 Mathematical Model of Thermo-poroelasticity .....	10
3. Finite Element Method .....	17
3.1 Basis for FEM.....	17
3.2 FEM Solution to Thermo-poroelasticity.....	24
4. Natural Fracture Network Model.....	35
4.1 Literature Review.....	35
4.2 Stochastic Fracture Network Generation .....	40
4.3 Equivalent Permeability.....	49
4.4 Pressure Distribution on Individual Fractures .....	52
4.5 Heat Transfer within Fracture Network.....	57
4.6 Fracture Deformation and Shear Dilation.....	65

4.7 Fracture Growth .....	75
4.8 Integration with the Coupled FEM .....	83
5. Model Verification.....	85
5.1 FEM Solution to Thermo-poroelasticity.....	85
5.2 Heat Transfer in Fracture Network .....	95
5.3 Fracture Growth .....	100
5.4 Rate-and-state Friction Model .....	103
6. Numerical Examples.....	105
6.1 Injection Response of Fractured Reservoirs .....	105
6.2 Sensitivity Analysis .....	124
7. Model Applications.....	169
7.1 Newberry EGS Stimulation .....	169
7.2 Oklahoma Wastewater Injection.....	189
8. Summary.....	219
8.1 Conclusions.....	219
8.2 Contributions.....	221
8.3 Recommendations.....	222
References.....	224

## List of Tables

Table 3.1 General remarks on the PDE discretization (Smith and Griffiths 2004) .....	22
Table 5.1 Properties used in the Terzaghi's problem .....	87
Table 5.2 Properties used in the thermoelastic consolidation problem (Aboustit el al. 1982 and Noorishad et al. 1984).....	90
Table 5.3 Properties used in the benchmark problem (White et al. 2016).....	93
Table 5.4 Properties used in the heat transfer verification problem .....	96
Table 5.5 Properties used in the crack propagation model .....	100
Table 5.6 Properties used in the RSF friction model verification.....	103
Table 6.1 Fracture network generation inputs .....	106
Table 6.2 Reservoir, fracture and fluid properties .....	107
Table 6.3 Fracture generation inputs .....	125
Table 7.1 Reservoir properties used in model .....	173
Table 7.2 Fracture parameters used in model .....	177
Table 7.3 Overview of the SWD injection wells .....	195
Table 7.4 Input parameters in the model .....	198



## List of Figures

Figure 2.1. Illustration of the coupling process in thermo-poroelasticity. ....	10
Figure 3.1. Example of a 1D rod element with two nodes. ....	19
Figure 3.2. Commonly used 2D and 3D finite elements and their shape functions. ....	23
Figure 3.3. The penalty method used to define boundary conditions of displacement, pore pressure and temperature (revised from Lee 2011). ....	30
Figure 3.4. The method used to define boundary conditions of injection rate (revised from Lee 2011). ....	31
Figure 3.5. The method used to define boundary conditions of mechanical loading (revised from Lee 2011). ....	32
Figure 4.1. Discrete fracture network model for a naturally fractured reservoir (La Pointe et al. 1997). ....	37
Figure 4.2. Dual porosity model for a naturally fractured reservoir (Warren and Root 1963).....	38
Figure 4.3. Conversion of fractures to continuum mesh in a hybrid model (Rahman et al. 2002). ....	38
Figure 4.4. Representation of a penny-shaped fracture in the model. ....	40
Figure 4.5. Example of a stochastic fracture network of 20 penny-shaped fractures. ....	41
Figure 4.6. Fracture center distributions with different density parameters. ....	42
Figure 4.7. Fracture distributions with different size parameters. ....	44
Figure 4.8. Fracture normal directions generated with a mean direction at (0.866, 0, 0.5) and a Fisher parameter of 0.2, 1.0, 5.0, and 9.0, respectively. ....	46
Figure 4.9. Fracture networks with different orientation distributions. ....	47

Figure 4.10. An example of the fracture network in the Newberry EGS site generated from hybrid approach.....	48
Figure 4.11. An example of a fracture network consists of two orthogonal sets of rectangular shaped fractures. ....	48
Figure 4.12. Intersection between a penny-shaped fracture and finite element face.....	49
Figure 4.13. Image system for a point source in a disc (reproduced from Long 1983).....	53
Figure 4.14. Image systems for radial and non-radial line sources in a disc (reproduced from Long 1983). ....	53
Figure 4.15. Geometry for radial line intersection and its image in a disc (taken from Long 1983). .....	55
Figure 4.16. Geometry for non-radial line intersection and its image in a disc (taken from Long 1983). ....	56
Figure 4.17. An example of flow channel of 1D pipes formed by intersecting fractures. $O_1$ , $O_2$ , $O_3$ and $O_4$ are fracture centers; the intersections between fractures are shown as blue lines; the flow channel is shown in red.....	57
Figure 4.18. Detection of interconnected fractures (colored) and isolated fractures (grey). ....	58
Figure 4.19. Energy conservation in the interconnected fracture network. ....	59
Figure 4.20. Flow channel between two connected fractures. ....	60
Figure 4.21. Discretization of the rock matrix adjacent to a fracture surface.....	63
Figure 4.22. Fracture surfaces slip and cause dilation in fracture aperture. ....	67
Figure 4.23. Fracture aperture evolution with respect to different effective normal stress. ....	68
Figure 4.24. Linear slip weakening friction law assumes friction decreases from a static value to a kinetic value linearly over the slip distance.....	71

Figure 4.25. Rate-and-state friction law. Left: stable (velocity strengthening); Right: unstable (velocity weakening).....	73
Figure 4.26. A penny-shaped fracture subjected to far field stresses ( $\sigma_1$ and $\sigma_3$ ) and internal pressure ( $P_f$ ) (reproduced from Rahman et al. 2002).....	76
Figure 4.27. Illustration of fracture tip propagation path (reproduced from Rahman et al. 2000). .....	79
Figure 4.28. Illustration of wing crack propagation (reproduced from Jung 2013). ....	81
Figure 4.29. Updated fracture geometry considering the propagated wing cracks. ....	82
Figure 4.30. Step-by-step solution procedure for the integrated model. ....	84
Figure 5.1. Illustration of Terzaghi’s consolidation problem. ....	86
Figure 5.2. Finite element mesh for the Terzaghi’s consolidation problem. ....	87
Figure 5.3. Pore pressure profiles at different time. ....	88
Figure 5.4. Displacement profiles at different time. ....	89
Figure 5.5. Illustration of the 1D thermoelastic consolidation problem. ....	89
Figure 5.6. Finite element mesh for the thermoelastic consolidation problem.....	90
Figure 5.7. Comparisons of our numerical solutions for displacement at the top surface in the thermoelastic consolidation problem (solid lines); and comparison to the analytical solution for the isothermal consolidation problem (dash lines). Good agreement is achieved.....	91
Figure 5.8. Schematic of the benchmark problem (modified from White et al. 2016).....	92
Figure 5.9. A 1/8 symmetric domain of the benchmark problem. Left: It includes 2 m of fault zone and 20 m of dense reservoir rock; Right: 2D planar view of the domain showing the applied surface traction on the wellbore. ....	93

Figure 5.10. Pressure evolution versus time at  $r=14.142$  m for the no leak-off scenario (White et al. 2016). Our result is labeled as “OU”, which agrees well with the results of other participating teams. .... 94

Figure 5.11. Pressure evolution at  $r=14.142$  m for the leak-off scenario (White et al. 2016). Our result is labeled as “OU”, which agrees well with the results of other participating teams. .... 95

Figure 5.12. Geometry of the heat extraction problem. The fracture radius is 50 m. The distance between injection and production well is 62.5 m. .... 97

Figure 5.13. Pressure profile on the fracture. Fluid flows from the injection fracture to the extraction fracture under the pressure gradient..... 98

Figure 5.14. Temperature distribution within the fracture network. At the time of 3 days, the extraction fluid temperature is  $136.8$  °C..... 99

Figure 5.15. Fluid temperature distribution in a circular fracture after 3 days injection. Left: from analytical solution (Rodemann 1982); Right: from an integral equation solution (Ghassemi et al. 2003). Both show an extraction temperature of approximately  $137$  °C, which is close to our results. .... 99

Figure 5.16. An inclined penny-shaped fracture subjected to internal pressure and far field stresses (left); 2D view of the inclined penny-shaped fracture (right)..... 101

Figure 5.17. Comparison of stress intensity factors from the analytical method with numerical results from FRANC3D (Hossain 2001) and GeoFrac3D (Kumar 2018). .... 102

Figure 5.18. Comparison of fracture tip propagation path from the analytical method with numerical results from FRANC3D (data digitized from Hossain 2001). .... 103

Figure 5.19. Comparison of friction evolutions predicted by our RSF model (red line) and published data (blue symbols). Perfect agreement is observed. .... 104

Figure 6.1. Simulation domain contains 20 stochastic fractures (left); A uniform mesh with 64,000 elements (right). .....	106
Figure 6.2. Comparison of fracture network connectivity before (top left) and after fracture propagations (after 6, 8 and 9 hours injection). The interconnected fractures on the injection flow path are shown in green. The isolated fractures are shown in grey. The edges of the propagated fractures are shown in pink. ....	109
Figure 6.3. Pore pressure development within the reservoir at different injection time (central slice $x=0$ and central slice $z=0$ are shown).....	110
Figure 6.4. Pore pressure development within the fracture network at different injection time.	111
Figure 6.5. Example of 2D pore pressure development on a fracture plane at different injection time. The center point of this fracture is located at $(0, 0, 0.5)$ .....	112
Figure 6.6. Temperature development within the fracture network at different injection time..	113
Figure 6.7. Fracture status at different injection time. Slipped fractures are shown in red, and opened fractures are shown in green. The fractures shown in blue do not have status change..	114
Figure 6.8. Permeability development within the fracture network at different injection time..	115
Figure 6.9. Equivalent permeability development within the reservoir at different injection time (central slice $x=0$ and central slice $z=0$ are shown). ....	116
Figure 6.10. Injection induced microseismicity within the reservoir at different injection time.	117
Figure 6.11. Average fracture aperture profile and the corresponding fracture opening, shear slippage and propagation events. ....	119
Figure 6.12. Average permeability profile and the corresponding fracture opening, shear slippage and propagation events. ....	120
Figure 6.13. Comparison of average fracture aperture profiles predicted from different cases.	121

Figure 6.14. Comparison of average permeability profiles predicted from different cases. .... 122

Figure 6.15. Comparison of the injection induced microseismic clouds estimated from RSF model (left) and constant friction model (right), after 9 hours of injection. .... 123

Figure 6.16. Simulation domain contains 1000 stochastic fractures (left); A uniform mesh with 75,000 elements (right). .... 125

Figure 6.17. Comparison of permeability enhancement during 72 hrs of injection for the cases of different fracture number. .... 127

Figure 6.18. Comparison of microseismic events and pore pressure distribution in fracture network after 72 hrs of injection for the cases of different fracture number. .... 128

Figure 6.19. Comparison of permeability enhancement during 72 hrs of injection for the cases of different fracture size. .... 130

Figure 6.20. Comparison of microseismic events after 72 hrs of injection for the cases of different mean fracture radius value. .... 131

Figure 6.21. Comparison of permeability enhancement during 72 hrs of injection for the cases of different fracture orientation distribution. .... 132

Figure 6.22. Comparison of microseismic events after 72 hrs of injection for the cases of different fracture orientation distribution parameter. .... 133

Figure 6.23. Comparison of permeability enhancement during 72 hrs of injection for the cases of different fracture dilation angle. .... 135

Figure 6.24. Comparison of microseismic events after 72 hrs of injection for the cases of different differential stress. .... 136

Figure 6.25. Comparison of permeability enhancement during 72 hrs of injection for the cases of different matrix permeability. .... 137

Figure 6.26. Comparison of average fracture aperture increase during 72 hrs of injection for the cases of different matrix permeability. ....	138
Figure 6.27. Comparison of microseismic events and pore pressure distribution in fracture network after 72 hrs of injection for the cases of different matrix permeability. ....	139
Figure 6.28. Comparison of permeability enhancement during 72 hrs of injection for the cases of different maximum horizontal stress azimuth.....	141
Figure 6.29. Comparison of microseismic events after 72 hrs of injection for the cases of different maximum horizontal stress azimuth. ....	142
Figure 6.30. Comparison of orientations of slipped fractures after 72 hrs of injection for the cases of different maximum horizontal stress azimuth. ....	143
Figure 6.31. Comparison of permeability enhancement during 72 hrs of injection for the cases of different stress regime.....	144
Figure 6.32. Comparison of microseismic events and orientations of slipped fractures after 72 hrs of injection for the cases of different differential stress. ....	145
Figure 6.33. Comparison of permeability enhancement during 72 hrs of injection for the cases of different deviatoric stress between the vertical and the minimum horizontal stresses ( $dS= S_v - S_{hmin}$ ). ....	147
Figure 6.34. Comparison of microseismic events after 72 hrs of injection for the cases of different differential stress between the vertical and the minimum horizontal stresses (top left: $dS=23$ MPa; top right: $dS=20$ MPa; bottom: $dS=17$ MPa).....	148
Figure 6.35. Mohr diagram representation of different initial stress states. ....	149
Figure 6.36. Comparison of permeability enhancement during 72 hrs of injection for the cases of different stress magnitudes. ....	150

Figure 6.37. Comparison of microseismic events after 72 hrs of injection for the cases of different stress magnitudes (left: $S_v=50$ MPa and $S_{hmin}=30$ MPa; right: $S_v=47$ MPa and $S_{hmin}=27$ MPa). No microseismic events in Case 1 ( $S_v=53$ MPa and $S_{hmin}=33$ MPa).....	151
Figure 6.38. Mohr diagram representation of different initial stress magnitudes.....	152
Figure 6.39. Comparison of permeability enhancement during 72 hrs of injection for the cases of different fluid viscosities.....	153
Figure 6.40. Comparison of microseismic events and pore pressure distribution in fracture network after 72 hrs of injection for the cases of different fluid viscosities.....	155
Figure 6.41. Comparison of permeability enhancement during 72 hrs of injection for the cases of different injection rate.....	156
Figure 6.42. Comparison of permeability enhancement against injected volume for the cases of different injection rate.....	157
Figure 6.43. Comparison of microseismic events and pore pressure distribution in fracture network after injecting the same volume of fluid ( $6480\text{ m}^3$ ) using different injection rate.....	158
Figure 6.44. Comparison of permeability enhancement against injected volume for the cases of different injection rate and different stress differential: low injection rate of $0.075\text{ m}^3/\text{s}$ (dashed lines) and high injection rate of $0.15\text{ m}^3/\text{s}$ (solid lines), low differential stress of 1 MPa (red colored) and high differential stress of 15 MPa (blue colored). .....	160
Figure 6.45. Comparison of microseismic events and the average reservoir permeability after injecting the same volume ( $19400\text{ m}^3$ ) of fluid for the cases of different injection rate (low injection rate of $0.075\text{ m}^3/\text{s}$ and high injection rate of $0.15\text{ m}^3/\text{s}$ ) and different horizontal stress differential (low differential stress of 1 MPa and high differential stress of 15 MPa).....	161



Figure 6.46. Comparison of permeability enhancement during 72 hrs of injection for the cases of different injection temperature difference. .... 163

Figure 6.47. Comparison of microseismic events (left) and temperature drawdown (right) in fracture network after 72 hrs of injection for the cases of different temperature difference. For better visualizations, in the right panels, the temperature drawdowns are only shown on the thermal affected fractures..... 165

Figure 7.1. Location map of the Newberry EGS Demonstration site (taken from Alta Rock 2014). ..... 169

Figure 7.2. Wellhead pressure and flow rate profiles of Newberry EGS Phase 2.2 stimulation 170

Figure 7.3. Left: The simulation domain is 2000 m in N-S (x-direction), 3000 m in E-W (y-direction), and 2200 m in vertical (z-direction). The wellbore is located in the center (grey line), which has two open intervals (red lines). Right: The domain consisting of three geological formations is discretized into 55,924 elements..... 172

Figure 7.4. Location maps of MEQs detected during Phase 2.2 stimulation. The seismic cloud plots within 400 m from the wellbore and at a depth between 2000 m and 3000 m. .... 174

Figure 7.5. Rose diagram of dip directions (top) and histogram of dip angles (bottom) of generated fractures, and obtained from BHTV and MEQ data. .... 175

Figure 7.6. Fracture network in the simulation domain. A total of 750 fractures are generated and introduced to the simulation domain..... 176

Figure 7.7. Wellhead pressure and injection rate profiles. As the WHP increases, a simultaneously significant increase in flow rate is observed and following by a decline to lower rates. The flow spikes may due to fracture volume increase as a result of fracture opening. When there is no sufficient injection pressure to promote further opening, the flow required for fracture volume

increase vanishes, resulting in a decline in flow rate. The resulting flow rates generally agree with the field measured values..... 178

Figure 7.8. Pore pressure evolution after 3 hrs injection (left) and 254 hrs injection (right) shows that pore pressure development is mostly controlled by the fracture network connectivity. .... 180

Figure 7.9. Fracture permeability evolution after 3 hrs injection (left) and 254 hrs injection (right) shows the permeability of most of the fractures is improved during injection..... 181

Figure 7.10. Injection induced MEQs evolution after 3 hrs injection (left) and 254 hrs injection (right) shows that MEQ events were induced as injection continued..... 181

Figure 7.11. Location maps of 39 MEQs obtained in the preliminary simulation (from September 28 to October 7). The plane views show that the induced MEQs locate within 200 m radius from the wellbore, and are close to the depths of the injection intervals, which are in good agreement with the field observations. .... 183

Figure 7.12. Normals to the fracture planes and the MEQ magnitudes of the slipped fractures (colored squares) after 254 hours injection. The fractures that did not slip are shown as blank squares..... 184

Figure 7.13. Left: distribution of temperature after 254 hours injection. Right: zoom in view of temperature distribution on fractures. Only the temperature of fractures around the injection well is reduced. .... 185

Figure 7.14. Distribution of the maximum principal stress and its vector after 254 hours injection (left: central slice in x-z plane; right: zoom in view of the area near injection intervals). The maximum principal stress near the injection well rotated from vertical toward the horizontal direction and resulted in a strike-slip regime. .... 186

Figure 7.15. Stress profile along a line in the x-z plane central slice ( $y=0$  m) at the middle depth of the injection interval ( $z=2500$  m) after 254 hours injection. It shows two stress rotation regions (in grey dashed lines) where the maximum principal stress rotates from the initial vertical direction towards horizontal. Excess compressive stresses in the vicinity of injection well (-500 m to 500 m) is due to poroelastic stress induced by pore pressure increase. The compressive stress reduction at the wellbore is due to cooling induced tensile stress. .... 187

Figure 7.16. Increasing rate of earthquakes in the central United States beginning in 2009 (Rubinstein 2018)..... 190

Figure 7.17. Relationship between wastewater injection and seismic activity in Oklahoma from 2008 to 2017 (Chen et al. 2017)..... 190

Figure 7.18. Location of the study area (shown in the yellow box). Oklahoma  $M_L \geq 3$  seismic events from the USGS PDE catalog. Events from 1975 to 2008 are shown by grey circles, and events from 2009 to 2011 are shown by red squares. Marker size indicates seismic magnitude. (modified from Llenos and Michael 2013)..... 193

Figure 7.19. Two major fault systems within the study area: the WFZ trending  $\sim N25-30E$  and the MPF trending  $\sim N55E$  (modified from McMahon et al. 2016). .... 194

Figure 7.20. Injection profiles of the 8 SWD wells between 2000 to 2011. Monthly injection volume data from Oklahoma Corporation Commission (OCC) database. Monthly average injection rate is calculated accordingly..... 197

Figure 7.21. Numerical model consists of two layers: the Arbuckle group (2000 m to 2600 m, shown in green) and the basement (2600 m to 3000 m, shown in blue)..... 198

Figure 7.22. Fracture network modeled in the basement: 3D view (top) and 2D view (bottom). The injection wells are shown in red squares..... 202

Figure 7.23. Pore pressure evolution at the middle depth of the Arbuckle formation (2D view, central slice: $z=2300$ m).....	205
Figure 7.24. Pore pressure evolution at the middle depth of the basement (2D view, central slice: $z=2800$ m).....	206
Figure 7.25. Change of the total stress after 12 years of injection at the middle depth of the Arbuckle formation (central slice: $z=2300$ m) and at the middle depth of the basement (central slice: $z=2800$ m). Top: total stress in the x direction ( $S_x$ ); bottom: total stress in the y direction ( $S_y$ ). .....	207
Figure 7.26. Change of the effective stress after 12 years of injection at the middle depth of the Arbuckle formation (central slice: $z=2300$ m) and at the middle depth of the basement (central slice: $z=2800$ m). Top: total stress in the x direction ( $S_x$ ); bottom: total stress in the y direction ( $S_y$ ). .....	208
Figure 7.27. Pore pressure evolution within the fracture network (2D view). The injection wells are shown in red squares. ....	209
Figure 7.28. Friction coefficient reduction of fractures (2D view). A maximum reduction of 0.05 is observed on fractures. ....	210
Figure 7.29. Distribution of the induced microseismic events (2D view). Most MEQs occur on the N55°E Meeker-Prague fault.....	211
Figure 7.30. 2D view of the fracture network within the selected small area (4 km x 4 km). The injection well is shown in red square. ....	213
Figure 7.31. Induced seismic events within the small area after 1 year of injection using a constant injection rate of $0.015 \text{ m}^3/\text{s}$ . The injection well is shown in red square. The seismic events are shown in circles.....	214

Figure 7.32. Maximum seismic moment as a function of cumulative injection volume in the cases of different injection rate. ....	215
Figure 7.33. Maximum seismic moment as a function of cumulative injection volume in the cases of different injection depth.....	217
Figure A.1. Possible relative locations for line segment overlapping (Wang 2013). ....	247
Figure A.2. Algorithm for searching for the connected fracture flow path. ....	248
Figure A.3. Non-radial line source (Long 1983). ....	250
Figure A.4. Non-radial line source image arc (Long 1983).....	251
Figure A.5. Radial line source image arc (Long 1983).....	253
Figure A.6. Radial line source image arc (Long 1983).....	254

## **Abstract**

Interests in naturally fractured reservoirs have grown rapidly in recent years due to the increasing energy needs. Understanding the behavior of naturally fractured reservoirs would be beneficial for a variety of engineering applications, including enhanced oil recovery in the petroleum industry, reservoir stimulation in enhanced geothermal systems, salt water disposal, carbon dioxide storage, and nuclear waste management. In naturally fractured reservoirs with low permeability rock matrix, natural fractures provide primary pathways for fluid flow and dominate the flow behavior of the fractured medium. Fractures are stress sensitive. They could dilate, slip in shear, and propagate possibly as a result of stress changes caused by fluid injection operations, thereby increasing fracture aperture and permeability, and influencing reservoir performance. Injection into fractured reservoirs could also induce seismicity, which is often attributed to shear slippage on fractures.

In this study, we developed a three dimensional fully coupled thermo-poroelastic model which is integrated with a stochastic natural fracture network to simulate the response of fractured reservoirs to fluid injection. Fluid injection induces significant perturbations in the pore pressure, temperature and stress fields within a reservoir, and involves coupling between fluid flow, heat transfer, and mechanical deformation. This coupling process is modeled using a linear theory of thermo-poroelasticity and solved using a finite element method. The presence of natural fractures is taken into consideration by implementing a fracture network model into the coupled thermo-poroelastic model. A discrete fracture network is generated based on stochastic descriptions of fracture distribution parameters, including fracture density, size and orientation. The available fracture geometry includes penny-shaped circular fractures, elliptical fractures and rectangular fractures. Since the calculations of flow in non-circular fractures require additional mathematical

treatments (Long et al. 1985) and the available solutions to heat transfer in the non-circular fractures are also limited, therefore, the commonly used penny-shaped circular fracture is modeled in this work. The permeability of the fractured rock is estimated using an equivalent permeability approach. The fracture permeability can increase by shear dilation and fracture propagation. For numerical simulations of fracture slip, two most widely used friction models are incorporated, including a constant friction model and a rate-and-state friction (RSF) model that considers the dependence of friction on the slip velocity and the past sliding history. The coupled FEM is solved for pressure, temperature, and deformation in the equivalent continuum medium formed by the fractures and the rock matrix. Knowing the flows and heads within the fracture network and the intersections between fractures, local pressure distribution on individual fracture planes is solved analytically based on an image theory (Rahman et al. 2002). Heat transfer within the interconnected fracture network is modeled by a flow pipe network model considering both the convection via fracture flow and the conduction between adjacent rock mass and the fluid in the fracture. Stress dependent fracture deformation behavior including opening, shear dilation, and possible propagation is considered, and the associated changes in fracture aperture and fracture network geometry are updated for permeability in the coupled FEM. The potential of microseismicity induced by fracture shear slippage is also modeled. The developed model is verified against analytical solutions and previously published numerical results.

This model is first used to simulate cold water injection into a naturally fractured reservoir to examine its capability of analyzing the dynamic reservoir response during injection. Results show that the fluid and heat flow within the fractured reservoir are primarily dominated by the connected fracture network. The results also indicate that the overall reservoir permeability enhancement can be attributed to the combined effects of fracture opening, shear slippage, and propagation. A

sensitivity study is carried out for investigating the effect of various parameters on the reservoir performance and on the occurrence of induced seismicity during injection. The results show that the injection response of a naturally fractured reservoir is a complex process controlled by multiple factors, including the properties of fracture network, in-situ stress conditions, rock matrix permeability, the properties of injecting fluid, injection scheme and injection temperature.

The developed model has a wide variety of engineering applications in naturally fractured rock. Two application examples are present in this dissertation. The first application example is the simulation of reservoir stimulation in the Newberry EGS Demonstration. Field data on the fracture network and in-situ stress and laboratory data on rock and fracture properties are used in model construction. The simulated injection profile, the evolution of permeability and induced microseismic events have good agreements with field observations. Simulation results also show the perturbation and rotation of the in-situ stress field adjacent to the injection well, which helps to explain the discrepancy between the stress models derived pre-injection and inverted from seismic data post-injection.

The second application example is a large scale simulation of the 12 years long term wastewater injection in central Oklahoma. A conceptual model is built based on the available data on the fault geometry, regional stress fields, and well injection history. Simulation results show that during injection, the elevated pore pressure can migrate downward from the Arbuckle injection layer into the deeper crystalline basement via the fault system. For nearly critical fractures, a small elevated pressure is sufficient to cause shear slippage of fractures along the optimally oriented Meeker-Prague fault and potentially induce seismicity. Injection strategies of capping the total injected volume, reducing the injection rate, and restricting the injection depth are proposed to reduce the size of the potentially induced seismicity.



The numerical model developed in this study is shown to have the capability of analyzing the dynamic reservoir response during fluid injection. It is useful for the design and evaluation of injection plans in naturally fractured reservoirs.

# **1. Introduction**

## **1.1 Naturally Fractured Reservoirs**

All reservoir rocks are fractured to some extent, with natural fractures occurring at various scales, from microscopic to continental kilometer sized (National Research Council 1996). Many underground reservoirs, including petroleum and geothermal reservoirs, are formed in naturally fractured rocks. A significant portion of the world's hydrocarbon reserves is discovered in naturally fractured reservoirs. More than 60% of the world's proven oil reserves and 40% of the world's gas reserves are held in fractured carbonates (Ahmed 2010). In the United States, the domestic petroleum target in naturally fractured reservoirs is estimated to be hundreds to thousands of trillions of cubic feet (Laubach et al. 2000). As a reliable, safe and stable source of renewable energy, geothermal energy has been attracting more and more attention in the past few decades. Most geothermal resources are located in low permeable hot rocks and are naturally fractured at various scales. Heat production from these type of reservoirs requires a successful stimulation by injecting cold water into hot rocks to enhance reservoir permeability, which has led to the concept of Enhanced Geothermal Systems (EGS). Many of the world's EGS projects extract geothermal energy from naturally fractured reservoirs, such as Northwest Geysers, Landau, Insheim, Urach, Bruchasl, Soultz-sous-Forets, Fjallabacka, Hijiori, Rosemanowes, Falkenberg, and Newberry (Breede et al. 2013). As increasing energy needs, interests in naturally fractured reservoirs have grown rapidly in recent years.

In naturally fractured reservoirs with low permeability rock matrix, natural fractures are the primary pathways for fluid flow through the rock. The behavior of natural fractures dominates the flow behavior of the fractured system and influences reservoir performance. Fractures are very sensitive to pore pressure and stress changes. When fluid production or injection operations occur,

pressure and temperature variations in the reservoir can perturb the in-situ reservoir stress state leading to fracture deformation, changing fracture aperture and permeability, and influencing reservoir performance. Injection of fluids into a fractured reservoir can increase the fluid pressure, which will lower the effective stress on fracture, causing fractures to dilate, thereby increasing fracture aperture and enhancing fracture permeability. When cold water is injected into hot reservoirs, temperature changes could induce tensile thermal stress which also causes changes in effective stress, and consequently influences the deformation behavior of fractures.

Natural fractures slip in shear when shear strength is exceeded. Shear slippage induces dilated aperture which will further enhance reservoir permeability. Due to the frictional resistance of rough natural fracture surfaces, the dilated flow conduit will remain open after shear slip without requiring proppants, and the dilated aperture is permanent, at least over a period. This permeability enhancement strategy is called shear dilation or hydroshearing. It was first recognized in rock joint deformation studies in the 1970s. Later, its role in enhancing the permeability of naturally fractured reservoirs has been recognized by the petroleum and geothermal industries. The shear dilation concept has been recognized as the dominant mechanism for permeability enhancement during the hydraulic stimulation in naturally fractured engineered geothermal systems (EGS) (e.g., Pine and Batchelor 1984; Rahman et al. 2002). Laboratory scale injection-driven shear stimulation tests on granite fractures (Ye et al. 2017; Huang et al., 2018) and fractured shale samples (Ye et al. 2018; Ye and Ghassemi 2018) have successfully observed permeability enhancement through shear slip and dilation.

Previous models of naturally fracture rock have not considered the possibility of fracture propagation. However, Kamali and Ghassemi (2018) have shown that natural fractures can propagate by shear slip in response to injection, contributing to fracture network connectivity.

Some fractures could propagate even at a low injection pressure that is below the minimum in-situ stress depending on their geometric parameters (Kamali and Ghassemi 2018) and strength properties of the fractures and the matrix. These theoretical considerations have been recently demonstrated in pioneering laboratory study of injection-induced fracture propagation (Ye and Ghassemi 2018) showing that the preexisting fractures could propagate and coalesce at treatment pressure lower than the minimum principal stress during injection. Their observations also confirmed the suggestion (Kamali and Ghassemi 2018) that both shear dilation and fracture propagation contribute to the hydraulic stimulation in fractured reservoirs. Therefore, it is crucial to simultaneously account for the effects of shear dilation and fracture propagation on the stimulation performance of naturally fractured reservoirs. Such a model has been developed in 2D for petroleum reservoir stimulation (Sesetty and Ghassemi 2017 and 2018).

Injection into fractured reservoirs not only change reservoir permeability, but also can induce seismicity. The occurrence of injection related seismicity is often attributed to shear slip on natural fractures in response to a reduction in the effective stress acting on the fractures due to an increase in the pore pressure field. The detection and interpretation of these seismic events can provide useful information for estimating the stimulated reservoir volume and the resulting permeability, geometry of the geological structures and the in-situ stress state (Pine and Batchelor 1984; Warpinski et al. 2001; Guitierrez-Negrin and Quijano-Leon 2003). On the other hand, extensive induced seismicity at levels above the tolerated magnitude or frequency can be a potential risk in reservoir development operations. Assessing potential injection induced seismicity is important for both interpretations of reservoir stimulation outcomes and management and mitigation of the hazards and risks associated with induced seismicity.

For a better reservoir development and management, it is necessary to better understand the processes and mechanisms associated with fluid injection induced changes in naturally fractured reservoirs. Numerical modeling provides a powerful tool for the investigation of the behavior of rock masses embedded with natural fractures. However, the development of numerical tools for naturally fractured reservoirs is very challenging. Fluid injection induces significant changes in the pore pressure, temperature and stress fields within reservoirs, and involves coupled fluid flow, heat transfer and deformation in the fractured rocks. Given the extensive development effort and expensive solution cost required for coupled modeling, in most existing models for fractured rocks, the coupling process has been either neglected (e.g., Willis-Richards et al. 1996; Walsh and Zoback 2016) or simplified using empirical correlations (e.g., Bruel 2002), and the pressure distribution within the fractured reservoir is usually estimated from simplified flow model (e.g., Rahman et al. 2002; Walsh et al. 2017). A fully coupled numerical model is necessary for improving understanding of reservoir behavior during various reservoir development activities. Moreover, the presence of natural fractures in the reservoirs makes the reservoir response more complicated and poses additional challenges in numerical modeling. Due to the variable spatial distribution, orientation and geometry of natural fractures, fluid and heat flow within fractured reservoirs are very complicated. The numerical model for a naturally fractured reservoir containing numerous natural fractures should include: 1) a realistic geometrical representation of complex three dimensional fracture networks, 2) a mathematical model for describing flow through the fractured medium, and 3) a geomechanical model for describing the dynamic fracture response to operation induced stress changes. Besides, since the deformation of natural fractures will have an influence on reservoir behavior by changing fracture permeability, the integration between fracture

model and the coupled thermo-poroelastic model should also be considered in the numerical models for fractured reservoirs.

Therefore, this study aimed to develop a numerical model which can consider the coupled thermo-poroelastic processes during injection and is capable of accounting for the stress dependent fracture deformation behavior including opening, shear dilation, and possible propagation.

## **1.2 Motivation and Objectives**

This study is motivated by the need of developing a comprehensive numerical model to help analyze the complex behavior of a naturally fractured reservoir subject to fluid injection. The objectives of this study are:

To develop a three dimensional fully coupled thermo-poroelastic model integrated with a fracture network model, for simulating the response of a naturally fractured reservoir to fluid injection.

To predict the injection induced pore pressure, temperature and stress variations within the fractured reservoir, to evaluate fracture deformation, permeability change and the potential of injection induced seismicity, and to investigate the influences of various reservoir, fracture and fluid parameters on the injection outcomes.

To apply the developed numerical model for solving relevant engineering problems, including enhanced geothermal systems (EGS) stimulation and wastewater injection.

## **1.3 Dissertation outline**

This dissertation is divided into eight chapters. The details of individual chapters are as follows:

Chapter 1 gives a general introduction, including an overview of naturally fractured reservoirs, as well as motivation and objectives of this research.

Chapter 2 provides a brief description of thermo-poroelasticity. First, the development history of thermo-poroelasticity theory is reviewed. Then, the derivation of governing equations for the coupled thermo-poroelastic processes in the reservoir during injection/production is illustrated.

Chapter 3 presents the basic theory of finite element model. The detailed FEM solution to the coupled thermo-poroelastic problems is also provided.

Chapter 4 focuses on the methodology for modeling natural fractures. A literature review of numerical models for the fractured medium is presented, followed by a detailed description of the proposed natural fracture network model. The integration between the fracture network model and the coupled thermo-poroelastic finite element model is also described.

Chapter 5 presents verifications of the developed model components using analytical solutions and previously published numerical results.

Chapter 6 presents two numerical examples. The first example aims to demonstrate the capability of the developed model for predicting the dynamic response of naturally fractured reservoirs to injection. The emphasis of the second example is to investigate the sensitivity of reservoir injection response to various parameters.

Chapter 7 consists of two applications on the study of relevant engineering problems. The first application is a simulation of the reservoir stimulation in the Newberry EGS Demonstration project. The results from this modeling are used to better understand and explain the field observations on injection rate and stress reorientation. The second application presents a simulation of wastewater injection in central Oklahoma region. A conceptual model is built for investigating the injection induced poroelastic effects on the geomechanical behavior of the fault systems and evaluating the potential for seismicity.

Chapter 8 summarizes the major findings of this study and outlines the main contributions and achievements of the whole Ph.D. work. Recommendations for future research works are also proposed.



## **2. Thermo-poroelasticity**

Cold water injection into a reservoir is a coupled process involving rock deformation, fluid flow and heat transfer in the porous rock. The coupled poroelastic process involving the influence of fluid flow in a porous rock was firstly recognized in a one-dimensional soil consolidation problem developed by Terzaghi (1923). He considered the impact of pore fluid diffusion on soil deformation and proposed the total stress concept consist of effective stress and pore pressure. The fundamental linear theory of poroelasticity was systematically formed by Biot (1941). He developed a coupled model between fluid and solid which accounts for solid-fluid coupling (change in applied stress results in a change in fluid pressure of fluid mass) and fluid-solid coupling (change in fluid pressure of fluid mass causes a change in the volume of the porous material). Poroelasticity was developed further by Rice and Cleary (1976). They extended Biot's linear poroelasticity theory by using different formulations of the coupled deformation-diffusion field equations. They also proposed two limiting behaviors by using drained and undrained parameters and the constituent compressibilities.

The theory of poroelasticity has been extended into the non-isothermal field, to include the effect of temperature changes on the stresses and displacements. Palciauskas and Domenico (1982) firstly presented the constitutive equations for thermo-poroelasticity theory by modifying the classical Biot's theory with additional parameters describing the thermal expansion of the solid, fluid and pore volume. Later, McTigue (1986) developed a linear theory for fluid saturated porous thermoelastic martial and presented a general solution. This theory accounts for compressibility and thermal expansion of both the fluid and solid constituents. The diffusion equation with a temperature-dependent source term governs a combination of the mean total stress and the fluid pore pressure. Kurashige (1989) extended the Rice and Cleary's theory to incorporate the heat

transportation by fluid flow through pores in addition to the difference in the thermal expansibility between the pore fluid and the solid skeleton. This theory has also been further extended in a chemically-active environment to analyze the coupled thermo-chemo-poroelastic process (e.g., Mody and Hale 1993; Heidug and Wong 1996; Ghassemi and Diek 2003; Ghassemi et al. 2009; Zhou and Ghassemi 2009).

The theory of thermo-poroelasticity has important contributions in a diverse range of engineering fields, such as wellbore stability analysis (e.g., Li et al. 1998; Ghassemi and Zhang 2004; Chen and Ewy 2005; Zhou and Ghassemi 2009; Lee and Ghassemi 2010) and enhanced oil recovery (e.g., Freeman et al. 2008; Yin et al. 2009; Hou et al. 2012) in petroleum engineering, reservoir stimulation in enhanced geothermal systems (e.g., Watanabe et al. 2011; Koh et al. 2011; Ghassemi and Zhou 2011; Wang and Ghassemi 2012; Rawal and Ghassemi 2014; Safari and Ghassemi 2015), carbon dioxide storage (e.g., Rutqvist et al. 2002; Goodarzi et al. 2013; Vilarrasa et al. 2014), and nuclear waste management (e.g., Yow and Hunt 2002; Boulton et al. 2004; Chan et al. 2005).

This chapter provides a brief introduction to the theory of thermo-poroelasticity, followed by a detailed description of its mathematical model.

## **2.1 Coupling in Thermo-poroelasticity**

The interaction between solid and fluid phase involves the coupling between rock deformation, pore fluid diffusion, and heat transfer. Although temperature has a significant influence on the stresses, strains, and pore pressure, in general, the deformation and pore pressure does not lead to significant temperature change. Therefore, the influences of rock deformation and fluid flow on

the temperature field are ignored in this work (Figure 2.1). The main mechanism of thermo-poroelastic coupling process can be summarized as:

- (1) rock volumetric deformation (compression or expansion) due to change in pore pressure;
- (2) change in pore pressure due to rock volumetric deformation;
- (3) change in pore pressure and volumetric stresses due to temperature change (heating or cooling).

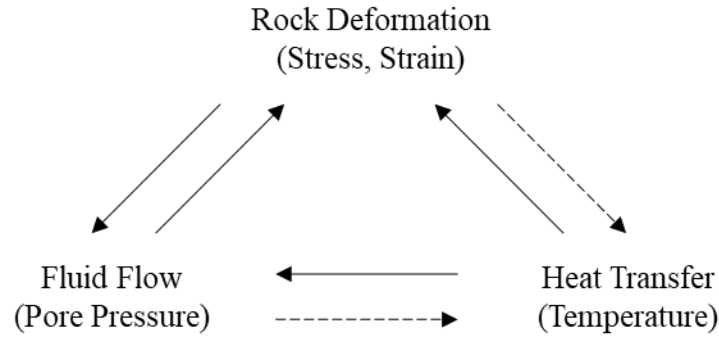


Figure 2.1. Illustration of the coupling process in thermo-poroelasticity.

## 2.2 Mathematical Model of Thermo-poroelasticity

In this work, the governing equations developed by McTigue (1986) and Kurashige (1989) are followed. The sign convention in this section is tension positive. The constitutive equations, conservation laws and field equations are summarized below:

### 2.2.1 Constitutive Equations

For a fluid saturated porous rock subjected to both mechanical and thermal disturbances, the general constitutive equations describing the influence of stresses, pore pressure and temperature on the deformation of the solid phase and the pore space can be written in the following form (Kurashige 1989):

$$\varepsilon_{ij} = C_{ijkl} \sigma_{kl} + B_{ij} p + \alpha_{ij}^T T \quad (2.1)$$

$$\Delta\phi = B_{kl} \sigma_{kl} + Dp + \alpha_p^T T \quad (2.2)$$

Assuming the rock is isotropic, the parameters are defined as:

$$C_{ijkl} = \frac{1}{4G} (\delta_{ik}\delta_{jl} + \delta_{il}\delta_{jk} - \frac{2}{1+\nu} \delta_{ij}\delta_{kl}) \quad (2.3)$$

$$B_{ij} = \frac{3(\nu_u - \nu)}{2GB(1+\nu)(1+\nu_u)} \delta_{ij} \quad (2.4)$$

$$D = \frac{1}{B} \left( \frac{1}{K} - \frac{1}{K'_s} \right) - \frac{\phi}{K_f} \quad (2.5)$$

$$B = \frac{3(\nu_u - \nu)}{\alpha(1-2\nu)(1+\nu_u)} \quad (2.6)$$

$$K = \frac{2G(1+\nu)}{3(1-2\nu)} \quad (2.7)$$

$$\alpha_{ij}^T = \alpha_m^T \delta_{ij} \quad (2.8)$$

Where  $\sigma_{ij}$ ,  $\varepsilon_{ij}$ ,  $p$  and  $T$  are the total stress, strain, pore pressure and the temperature change, respectively.  $\phi$ ,  $G$ ,  $K$ ,  $\nu$ ,  $\nu_u$  and  $\alpha_m^T$  are the porosity, shear modulus, bulk modulus, drained Poisson's ratio, undrained Poisson's ratio and the linear thermal expansion coefficient of the porous rock matrix, respectively;  $K_f$  is the bulk modulus of the pore fluid;  $K'_s$  is the effective bulk modulus of the solid constituent;  $\alpha_m^T$  and  $\alpha_p^T$  are the volumetric thermal expansion coefficient of the rock and the pore space, respectively; If the pores expand with their shapes remaining similar as the porous matrix expands thermally,  $\alpha_p^T = 3\phi\alpha_m^T$ ;  $B$  is the Skempton's pore pressure coefficient;  $\alpha$  is the Biot's coefficient.

Eqn. (2.1) and (2.2) can be rewrite in terms of total stress and pore space change:

$$\sigma_{ij} = 2G\varepsilon_{ij} + \left( K - \frac{2G}{3} \right) \varepsilon_{kk} \delta_{ij} - \alpha p \delta_{ij} - \frac{2G(1+\nu)}{3(1-2\nu)} \alpha_m^T T \delta_{ij} \quad (2.9)$$

$$\Delta\phi = \frac{1}{2G} \frac{\alpha(1-2\nu)}{(1+\nu)} \sigma_{kk} + \left[ \frac{1}{B} \left( \frac{1}{K} - \frac{1}{K_s} \right) - \frac{\phi}{K_f} \right] p + \alpha_p^T T \quad (2.10)$$

Since the local heat exchange between the matrix solid and pore fluid may be rapid enough compared to the global heat and fluid diffusions, the same temperature is used for thermal expansion (Kurashige 1989).

Linearization of the pressure-density-temperature curve of the pore fluid gives the change in fluid density due to pore pressure and temperature variation:

$$\frac{\Delta\rho_f}{\rho_f} = \frac{p}{K_f} - \alpha_f^T T \quad (2.11)$$

Where  $\alpha_f^T$  is the volumetric thermal expansion coefficient of the pore fluid;  $\rho_f$  and  $\Delta\rho_f$  are the fluid density and the change in fluid density, respectively.

The mass content of pore fluid in a unit bulk volume of the material is:

$$m = \rho_f \phi \quad (2.12)$$

A change in fluid mass per unit volume is given by:

$$\Delta m = \rho_f \Delta\phi + \phi \Delta\rho_f \quad (2.13)$$

Substituting (2.10) and (2.11) into (2.13) yields:

$$\frac{\Delta m}{\rho_f} = \frac{1}{2G} \frac{\alpha(1-2\nu)}{(1+\nu)} \sigma_{kk} + \frac{1}{B} \left( \frac{1}{K} - \frac{1}{K_s} \right) p + (\alpha_p^T - \alpha_f^T \phi) T \quad (2.14)$$

The relations between the material parameters are:

$$\frac{1}{B} \left( \frac{1}{K} - \frac{1}{K_s} \right) = \frac{9(\nu_u - \nu)}{2GB^2(1+\nu_u)(1+\nu)} \quad (2.15)$$

Eqn. (2.14) can be rewritten in terms of the change of fluid volume content per unit reference volume:

$$\zeta = \frac{1}{2G} \frac{\alpha(1-2\nu)}{(1+\nu)} (\sigma_{kk} + \frac{3}{B} p) + (\alpha_p^T - \alpha_f^T \phi) T \quad (2.16)$$

Eqn. (2.9) and (2.16) are convenient forms of the constitutive relation for thermo-poroelasticity.

The constitutive relations associated with heat and fluid diffusion processes are also considered.

By identifying the consequence of positive entropy production as an implied relationship between

the fluxes and their driving forces, the coupled Fourier-Darcy laws is obtained for the case of no

body force:

$$q_i = -\rho_f \kappa_{ij} p_{,j} + L_{ij} T_{,j} \quad (2.17)$$

$$h_i = -\kappa_{ij}^T \Delta T_{,j} + L'_{ij} p_{,j} \quad (2.18)$$

Where  $h_i$  and  $q_i$  are the heat flux and fluid mass flux, respectively;  $\kappa_{ij}$  is the permeability;  $\kappa_{ij}^T$  is

the thermal conductivity;  $L_{ij}$  and  $L'_{ij}$  are the cross-effect coefficients.

Since in general the last terms on the right hand sides in Eqn. (2.17) and (2.18) are much smaller

than the first terms, they could be neglected:

$$q_i = -\rho_f \kappa_{ij} p_{,j} \quad (2.19)$$

$$h_i = -\kappa_{ij}^T T_{,j} \quad (2.20)$$

### 2.2.2 Conservation Laws

Three conservation laws are involved in the thermo-poroelastic analysis.

The first is a momentum balance or equilibrium equation, for the case of no body force:

$$\sigma_{ij,j} = 0 \quad (2.21)$$

The second is the fluid mass conservation equation, for case of no fluid mass supply:

$$\frac{\partial \Delta m}{\partial t} = -q_{i,i} \quad (2.22)$$

The above equations (Eqn. (2.21) and (2.22)) are the same as those of an isothermal case.

The third equation is an energy conservation equation. In fractured reservoirs with very low matrix permeability, fluid flows mainly within fractures. For such systems, convective heat transfer within the low permeable rock matrix is negligible (Delaney 1982) and is not considered. Heat transfer in the reservoir is assumed to occur via fracture flow and heat conduction between rock matrix and fracture fluid. If there is no heat source:

$$\rho_t C_t \frac{\partial T}{\partial t} = -h_{t,i} - C_f T q_{i,i} \quad (2.23)$$

Where  $\rho_t$  is the total mass density;  $C_t$  and  $C_f$  are the specific heat of the total mass and pore fluid, respectively. The first and last term on the right-hand side of this equation represents the conductive heat transfer through the porous matrix and the convective heat transfer via fluid flow through pores, respectively.

### 2.2.3 Field Equations

The deformation of a material is described by a strain-displacement relation as follows:

$$\varepsilon_{ij} = \frac{1}{2}(u_{i,j} + u_{j,i}) \quad (2.24)$$

Substituting Eqn. (2.24) into Eqn. (2.9), equilibrium equation Eqn. (2.21) can be reduced to a modified Navier equation in terms of displacement, which is the deformation field equation:

$$G u_{i,jj} + \left(K + \frac{G}{3}\right) u_{j,ji} - \alpha p_{,j} - \gamma_1 T_{,j} = 0 \quad (2.25)$$

$$\gamma_1 = \frac{2G(1+\nu)}{3(1-2\nu)} \alpha_m^T \quad (2.26)$$

Next, we consider the fluid diffusion field equation. Differentiating Eqn. (2.16) with respect to time, we have:

$$\frac{\partial}{\partial t} \zeta = \frac{1}{2G} \frac{\alpha(1-2\nu)}{(1+\nu)} \left( \frac{\partial \sigma_{kk}}{\partial t} + \frac{3}{B} \frac{\partial p}{\partial t} \right) + (\alpha_p^T - \alpha_f^T \phi) \frac{\partial T}{\partial t} \quad (2.27)$$

The relationship between material properties is:

$$\frac{2GB^2(1+\nu)(1+\nu_u)}{9(\nu_u - \nu)} = \frac{2G(1+\nu)}{1-2\nu} \frac{1}{\alpha} \frac{B}{3} \quad (2.28)$$

Substituting Eqn. (2.19) into (2.22), we have:

$$\frac{\partial \zeta}{\partial t} = \kappa p_{,ij} \quad (2.29)$$

Rewriting Eqn. (2.27) using Eqn. (2.28) and (2.29):

$$\frac{B}{3} \frac{\partial \sigma_{kk}}{\partial t} + \frac{\partial p}{\partial t} + \frac{2GB^2(1+\nu)(1+\nu_u)}{9(\nu_u - \nu)} (\alpha_p^T - \alpha_f^T \phi) \frac{\partial T}{\partial t} - \frac{2GB^2(1+\nu)(1+\nu_u)}{9(\nu_u - \nu)} \kappa p_{,ij} = 0 \quad (2.30)$$

Differentiating Eqn. (2.9) with respect to time:

$$\frac{\partial \sigma_{kk}}{\partial t} = 2G \frac{1+\nu}{1-2\nu} \frac{\partial \varepsilon_{kk}}{\partial t} - 3\alpha \frac{\partial p}{\partial t} - \frac{2G(1+\nu)}{(1-2\nu)} \alpha_m^T \frac{\partial T}{\partial t} \quad (2.31)$$

Then, substituting Eqn. (2.31) back into Eqn. (2.30) and rearranging, we have:

$$\alpha \frac{\partial \varepsilon_{kk}}{\partial t} + \beta \frac{dp}{dt} - \kappa p_{,ij} - \gamma_2 \frac{dT}{dt} = 0 \quad (2.32)$$

$$\beta = \frac{\alpha^2(1-2\nu)(1-2\nu_u)}{2G(\nu_u - \nu)} \quad (2.33)$$

$$\gamma_2 = \alpha \alpha_m^T + \alpha_f^T \phi - \alpha_p^T \quad (2.34)$$

The thermal diffusion field equation is obtained as follows. Substituting Eqn. (2.19) and (2.20)

into the energy conservation equation Eqn. (2.23):

$$\rho_t C_t \frac{\partial T}{\partial t} = k^T T_{,ij} + (\rho_f \kappa C_f T p_{,i})_{,i} \quad (2.35)$$

Rearranging Eqn. (2.35), we have:



$$\frac{\partial T}{\partial t} - c^T T_{,jj} - (\kappa^T T p_{,i})_{,i} = 0 \quad (2.36)$$

In which:

$$c^T = \frac{k^T}{\rho_t C_t} \quad (2.37)$$

$$\kappa^T = \kappa \frac{\rho_f C_f}{\rho_t C_t} \quad (2.38)$$

In summary, Eqn. (2.25), (2.32) and (2.36) are the fully coupled thermo-poroelastic field equations for deformation, fluid diffusion and thermal diffusion, respectively.

### **3. Finite Element Method**

Chapter 2 has described mathematical models for thermo-poroelasticity. The governing equations for thermo-poroelasticity (Eqn. (2.25), (2.32) and (2.36)) are a set of partial differential equations with respect to space and time. Unfortunately, analytical solutions are available only for problems with simple geometry and boundary conditions. Numerical solutions are required for complex problems. Finite element method (FEM) is a powerful numerical tool for solving problems governed by PDEs. This chapter gives a theoretical background for FEM and presents the FEM formulation used for solving the coupled thermo-poroelastic problems. A FORTRAN computer code is extensively developed based on the previous modeling effort by Lee and Ghassemi (2000 and 2011) and Wang and Ghassemi (2011, 2012 and 2013).

#### **3.1 Basis for FEM**

Many physical phenomena can be described in terms of partial differential equations (PDE). Classical analytical solutions only exist for relatively simple geometries and material properties and are generally subjected to many strict assumptions, such as homogeneous, continuum, and simple boundary. To deal with complex physical conditions, such as arbitrary shapes, heterogeneity, and nonlinearity, numerical solutions are required. There exist a large number of numerical methods for solving a set of PDEs, such as finite difference method (FDM), finite element method (FEM), finite volume method (FVM) and boundary element method (BEM). The finite element method (FEM) was firstly developed in the 1950s for the aerospace industry. FEM has become one of the most common numerical tools for solving rock mechanics problems, due to its great flexibility in the treatment of arbitrary geometries, material heterogeneity, anisotropy, non-linear deformability, complex boundary conditions (Hutton 2003).

In the methodology of FEM, the solution domain is divided into small finite elements connected by nodes, and the governing equations are approximated over these finite elements. The FEM consists of the following steps:

(1) Discretization/meshing: The solution domain is discretized into small finite elements which could have simple but arbitrary geometry with finite number of degree of freedoms.

(2) Element formulation: The equations of the individual elements are established according to the properties of the elements.

(3) Matrix assembly: The global equations for the entire system are obtained from the elemental equations based on element connectivity.

(4) Solution and post-processing: After the initial and boundary conditions are imposed, the equations are solved. The results of the FEM solution are shown in displacement, pressure, temperature, etc. Additional parameters such as strains and stresses can also be computed after the FEM solution.

### 3.1.1 Spatial Discretization

Numerical implementation of the governing equations of thermo-poroelasticity requires both spatial and temporal discretization. Spatial discretization is performed by dividing the solution domain into a number of finite elements. Temporal discretization is performed by dividing the time domain into a number of time steps and utilizing a time marching scheme.

The PDEs of physical problems need to be firstly discretized in their spatial dimensions. Several approaches can be used to transform the PDEs to its finite element discrete formula. The most popular approach is the Galerkin method. The following simple example is present to explain the technique of applying the Galerkin method in the finite element formulation (Smith and Griffiths 2004).

Figure 3.1 shows the simplest solid element, an 1D rod element of length  $L$ , with two end nodes 1 and 2.

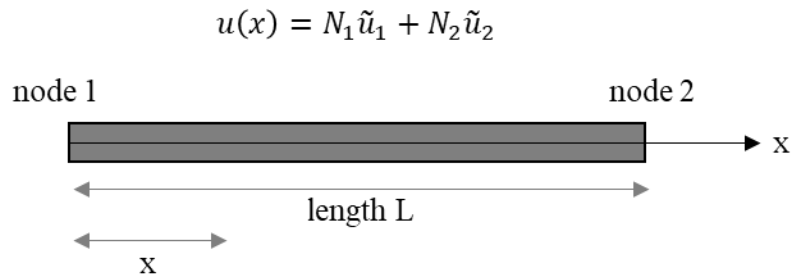


Figure 3.1. Example of a 1D rod element with two nodes.

When an external force is applied on this element, the differential equation for displacement can be written as (Smith and Griffiths 2004):

$$EA \frac{d^2 u}{dx^2} + F = 0 \quad (3.1)$$

Where  $E$  is the Young's modulus;  $A$  is the cross sectional area;  $u$  is the longitudinal displacement along the axial loading direction ( $x$  direction);  $F$  is the applied body force (units of force/length).

In FEM, the continuous variables can be approximated in terms of their nodal values interpolating by shape functions.

$$u = \sum_{i=1}^m N_i \tilde{u}_i \quad (3.2)$$

Where  $u$  is the polynomial interpolation of continuous displacement;  $\tilde{u}_i$  is the value on the corresponding node  $i$ ;  $N_i$  is the interpolation function, and is generally referred to as a shape function; and  $m$  is the number of nodes.

For this rod element, we have:

$$u(x) = N_1 \tilde{u}_1 + N_2 \tilde{u}_2 \quad (3.3)$$

Where  $N_1 = 1 - \frac{x}{L}$  and  $N_2 = \frac{x}{L}$ .

Eqn. (3.3) can be rewritten as:

$$u = [N_1 \quad N_2] \begin{Bmatrix} \tilde{u}_1 \\ \tilde{u}_2 \end{Bmatrix} = [N] \{\tilde{u}\} \quad (3.4)$$

After substituting Eqn. (3.4) in Eqn. (3.1), the differential equation has now been replaced by an equation in terms of the nodal values, which has the following approximate form:

$$EA \frac{d^2}{dx^2} [N_1 \quad N_2] \begin{Bmatrix} \tilde{u}_1 \\ \tilde{u}_2 \end{Bmatrix} + F = R \quad (3.5)$$

Where  $R$  is a nonzero residual, which is a measure of the error introduced during discretization.

To minimize the residual, many methods have been developed, such as collocation, subdomain, Galerkin and least squares methods (Smith and Griffiths 2004). The difference between them depends on the choice of the weighting functions.

The most popular method is the Galerkin method (Finlayson 1972). It minimizes residual by multiplying or weighting the residual in the above equations by each shape functions in turn, integrating over the element and equating to zero.

$$\int_0^L \begin{Bmatrix} N_1 \\ N_2 \end{Bmatrix} EA \frac{d^2}{dx^2} [N_1 \quad N_2] dx \begin{Bmatrix} \tilde{u}_1 \\ \tilde{u}_2 \end{Bmatrix} + \int_0^L \begin{Bmatrix} N_1 \\ N_2 \end{Bmatrix} F dx = \begin{Bmatrix} 0 \\ 0 \end{Bmatrix} \quad (3.6)$$

Since in this example linear shape functions are used, double differentiation of these functions would cause them to vanish, which is not desirable. This difficulty is resolved by applying Green's theorem, i.e., integration by parts (Smith and Griffiths 2004). Integral terms with double differentiation can be calculated as:

$$\int N_i \frac{\partial^2 N_j}{\partial x^2} dx = -\int \frac{\partial N_i}{\partial x} \frac{\partial N_j}{\partial x} dx + \text{boundary terms (usually neglected)} \quad (3.7)$$

Assuming  $EA$  and  $F$  are not functions of  $x$ , Eqn. (3.6) becomes:

$$-EA \int_0^L \begin{bmatrix} \frac{\partial N_1}{\partial x} & \frac{\partial N_1}{\partial x} & \frac{\partial N_1}{\partial x} & \frac{\partial N_2}{\partial x} \\ \frac{\partial N_2}{\partial x} & \frac{\partial N_2}{\partial x} & \frac{\partial N_2}{\partial x} & \frac{\partial N_2}{\partial x} \end{bmatrix} dx \begin{Bmatrix} \tilde{u}_1 \\ \tilde{u}_2 \end{Bmatrix} + F \int_0^L \begin{Bmatrix} N_1 \\ N_2 \end{Bmatrix} dx = \begin{Bmatrix} 0 \\ 0 \end{Bmatrix} \quad (3.8)$$

After integration, we have:

$$-EA \begin{bmatrix} \frac{1}{L} & -\frac{1}{L} \\ -\frac{1}{L} & \frac{1}{L} \end{bmatrix} \begin{Bmatrix} \tilde{u}_1 \\ \tilde{u}_2 \end{Bmatrix} + F \begin{Bmatrix} \frac{L}{2} \\ \frac{L}{2} \end{Bmatrix} = \begin{Bmatrix} 0 \\ 0 \end{Bmatrix} \quad (3.9)$$

The above equation represents the rod element stiffness relationship, and it is usually simplified using matrix notation as:

$$[K]\{\tilde{u}\} = \{\tilde{f}\} \quad (3.10)$$

Where  $[K]$  is the element stiffness matrix;  $\{\tilde{u}\}$  is the element nodal displacement vector, and  $\{\tilde{f}\}$  is the element nodal force vector.

### 3.1.2 Finite Elements and Shape Functions

The choice of element type and shape function is essential for spatial discretization, and it depends on the purpose of numerical simulations. The commonly used types of 2D finite elements include triangular and quadrilateral elements. In 3D, tetrahedrons and hexahedrons are commonly used.

Shape functions are often taken to be polynomials which depend on the element type and the number of nodes in the element. Examples of various types of 2D and 3D elements and their shape functions are illustrated in Figure 3.2. In this study, 8-node hexahedron (brick) element is used for discretization. As mentioned previously, Green's theorem is used to avoid the vanishing of shape functions under a high order of differentiation. The general pattern of how terms in a differential equation appear in the matrix form after discretization has been summarized in Table 3.1 (Smith and Griffiths 2004).

Table 3.1 General remarks on the PDE discretization (Smith and Griffiths 2004)

Term in differential equation	Term in matrix equation
$u$	$\int N_i N_j dx$
$\frac{du}{dx}$	$\int N_i \frac{dN_j}{dx} dx$
$\frac{d^2u}{dx^2}$	$-\int \frac{dN_i}{dx} \frac{dN_j}{dx} dx$
$\frac{d^4u}{dx^4}$	$\int \frac{d^2N_i}{dx^2} \frac{d^2N_j}{dx^2} dx$

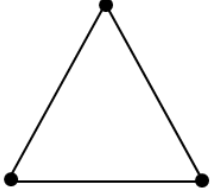

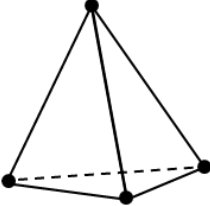
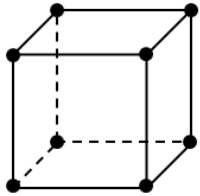
 2D 3-node triangular element	$N_1 = \xi$ $N_2 = \eta$ $N_3 = 1 - \eta - \xi$
 2D 4-node quadrilateral element	$N_1 = \frac{1}{4}(1 - \xi)(1 - \eta) \quad N_3 = \frac{1}{4}(1 + \xi)(1 + \eta)$ $N_2 = \frac{1}{4}(1 - \xi)(1 + \eta) \quad N_4 = \frac{1}{4}(1 + \xi)(1 - \eta)$
 3D 4-node tetrahedron element	$N_1 = 1 - \xi - \eta - \zeta$ $N_2 = \xi$ $N_3 = \eta$ $N_4 = \zeta$
 3D 8-node hexahedron element	$N_1 = (1 - \xi)(1 - \eta)(1 - \zeta) / 8 \quad N_5 = (1 - \xi)(1 - \eta)(1 + \zeta) / 8$ $N_2 = (1 + \xi)(1 - \eta)(1 - \zeta) / 8 \quad N_6 = (1 + \xi)(1 - \eta)(1 + \zeta) / 8$ $N_3 = (1 + \xi)(1 + \eta)(1 - \zeta) / 8 \quad N_7 = (1 + \xi)(1 + \eta)(1 + \zeta) / 8$ $N_4 = (1 - \xi)(1 + \eta)(1 - \zeta) / 8 \quad N_8 = (1 - \xi)(1 + \eta)(1 + \zeta) / 8$

Figure 3.2. Commonly used 2D and 3D finite elements and their shape functions.

### 3.1.3 Temporal Discretization

For time dependent problems, there exist various methods to discretize the time steps in FEM formulation. Here, we introduce the most commonly used method for time integration, the  $\theta$ -method.

In the  $\theta$ -method, the time derivative of a variable is approximated using a linear interpolation between its values at two consecutive time steps as (Pepper and Heinrich 2017):



$$\frac{d\phi}{dt} = \frac{\theta\phi_1 + (1-\theta)\phi_0}{\Delta t} \quad (3.11)$$

Where  $\phi$  is the time dependent variable;  $\theta$  is the relaxation parameter;  $\Delta t$  is the time step; and the subscripts represent two consecutive time steps “0” and “1”.

The solution from time step “0” to “1” is obtained using a weighted average of the gradients at the beginning and end of the time interval:

$$\phi = \theta\phi_1 + (1-\theta)\phi_0 \quad (3.12)$$

The parameter  $\theta$  is used to control the accuracy and stability of the solution (Pepper and Heinrich 2017). It is usually specified within the range between 0 and 1. The commonly used values are:  $\theta=0$  (explicit Euler forward method),  $\theta=1/2$  (Crank-Nicolson method) (Crank and Nicolson 1947) and  $\theta=1$  (fully implicit backward method). The solution is unconditionally stable when  $\theta \geq 1/2$  (Smith and Griffiths 2004). In this study,  $\theta$  is assumed to be 1, which means fully implicit time stepping scheme in FEM discretization.

## 3.2 FEM Solution to Thermo-poroelasticity

### 3.2.1 Discretization in Space

In the Chapter 2, the governing equations (Eqn. (2.25), (2.32) and (2.36)) for the case of thermo-poroelasticity are given as follows:

$$Gu_{i,jj} + (K + \frac{G}{3})u_{j,ji} - \alpha p_{,j} - \gamma_1 T_{,j} = 0 \quad (3.13)$$

$$\alpha \frac{\partial \varepsilon_{kk}}{\partial t} + \beta \frac{dp}{dt} - \kappa p_{,jj} - \gamma_2 \frac{dT}{dt} = 0 \quad (3.14)$$

$$\frac{\partial T}{\partial t} - c^T T_{,jj} - (\kappa^T T p_{,i})_{,i} = 0 \quad (3.15)$$

The above governing equations use the second order for the space domain and the first order for the time domain. Firstly, spatial discretization is performed using 8-node brick element.

According to Eqn. (3.2), the numerical interpolation of displacement, pore pressure and temperature can be expressed as:

$$u = [N_u][\tilde{u}] \quad (3.16)$$

$$p = [N_p][\tilde{p}] \quad (3.17)$$

$$T = [N_T][\tilde{T}] \quad (3.18)$$

Where  $u$ ,  $p$ , and  $T$  are displacement, pore pressure, and temperature field variables, respectively;  $\tilde{u}$ ,  $\tilde{p}$  and  $\tilde{T}$  are nodal values of displacement, pore pressure and temperature, respectively;  $N_u$ ,  $N_p$  and  $N_T$  are shape function matrices.

For a 3D 8-node brick element:

$$u = \{u_x \quad u_y \quad u_z\}^T \quad (3.19)$$

$$[\tilde{u}] = [\tilde{u}_x^1 \quad \tilde{u}_y^1 \quad \tilde{u}_z^1 \quad \dots \quad \tilde{u}_x^8 \quad \tilde{u}_y^8 \quad \tilde{u}_z^8]^T \quad (3.20)$$

$$[\tilde{p}] = [\tilde{p}^1 \quad \dots \quad \tilde{p}^8]^T \quad (3.21)$$

$$[\tilde{T}] = [\tilde{T}^1 \quad \dots \quad \tilde{T}^8]^T \quad (3.22)$$

$$[N_u] = \begin{bmatrix} N_u^1 & 0 & 0 & \dots & N_u^8 & 0 & 0 \\ 0 & N_u^1 & 0 & \dots & 0 & N_u^8 & 0 \\ 0 & 0 & N_u^1 & \dots & 0 & 0 & N_u^8 \end{bmatrix} \quad (3.23)$$

$$[N_p] = [N_p^1 \quad \dots \quad N_p^8] \quad (3.24)$$

$$[N_T] = [N_T^1 \quad \dots \quad N_T^8] \quad (3.25)$$

The single and double differentiations of the variables can be expressed as:

$$\{\varepsilon\} = [B_u]\{\tilde{u}\} \quad (3.26)$$

$$\{p_{,j}\} = [B_p]\{\tilde{p}\} \quad (3.27)$$

$$\{T_{,j}\} = [B_T]\{\tilde{T}\} \quad (3.28)$$

$$\{p_{,jj}\} = -[B_p]^T [B_p]\{\tilde{p}\} \quad (3.29)$$

Where  $[B_u]$ ,  $[B_p]$  and  $[B_T]$  calculate the derivatives of shape functions for displacement, pore pressure and temperature, respectively:

$$[B_u] = \begin{bmatrix} N_{u,x}^1 & 0 & 0 & \dots & N_{u,x}^8 & 0 & 0 \\ 0 & N_{u,y}^1 & 0 & \dots & 0 & N_{u,y}^8 & 0 \\ 0 & 0 & N_{u,z}^1 & \dots & 0 & 0 & N_{u,z}^8 \\ N_{u,x}^1 & N_{u,y}^1 & 0 & \dots & N_{u,x}^8 & N_{u,y}^8 & 0 \\ 0 & N_{u,y}^1 & N_{u,z}^1 & \dots & 0 & N_{u,y}^8 & N_{u,z}^8 \\ N_{u,x}^1 & 0 & N_{u,z}^1 & \dots & N_{u,x}^8 & 0 & N_{u,z}^8 \end{bmatrix} \quad (3.30)$$

$$[B_p] = \begin{bmatrix} N_{p,x}^1 & \dots & N_{p,x}^8 \\ N_{p,y}^1 & \dots & N_{p,y}^8 \\ N_{p,z}^1 & \dots & N_{p,z}^8 \end{bmatrix} \quad (3.31)$$

$$[B_T] = \begin{bmatrix} N_{T,x}^1 & \dots & N_{T,x}^8 \\ N_{T,y}^1 & \dots & N_{T,y}^8 \\ N_{T,z}^1 & \dots & N_{T,z}^8 \end{bmatrix} \quad (3.32)$$

Substituting the shape functions for the factors (Eqn. (3.16), (3.17) and (3.18)) into the thermo-poroelasticity field equations (Eqn. (3.13), (3.14) and (3.15)), and then using Galerkin's method, the finite element formulations for displacement, pore pressure and temperature can be written as (Zhou and Ghassemi 2009; Lee and Ghassemi 2010; Wang and Ghassemi 2011):

$$K_u \tilde{u} - C_{up} \tilde{p} - C_{uT} \tilde{T} = F_u \quad (3.33)$$

$$C_{pu} \frac{d\tilde{u}}{dt} + K_p \tilde{p} + C_{pp} \frac{d\tilde{p}}{dt} - C_{pT} \frac{d\tilde{T}}{dt} = -F_q \quad (3.34)$$

$$C_{TT} \frac{d\tilde{T}}{dt} + K_{cdT} \tilde{T} + K_{cvT} \tilde{T} = -F_h \quad (3.35)$$

Where  $F_u$ ,  $F_q$ , and  $F_h$  are the term of external force, fluid and heat sink/source, respectively.

Other matrices are described as following:

$$K_u = \int_{V_e} B_u^T D B_u dV \quad (3.36)$$

$$C_{up} = \int_{V_e} B_u^T \alpha I N_p dV \quad (3.37)$$

$$C_{uT} = \int_{V_e} B_u^T \gamma_1 I N_T dV \quad (3.38)$$

$$K_p = \int_{V_e} B_p^T \kappa B_p dV \quad (3.39)$$

$$C_{pu} = C_{up}^T \quad (3.40)$$

$$C_{pT} = \int_{V_e} N_p^T \gamma_2 N_T dV \quad (3.41)$$

$$C_{pp} = \int_{V_e} N_p^T \beta N_p dV \quad (3.42)$$

$$K_{cdT} = \int_{V_e} B_T^T C^T B_T dV \quad (3.43)$$

$$K_{cvT} = \int_{V_e} B_T^T \kappa^T B_p \tilde{p} N_T dV \quad (3.44)$$

$$C_{TT} = \int_{V_e} N_T^T N_T dV \quad (3.45)$$

$$[D] = \frac{E(1-\nu)}{(1+\nu)(1-2\nu)} \begin{bmatrix} 1 & \frac{\nu}{1-\nu} & \frac{\nu}{1-\nu} & 0 & 0 & 0 \\ \frac{\nu}{1-\nu} & 1 & \frac{\nu}{1-\nu} & 0 & 0 & 0 \\ \frac{\nu}{1-\nu} & \frac{\nu}{1-\nu} & 1 & 0 & 0 & 0 \\ 0 & 0 & 0 & \frac{1-2\nu}{2(1-\nu)} & 0 & 0 \\ 0 & 0 & 0 & 0 & \frac{1-2\nu}{2(1-\nu)} & 0 \\ 0 & 0 & 0 & 0 & 0 & \frac{1-2\nu}{2(1-\nu)} \end{bmatrix} \quad (3.46)$$

$$I = [1 \ 1 \ 1 \ 0 \ 0 \ 0]^T \quad (3.47)$$

### 3.2.2 Discretization in Time

The finite element formulations derived in the previous section also include time dependent variables for displacement, pore pressure and temperature, and require temporal discretization. After differentiating both sides with time, the set of equations (Eqn. (3.33), (3.34) and (3.35)) can be rearranged in the matrix form as:

$$\begin{bmatrix} K & -C_{up} & -C_{uT} \\ C_{pu} & C_{pp} & -C_{pT} \\ 0 & 0 & C_{TT} \end{bmatrix} \begin{bmatrix} \frac{d\tilde{u}}{dt} \\ \frac{d\tilde{p}}{dt} \\ \frac{d\tilde{T}}{dt} \end{bmatrix} + \begin{bmatrix} 0 & 0 & 0 \\ 0 & K_p & 0 \\ 0 & 0 & K_{cdT} + K_{cvT} \end{bmatrix} \begin{bmatrix} \tilde{u} \\ \tilde{p} \\ \tilde{T} \end{bmatrix} = \begin{bmatrix} \dot{F}_u \\ F_q \\ F_h \end{bmatrix} \quad (3.48)$$

To discretize the time domain, the  $\theta$ -approximation method (Eqn. (3.11)) is used:

$$\frac{du}{dt} = \frac{\theta u_t + (1-\theta)u_{t-\Delta t}}{\Delta t} \quad (3.49)$$

$$\frac{dp}{dt} = \frac{\theta p_t + (1-\theta)p_{t-\Delta t}}{\Delta t} \quad (3.50)$$

$$\frac{dT}{dt} = \frac{\theta T_t + (1-\theta)T_{t-\Delta t}}{\Delta t} \quad (3.51)$$

Substituting the above equations back into Eqn. (3.48), we have:

$$\begin{bmatrix} K & -C_{up} & -C_{uT} \\ C_{pu} & C_{pp} & -C_{pT} \\ 0 & 0 & C_{TT} \end{bmatrix} \begin{bmatrix} \Delta u \\ \Delta p \\ \Delta T \end{bmatrix} + \begin{bmatrix} 0 & 0 & 0 \\ 0 & \Delta t K_p & 0 \\ 0 & 0 & \Delta t (K_{cdT} + K_{cvT}) \end{bmatrix} \begin{bmatrix} u_{t-\Delta t} + \theta \Delta u \\ p_{t-\Delta t} + \theta \Delta p \\ T_{t-\Delta t} + \theta \Delta T \end{bmatrix} = \begin{bmatrix} \Delta t \dot{F}_u \\ \Delta t F_q \\ \Delta t F_h \end{bmatrix} \quad (3.52)$$

It can be rearranged as:

$$\begin{bmatrix} K & -C_{up} & -C_{uT} \\ C_{pu} & C_{pp} + \Delta t \theta C_{pp} & -C_{pT} \\ 0 & 0 & C_{TT} + \Delta t \theta (K_{cdT} + K_{cvT}) \end{bmatrix} \begin{bmatrix} \Delta u \\ \Delta p \\ \Delta T \end{bmatrix} = \begin{bmatrix} \Delta t \dot{F}_u \\ \Delta t F_q - \Delta t K_p p_{t-\Delta t} \\ \Delta t F_h - \Delta t (K_{cdT} + K_{cvT}) T_{t-\Delta t} \end{bmatrix} \quad (3.53)$$

In this work,  $\theta$  is set to be 1, which means implicit scheme in spatial discretization. The finite element formula of the governing field equations in thermo-poroelasticity is obtained as (Zhou and Ghassemi 2009; Wang and Ghassemi 2011):

$$\begin{bmatrix} K & -C_{up} & -C_{uT} \\ C_{pu} & C_{pp} + \Delta t C_{pp} & -C_{pT} \\ 0 & 0 & C_{TT} + \Delta t (K_{cdT} + K_{cvT}) \end{bmatrix} \begin{bmatrix} \Delta u \\ \Delta p \\ \Delta T \end{bmatrix} = \begin{bmatrix} \Delta t \dot{F}_u \\ \Delta t F_q - \Delta t K_p p_{t-\Delta t} \\ \Delta t F_h - \Delta t (K_{cdT} + K_{cvT}) T_{t-\Delta t} \end{bmatrix} \quad (3.54)$$

Where the primary unknowns  $\Delta u$ ,  $\Delta p$  and  $\Delta T$  are the incremental values of displacement, pore pressure and temperature between successive time steps, respectively;  $\Delta t$  is the time step size.

For each node, there are a total of 5 degree of freedoms: 3 for displacements ( $u_x$ ,  $u_y$  and  $u_z$ ), 1 for pore pressure  $p$  and 1 for temperature  $T$ . Therefore, for an 8-node brick element, Eqn. (3.54) represents a set of 40 equations.

### 3.2.3 Boundary Conditions

Before solving the finite element equations, initial and boundary conditions need to be applied. The initial conditions, such as in-situ stresses, initial pressure and temperature, are relatively easy to handle and can be directly defined on the related elements/nodes at the beginning of time.

The numerical model for coupled fluid flow and solid deformation problems should be able to handle various types of boundary conditions that may arise in different operation conditions (Raghavan and Chin 2004). The boundary conditions for the fluid phase include the prescribed wellbore pressure boundary or the flow rate boundary. For the solid phase, either the prescribed displacement or stress boundary condition could be applied.

Boundary conditions of explicit variables, such as displacement, injection pressure and injection temperature, can be defined by the penalty method. In this method, the corresponding diagonal entry in the stiffness matrix on the left hand side is multiplied by a large number (e.g.,  $10^{30}$ ), and the corresponding entry on the right hand side vector is replaced by the prescribed boundary values scaled by the same large number. This is to impose a prescribed known value on the boundary nodes for the unknown variables.

$$\begin{pmatrix} a_{11} & a_{12} & a_{13} & \dots & \dots & \dots \\ a_{21} & 10^{30} \times a_{22} & a_{23} & \dots & \dots & \dots \\ a_{31} & a_{32} & a_{33} & \dots & \dots & \dots \\ \vdots & \vdots & \vdots & \ddots & \ddots & \ddots \\ \vdots & \vdots & \vdots & \ddots & \ddots & \ddots \\ \vdots & \vdots & \vdots & \ddots & \ddots & \ddots \end{pmatrix} \begin{pmatrix} \Delta u_1 \\ \Delta p_1 \\ \Delta T_1 \\ \vdots \\ \vdots \\ \vdots \end{pmatrix} = \begin{pmatrix} f_1 \\ 10^{30} \times p_{inj} \\ f_3 \\ \vdots \\ \vdots \\ \vdots \end{pmatrix}$$

injection pressure boundary ←

Figure 3.3. The penalty method used to define boundary conditions of displacement, pore pressure and temperature (revised from Lee 2011).

Since Eqn. (3.54) is the incremental version of the FEM formulations, it gives the relative values for displacement, pore pressure and temperature. For a constant boundary condition, the prescribed values are applied only for the first time step, and there will be no relative changes in the following time steps. If the absolute version of the FEM discretization is used, the prescribed values of boundary conditions should be applied in each time step.

The boundary condition of injection rate is defined in a different way. Writing out again the finite element formulations for the fluid mass balance equation:

$$C_{pu} \frac{d\tilde{u}}{dt} + K_p \tilde{p} + C_{pp} \frac{d\tilde{p}}{dt} - C_{pT} \frac{d\tilde{T}}{dt} = -F_q \quad (3.55)$$

The fluid source/sink term on the right hand side can be defined by injection rate  $Q$  at the injection wellbore elements, as shown in Figure 3.4. In the case of injection rate boundary condition, the pore pressure at the wellbore for a given injection rate is computed from FEM as an output.

$$F_q = \sum_{i=1}^{nip} (N_i Q) d\Omega \quad (3.56)$$

Where  $Q$  is the injection rate;  $nip$  is the number of Gaussian points and  $N_i$  is the shape function.

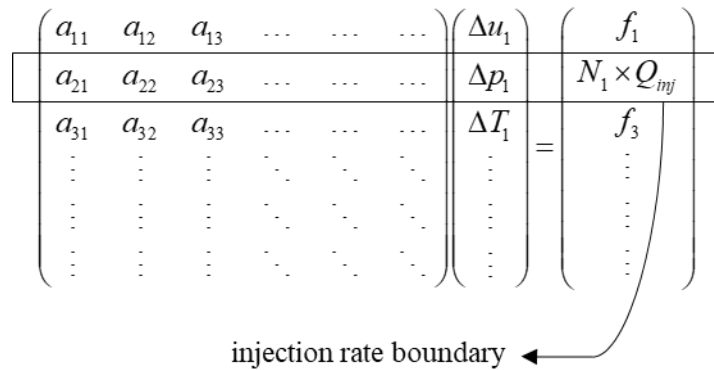


Figure 3.4. The method used to define boundary conditions of injection rate (revised from Lee 2011).



Mechanical loading is another commonly used boundary condition in the coupled fluid flow and solid problems, such as tractions applying on the wellbore surface, and overburden loads acting on the top surface of the simulation domain. The finite element formulation including a mechanical loading term at the boundary for the solid is written as:

$$K_u \tilde{u} - C_{up} \tilde{p} - C_{uT} \tilde{T} = F_u \quad (3.57)$$

$$F_u = \sum_{i=1}^{nip} (N_i f) d\Omega \quad (3.58)$$

The mechanical loading term on the right hand side of Eqn. (3.57) is applied as traction, as shown in Figure 3.5.

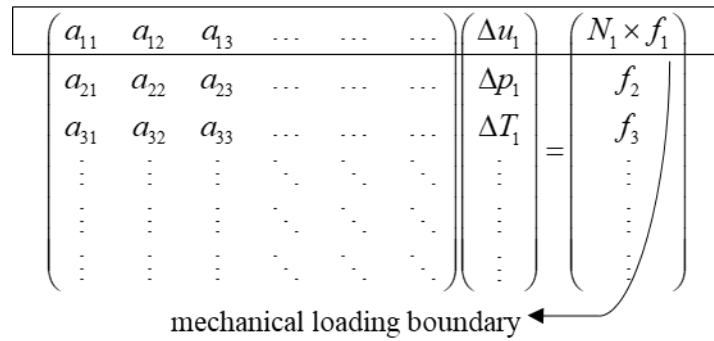


Figure 3.5. The method used to define boundary conditions of mechanical loading (revised from Lee 2011).

The inclusion of gravity is another important concern in geomechanical modeling. There exist two approaches to account for gravity in the simulation (Lee 2011). The first approach is to directly apply gravity to the entire model by specifying a gravitational body force to the vertical direction in each element based on rock density data. The other approach is to use the measured reservoir initial pore pressure and far-field stress as initial background stresses that increases with depth.

One of the most challenging tasks in modeling geomechanics problems is to properly handle the initial in-situ stresses (Fredrich and Fossum 2002). After applying initial and boundary conditions to the model, an initialization step is usually introduced, to ensure the initial stress field equilibrates with the applied loads and boundary conditions at the beginning of actual analysis. This initialization can be done by performing a pre-run to calculate the state of stress generated under the applied conditions and then pre-stressing the model with the state of stress calculated from the pre-run step (Altman 2010; Holzbecher 2017). Ideally, after the initialization, the system should exactly be in equilibrium and produce zero deformations (Fredrich and Fossum 2002; Aliguer et al. 2015). In practice, the model is run for a sufficient time to approach to a nearly equilibrium steady state with displacements and strains converged to a static value. Then the newly developed stresses are considered as the initial stress state and the resulting displacements and strains are reset to zero for subsequent analyses (Hammond and Grzebieta 2000; Fredrich and Fossum 2002). In our simulations, the pore pressure field is initialized with the reservoir pore pressure data and the reservoir regional stresses are considered as initial background stresses. The evolution of reservoir stress distribution during field operations is computed by adding the induced stress changes to the initial background stress in each Gaussian point of the element (Lee 2010).

#### 3.2.4 FEM Modeling for Fractured Reservoirs

In the finite element modeling of a fractured reservoir, the domain is firstly discretized into small elements. Natural fractures are generated and mapped into the FEM mesh using an equivalent continuum approach (Chapter 4). After elemental properties (such as mechanical, hydraulic and thermal properties) are obtained, the coefficient matrix for each element can be formed. They are used to assemble the global coefficient matrix for the entire system in the left hand side of Eqn. (3.54). Next, initial conditions (such as in-situ stress, initial pressure and temperature) and

boundary conditions (such as injection pressure/rate, injection temperature, far field boundary pressure and stress) are defined in the FEM model. The solutions of Eqn. (3.54) gives the incremental results of displacements, pore pressure and temperature. After FEM analysis, a post-processing step is employed to analyze the response of natural fracture networks. The integration scheme of the natural fracture network model to the FEM model will be described in the next Chapter.

## **4. Natural Fracture Network Model**

Reservoir stimulation in unconventional petroleum and geothermal reservoirs is significantly impacted by the presence of natural fractures. Injection causes the change of fluid pressure inside a fracture network, and consequently, changes the effective normal and shear stresses over the fracture surfaces. These changes could cause natural fractures to deform and modify the hydraulic properties of the fracture network. Slip on fractures increases reservoir permeability through shear dilation and results in injection induced micro-seismicity. Natural fractures could also propagate due to gradually increased fluid pressure during stimulation, which contributes to the improvement of fracture network connectivity and reservoir permeability. Numerical modeling of these phenomena can help understand how fractures contribute to the stimulation outcome, which is essential for stimulation optimization.

In this chapter, a brief literature review of the numerical models and approaches for naturally fractured reservoirs is presented. Following that, the natural fracture network modeling approach used in this study is described.

### **4.1 Literature Review**

Due to the variable spatial distribution, orientation and geometry of natural fractures, fluid and heat flow within fractured reservoirs are very complicated. The major components in modeling naturally fractured rocks should include: 1) realistic geometrical representations of complex three dimensional fracture networks, 2) mathematical models for describing flow through the fractured medium, and 3) geomechanical models for describing the dynamic fracture response to injection/production induced stress changes.

#### 4.1.1 Fracture Generation

Based on how natural fractures are generated, the geometrical models of fracture networks can be classified into two categories: deterministic fracture network model which locates individual fracture explicitly (e.g., Kolditz 1995; Hicks et al. 1996; Kolditz and Clauser 1998; Ghassemi et al., 2003; Safari and Ghassemi 2011), and stochastic fracture network model which generates the fractures from statistical distributions (e.g., Long 1983; Dershowitz 1985; Bruel and Cacas 1992; Willis-Richards et al. 1996; Tezuka et al. 2005; Wang and Ghassemi 2011, 2012 and 2013; Farmahini-Farahani and Ghassemi 2016; Cheng and Ghassemi 2017). In practice, since the details of individual fractures embedded in a three dimensional rock volume are not available, a stochastic method is necessary for fracture network modeling.

#### 4.1.2 Mathematical Models

Naturally fractured reservoirs are usually characterized by a system of fractures existing within a background rock matrix. Mathematical models for simulating the behavior of rock mass embedded with natural fractures are grouped into three main classes (National Research Council 1996): (1) discrete fracture network (DFN) models, (2) equivalent continuum models (ECM), and (3) hybrid models.

DFN (e.g., Hudson and La Pointe 1980; Long et al. 1982; La Pointe et al. 1997) treats the rock mass as a set of impermeable blocks, separated by systems of fractures. Since it models individual fractures explicitly, it has the ability to accurately describe the fractured reservoir. However, it could be very expensive regarding computational cost, especially when dealing with a large number of fractures.

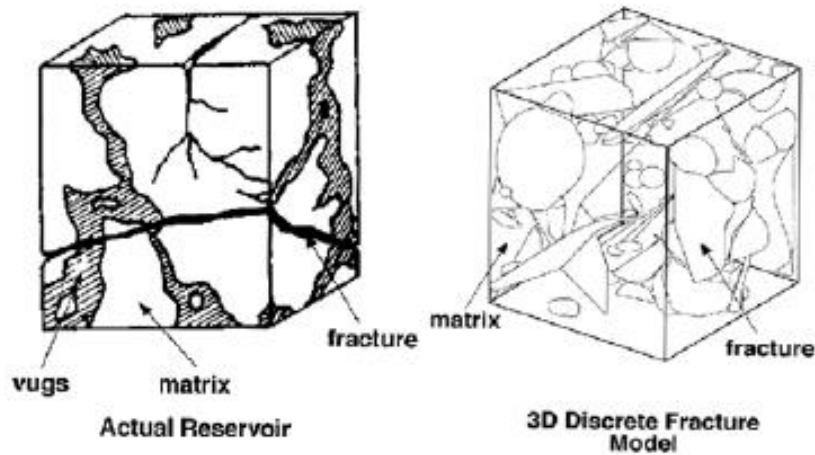


Figure 4.1. Discrete fracture network model for a naturally fractured reservoir (La Pointe et al. 1997).

Conversely, continuum models have the advantage of modeling the fractured masses at a larger scale. In a conventional ECM (e.g., Snow 1970; Long et al. 1982; Oda 1986; Carrera et al. 1990; Lee and Ghassemi 2011), a fractured reservoir is treated as an equivalent porous system and averaged rock properties are assigned. In a dual continuum model (DCM) (e.g., Warren and Root 1963; Kazemi 1969; Kazemi et al. 1976), fracture and rock matrix are modeled as two separate but overlapping systems. Equivalent properties are assigned to the model grids to represent the combined effects of fractures and matrix. These continuum approaches are simple but not accurate, especially for highly heterogeneous porous medium (Lee et al. 1999).

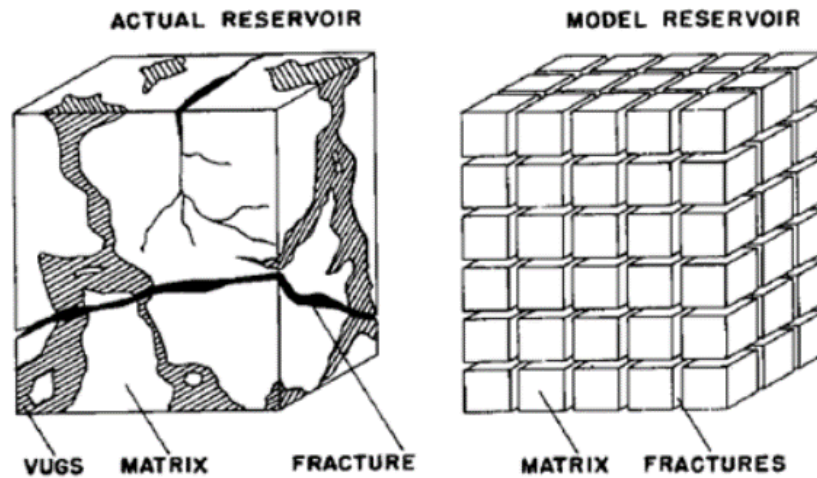


Figure 4.2. Dual porosity model for a naturally fractured reservoir (Warren and Root 1963).

Hybrid models (e.g., Tezuka and Watanabe 2000; Rahman et al. 2002; Wang and Ghassemi 2011, 2012 and 2013) have been considered and developed. It uses a discrete fracture network to estimate the effective properties for continuum approximations. As the hybrid model combines the advantages from both DFN and continuum models, it is efficient but still could provide reasonably accurate solutions.

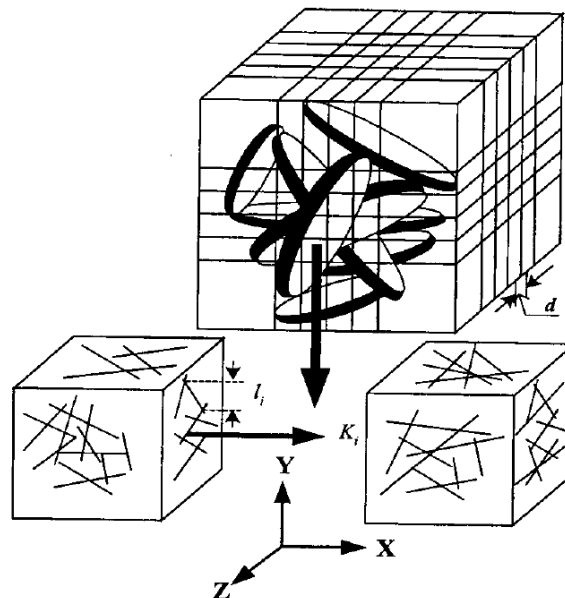


Figure 4.3. Conversion of fractures to continuum mesh in a hybrid model (Rahman et al. 2002).

### 4.1.3 Geomechanical Models

The response of natural fractures to stimulation has been studied for many years, and several geomechanical models are available for simulating low pressure shear stimulation. Willis-Richards et al. (1996) developed a preliminary shear dilation based model. They assumed that the fracture aperture is affected by effective normal stress acting on the fracture surface and shear displacement. This approach has been further developed and widely used for fractured geothermal reservoir stimulation design (e.g., Wang and Ghassemi 2011; Cladouhous et al. 2011). Rahman et al. (2002) improved the shear dilation-based model by considering the combined effects of shear dilation and natural fracture propagation on reservoir performance. It was assumed that fractures might propagate and then interconnect with other fractures due to the gradually increased fluid pressure during injection. An analytical mixed-mode crack propagation model was developed to improve the computational efficiency for analysis of a large number of natural fractures.

However, in most of the shear stimulation models, the pressure distribution within the fractured reservoir is estimated from approximate methods (e.g., Rahman et al. 2002) and the thermo-poroelastic coupling process is neglected (e.g., Willis-Richards et al. 1996; Ucar et al. 2016) or simplified using empirical correlations (e.g., Bruel 2002). Wang and Ghassemi (2011) developed a fully coupled thermal-poroelastic FEM model with stochastic fracture networks. Stress, pore pressure and temperature results obtained from coupled finite element model are used for fracture deformation analysis.

In this work, a numerical model for stimulation in naturally fractured reservoirs is developed. It consists of four main sub-models: 1) a stochastically generated fracture network model describing the fracture geometry and fluid transport within the fractures; 2) a heat transfer model describing the heat transport within the interconnected fracture network; 3) a shear dilation based geomechanical model to analyze fracture deformation and induced micro-seismicity; 3) a natural



fracture propagation model to evaluate fracture extension. The numerical models are described in the following sections.

## 4.2 Stochastic Fracture Network Generation

In this work, a 3D stochastic fracture network model is generated and implemented into the 3D coupled finite element model. Each fracture is assumed to be a penny-shaped circular plate, and is specified by its location (center point), size (radius and aperture) and orientation (dip and azimuth or plane normal direction).

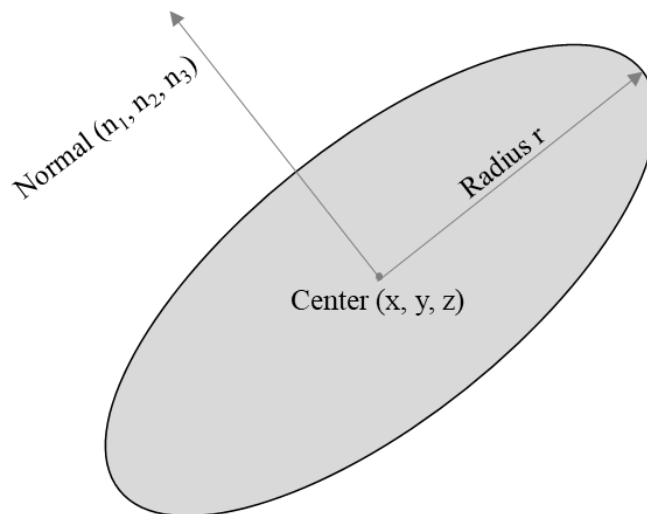


Figure 4.4. Representation of a penny-shaped fracture in the model.

Since the location, size and orientation of individual fracture within a fractured medium are usually unavailable, they can be treated as random variables with inferred probability distributions (Cacas et al. 1990). The following stochastic descriptions are used in this study to generate fracture networks: Poisson's distribution for fracture density, log-normal distribution for the fracture size, and Fisher von Mises distribution for the fracture orientation. Natural fracture characterization

from field observations, core measurements, borehole images, and logging operations provides input values for these stochastic models.

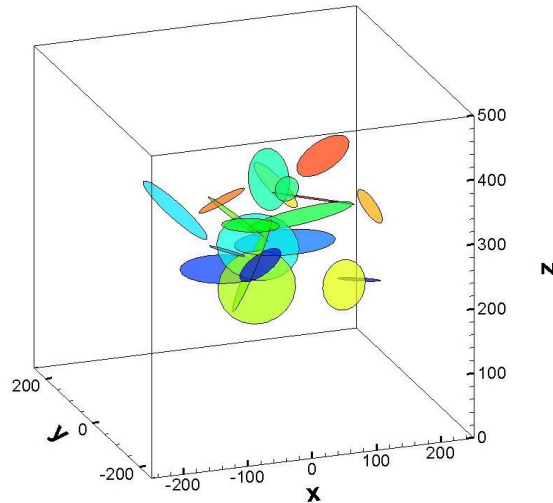


Figure 4.5. Example of a stochastic fracture network of 20 penny-shaped fractures.

#### 4.2.1 Fracture Location

Fracture location is a fundamental parameter describing the spatial distribution of fracture networks. The most common approach is to use the center point of a fracture to represent its location and assume fracture centers are randomly distributed within the simulation region following Poisson distribution (e.g., Long et al. 1982; Bruel 2002; Min et al. 2004; Xu and Dowd 2010; Wang and Ghassemi 2011).

The 3D coordinates  $(x, y, z)$  of fracture centers are assumed independently and uniformly distributed within the domain according to a homogeneous Poisson point process. The detailed procedure has been described in Xu and Dowd (2010): The interest domain  $V$  is firstly divided into several sub-domains. The number of fractures  $N_i$  falling inside a sub-domain  $V_i$  follows a Poisson distribution:

$$P(N_i = k) = \frac{\mu_i^k e^{-\mu_i}}{k!} \quad (4.1)$$

Where  $\mu_i = \lambda V_i$  is the mean value, or the expected number of fractures;  $\lambda$  is the fracture density, i.e., the number of fractures within a unit volume;  $V_i$  is the volume of the sub-domain.

Considering  $N_i = k$ , for each of the  $k$  fractures in the sub-domain  $V_i$ , three values are independently generated using uniform distributions to represent the three coordinates  $(x, y, z)$  of the fracture center point located within the sub-domain. The total number of fractures generated within the domain is the sum of that of all sub-domains,  $N = \sum N_i$ .

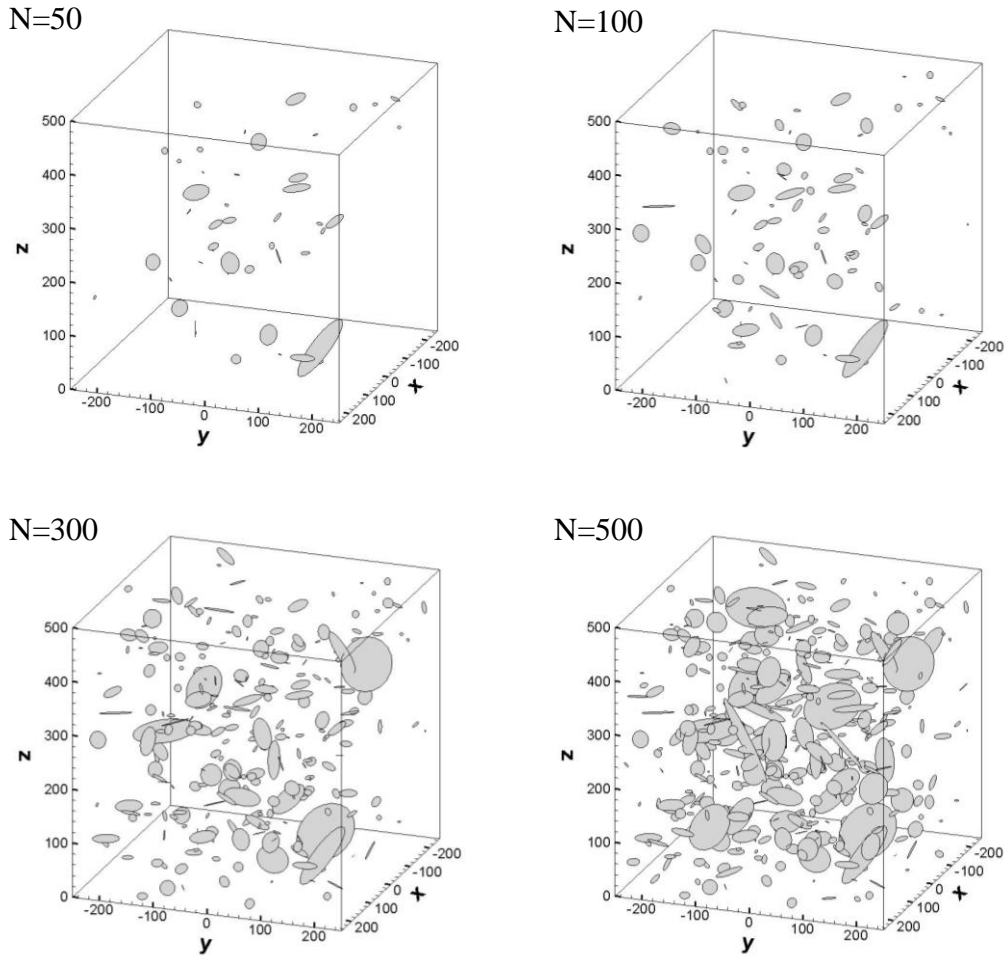


Figure 4.6. Fracture center distributions with different density parameters.

An example of fracture center distributions with different density parameters is shown in Figure 4.6. A network of fractures is randomly generated in a 500 m x 500 m x 500 m 3D domain, on the basis of a fracture density of  $4.0\text{E-}7 \text{ m}^{-3}$ ,  $8.0\text{E-}7 \text{ m}^{-3}$ ,  $2.4\text{E-}6 \text{ m}^{-3}$  and  $4.0\text{E-}6 \text{ m}^{-3}$ , respectively. The total number of fractures is 50, 100, 300 and 500, respectively. Same size ( $\mu=2.3$ ,  $\sigma=0.7$ ) and orientation distribution parameters ( $\kappa=1.0$ ) are used in all cases.

#### 4.2.2 Fracture Size

The size of a penny-shaped fracture is described by its radius and aperture. A log-normal distribution is commonly used for fracture radii (e.g., McMahon, 1971; Baecher et al., 1977; Long et al., 1982; Dershowitz and Einstein, 1988). The choice of a log-normal distribution for fracture size has been validated based on laboratory measurements (e.g., Gentier 1986; Gale 1987; Hakami and Barton 1990) as well as observations in the field (e.g., Bourke et al. 1985; Cacas et al. 1990; Massiot et al. 2015).

The input variables of log-normal distribution include the mean and standard deviation of log values of fracture radii, and the output variables are fracture radii:

$$f(r) = \frac{1}{\sqrt{2\pi}\sigma r} \exp\left[-\frac{(\ln r - \mu)^2}{2\sigma^2}\right] \quad (4.2)$$

Where  $r$  is the fracture radius;  $\mu$  is the mean of  $\ln r$ ; and  $\sigma$  is the standard deviation of  $\ln r$ .

Figure 4.7 shows four sets of fractures with different size distribution parameters. Same distributions for fracture locations ( $N=500$ ) and orientations ( $\kappa=1.0$ ) are assumed. It can be seen that the average size of fractures is controlled by the mean value  $\mu$ , and the spread out range is controlled by the standard deviation  $\sigma$ .

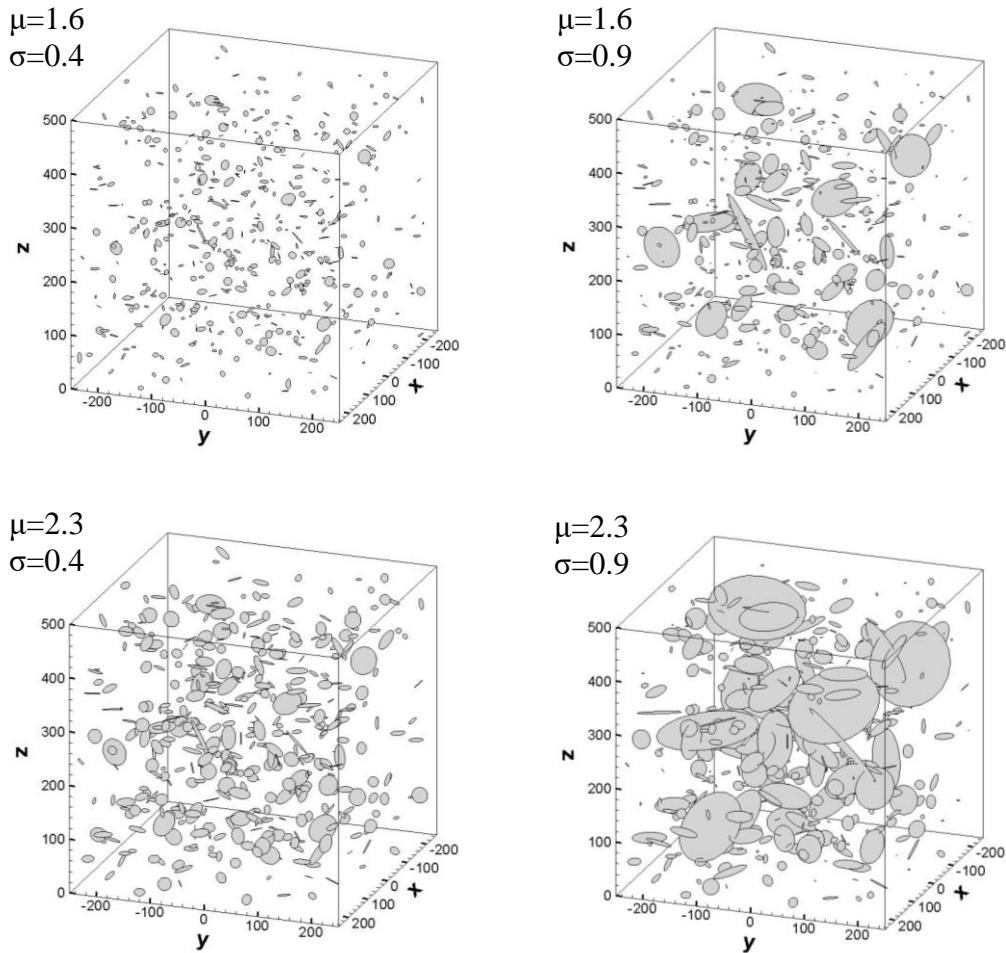


Figure 4.7. Fracture distributions with different size parameters.

Fracture aperture governs fracture permeability, hence, it is an important property that controls the flow and transport in the fractured rock mass. However, compared with the studies on the distribution of fracture length, there are relatively few studies on aperture distribution. Similar distribution functions are usually used for fracture length and aperture in stochastic fracture modeling. Once the fracture length distribution is obtained, fracture radii can be calculated from a length-aperture relationship.

The initial fracture aperture,  $a$ , at zero effective stress, is assumed to be proportional to its radius (Vermilye and Scholz 1995; Willis-Richards et al. 1996; Tezuka and Watanabe 2000).

$$a = \beta r^n \quad (4.3)$$

Where  $r$  is fracture radius;  $\beta$  is an coefficient which can be estimated in terms of the average virgin permeability of the fractured medium (Willis-Richards et al. 1996);  $n$  is the length-aperture exponent which varies between 0.5 and 2 (Bonnet et al. 2001).

#### 4.2.3 Fracture Orientation

The orientation of a fracture can be specified either by its dip angle and azimuth or by the normal of the fracture plane. The most common distribution used for fracture orientations in rock masses is the Fisher von Mises distribution (e.g., Cacas et al. 1990; McKenna and Reeves 2006; Klimczak et al. 2010).

Fracture orientations are assumed to follow the Fisher von Mises distribution around the mean orientation. Two angles (dip and azimuth) are stochastically generated for each fracture:

$$f(\alpha) = \frac{\kappa}{2sh(\kappa)} \exp(\kappa \cos \alpha) \sin \alpha \quad (4.4)$$

Where  $\alpha$  is the angle variable, dip or azimuth angle; and  $\kappa$  is the Fisher coefficient which measures the dispersion in fracture orientations (Fisher 1953). The distribution is uniform for  $\kappa$  equals zero, whereas a high value of  $\kappa$  will generate fractures aligned primarily in one orientation.

The normal directions of each fracture plane are calculated in terms of fracture dip and azimuth angles:

$$l = \sin \delta \sin \gamma \quad (4.5)$$

$$m = \sin \delta \cos \gamma \quad (4.6)$$

$$n = \cos \delta \quad (4.7)$$

Where  $\delta$  and  $\gamma$  are the fracture dip angle and azimuth angle, respectively.

Figure 4.8 shows the examples of four sets of fracture normal directions generated from Fisher von Mises distribution by setting the Fisher parameter equal to 0.2, 1.0, 5.0 and 9.0. The mean orientation (0.866, 0, 0.5) is the same for all four sets. Same distributions for fracture locations (N=500) and size ( $\mu=2.3$ ,  $\sigma=0.7$ ) are assumed.

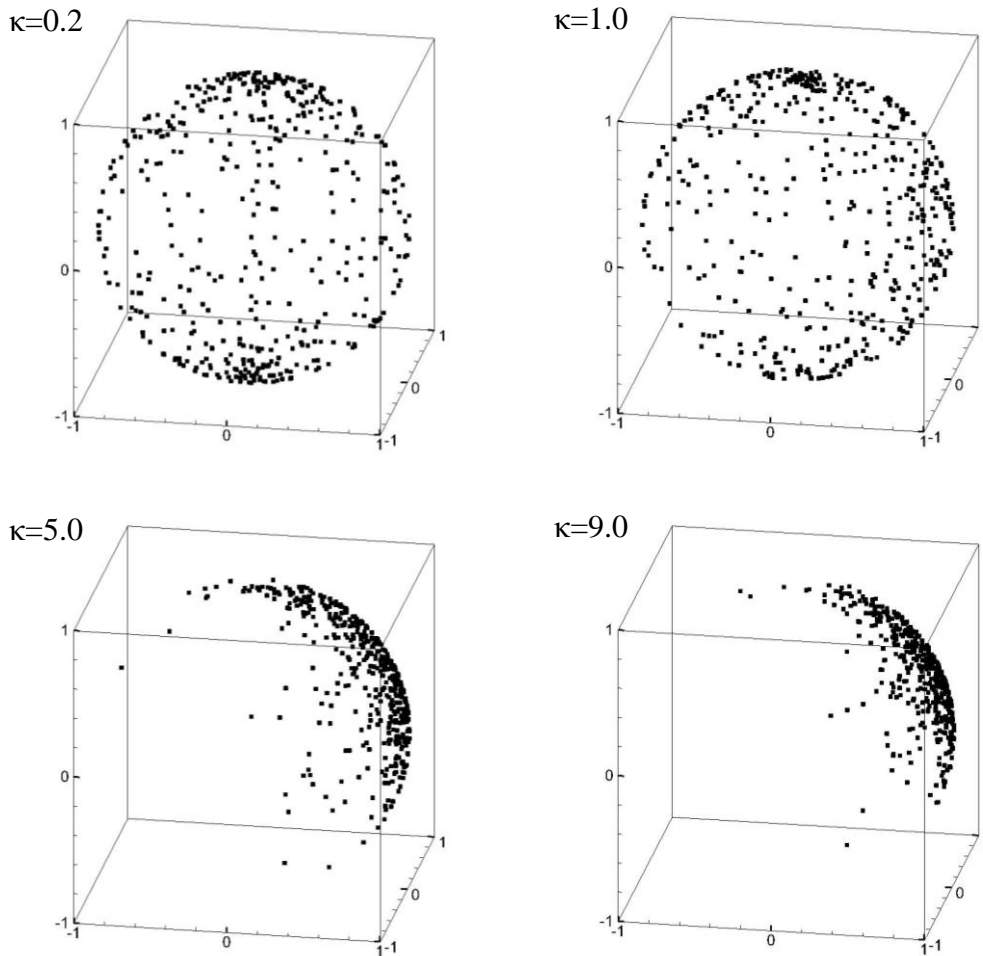


Figure 4.8. Fracture normal directions generated with a mean direction at (0.866, 0, 0.5) and a Fisher parameter of 0.2, 1.0, 5.0, and 9.0, respectively.

The corresponding fracture networks are shown in Figure 4.9. Significant visual differences are seen. The larger the Fisher coefficient, the higher the concentration of the distribution around the

mean direction. Fracture planes generated from a large Fisher coefficient mostly align parallel to each other.

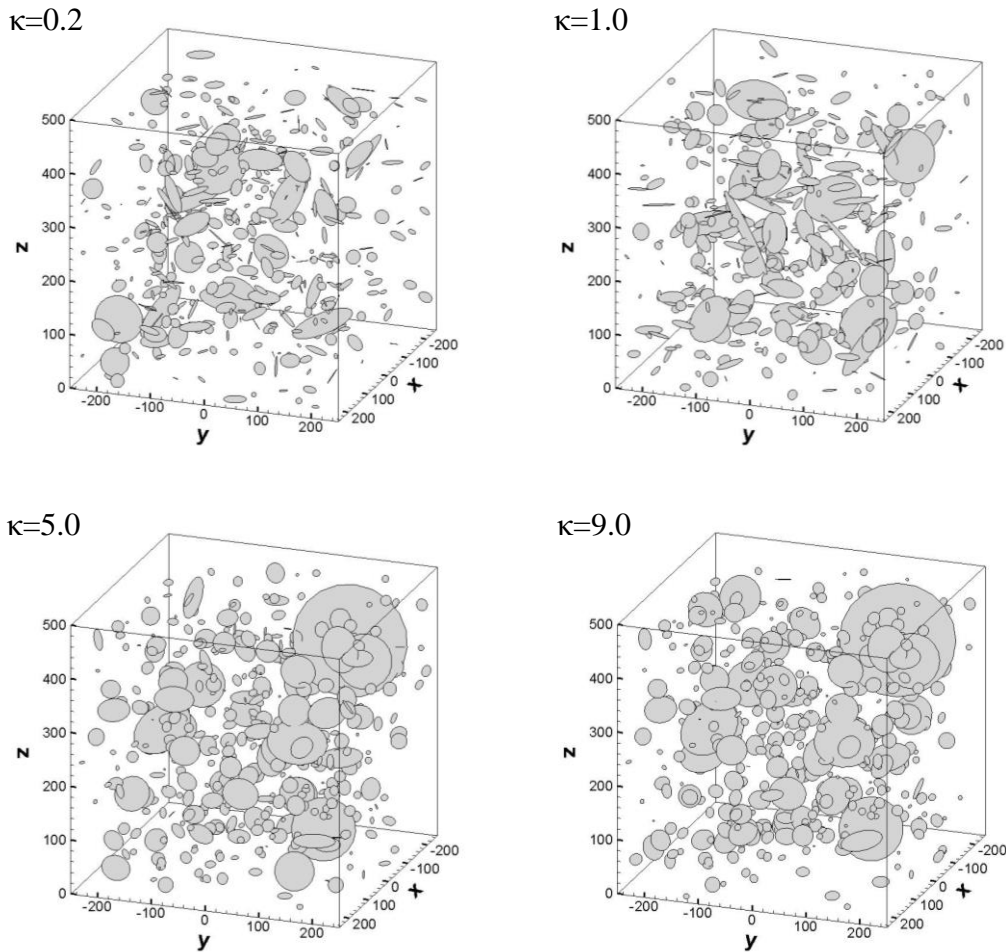


Figure 4.9. Fracture networks with different orientation distributions.

In general, we assume all fractures in the generation domain follow the same distribution with one single set of parameters. However, this approach could be adopted when necessary. More complex fracture models can be generated by defining different distribution parameters for specific fracture sub-sets or by combining several different distributions. In Chapter 7, the natural fracture network in the Newberry EGS site is generated from a hybrid approach. Two sets of fractures are generated: one set is deterministically generated using borehole televiewer (BHTV) scanning results to



represent the fractures intersecting the wellbore; the other set to represent fractures in the near wellbore region is generated stochastically based on field observed micro-earthquake (MEQ) data.

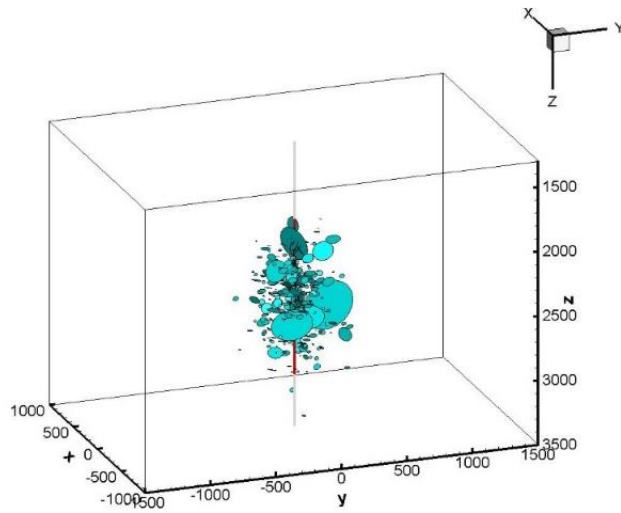


Figure 4.10. An example of the fracture network in the Newberry EGS site generated from hybrid approach.

In addition to penny-shaped fractures, the geometry shape of fractures could also be specified as rectangular, elliptical or polygon. Figure 4.11 shows an example of a fracture network consists of two orthogonal sets of rectangular shaped fractures. This fracture network generation approach has the flexibility to model almost any form of complex fracture networks.

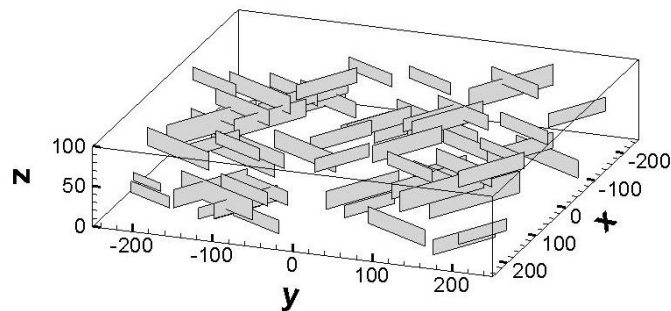


Figure 4.11. An example of a fracture network consists of two orthogonal sets of rectangular shaped fractures.

### 4.3 Equivalent Permeability

Once a fracture network has been generated, it is implemented into the finite element model. In the equivalent continuum approach for modeling fractured rocks, the rock blocks which contain natural fractures are treated as a continuum media with a permeability equivalent to the fractured rock. The equivalent permeability concept used in Rahman et al. (2002) is applied to estimate the overall permeability of the fractured reservoir.

Using finite elements, the reservoir block is discretized into small elements. Before computing equivalent permeability, a preliminary step is to calculate intersections between penny-shaped fractures and finite element faces based on a geometric surface-surface intersection algorithm. Fracture intersection lengths along the x, y and z directions are determined for each element. This algorithm of introducing a fracture network into the finite element mesh is described in Appendix A at the end of this dissertation.

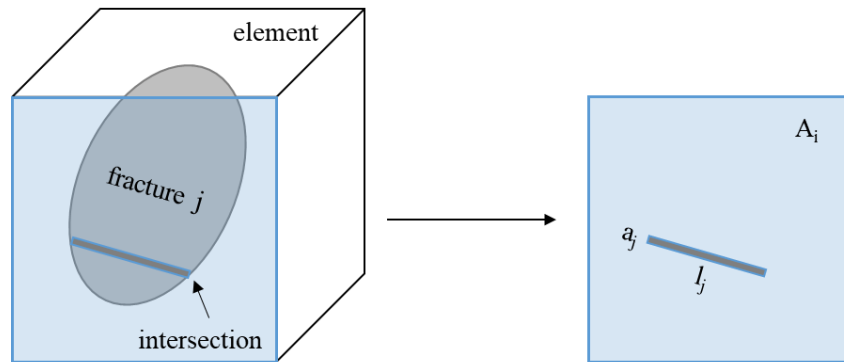


Figure 4.12. Intersection between a penny-shaped fracture and finite element face.

For an individual element, matrix flow and fracture flow are considered separately, and are superposed together.

$$Q = Q_f + Q_m \quad (4.8)$$

For matrix flow, Darcy's law is applied:

$$Q_m = \frac{k_m}{\mu} A_m \nabla p \quad (4.9)$$

The flow within each fracture is assumed to be parallel plate flow without tortuosity, and governed by cubic law (Jing et al. 2000; Rahman et al. 2002):

$$Q_f = \frac{a^3 l}{12\mu} \nabla p \quad (4.10)$$

Therefore, Eqn. (4.8) can be written as:

$$Q = \frac{k_m A_m + a^3 l / 12}{\mu A} A \nabla p \quad (4.11)$$

Where  $Q$  is the volumetric flow rate;  $k_m$  is the matrix permeability;  $l$  is the length of intersection line between the fracture and element interface;  $a$  is the aperture of the fracture;  $\mu$  is the fluid viscosity;  $\nabla p$  is the pressure gradient; and  $A$  is the interface area.

The equivalent permeability at interface  $A$  can be obtained:

$$k = \frac{k_m A_m + (a^2 / 12) A_f}{A} \quad (4.12)$$

Where  $A_f$  is the fracture cross-section area,  $A_f = al$ .

Since each element could contain more than one fracture, the total directional permeability (along x, y or z direction) on an element interface with contributions from all fractures it intersects can be expressed in the following way (Rahman et al. 2002):

$$k = k_m + \sum_{i=1}^n \frac{a_i^3 l_i}{12A} - \frac{k_m \sum_{i=1}^n a_i l_i}{A} \quad (4.13)$$

Where  $n$  is the total number of fractures in the element;  $a_i$  is the aperture of the  $i^{th}$  fracture;  $l_i$  is the length of intersection line on the element interface  $A$ .

In fractured reservoirs with very low matrix permeability, the rock matrix permeability could be several orders ( $10^4$  to  $10^6$ ) lower than fracture permeability. Furthermore, the fracture cross-section area  $A_f$  (in  $\text{mm}^2$ ) is much smaller than the element interface  $A$  (in  $\text{m}^2$ ). The last term in Eqn. (4.13) is a higher order term and can be ignored.

For an individual element, the total permeability is the sum of the rock matrix permeability and the fracture permeability. It should be noted that for a small isolated fracture that are contained within a single element, there will be no intersections between its edge and the element faces. In this case, its bulk fracture permeability is considered zero, and it would not have a contribution to the total equivalent permeability.

$$k = k_m + \sum_{i=1}^n \frac{a_i^3 l_i}{12A} \quad (4.14)$$

To quantify the contributions of natural fractures to the equivalent permeability of the entire reservoir, an average reservoir permeability is introduced. For a reservoir block with a log-normal size distribution of fractures, a 1/3 power average is used to approximate the average effective permeability in each direction (Hristopulos and Christokos 1999; Wang 2014).

$$\bar{K}_i = \left( \frac{1}{n_{els}} \sum_{iel=1}^{n_{els}} (k_i)^{\frac{1}{3}} \right)^3 \quad (4.15)$$

Where  $\bar{K}_i$  is the average effective permeability in the  $i^{\text{th}}$  direction,  $i=1,2,3$ ;  $n_{els}$  is the total number of elements; and  $k_i$  is the permeability in the  $i^{\text{th}}$  direction of the  $iel^{\text{th}}$  element.

The overall average reservoir permeability is then calculated as the root mean square value of the total directional permeabilities (Rahman et al. 2002):

$$\bar{K}_{rms} = \sqrt{\frac{(\bar{K}_x)^2 + (\bar{K}_y)^2 + (\bar{K}_z)^2}{3}} \quad (4.16)$$

This average reservoir permeability is used as an index for evaluating stimulation efficiency, as presented in the Chapter 6.

#### **4.4 Pressure Distribution on Individual Fractures**

During fluid injection, the fluid pressure and temperature inside the fracture network are changed, which alters the stress distribution around fractures and affects the deformation behavior of fractures. Fracture aperture changes upon deformation and slip, and influences the permeability evolution of the equivalent continuum medium. Therefore, the solutions for pressure, temperature and stresses within the fracture network are integrated with those of the equivalent medium.

At each time step, the fluid pressure in the equivalent continuum medium is a direct output of the coupled thermo-poroelastic finite element model. The average fluid pressure on a fracture is approximated by averaging the values of all elements intersected by it. However, the exact solution of fluid pressure inside individual fractures is a complex task. In this study, an analytical solution (Long 1983) is used for the 2D pressure distribution on individual fracture planes.

Fractures are treated as circular shaped disc discontinuities in an impermeable matrix. The flow problem in individual fracture planes is solved using image theory to account for the impermeable disc boundaries. In a 3D fracture network, fracture intersections are lines instead of intersection points in a 2D network. Each intersection could play a line source or sink on the fracture plane. The head distribution within a fracture containing an arbitrary number of lines sources and sinks is based on the solution for a point source within a circular flow region.

For a disc which contains a point source of strength  $+m$  at the location  $(g, 0)$ , if steady state condition is assumed, the image system which accounts for the impermeable disc boundary gives an image source of strength  $+m$  on the same radial direction at the location  $(a^2/g, 0)$  and an image

sink of strength  $-m$  at the disc center  $(0, 0)$ . The head at any point in the fracture disc can be found by accumulating the head contributions of the source and the two images.

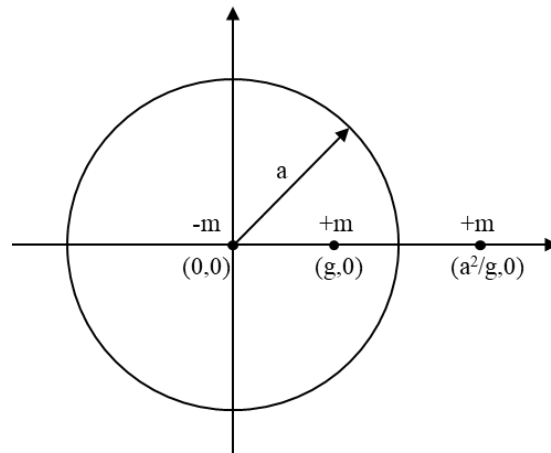


Figure 4.13. Image system for a point source in a disc (reproduced from Long 1983).

The point source solution is extended for a line source by assuming many point sources distributed along an arbitrary line segment. A non-radial line segment source will have an arc shaped image, and a radial line source will have a radial segment image, as shown in Figure 4.14.

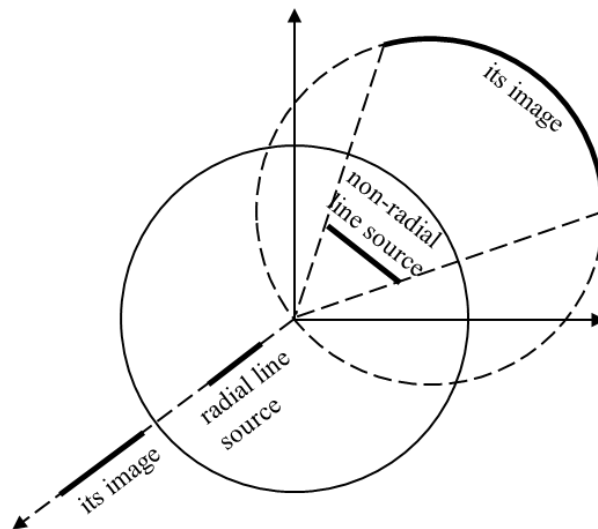


Figure 4.14. Image systems for radial and non-radial line sources in a disc (reproduced from Long 1983).

The fundamental solution of the Laplace equation for the potential due to a point source in an infinite plane is:

$$\phi = Kbh = -\frac{Q}{2\pi} \ln(r) \quad (4.17)$$

Assume such point sources are distributed over a line segment in the fracture plane, and the potential due to the line source is given by:

$$\phi_{iN}^k = -\frac{Q}{2\pi l} \int_0^l \ln(r_p(\xi)) d\xi \quad (4.18)$$

The potential due to the image is similar:

$$\phi_{iI}^k = -\frac{Q}{2\pi l} \int_{s_1}^{s_2} \frac{d\xi}{ds} \ln(r_p(s)) ds \quad (4.19)$$

The expressions for the potentials of radial line intersections and their images (Figure 4.15) are listed in Eqn. (4.18) and (4.19). The detailed procedures to find these expressions are given in Appendix B.

$$\phi_{iN}^k = -\frac{Q_i}{4\pi l_i} \left\{ (\xi - x) \ln[(x - \xi)^2 + y^2] - 2\xi + 2|y| \tan^{-1}\left(\frac{\xi - x}{|y|}\right) \right\}_{\xi_1}^{\xi_2} \quad (4.20)$$

$$\phi_{iI}^k = -\frac{Q_i}{4\pi l_i} \left\{ \left( \xi + \frac{\beta}{2\gamma} \right) \ln \Omega - 2\xi + \frac{\sqrt{4\alpha\gamma - \beta^2}}{\gamma} \tan^{-1}\left(\frac{2\gamma\xi + \beta}{\sqrt{4\alpha\gamma - \beta^2}}\right) - 2\left[\xi \ln \xi - \xi\right] \right\}_{\xi_1}^{\xi_2} \quad (4.21)$$

Where  $\Omega = \alpha + \beta\xi + \gamma\xi^2$ ;  $\alpha = a^4$ ;  $\beta = -2a^2x$ ;  $\gamma = x^2 + y^2$ .

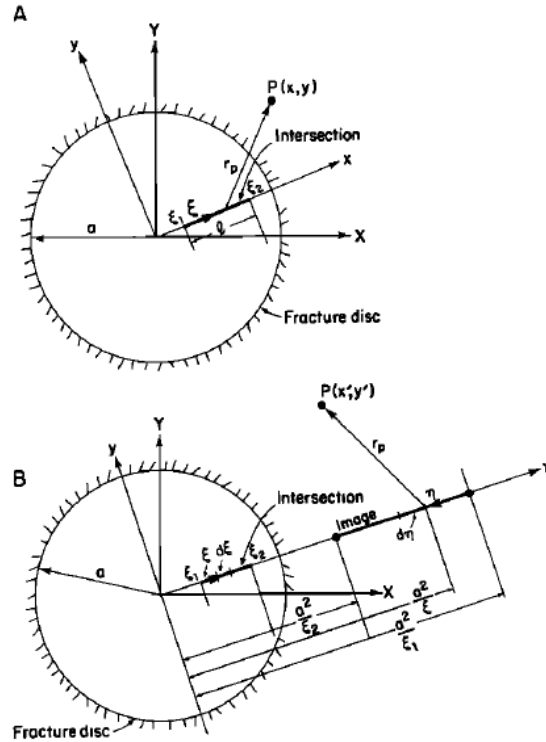


Figure 4.15. Geometry for radial line intersection and its image in a disc (taken from Long 1983).

The expressions for the potentials of non-radial line intersections and their images (Figure 4.16) are:

$$\phi_{iN}^k = -\frac{Q_i}{4\pi l_i} \left\{ (\xi - y') \ln [x'^2 + (y' - \xi)^2] - 2\xi + 2|x'| \tan^{-1} \left( \frac{\xi - y'}{|x'|} \right) \right\}_0^{l_i} \quad (4.22)$$

$$\phi_{il}^k = -\frac{Q_i}{4\pi l_i} \left\{ \left( \xi + \frac{\beta}{2\gamma} \right) \ln \Omega + \frac{\sqrt{|4\alpha\gamma - \beta^2|}}{\gamma} \tan^{-1} \left( \frac{2\gamma\xi + \beta}{\sqrt{|4\alpha\gamma - \beta^2|}} \right) - 2 \left[ \xi \ln (\xi^2 + B^2) + 2B \tan^{-1} \left( \frac{\xi}{B} \right) \right] \right\}_{\xi_1}^{\xi_2} \quad (4.23)$$



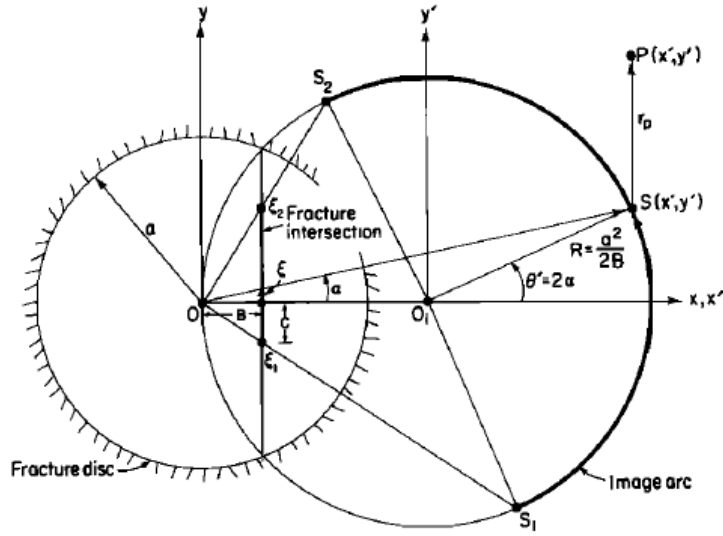


Figure 4.16. Geometry for non-radial line intersection and its image in a disc (taken from Long 1983).

For each intersection  $i$  in the fracture  $k$ , the total potential is the sum of potential due to the intersection source and its image.

$$\phi_i^k = \phi_{iN}^k + \phi_{iI}^k \quad (4.24)$$

The total potential in fracture  $k$  is the sum of the potential due to all intersections on it:

$$\phi^k = \sum_{i=1}^n \phi_i^k = \sum_{i=1}^n (\phi_{iN}^k + \phi_{iI}^k) \quad (4.25)$$

The intersections between fracture discs are identified using the geometry algorithm described in Appendix A. At each time step, the local 2D potential distributions are calculated for each fracture plane using the above method, and then head distributions can be obtained. Note that the above calculations involve using different local coordinates. A local arbitrary  $(X, Y)$  coordinate system is established for each fracture disc. All these equations for potential distribution must be translated to  $(X, Y)$  coordinates before they are added.

## 4.5 Heat Transfer within Fracture Network

Temperature usually has a significant influence on stresses, strains and pore pressure. However, deformation and pore pressure change do not lead to significant temperature change. Therefore, temperature field and heat transfer can be decoupled from the poro-mechanical response analysis. In this work, heat transfer within the interconnected fracture network is solved independently from the FEM analysis. The approach of Bruel (2002) is used by assuming a 3D flow channel consists of 1D pipes (Cacas et al. 1990). Each connected fracture is treated as a 1D flow pipe connecting fracture center and mid-point of the intersection with the adjacent fracture. An example of the pipe flow model is shown in Figure 4.17.

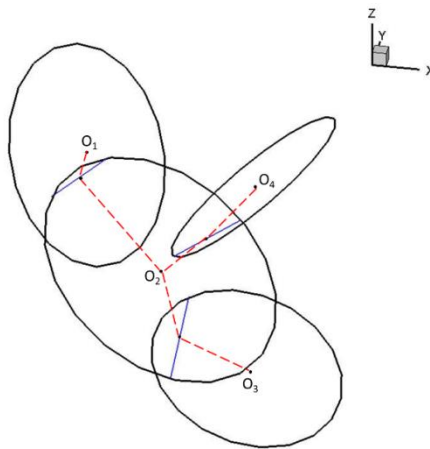


Figure 4.17. An example of flow channel of 1D pipes formed by intersecting fractures. O<sub>1</sub>, O<sub>2</sub>, O<sub>3</sub> and O<sub>4</sub> are fracture centers; the intersections between fractures are shown as blue lines; the flow channel is shown in red.

### 4.5.1 Fracture Network Connectivity

In the decoupled heat transfer analysis, the fluid flow through the rock matrix is ignored. We assume the fluid flow is confined within the interconnected fracture network. Before computing heat transfer in the fracture network, a preliminary step is the evaluation of fracture network

connectivity, which means calculating fracture intersections and finding out the interconnected fractures.

A special search algorithm is employed: The first step is to determine whether or not two fractures in three dimensional space intersect. If they intersect, the intersection between them is calculated. Then each fracture is checked if it directly intersects the injection wellbore or it is included in the connected flow path. Performing connectivity searching between a large number of discrete fractures is computationally intensive. In order to speed up the computation, an iterative process is developed to do the searching. Finally, the fractures are identified as connected fractures and isolated fractures. The details of this algorithm are described in Appendix A.

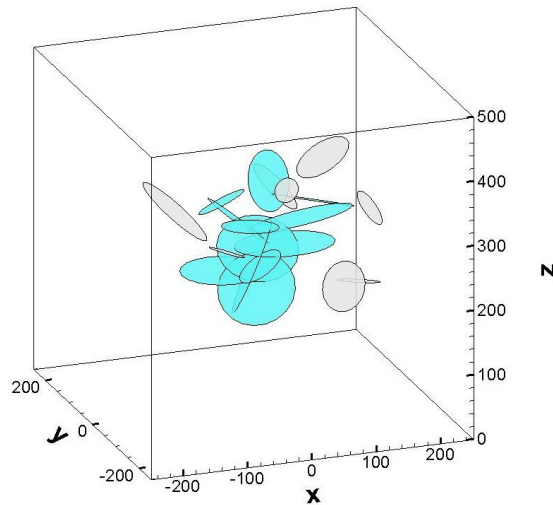


Figure 4.18. Detection of interconnected fractures (colored) and isolated fractures (grey).

#### 4.5.2 Heat Transfer Model

In fractured reservoirs, convective heat flow within interconnected fracture network takes place so rapidly during simulation time that the convection from adjacent rock to fractures can be ignored.

Therefore, the heat transfer model includes two mechanisms: 1) 1D linear heat conduction from

adjacent rock matrix to fractures; and 2) 1D liner heat convection through flow pipes formed by interconnected fractures. This heat transfer model is connected to that of the rock matrix by a heat exchange model at the fracture wall assuming continuity of temperature between the fluid in the fracture and the rock matrix.

The assumptions of this model are: 1) flow in the fractured reservoirs primarily occurs on channels within fractures; and 2) heat conduction develops perpendicular to the fracture plane (Brueel 2002). In this study, since fracture aperture is assumed to be pressure-dependent, the change in thermal energy retained by the fluid within the fractures due to fracture volume change is also considered. The energy conservation equation is written for each fracture by balancing the convective heat transport from fluid flow, heat conduction between adjacent rock mass and the fluid in the fracture, and the change of internal energy retained by the volume of fluid within the fractures.

$$dQ_{conv} + dQ_{cond} + dQ_f = 0 \tag{4.26}$$

Where  $Q_{conv}$  and  $Q_{cond}$  are convective and conductive thermal energy, respectively;  $Q_f$  is the energy retained by the fluid within a fracture.

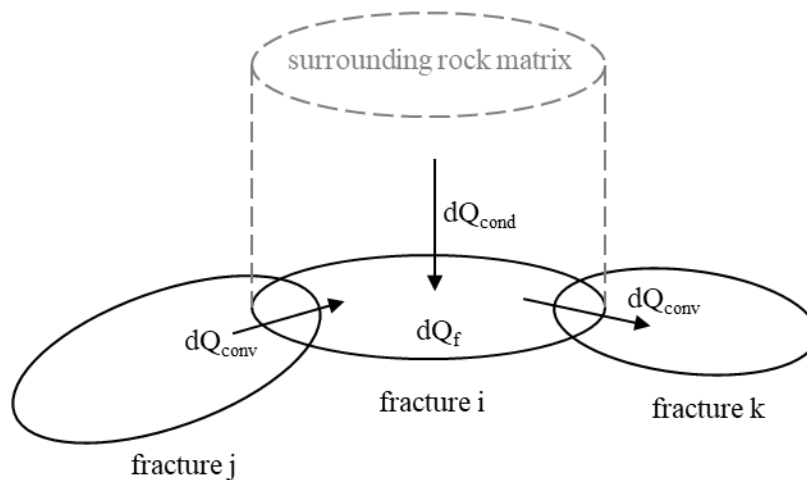


Figure 4.19. Energy conservation in the interconnected fracture network.

### 4.5.3 Convective Energy

The convective thermal energy exchanged during a time interval is given in Eqn. (4.25) (Bruehl 2002):

$$dQ_{conv} = \sum_{in} \rho_f C_f q_{ij} T_{fj}(t) dt - \sum_{out} \rho_f C_f q_{ik} T_{fi}(t+\Delta t) dt \quad (4.27)$$

Where  $q_{ij}$  is the flux entering a given fracture  $i$  from the adjacent fracture  $j$  at time  $t$ ;  $q_{ik}$  is the flux leaving fracture  $i$  to the next fracture  $k$ ;  $T_{fi}$  and  $T_{fj}$  are the temperature of fracture  $i$  and  $j$ , respectively;  $\rho_f$  is fluid density;  $C_f$  is heat capacity of the fluid.

The pipe flow model assumes that the flow occurs through channels joining the center of each fracture to the center of the adjacent fractures. As shown in Figure 4.20, the channels are made up of two pipes, one for each connected fracture, meeting at their intersection center.

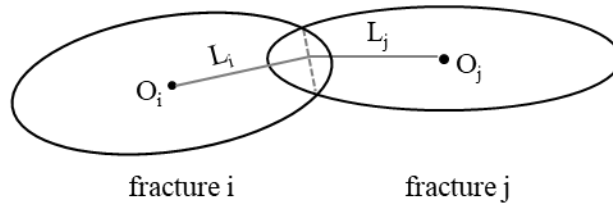


Figure 4.20. Flow channel between two connected fractures.

The hydraulic conductivity of each pipe is determined from fracture permeability and aperture based on cubic law:

$$k_i = \frac{-a_i^3 L_i}{12\mu} \quad (4.28)$$

The flow rate in a given bond between two fractures is given by (Cacas et al. 1990):

$$Q_{ij} = k_{ij} \frac{p_i - p_j}{L_i + L_j} \quad (4.29)$$

$$k_{ij} = \frac{L_i + L_j}{L_i / k_i + L_j / k_j} \quad (4.30)$$

Where  $k_i$  and  $k_j$  are the conductivity of fracture  $i$  and  $j$ , respectively;  $L_i$  and  $L_j$  are the pipe length in fracture  $i$  and  $j$ , respectively, which is the distance between fracture center and the intersection in the fracture;  $p_i$  and  $p_j$  are the pore pressure at each fracture center, respectively, which have been obtained by averaging the pore pressure of all elements intersected by the fracture.

#### 4.5.4 Conductive Energy

Heat conduction between adjacent rock mass and the fluid in the fracture is assumed to develop perpendicular to the fracture plane. At any time, the continuity of the temperature at the fracture surface is:

$$T_f = T_m \text{ at } y=0 \quad (4.31)$$

Where  $T_f$  and  $T_m$  are the temperature of fluid and matrix, respectively.

Conductive energy (Eqn. (4.30)) is related to the heat flux at the fracture surface (Eqn. (4.31)) which has to dissipate in its adjacent rock block according to the diffusion equation (Eqn. (4.32)).

The heat exchange on the fracture surface is given as (Brueel 2002):

$$dQ_{condi} = \Phi_i S_i dt \quad (4.32)$$

$$\Phi_i = K_m \left( \frac{dT_m}{dy} \right)_{y=0} \quad (4.33)$$

$$\alpha_m \nabla^2 T_m = \frac{\partial T_m}{\partial t} \quad (4.34)$$

$$\alpha_m = \frac{K_m}{\rho_m C_m} \quad (4.35)$$

Where  $\Phi_i$  is the heat flux at the fracture surface;  $S_i$  is the exchange area;  $K_m$  is the matrix heat conductivity;  $\alpha_m$  is the heat diffusivity of rock mass;  $\rho_m$  and  $C_m$  are the density and heat capacity of the matrix, respectively.

The above diffusion equations are solved using a finite difference method (FDM) to obtain the temperature in the adjacent rock matrix and the conductive heat energy developed on each fracture surface.

As shown in Figure 4.21, the shape of the surrounding rock block is assumed to be cylindrical, with a radius equal to the fracture radius. The height of the block should allow the temperature at the opposite end of the block to remain unchanged during the simulation.

The distance at which a heat transfer takes places after a period can be defined as a thermal diffusion characteristic length (Marin 2010). After time  $t$  has elapsed, the heat outspread over a sphere of radius  $\mu$  :

$$\mu = 2\sqrt{\alpha t} \quad (4.36)$$

Where  $\mu$  is the thermal diffusion characteristic length;  $\alpha$  is the heat diffusivity;  $t$  is the time duration.

Since thermal diffusivity coefficient is usually very small for rocks, the temperature change will not develop at a considerable distance from fracture surface within the simulation period. Therefore, the block to block thermal interactions and the thermal stress effects are ignored in the current study. For a rock with a heat diffusivity of  $1.15E-6 \text{ m}^2/\text{s}$ , the thermal diffusion characteristic

length is 12 m per year. In short term simulations, the thermal diffusion characteristic length is much shorter. A height of 12 m is used for the height of the surrounding rock block to ensure the temperature at the opposite end of the block is unchanged after one year of heat transfer.

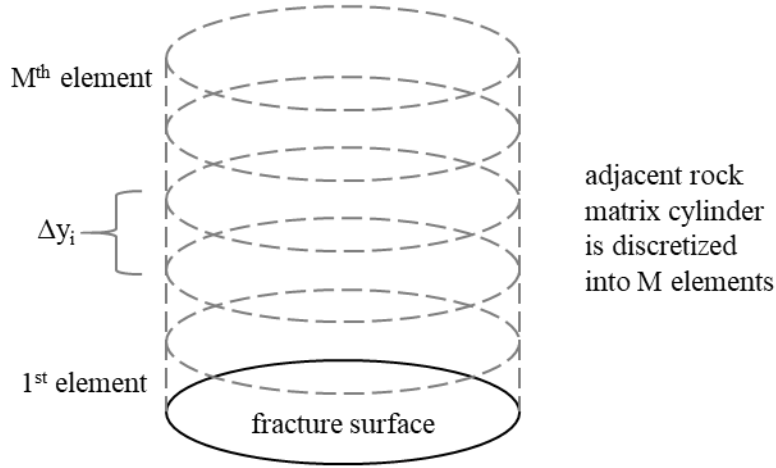


Figure 4.21. Discretization of the rock matrix adjacent to a fracture surface.

The adjacent rock matrix is discretized into a total of M small elements with an element size of  $dy_i$ . Eqn. (4.32) can be rewritten using the Backward-Time Central-Space (BTCS) scheme as:

$$\frac{T_i^n - T_i^{n-1}}{dt} = \alpha_m \frac{T_{i+1}^n - 2T_i^n + T_{i-1}^n}{(dy_i)^2} + O(dt, (dy_i)^2) \quad (4.37)$$

Ignoring the last term, and then Eqn. (4.35) can be rewritten as:

$$-\frac{\alpha_m dt}{(dy_i)^2} T_{i-1}^n + \left[ 1 + 2 \frac{\alpha_m dt}{(dy_i)^2} \right] T_i^n - \frac{\alpha_m dt}{(dy_i)^2} T_{i+1}^n = T_i^{n-1} \quad (4.38)$$

The boundary conditions are:

$$\frac{T_1^n - T_1^{n-1}}{dt} = \frac{\alpha_m}{(dy_i)^2} (T_2^n - T_1^n) \quad (4.39)$$



$$\frac{T_M^n - T_M^{n-1}}{dt} = \frac{\alpha_m}{(dy_i)^2} (T_M^n - T_{M-1}^n) \quad (4.40)$$

If the element size is uniform, i.e.,  $dy_i$  is a constant value, let  $\frac{\alpha_m dt}{(dy_i)^2} = a$ .

The above equations yield:

$$-aT_{i-1}^n + (1+2a)T_i^n - aT_{i+1}^n = T_i^{n-1} \quad (4.41)$$

$$(1+a)T_1^n - aT_2^n = T_1^{n-1} \quad (4.42)$$

$$aT_{M-1}^n + (1-a)T_M^n = T_M^{n-1} \quad (4.43)$$

Eqn. (4.39) can be written in matrix form as:

$$\begin{bmatrix} 1+a & -a & 0 & 0 & 0 & 0 & 0 \\ & \ddots & & & & & \\ & & \ddots & & & & \\ 0 & \cdots & -a & 1+2a & -a & \cdots & 0 \\ & & & \ddots & & & \\ & & & & \ddots & & \\ 0 & 0 & 0 & 0 & 0 & a & 1-a \end{bmatrix} \begin{bmatrix} T_1^n \\ \vdots \\ T_{i-1}^n \\ T_i^n \\ T_{i+1}^n \\ \vdots \\ T_M^n \end{bmatrix} = \begin{bmatrix} T_1^{n-1} \\ \vdots \\ T_{i-1}^{n-1} \\ T_i^{n-1} \\ T_{i+1}^{n-1} \\ \vdots \\ T_M^{n-1} \end{bmatrix} \quad (4.44)$$

For each fracture, one set of diffusion equations is set up at its surrounding rock blocks. The finite difference solution will return the temperature distribution from the fracture surface to the other end of this rock block. Then, the heat flux  $\phi_i$  and the conductive energy changed at the fracture surface  $dQ_{conv_i}$  can be obtained.

#### 4.5.5 Internal Heat Energy

The change of internal heat energy retained by the volume of fluid within the fractures is due to temperature change and the change of fracture volume:

$$dQ_{fi} = \rho_f C_f T_{fi(t)} (V_{fi(t)} + \Delta V_{c_{fi(t)}}) - \rho_f C_f T_{fi(t-\Delta t)} (V_{fi(t-\Delta t)} + \Delta V_{c_{fi(t)}}) \quad (4.45)$$

Where  $\rho_f$  and  $C_f$  are the density and heat capacity of the fluid, respectively;  $V_{fi(t)}$  and  $V_{fi(t-\Delta t)}$  are the fracture volume at time  $t$  and  $t - \Delta t$ , respectively;  $\Delta V_{c_{fi(t)}}$  is the fluid volume change due to expansion or compression.

At each fracture center, the energy balance equation (Eqn. (4.26)) is applied. The temperature change between time steps is usually small, therefore, knowing the fracture aperture and pressure change from the FEM solutions and the temperature from the previous time step, the set of energy balance equations for all fractures are solved for the temperature at the current time step. The initial fracture temperature is prescribed and the temperature of the injection fluid is also prescribed on the fluid entering fractures.

Once the changes in fluid pressure and temperature within the fracture network are known, the effects of these changes on fracture deformation behavior are taken into consideration in terms of poroelastic and thermoelastic induced stresses. At each time step, the pressure and temperature changes are substituted into Eqn. (2.25) for all elements that contain fractures, to obtain the total in-situ stresses in the rock medium surrounding the fractures.

#### 4.6 Fracture Deformation and Shear Dilation

Natural fractures are usually stress sensitive, i.e., they deform, and slip/open due to the stresses caused by injection/extraction operations. In this work, the fracture deformation analysis is based on the injection perturbed pore pressure and stress. It is assumed that the fracture deformation is mechanically decoupled from the FEM analysis and it does not impact stress distributions in the FEM analysis (Wang 2014), thus it is carried out sequentially after FEM analysis at each time step. It consists of three main steps: 1) obtain the effective stresses acting on the fracture surface from

the FEM analysis; 2) calculate fracture deformation and aperture changes under the new effective stresses; 3) update the fracture permeability and equivalent elemental permeability for the next time step in the FEM solution. Considering the negligible fracture aperture change with respect to the matrix element size, to keep the problem complexity at a manageable level, the induced stress in the rock matrix due to fracture deformation is not included, which means it is mechanically decoupled with the thermo-poroelastic model.

#### 4.6.1 Shear Dilation

The deformation of natural fractures depends on the combined effects of pore pressure and total in-situ stress, which can be expressed by effective stress:

$$\sigma_{eff} = \sigma_n - P \quad (4.46)$$

By applying the Mohr-Coulomb failure criterion to the Patton's saw-tooth fracture model (Patton 1966), the shear strength of a fracture is written as:

$$\tau_p = \sigma_{eff} \tan(\phi_{basic} + \phi_{dil}^{eff}) \quad (4.47)$$

$$\phi_{dil}^{eff} = \frac{\phi_{dil}}{1 + 9\sigma_{eff} / \sigma_{nref}} \quad (4.48)$$

Where  $\sigma_{eff}$  is the effective normal stress on fracture surface;  $\phi_{basic}$  is basic friction angle;  $\phi_{dil}^{eff}$  is the effective shear dilation angle;  $\phi_{dil}$  is the laboratory measured dilation angle and  $\sigma_{nref}$  is the effective normal stress required to cause 90% reduction in fracture aperture. When the shear stress acting on fracture surface exceeds fracture shear strength, the fracture slips.

$$\tau > \tau_p \quad (4.49)$$

As a result of shear slippage, shear displacement occurs on fracture surfaces. This permanent displacement has a significant influence on the permeability enhancement of fractured reservoirs (Ye et al. 2017 and 2018). The shear slip displacement is a function of the excess shear stress (Hicks et al. 1996):

$$U_s = \frac{\tau - \tau_p}{K_s} \quad (4.50)$$

Where  $U_s$  is the shear slip displacement;  $\tau$  is the shear stress acting on fracture surface; and  $K_s$  is the geometrical stiffness of the fracture. For a penny-shaped circular fracture,  $K_s = \frac{7\pi G}{24 r}$  (Dieterich 1992),  $G$  is the shear modulus of surrounding intact rock and  $r$  is the radius of the fracture.

Shear slip on natural fractures can induce fracture opening as the opposing fracture asperities slide over each other and cause a dilation in aperture (Figure 4.22).

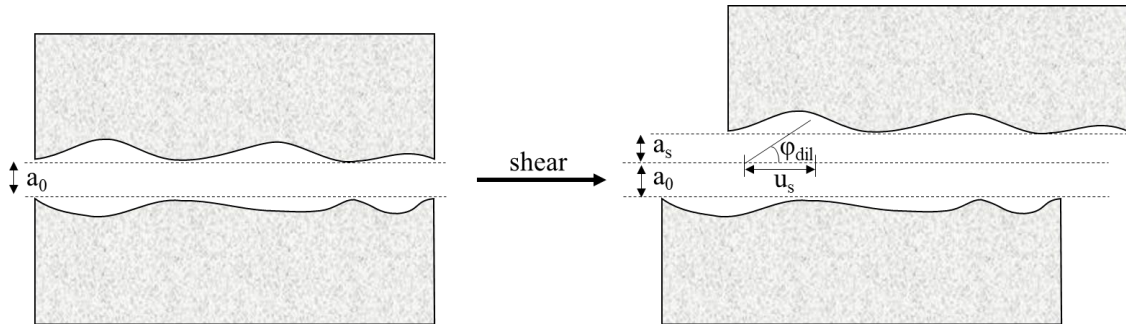


Figure 4.22. Fracture surfaces slip and cause dilation in fracture aperture.

The dilated aperture due to shear slippage is proportional to shear displacement:

$$a_s = U_s \tan(\phi_{dil}^{eff}) \quad (4.51)$$

For in contact fractures that have slipped, the total stimulated fracture aperture (Willis-Richards et al. 1996) is written as:

$$a = \frac{a_0}{1 + 9\sigma_{eff} / \sigma_{nref}} + a_s + a_{res} \quad (4.52)$$

Where  $a_0$  is the initial aperture;  $a_s$  is the aperture change due to shear slippage; and  $a_{res}$  is the residual aperture at very high effective stress which is usually small (Willis-Richards et al. 1996) and is assumed to be zero in this study.

A typical behavior of fracture aperture as a function of effective normal stress is shown in Figure 4.23. As fluid injection pressurizes the fracture, the effective normal stress is reduced and fracture aperture increases due to deformation in the normal direction. Once shear slippage occurs, the increase in aperture is due to the combined effects of both normal deformation and shear dilation.

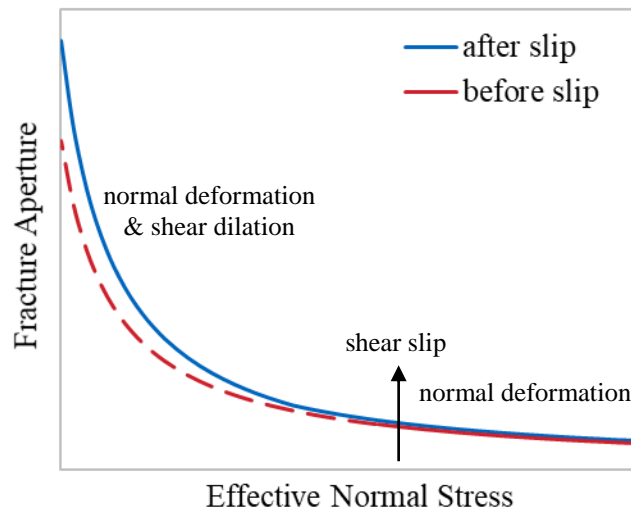


Figure 4.23. Fracture aperture evolution with respect to different effective normal stress.

When the effective normal stress acting on the fracture becomes negative, i.e., when  $P > \sigma_n$ , the fracture will be mechanically open, which is usually termed as hydraulic jacking. Subsequent pressurization will further open the fracture. For fully-open fractures, the aperture is the relative normal displacements of the two fracture surfaces (Willis-Richards et al. 1996). The normal

displacement of any point on the circular crack surface of a circular shape fracture is given in Eqn. (4.51) (Jaeger and Cook 1969), which indicates that the maximum normal displacement is at the center of the fracture.

$$u(r) = \frac{2(1-\nu)\sigma_n}{\pi G} \sqrt{R^2 - r^2} \quad (4.53)$$

Therefore, the maximum opening aperture is also at the center, and equals to twice the normal displacement of one surface:

$$a = \frac{4(1-\nu)R\sigma_n}{\pi G} \quad (4.54)$$

The average crack aperture can be calculated from an equal volume penny-shaped crack (Willis-Richards et al. 1996):

$$V = \frac{8(1-\nu)R^3\sigma_n}{3G} \quad (4.55)$$

$$\bar{a} = \frac{8(1-\nu)R\sigma_n}{3\pi G} \quad (4.56)$$

Since the fracture aperture change has a direct influence on reservoir permeability evolution, the fracture deformation model is integrated with the thermo-poroelastic FEM model. After fracture aperture calculations, the updated values are used as inputs to calculate the equivalent permeability in the FEM model for the next time step.

Generally, fracture aperture change ( $\sim 10^{-4}$  m) is negligible compared with the element size ( $\sim 10^1$  m). Therefore, for simplicity, the elemental strain induced by fracture dilation is not considered in this current study, which means this fracture deformation model is mechanically decoupled from FEM analysis. To solve the coupling between fracture deformation and elemental strain, sophisticated fracture deformation models (e.g., Huang et al. 2011) are required.

#### 4.6.2 Rate-and-state Friction (RSF) Model

Slip on natural fractures is an important mechanism to increase permeability and to cause microseismicity during reservoir stimulation. The mechanism of slip on fractures is a highly complex process involving many factors such as fracture geometry, the stress field and the constitutive frictional law. Among these factors, the constitutive friction law is a particularly important one, since it represents the material characteristics of a fracture, while other factors are condition dependent. There are various forms of constitutive frictional laws existing, such as constant friction law, slip weakening law and rate-and-state (RSF) dependent friction law.

Slip weakening law is a widely used constitutive law to simulate the loss of frictional resistance to shear and the residual strength of the pre-existing fractures. It assumes that the weakening process of the frictional strength is a function of the slip distance only. The simplest slip weakening law is in a linear form (Ide 1972; Palmer & Rice 1973), which implies a constant weakening rate:

$$\mu = \mu_s - (\mu_s - \mu_k) \frac{u}{d_c} \text{ when } u < d_c \quad (4.57)$$

$$\mu = \mu_k \text{ when } u \geq d_c \quad (4.58)$$

Where  $\mu_s$  is the static friction coefficient;  $\mu_k$  is kinetic friction coefficient, which is independent of slip velocity;  $d_c$  is the critical value of slip, i.e., the characteristic slip distance, and  $u$  is the slip distance.

As shown in Figure 4.24, for a certain value of the relative shear slip along the fracture, friction decreases linearly from the peak value to a residual value. Although the slip weakening friction law can describe the dynamic behavior of fault slip and has a straightforward numerical implementation, it could not precisely capture the velocity dependence and time dependence of friction in experimental observations (Dieterich 1979).

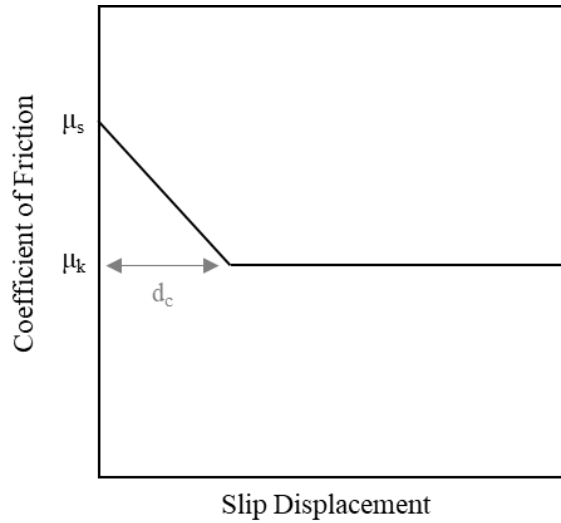


Figure 4.24. Linear slip weakening friction law assumes friction decreases from a static value to a kinetic value linearly over the slip distance.

Rate-and-state friction (RSF) is another commonly used constitutive frictional law to describe friction evolution on a fault. It was introduced by Dieterich (1979) and Ruina (1983) in the early 1980s based on laboratory observations of rock friction. Now it is widely used in earthquake modeling to describe friction evolution on a fault. According to RSF, the coefficient of friction changes over time as a function of sliding velocity and the past sliding history of the fault (Dieterich 1979; Ruina 1983):

$$\mu = \mu_0 + a \ln \frac{v}{v_0} + b \ln \frac{\theta v_0}{d_c} \quad (4.59)$$

Where  $v_0$  is a reference velocity;  $\mu_0$  is the steady state friction at  $v = v_0$ ;  $a$  and  $b$  are dimensionless material constants, representing the magnitude of the direct effect and the evolution effect, respectively, i.e., the rate at which the friction coefficient varies with the change in velocity and in the state variable, respectively;  $d_c$  is the characteristic slip distance over which evolution



to a new steady state occurs, which can be estimated from laboratory friction measurements; The magnitude of  $d_c$  depends on the surface roughness and fault gouge (Dieterich 1979), which is typically on the order of microns in the laboratory scale;  $\theta$  is a state variable which changes over time as friction evolves on the fault; It represents the surface memory of previous sliding history (Ruina 1983) and can be interpreted as the damage that has occurred on the fault surface.

Among many empirical state evolution laws that have been proposed, the two most commonly used forms are the aging law (Dieterich 1979) and the slip law (Ruina 1983).

The aging law (Dieterich 1979) allows the state to evolve even as  $v \rightarrow 0$ . At zero slip velocity,  $\theta$  increases linearly with the elapsed time:

$$\frac{d\theta}{dt} = 1 - \frac{\theta v}{d_c} \quad (4.60)$$

The slip law (Ruina 1983) allows the state to evolve only with slip, i.e.,  $\frac{d\theta}{dt}$  vanishes when  $v = 0$

:

$$\frac{d\theta}{dt} = -\frac{\theta v}{d_c} \ln\left(\frac{\theta v}{d_c}\right) \quad (4.61)$$

The aging law is more consistent with laboratory test data (Ruina 1983; Segall et al. 2010), while the slip law appears to be more relevant to nucleation (Ampuero and Rubin 2008; Segall et al. 2010). Although the two state evolution laws have their own physical implications, they will exhibit the steady state sliding ( $\frac{d\theta}{dt} = 0$ ) when  $\frac{\theta v}{d_c} = 1$ , i.e., the steady state friction coefficient is

the same for both laws. The steady state  $\theta$  at slip velocity  $v$  is identical for the two laws:

$$\theta = \frac{d_c}{v} \quad (4.62)$$

Therefore, irrespective of the choice of state evolution law, the steady state friction coefficient is given by:

$$\mu = \mu_0 + (a - b) \ln \frac{v}{v_0} \quad (4.63)$$

The magnitudes of the parameters  $a$  and  $b$  are of order 0.01 (Ruina 1983), which are much smaller than the friction coefficient (of order 0.6~1.0). Their relatively small values are consistent with the observation that the variation in friction coefficient during a sliding event is usually small. The relative magnitudes of the parameters  $a$  and  $b$  determine whether or not the slip occurs in a stable or unstable condition (Ruina 1983; Dieterich 2007). The coefficient for the logarithmic term in Eqn. (4.63),  $a-b$ , may be either positive or negative, depending on the experimental conditions and the rock specimens. The condition  $a > b$  is referred to as velocity strengthening. The friction coefficient increases following an increase in velocity, and slips are stable. In contrast, the condition  $a < b$  is referred to as velocity weakening, and unstable slips will occur.

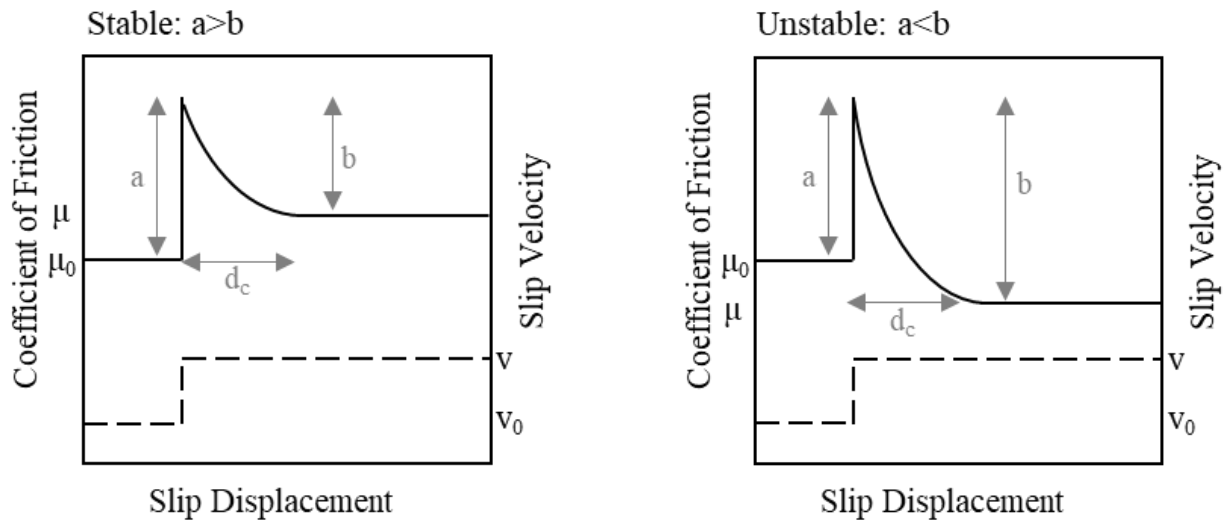


Figure 4.25. Rate-and-state friction law. Left: stable (velocity strengthening); Right: unstable (velocity weakening).

The numerical implementation of a RSF model is significantly more computationally intensive than a constant friction coefficient model as it requires very fine spatial and temporal discretization to avoid numerical instability and to capture the rapidly changing rate-and-state dependent evolution (LaPusta 2011). In this work, to make a tradeoff between accuracy and efficiency, we assume the friction evolution on the fractures caused by shear slippage is in the steady state. Considering the time scale over which the evolution to steady state occurs (on the order of  $10^{-8} \sim 10^{-1}$  s; based on fracture slip velocity on the order of  $10^{-5} \sim 10^2$  m/s (Rowe and Griffith 2015) and characteristic slip distance on the order of  $10^{-6}$  m) is extremely small compared to the numerical time step (on the order of  $10^0 \sim 10^4$  s), it is reasonable to make this assumption.

The RSF model is carried out sequentially after fracture shear slippage analysis. At each time step, the slip velocity for each slipped fracture is approximately calculated from its shear slip displacement over the time interval:

$$v = \frac{U_s}{t} \quad (4.64)$$

Then the steady state friction coefficient is calculated using Eqn. (4.59), and updated for the next time step to evaluate the slip condition for this fracture.

#### 4.6.3 Induced Microseismicity

When shear slip on a fracture plane occurs, seismic energy is released and micro-earthquake (MEQ) is induced. The released seismic energy can be quantified by the event moment (McGarr et al. 1979), which is an integral of shear modulus times the shear displacement over the fracture area:

$$M_0 = \int GU_s dA \quad (4.65)$$

Where  $M_0$  is the seismic moment;  $G$  is the shear modulus of the fracture embedded in the rock;  $A$  is the slip area, i.e., the area of fracture surface.

The location of the induced MEQ is assumed to be the center of each slipped fracture. The moment magnitude of an MEQ can be obtained from the relationship (Hanks and Kanamori 1979):

$$M = \frac{2}{3} \log M_0 - 10.7 \quad (4.66)$$

Where  $M$  is the seismic magnitude;  $M_0$  is in dyn·cm.

#### 4.7 Fracture Growth

In this work, an analytical method of mixed-mode (mode I and mode II) fracture propagation (Rahman et al. 2002) is used to examine the growth of a natural fracture.

A penny-shaped fracture embedded in a rock block is compressed by in-situ stresses, as shown in Figure 4.26. The fracture is oriented at an angle of  $\alpha$  with the maximum principal stress  $\sigma_1$ . The fracture is internally pressurized by a fluid pressure  $P_f$ . Although a penny-shaped crack is more of a 3D nature, it can be treated as 2D problem when the fracture is assumed to be axially symmetric and a plane strain condition exists (Sneddon 1946, Valko and Economides 1995, Rahman et al. 2000).

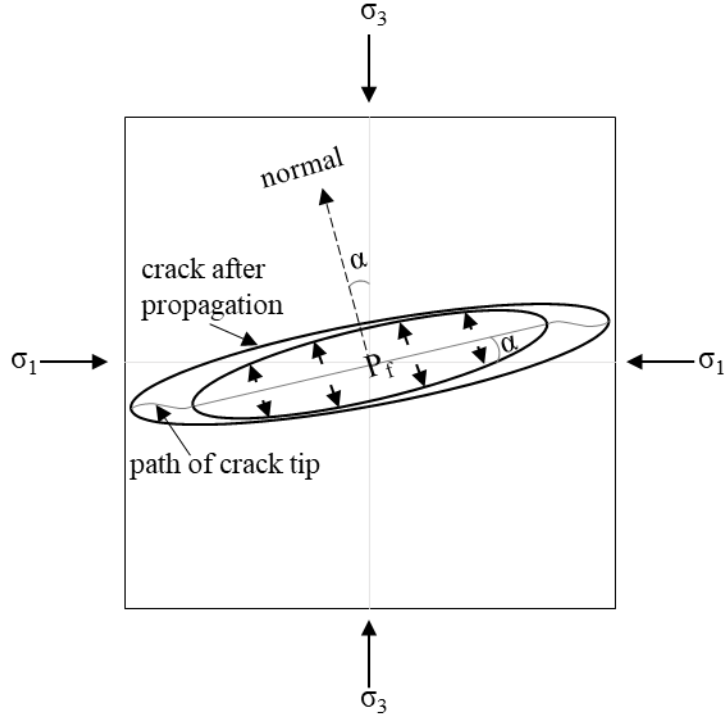


Figure 4.26. A penny-shaped fracture subjected to far field stresses ( $\sigma_1$  and  $\sigma_3$ ) and internal pressure ( $P_f$ ) (reproduced from Rahman et al. 2002).

The normal and shear stresses acting on a fracture plane are:

$$\sigma_n = \sigma_1 \sin^2 \alpha + \sigma_3 \cos^2 \alpha \quad (4.67)$$

$$\tau = \frac{1}{2}(\sigma_1 - \sigma_3) \sin 2\alpha \quad (4.68)$$

The value of shear resistance  $\tau_f$  for the case of a fracture opened by fluid pressure is very small compared to the applied shear stress  $\tau$ , and therefore is neglected. The net pressure and the effective shear stresses acting on the fracture surface could be written as:

$$P_n = P_f - \sigma_n = P_f - (\sigma_1 \sin^2 \alpha + \sigma_3 \cos^2 \alpha) \quad (4.69)$$

$$\tau_{eff} = \tau - \tau_f = \frac{1}{2}(\sigma_1 - \sigma_3) \sin 2\alpha \quad (4.70)$$

The stress intensity factor is a parameter used to predict the stress state in the vicinity of a crack tip caused by a remote loading or residual stress. The mode I (opening) and mode II (shearing) stress intensity factors (Rice 1968) for a crack are:

$$K_I = C\sqrt{l}P_n \quad (4.71)$$

$$K_{II} = C\sqrt{l}\tau_{eff} \quad (4.72)$$

Where  $K_I$  and  $K_{II}$  are the mode I and mode II stress intensity factor, respectively;  $P_n$  and  $\tau_{eff}$  are the net pressure and the effective shear stresses acting on the fracture surface, respectively;  $l$  is the fracture half length, i.e., radius;  $C$  is the geometry coefficient. For a penny-shaped fracture,  $C$  is  $2/\sqrt{\pi}$  (Rice 1968).

As shown in Figure 4.26, for an internally pressurized penny-shaped fracture oriented with the maximum principal stress  $\sigma_1$  by an angle  $\alpha$ , the stress intensity factors are:

$$K_I = 2\sqrt{\frac{l}{\pi}}(P_f - \sigma_1 \sin^2 \alpha - \sigma_3 \cos^2 \alpha) \quad (4.73)$$

$$K_{II} = \sqrt{\frac{l}{\pi}}(\sigma_1 - \sigma_3) \sin 2\alpha \quad (4.74)$$

The equivalent mode I stress intensity factor is calculated as:

$$K_I^{eff} = \cos \frac{\theta_0}{2} (K_I \cos^2 \frac{\theta_0}{2} - \frac{3}{2} K_{II} \sin \theta_0) \quad (4.75)$$

According to the maximum tensile stress criterion (Erdogan and Sih 1963), the fracture will propagate if:

$$K_I^{eff} \geq K_{Ic} \quad (4.76)$$

Where  $K_{Ic}$  is the mode I fracture toughness, which is material dependent and can be determined from laboratory measurements.

The fracture tip propagation angle is:

$$\theta_0 = 0 \text{ if } K_{II} = 0 \quad (4.77)$$

$$\theta_0 = 2 \tan^{-1} \left[ \frac{K_I \pm \sqrt{K_I^2 + 8K_{II}^2}}{4K_{II}} \right] \text{ if } K_{II} \neq 0 \quad (4.78)$$

Two values of  $\theta_0$  are obtained from Eqn. (4.78) using positive and negative signs before the square root term. The angle which produces the maximum tensile stress  $\sigma_{\theta_{\max}}$  (Eqn. (4.79)) is taken as the propagation direction of the fracture tip.

$$\sigma_{\theta_{\max}} = \frac{1}{\sqrt{2\pi\Delta r}} \left[ \cos \frac{\theta_0}{2} \left( K_I \cos^2 \frac{\theta_0}{2} - \frac{3}{2} K_{II} \sin \theta_0 \right) \right] \quad (4.79)$$

To estimate how far the fracture tip will propagate along  $\theta_0$  with respect to its current direction and to predict the propagation path, a pure analytical approach (Rahman et al. 2000) is used. For an initial internally pressurized penny-shaped fracture subjected to far field stresses, the stress intensity factors  $K_I$  and  $K_{II}$  and the fracture tip propagation angle  $\theta_0$  can be calculated as discussed before. The tip of the initial fracture propagates along  $\theta_0$  up to a new location by an incremental length in fracture radius,  $\Delta r$ . Rahman et al. (2000) suggested that any value of  $\Delta r$  between 5% and 10% of the original fracture radius would provide reasonably accurate results.

As shown in Figure 4.27, the center of an initial fracture is located at the origin O. The tip of the initial fracture A propagates along  $\theta_{0i}$  to the new tip B by an incremental length,  $\Delta r$ . The new fracture plane O-B rotates at an angle of  $\Delta\alpha_{i+1}$  from the initial fracture plane O-A.

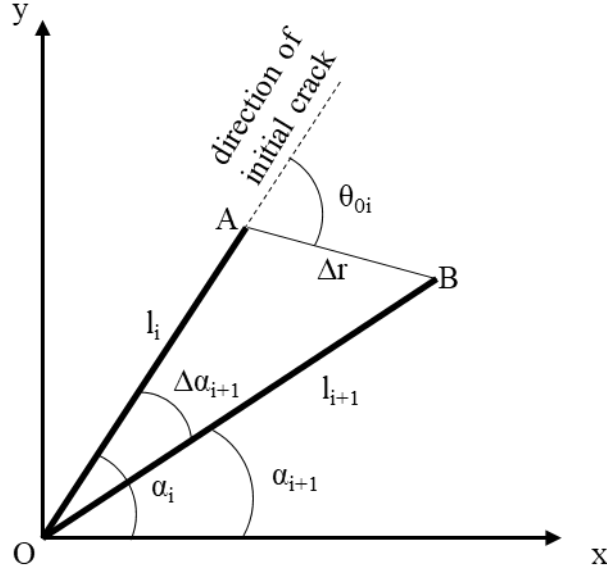


Figure 4.27. Illustration of fracture tip propagation path (reproduced from Rahman et al. 2000).

The change in the orientation angle of a propagated fracture can be calculated from geometric relationships (Rahman et al. 2000):

$$\Delta\alpha_{i+1} = \cos^{-1}\left(\frac{l_i^2 + l_{i+1}^2 - \Delta r^2}{2l_i l_{i+1}}\right) \quad (4.80)$$

The new half-length and the new orientation of the new fracture plane can be calculated as:

$$l_{i+1} = \sqrt{l_i^2 + \Delta r^2 + 2l_i \Delta r \cos \theta_{0i}} \quad (4.81)$$

$$\alpha_{i+1} = \alpha_i + j\Delta\alpha_{i+1} \quad (4.82)$$

Where  $j$  is the direction vector;  $j=1$  if  $\theta_{0i}$  is positive (counterclockwise);  $j=-1$  if  $\theta_{0i}$  is negative (clockwise).

The coordinates of the new fracture tip are:

$$X_{i+1} = l_{i+1} \cos \alpha_{i+1} \quad (4.83)$$

$$Y_{i+1} = l_{i+1} \sin \alpha_{i+1} \quad (4.84)$$



At the new location, the new stress intensity factors and new propagation direction are calculated to determine the next step of propagation. This process is repeated sequentially until the fracture becomes stable (i.e.,  $K_I^{eff} < K_{Ic}$ ).

When modeling the deformational response of a natural fracture network, it is assumed that a fracture will propagate if its net fracture pressure is positive ( $P_n > 0$ ), i.e., when the pressure inside the fracture exceeds the normal stress acting on it. In the case of negative net fracture pressure ( $P_n < 0$ ), the mode I (opening) stress intensity factor  $K_I$  is negative. However, the presence of mode II (shearing) stress intensity factor  $K_{II}$  may cause the effective stress intensity factor  $K_I^{eff}$  to be greater than the fracture toughness  $K_{Ic}$ , and it may result in a very complex twisted non-planar geometry (Rahman et al. 2000), which is not considered in this study. In a natural fracture network, once the propagated fracture coalesces with another nearby fracture or reaches the model boundary or the net fracture pressure becomes compressive (Rahman et al. 2000), the propagation process will be terminated.

In practice, due to the effect of mixed-mode propagation, the final shape of the propagated fractures can be reoriented or twisted, which requires sophisticated mathematical tools for exact solutions to the non-planar problems. Since the propagated length is relatively short compared to the initial length and the amount of the fracture plane reorientation is usually smaller than that of the initial orientation, it is reasonable to assume the final fracture remains in the same initial plane (Hossain 2001). After the propagation process, the radius of the propagated fractures is updated for the next time step.

When natural fractures are subjected to fluid injection and slipped in shear, the stress intensity at the fracture tips could be increased, and wing cracks could initiate from the fracture tips at an angle of approximately  $70^\circ$  from the pre-existing fracture plane and propagate toward the maximum in-

situ direction (e.g., Jung 2013; Kamali and Ghassemi 2016 and 2018; Ye and Ghassemi 2018). To include the propagation of shear slippage induced wing cracks, an analytical approach (Jung 2013) is used.

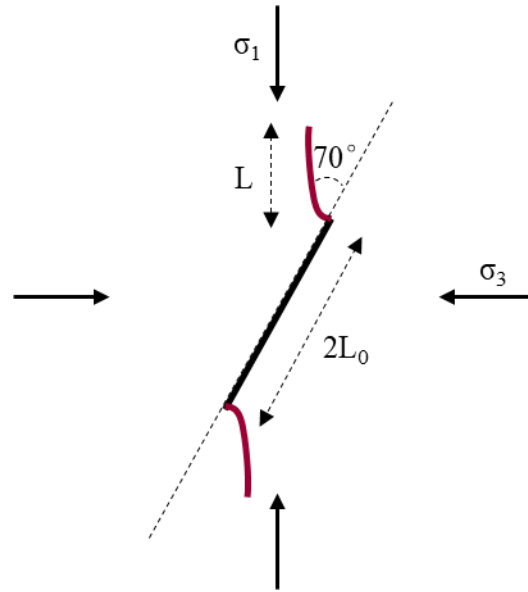


Figure 4.28. Illustration of wing crack propagation (reproduced from Jung 2013).

The criterion of the initiation of wing cracks (Cotterell and Rice 1980; Jung 2013) is given as:

$$\tau_{ex} \geq \frac{\sqrt{3}K_{Ic}}{2\sqrt{\pi L_0}} \quad (4.85)$$

Where  $\tau_{ex} = \tau - \mu(\sigma_n - P)$  is the excess shear stress exceeding the Coulomb friction failure line;

$\tau$  and  $\sigma_n$  are the shear stress and normal stress acting on the fracture, respectively;  $\mu$  is the friction coefficient;  $P$  is the fluid pressure in the fracture;  $K_{Ic}$  is the fracture toughness; and  $L_0$  is the half length of the fracture, i.e., the radius.

The length of the propagated wing crack parallel to the direction of the maximum principal stress is approximated as:

$$\sqrt{\frac{L}{L_0}} = \frac{K_{Ic}}{2(\sigma_3 - P)\sqrt{\pi L_0}} + \sqrt{\left(\frac{K_{Ic}}{2(\sigma_3 - P)\sqrt{\pi L_0}}\right)^2 + \frac{2\tau_{ex} \cos \phi}{\pi(\sigma_3 - P)}} \quad (4.86)$$

Where  $L$  is the length of the wings;  $\sigma_3$  is the minimum principal stress; and  $\phi$  is the angle between the fracture normal direction and the maximum principal stress, as shown in Figure 4.28. For each slipped fracture, its excess shear stress is calculated. If the criterion of wing crack initiation is satisfied, two wing cracks are considered to be initiated at the fracture tips and their propagation lengths are calculated from Eqn. (4.86). In this current work, the final geometry of the propagated fracture with shear slippage induced wings is approximated by adding two penny-shaped fractures at the tips of the original fracture, orienting  $70^\circ$  to the initial fracture plane and with a radius equals to the half-length of the wings.

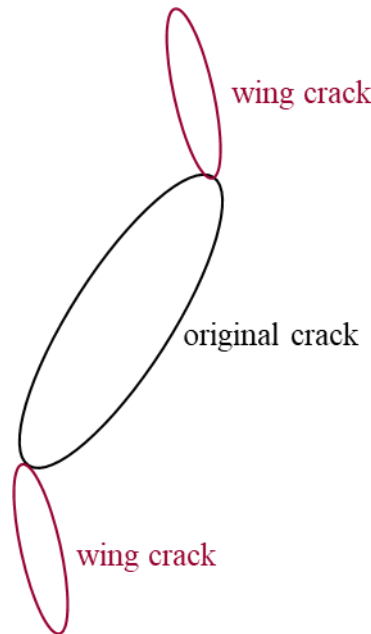


Figure 4.29. Updated fracture geometry considering the propagated wing cracks.

At each time step, the fracture growth condition is checked for each fracture. If a fracture grows, its geometry is updated for the next step. Consequently, the intersections between fractures are re-

calculated to update the connectivity of the fracture network. The intersection relationships between fractures and finite element surfaces should also be re-calculated for equivalent permeability calculations.

This analytical approach for modeling fracture propagation in naturally fractured reservoirs is computationally efficient compared to numerical methods, especially when dealing with a large number of natural fractures. However, due to its simplified 2D approximate solutions, the model does not have the capability to predict the geometry of the propagated fractures in 3D space. In addition, since this model assumes a planar extension for the pressurized fractures and approximates wing crack propagations by adding new fractures at the fracture tips, it is a simplified representation of the actual non-planar propagation problem. It may not accurately capture the changes in the fracture network connectivity caused by fracture propagation and consequently the overall reservoir hydraulic conductivity changes. Future model development effort in these areas is suggested.

#### **4.8 Integration with the Coupled FEM**

The fracture network model is integrated with the coupled thermo-poroelastic FEM by linking the equivalent permeability change with the fracture deformation and growth. On the one hand, at each time step, the fracture aperture data are input for the equivalent permeability used in the FEM. The stresses required for subsequent fracture deformation analysis are calculated from the FEM solutions. Once fractures deform, their apertures are updated in the next time step for following solutions. Permeability could also change as a result of fracture growth. The enlargement of fracture radii improves the connectivity of the fracture network, and consequently, enhances the hydraulic conductivity of the fractured medium. Therefore, fracture network geometry should also

be updated in the next time step. The step-by-step solution procedure for the integrated model is shown in Figure 4.30.

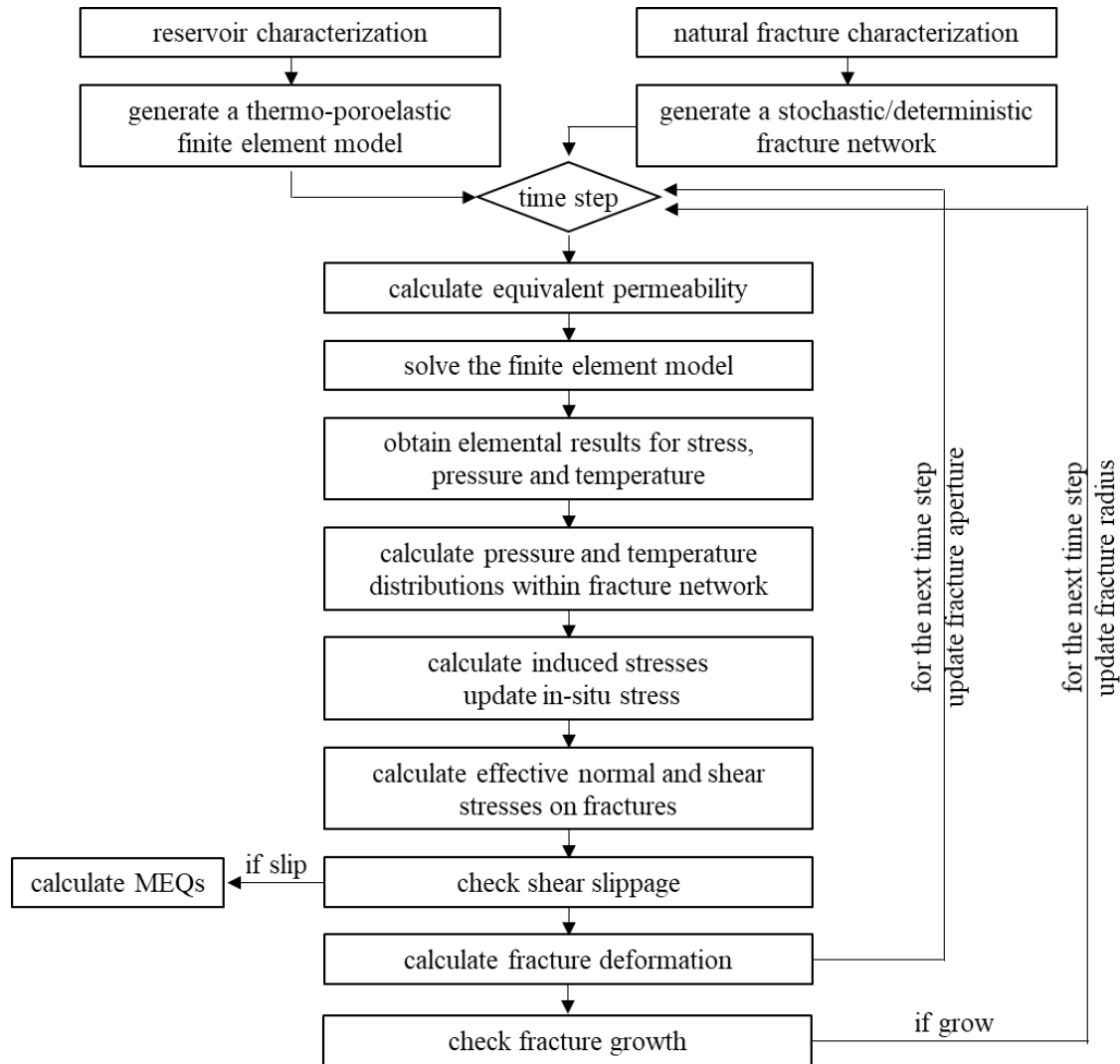


Figure 4.30. Step-by-step solution procedure for the integrated model.

## **5. Model Verification**

In this chapter, we present the verification process of the developed numerical model. As fully verification of numerical models of complex natural geological systems is impossible (Oreskes et al. 1994), the individual components of this model are verified against analytical solutions or previously published numerical solutions when possible.

### **5.1 FEM Solution to Thermo-poroelasticity**

In this section, the FEM solution to thermo-poroelasticity is firstly verified using problems of poroelastic consolidation and thermoelastic consolidation. The result from a code comparison against a benchmark problem of the poroelastic response in a fault zone is provided as well. The verifications have also been performed using thermo-poroelastic wellbore loading problem (Lee 2011) and the poroelastic consolidation problems of Terzaghi and Mandel (Wang 2014).

#### **5.1.1 Poroelastic Consolidation**

The finite element model is firstly verified by compared to analytical solutions of Terzaghi's classical 1D consolidation problem (Terzaghi 1923). An external normal load is applied instantaneously on the top surface of a fluid saturated porous sample. The fluid is allowed to dissipate only at the drained top surface. It is known as 1D consolidation since the deformation and pore fluid flow only occur in one direction.

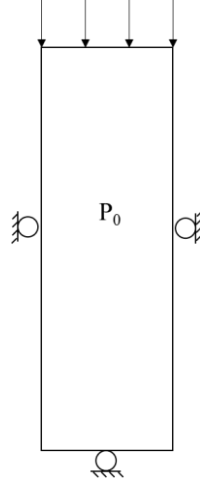


Figure 5.1. Illustration of Terzaghi's consolidation problem.

The analytical solution for the pore pressure field as a function of time and space is (Terzaghi 1923; Jaeger et al. 2007; Cheng 2016):

$$\frac{p(z,t)}{p_0} = 1 - \sum_{n=0}^{\infty} (-1)^n \left\{ \operatorname{erfc} \left[ \frac{2nh + z}{(4kt / \mu S)^{\frac{1}{2}}} \right] + \operatorname{erfc} \left[ \frac{2(n+1)h - z}{(4kt / \mu S)^{\frac{1}{2}}} \right] \right\} \quad (5.1)$$

Where  $p(z,t)$  is the pore pressure in depth  $z$  at time  $t$ ;  $p_0$  is the initial pore pressure;  $h$  is the thickness of the sample;  $k$  is permeability;  $\mu$  is fluid viscosity;  $S$  is storage coefficient;  $\operatorname{erfc}(x)$  is

the coerror function,  $\operatorname{erfc}(x) = 1 - \operatorname{erf}(x) = \frac{2}{\pi} \int_x^{\infty} e^{-\eta^2} d\eta$ .

The analytical solution of vertical displacement is:

$$w(z,t) = \frac{p}{\lambda + 2G} \left[ (z - h) + \frac{\alpha^2 M h}{\lambda + 2G + \alpha^2 M} \sum_{n=1,3,\dots}^{\infty} \frac{8}{n^2 \pi^2} \cos \left( \frac{n\pi z}{2h} \right) \exp \left( \frac{-n^2 \pi^2 k t}{4\mu S h^2} \right) \right] \quad (5.2)$$

Where  $w(z,t)$  is the displacement in depth  $z$  at time  $t$ ;  $\lambda$  is the Lamé's parameter;  $G$  is the shear modulus;  $\alpha$  is the Biot effective stress coefficient;  $M$  is the Biot modulus.

To verify our finite element model, the same problem is analyzed. The model setup is shown in Figure 5.2. The model extends from the top surface of  $z=0$  m down to a depth of  $z=10$  m. To consider a 1D consolidation problem, it is discretized using 8-node brick elements with 10 elements and 44 nodes. The initial pore pressure in the domain is set to be 0 MPa. On the top surface where drainage is allowed, a uniform downward load of 1 MPa is applied suddenly, and the excess pore pressure on this surface is kept at 0 MPa. On all other sides, the normal component of displacement is fixed, and no flow of pore fluid is permitted. The material properties used in this example are given in Table 5.1.

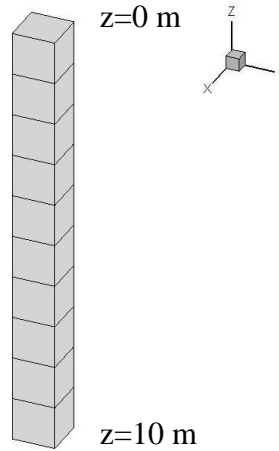


Figure 5.2. Finite element mesh for the Terzaghi's consolidation problem.

Table 5.1 Properties used in the Terzaghi's problem

Model Geometry	10 m x 1 m x 1 m
Shear Modulus	12 GPa
Poisson's Ratio	0.15
Undrained Poisson's Ratio	0.29
Biot's Coefficient	1.0
Permeability	0.5 md
Fluid Viscosity	0.0003 Pa · s
Applied Load	1 MPa



The FEM simulation results (shown in symbols) for pore pressure at different time are compared to analytical solutions (shown in solid lines) in Figure 5.3. The excess pore pressure is normalized by the magnitude of the applied load. The evolution of pore pressure shows that initially excess pore pressure is induced as a result of the applied load. As the pore fluid drains out from the top surface, the excess pore pressure dissipates, and pore pressure gradually returns to its initial value.

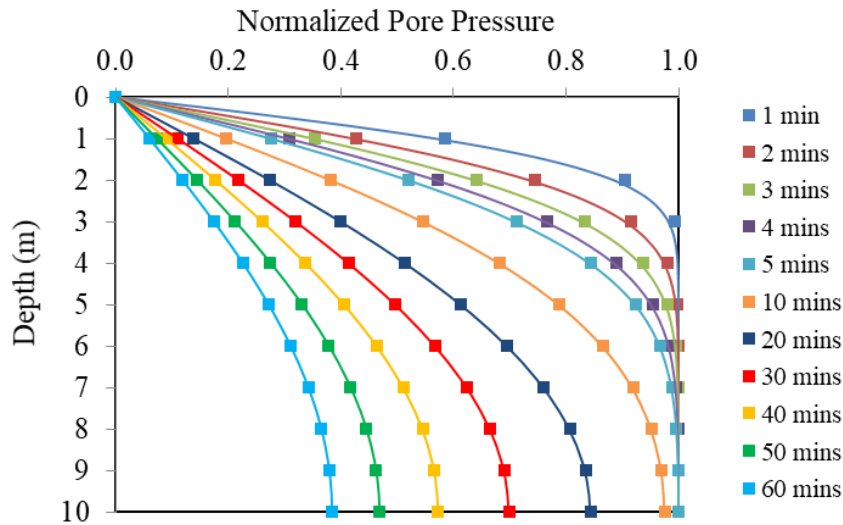


Figure 5.3. Pore pressure profiles at different time.

Similarly, simulation results for top surface displacement from FEM (shown in symbols) and analytical solutions (shown in solid lines) are compared in Figure 5.4. The applied load instantaneously induces rock deformation. As pore fluid drainage starts, the sample gradually consolidates. In both comparisons, our FEM results match excellently with the analytical solutions, which verify the capability of our FEM model for poroelastic analysis.

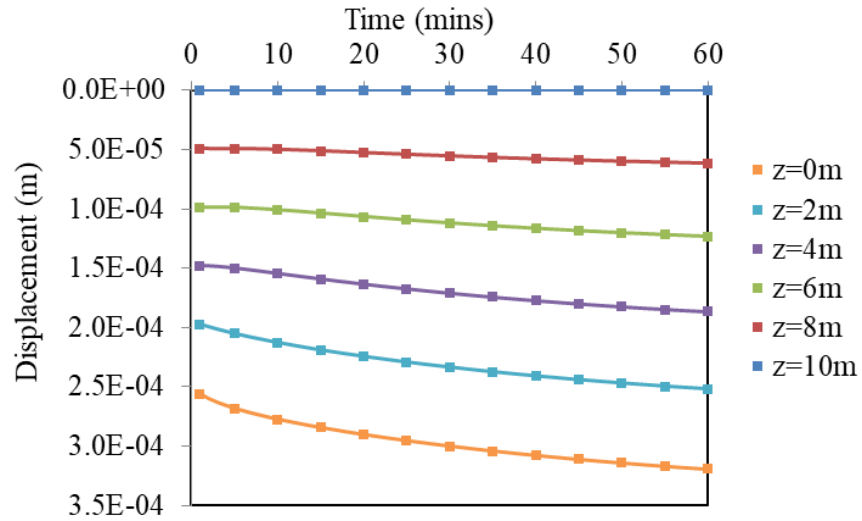


Figure 5.4. Displacement profiles at different time.

### 5.1.2 Thermoelastic Consolidation

The thermo-poroelastic part of the finite element model is verified by simulating the 1D thermoelastic consolidation behavior of a fully saturated soil column.

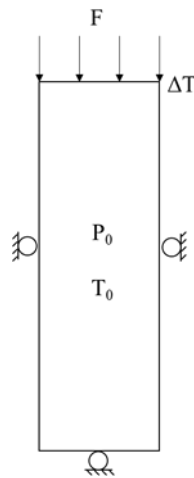


Figure 5.5. Illustration of the 1D thermoelastic consolidation problem.

The saturated soil column is 7 m in height, at an initial temperature of 0 °C and pore pressure of 0 Pa. A constant surface compression load of 1 Pa and a constant temperature boundary of 50 °C are

applied on the top surface of the soil column. All the boundaries are assumed to be thermally insulated and impermeable with normal displacements constrained, except at the top surface. As shown in Figure 5.6, the column is discretized into 50 elements and 204 nodes. A refined mesh is used near the top surface to eliminate the numerical errors in transient heat transfer solutions. Parameters used in the model are listed in Table 5.2.

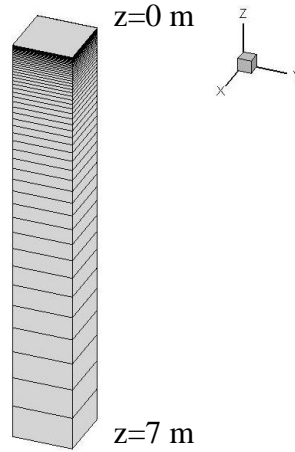


Figure 5.6. Finite element mesh for the thermoelastic consolidation problem.

Table 5.2 Properties used in the thermoelastic consolidation problem (Aboustit et al. 1982 and Noorishad et al. 1984)

Model Geometry	7 m x 1 m x 1 m
Young's Modulus	6000 Pa
Poisson's Ratio	0.4
Biot's Coefficient	1.0
Porosity	0.2
Hydraulic Conductivity	4e-6 m/s
Heat Capacity	167.2 KJ/m <sup>3</sup> /°C
Thermal Conductivity	836.0 W/m/°C
Thermal Expansion Coefficient	9e-7
Initial Pore Pressure	0 Pa
Initial Temperature	0 °C
Surface Temperature	50 °C
Applied Load	1 Pa

Due to lack of an analytical solution for the thermoelastic consolidation problem, a code-to-code comparison is performed. The results of the top surface displacement from the coupled finite element model are plotted in Figure 5.7, along with the numerical results obtained by Aboustit et al. (1982) and Noorishad et al. (1984) for comparison. The numerical results of an isothermal case are also compared with an analytical solution (Biot's 1941). It shows that our finite element modeling results agree well with the results published in the literature, which verifies the capability of our model for fully coupled thermo-poroelastic analysis.

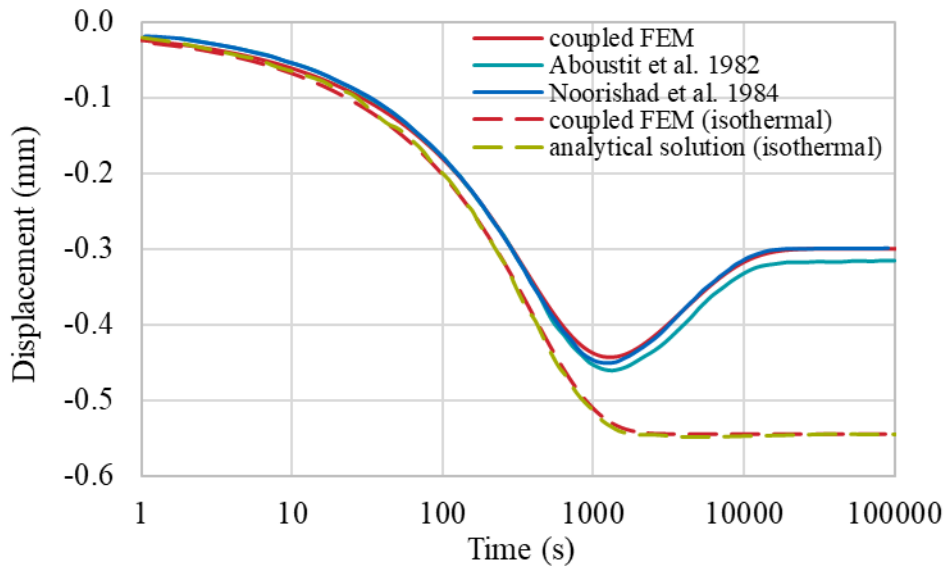


Figure 5.7. Comparisons of our numerical solutions for displacement at the top surface in the thermoelastic consolidation problem (solid lines); and comparison to the analytical solution for the isothermal consolidation problem (dash lines). Good agreement is achieved.

### 5.1.3 Benchmark Problem

The finite element model has also been used in a code comparison study for solving a benchmark problem structured by the United States Department of Energy, Geothermal Technologies Office. This problem involves a poroelastic response to water injection in a fault zone within a geothermal

reservoir. It is based on recent observations at a test well in the Raft River EGS demonstration site in southern Idaho, which demonstrates a nonlinear permeability feedback from pressure changes (White et al. 2016).

The schematic representation of this problem is shown in Figure 5.8. Water is injected from a vertical well at a constant rate of 80 kg/s, with the fluid entering the reservoir in a narrow (4 m thick) horizontal faulted layer at the depth of 2000 m. The injection is assumed under isothermal conditions, therefore, only the coupled poroelastic response is involved.

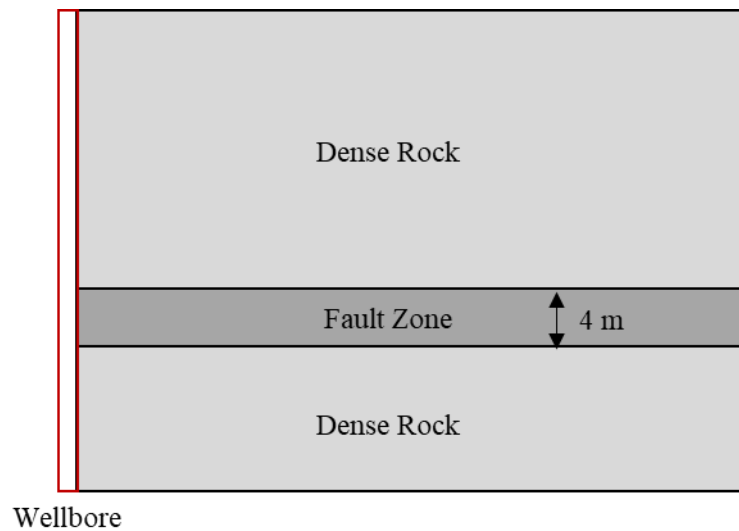


Figure 5.8. Schematic of the benchmark problem (modified from White et al. 2016).

A 1/8 symmetric Cartesian domain (Figure 5.9) is modeled. It includes 2 m of fault zone and 20 m of dense reservoir rock surrounding the fault zone, and extends 2000 m away in the x and y directions. The bottom, top, left and front boundaries are treated as no flow, while fixed fluid pressure is applied on the right and back sides, with values equal to the initial fluid pressure. Actual wellbore injection boundary is taken into consideration by modeling the wellbore geometry explicitly. The constant injection rate is specified at the wellbore nodes and its corresponding

surface traction is applied on the wellbore. Water density and viscosity are kept constant. The parameters specified in this benchmark problem are given in Table 5.3.

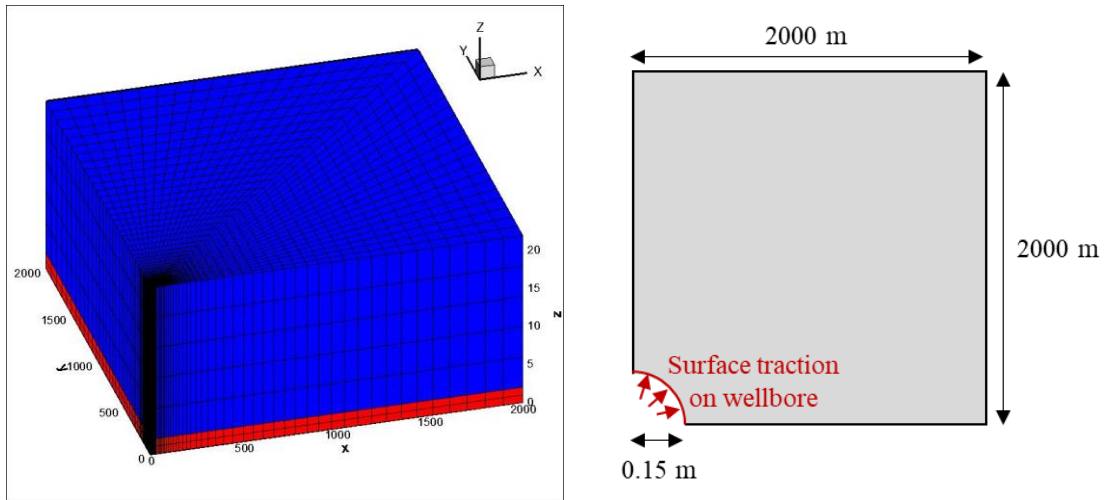


Figure 5.9. A 1/8 symmetric domain of the benchmark problem. Left: It includes 2 m of fault zone and 20 m of dense reservoir rock; Right: 2D planar view of the domain showing the applied surface traction on the wellbore.

Table 5.3 Properties used in the benchmark problem (White et al. 2016)

	Dense Rock	Fault Zone
Thickness (m)	20	2
Young's Modulus (GPa)	600	800
Poisson's Ratio	0.1	0.2
Permeability (m <sup>2</sup> )	1.0E-18	1.0E-13
Porosity	0.01	0.0001
Pore Compressibility (Pa <sup>-1</sup> )	4.0E-10	1.0E-07
Bulk Compressibility (Pa <sup>-1</sup> )	4.0E-12	1.0E-11
Bulk Modulus (GPa)	250	100
Overburden Stress (MPa)	-	45
Exponential Coefficient	-	10
Rock Density (kg/m <sup>3</sup> )	2500	
Water Viscosity (Pa.s)	2.02E-04	
Water Density (kg/m <sup>3</sup> )	936.42	
Water Compressibility (Pa <sup>-1</sup> )	4.48E-10	

This problem considers a nonlinear permeability-fluid pressure feedback. Permeability is defined as an exponential function of hydrodynamic pressure in the fault zone (White et al. 2016).

$$k = k_0 \exp\left(\frac{c[P - P_0]}{\sigma}\right) \quad (5.3)$$

Where  $k_0$  is the permeability at zero stress; the exponent  $c$  is a fitting parameter which can be experimentally determined;  $P$  and  $P_0$  are the fluid pressure at the current time and at the initial condition, respectively;  $\sigma$  is the total overburden stress.

Two scenarios are modeled: (1) no leak-off scenario assuming the adjacent reservoir formation is impermeable and fluid is confined within the fault zone; (2) leak-off scenario considering a finite permeability of the reservoir formation, which allows the reservoir rock to receive fluid from the fault zone.

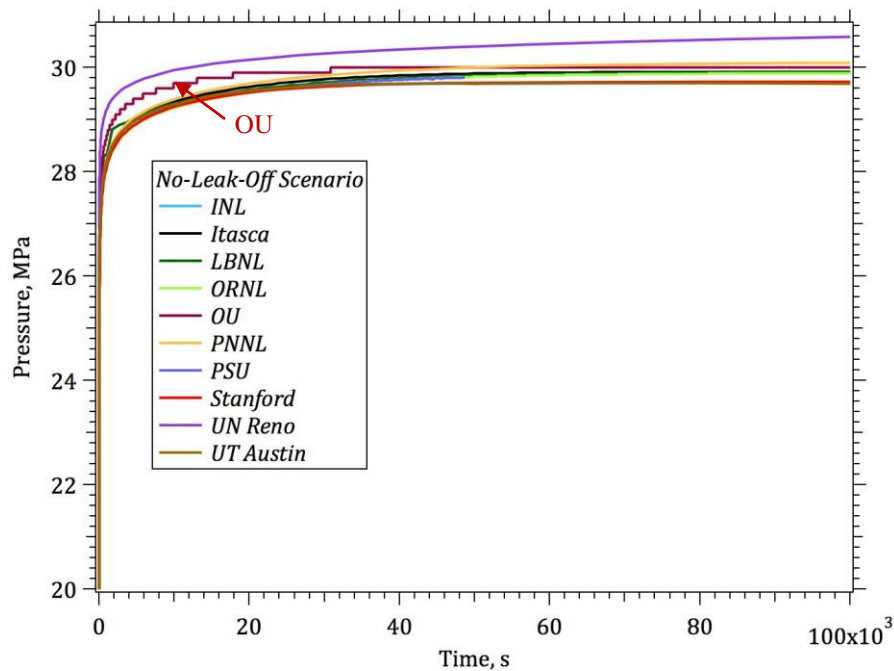


Figure 5.10. Pressure evolution versus time at  $r=14.142$  m for the no leak-off scenario (White et al. 2016). Our result is labeled as “OU”, which agrees well with the results of other participating teams.

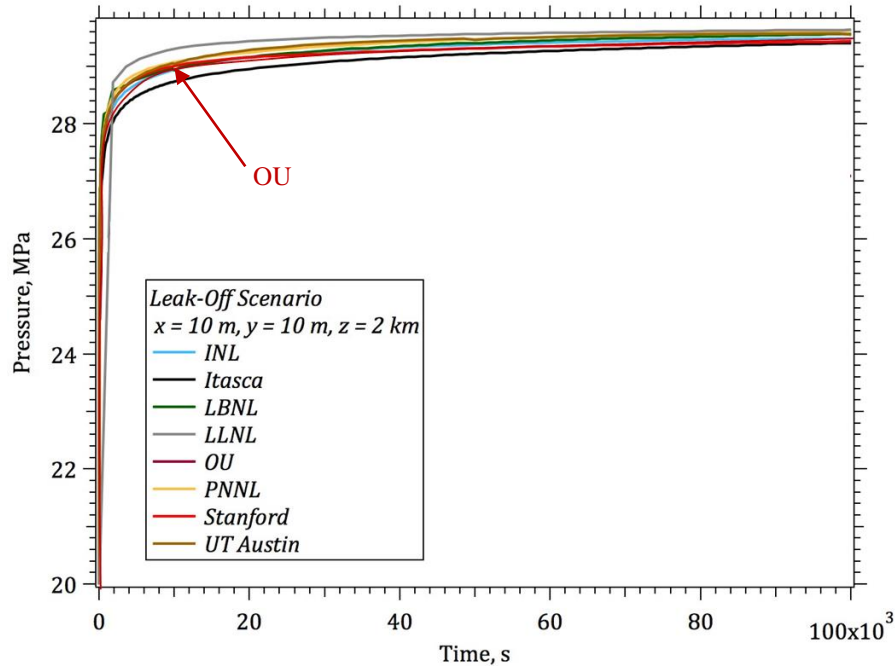


Figure 5.11. Pressure evolution at  $r=14.142$  m for the leak-off scenario (White et al. 2016). Our result is labeled as “OU”, which agrees well with the results of other participating teams.

Comparisons of pressure solutions among all participating teams including universities, industry and U.S. national laboratories are illustrated in Figure 5.10 and Figure 5.11, for the no leak-off and leak-off scenarios, respectively. In both scenarios, our modeling results (labeled as “OU”) are in good agreements with the results from other participating teams, which verifies the capability of our finite element code for solving the coupled poroelastic problems.

## 5.2 Heat Transfer in Fracture Network

For the verification of heat transfer model in the fracture network, we solve a heat extraction problem in a single circular shaped fracture with a borehole doublet.

A fracture of radius  $R$  is centered at the origin, containing a pair of injection and extraction wells, which are located at  $(-a, 0)$  and  $(a, 0)$ , with an equal magnitude but opposite flow rate of  $+Q$  and  $-$



Q, respectively. With known initial temperature, injection temperature and flow rate, the temperature at the extraction well is solved and compared with the results obtained from an analytical solution (Rodemann 1982) and an integral equation solution (Ghassemi et al. 2003).

The geometry and data set used in Rodemann (1982) for the Urach hot dry rock project is adopted for this numerical solution. As shown in Figure 5.12, the fracture radius is 50 m, and the spacing between the injection well (-31.25, 0) and extraction well (31.25, 0) is 62.5 m. The initial rock temperature is 140 °C, and the injection temperature is 60 °C. The flow rate is 0.003 m<sup>3</sup>/s. Other data are listed in Table 5.4.

Table 5.4 Properties used in the heat transfer verification problem

Rock Temperature	140 °C
Injection Temperature	60 °C
Fracture Radius	50 m
Fracture Width	0.001 m
Half Distance between Boreholes	31.25 m
Flow Rate	0.003 m <sup>3</sup> /s
Water Viscosity	0.0003 Pa·s
Water Density	1000 kg/m <sup>3</sup>
Rock Density	2700 kg/m <sup>3</sup>
Specific Heat Capacity of Water	4180 J/Kg/K
Specific Heat Capacity of Rock	840 J/Kg/K

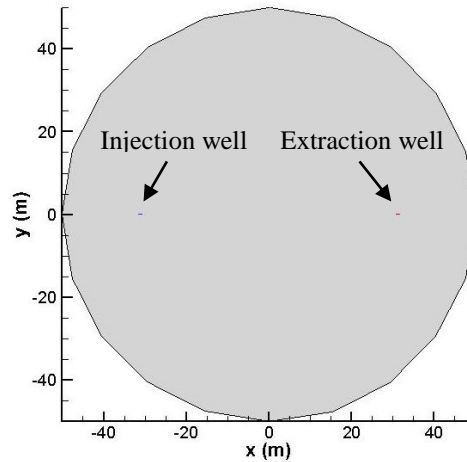


Figure 5.12. Geometry of the heat extraction problem. The fracture radius is 50 m. The distance between injection and production well is 62.5 m.

To represent the fracture and doublet system, we generated a fracture network that consists of 3 interconnected fractures: an injection fracture, a solution fracture, and an extraction fracture, with a radius set to be 0.1 m, 50 m, and 0.1m, respectively. The intersections with the injection and extraction fracture are at  $(-31.25, 0)$  and  $(31.25, 0)$ , respectively, which is the same as in the problem description. The intersection of the injection/extraction fracture and the solution fracture is a line with a length equal to the diameter of the injection/extraction fracture. Considering the contrast between the intersection line length (0.2 m) and the diameter of the fracture (100 m), it is still reasonable to treat the injection/extraction fractures as “point source”. A fracture width of 0.001 m is assigned to all three fractures, and is fixed during the simulation to exclude the change in internal thermal energy caused by fracture volume change.

To initiate the fluid flow from the injection fracture to the extraction fracture with a rate of  $0.003 \text{ m}^3/\text{s}$ , a pressure gradient is applied on the fracture network, as shown in Figure 5.13.

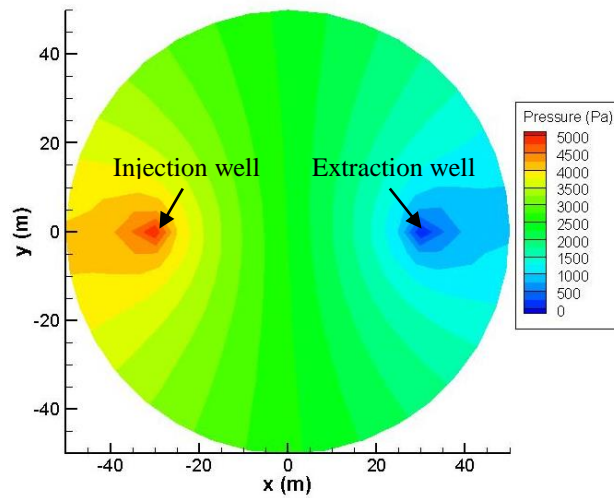


Figure 5.13. Pressure profile on the fracture. Fluid flows from the injection fracture to the extraction fracture under the pressure gradient.

Using the heat transfer model developed in this study (Chapter 4.5), the temperature distribution within the fracture network can be obtained. Figure 5.14 shows the temperature result after 3 days of injection. The temperature in the solution fracture is 136.8 °C. In our heat transfer model, the temperature on a fracture is assumed to be constant throughout the fracture surface, which results in a uniform temperature distribution pattern on each fracture. Besides, it is assumed that fluid exits a fracture at the same temperature as the current temperature in it. Therefore, the extraction temperature is 136.8 °C.

The fluid temperature in the fracture after 3 days of injection has also been obtained analytically by Rodemann (1982) and by using an integral equation solution by Ghassemi et al. (2003) (Figure 5.15). Both of them show that after 3 days of injection, the fluid temperature at the extraction point is approximately 137 °C, which is very close to our results.

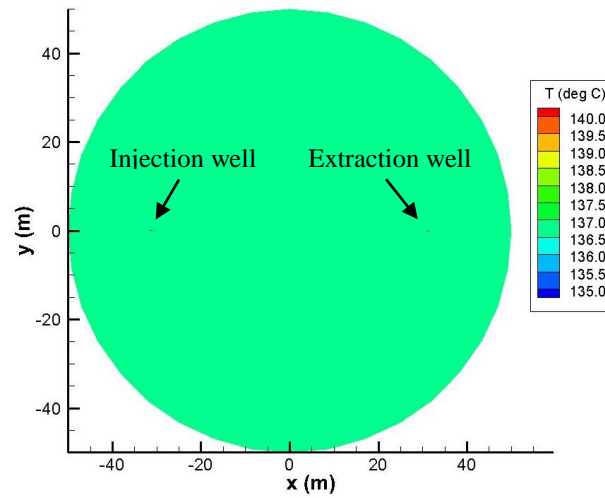


Figure 5.14. Temperature distribution within the fracture network. At the time of 3 days, the extraction fluid temperature is 136.8 °C.

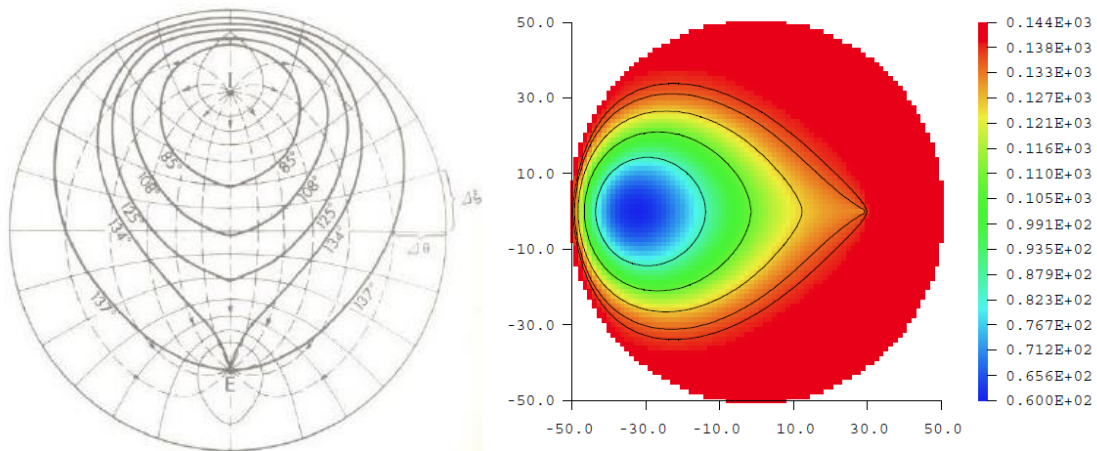


Figure 5.15. Fluid temperature distribution in a circular fracture after 3 days injection. Left: from analytical solution (Rodemann 1982); Right: from an integral equation solution (Ghassemi et al. 2003). Both show an extraction temperature of approximately 137 °C, which is close to our results.

The numerical results presented here are in good agreements with other published results, which verifies the capability of the proposed model in solving heat transfer problems in fracture networks.

At this moment, the detailed 2D temperature distribution on individual fracture plane is not available. It may be achieved by the implementation of the image theory and requires further model improvement in the future.

### 5.3 Fracture Growth

The analytical method of mixed-mode fracture propagation has been verified through numerical results by Hossain (2001) and Kumar (2018). The stress intensity factors were firstly compared with those obtained from a boundary element based fracture analysis program FRANC3D and those obtained from a boundary element method based simulator GeoFrac3D using a crack-tip opening displacement approach (Kumar and Ghassemi 2015). The tip propagation path predicted by the proposed analytical method was also compared with that obtained from the FRANC3D and the GeoFrac3D analysis. In this study, the same validation problems are solved, and the results are presented for comparisons.

As shown in Figure 5.16, an internally pressurized penny-shaped fracture is subjected to far field stresses. The half-length of the fracture is 10 m, and it inclines at an angle with respect to the maximum principal stress direction. The fluid pressure inside the fracture is assumed to be constant throughout the fracture surface. The geometrical and mechanical properties for the model are listed in Table 5.5.

Table 5.5 Properties used in the crack propagation model

Fracture radius (half length)	10 m
Fracture inclination	15°, 30° and 45°
Mode I fracture toughness	1.25 MPa·m <sup>0.5</sup>
Fracture internal pressure	80 MPa
Maximum principal stress	92 MPa
Maximum principal stress	63 MPa

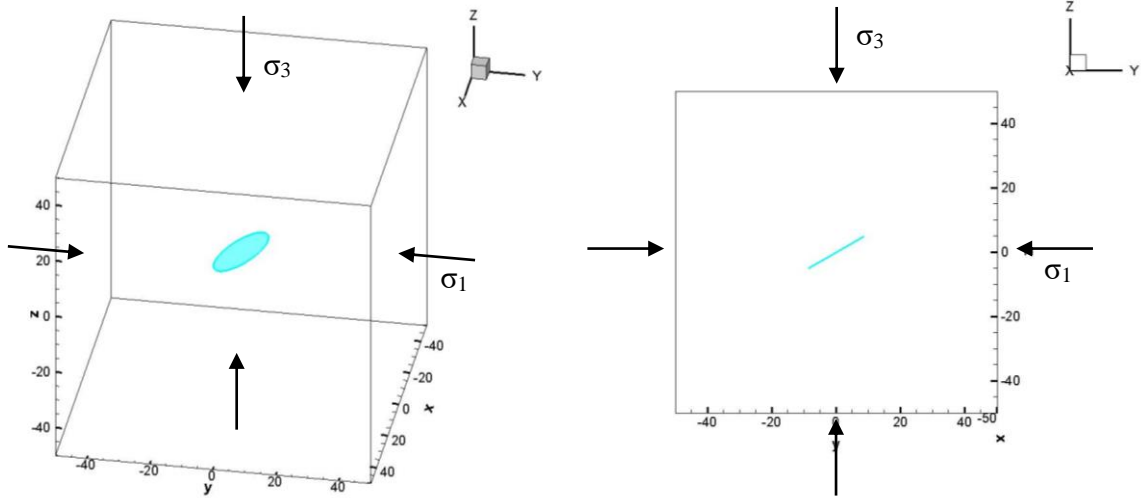


Figure 5.16. An inclined penny-shaped fracture subjected to internal pressure and far field stresses (left); 2D view of the inclined penny-shaped fracture (right).

The stress intensity factors are estimated using Eqn. (3.69) and (3.70), for different fracture orientations: inclined  $15^\circ$ ,  $30^\circ$  and  $45^\circ$  with respect to the maximum principal stress direction. The analytical results are plotted in Figure 5.17, along with those obtained from FRANC3D (Hossain 2001) and from GeoFrac3D (Kumar 2018). Our analytical results are identical to those published in Hossain 2011, since the same equations are applied for stress intensity factor calculations. It can be seen that the analytical results agree well with the numerical results for different fracture orientations.

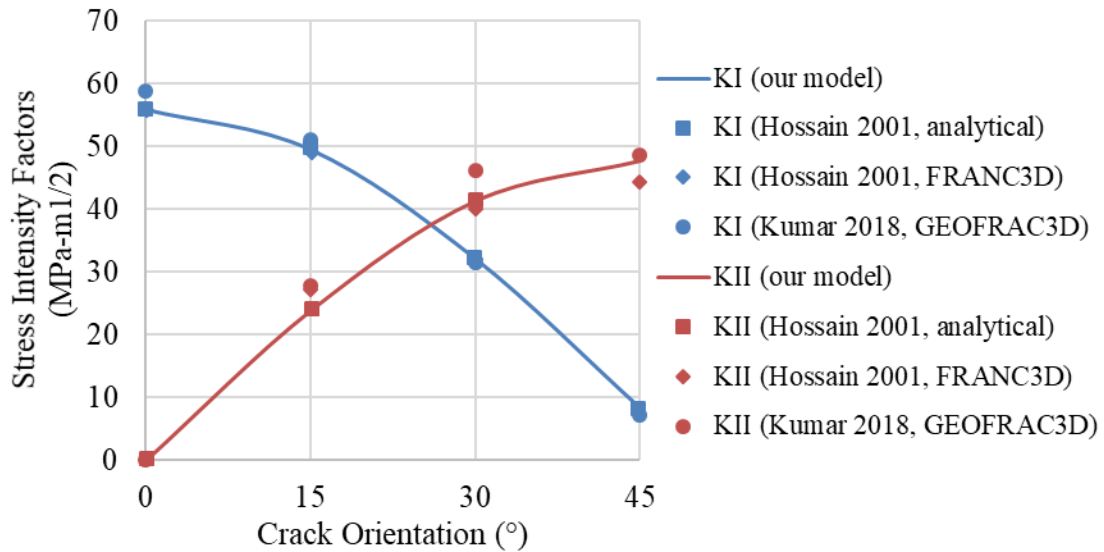


Figure 5.17. Comparison of stress intensity factors from the analytical method with numerical results from FRANC3D (Hossain 2001) and GeoFrac3D (Kumar 2018).

The comparisons between the fracture tip propagation paths predicted by the proposed method and those from FRANC3D (Hossain 2001) are plotted in Figure 5.18. As summarized by Hossain (2001), for all fracture orientations, good agreements between the analytical and the numerical results are obtained. The analytical results of this current study also have a perfect match with the published analytical results. Our analytical results are also in good agreements with those obtained from GeoFrac3D (Kumar 2018) for the fracture orientations at 15° and 30°.

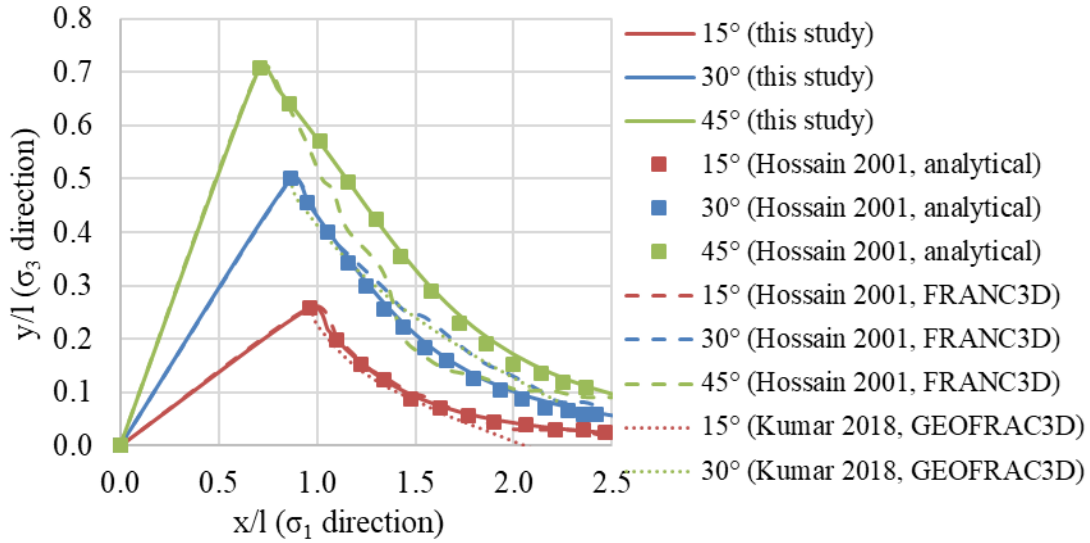


Figure 5.18. Comparison of fracture tip propagation path from the analytical method with numerical results from FRANC3D (data digitized from Hossain 2001).

#### 5.4 Rate-and-state Friction Model

The implementation of the rate-and-state-friction (RSF) in the fracture network model is verified by comparing with results published in literature. Samuelson et al. (2011) presented the velocity weakening frictional response of a slipped fracture to a change in sliding velocity from 10  $\mu\text{m/s}$  to 30  $\mu\text{m/s}$ , as described by a RSF model. For verification purpose, the same inputs are used in our RSF model, and the results are compared. The properties used in the verification problem are listed in Table 5.6.

Table 5.6 Properties used in the RSF friction model verification

Initial Friction Coefficient $\mu_0$	0.6
Sliding Velocity $v_0$	10 $\mu\text{m/s}$
Sliding Velocity $v$	30 $\mu\text{m/s}$
Parameter a	0.001
Parameter b	0.0015
Characteristic Slip Distance $d_c$	25 $\mu\text{m}$



The results are plotted in Figure 5.19. In this case, since the direct effect parameter  $a$  is lower than the evolution effect parameter  $b$ , a velocity weakening behavior in the friction coefficient is predicted by the RSF model. A nearly perfect agreement between our RSF model results and the published data is observed.

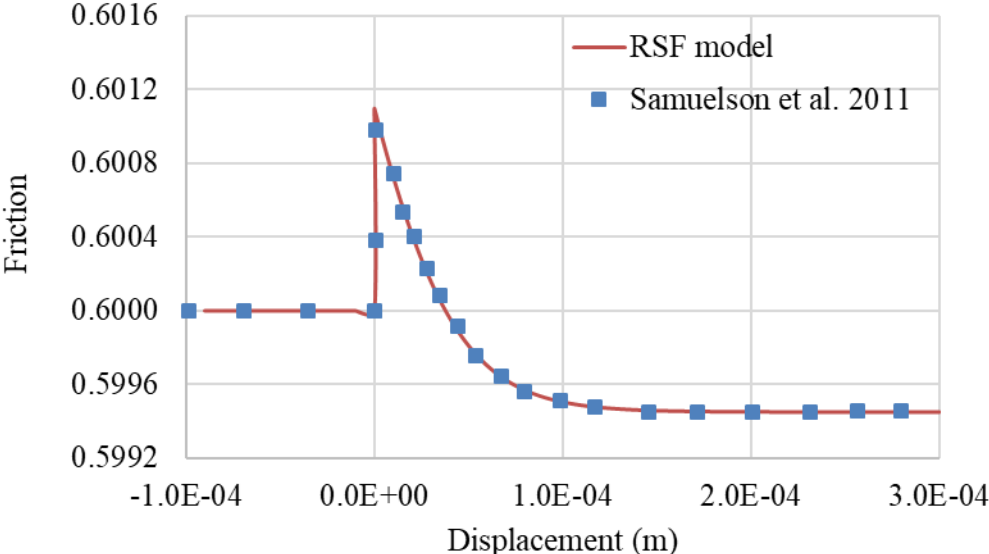


Figure 5.19. Comparison of friction evolutions predicted by our RSF model (red line) and published data (blue symbols). Perfect agreement is observed.

## **6. Numerical Examples**

In this chapter, we present numerical examples for injection experiments of naturally fractured reservoirs while taking into account thermo-poroelastic coupling and fracture network deformation. A sensitivity study is also performed to examine the influences of different fracture properties, reservoir parameters, and injection scheme on the shear stimulation outcome in fractured reservoirs.

### **6.1 Injection Response of Fractured Reservoirs**

A simulation is firstly carried out to obtain a general view of the response of a synthetic 3D naturally fractured reservoir to fluid injection.

#### **6.1.1 Model Setup**

The geometric model used in this study is a reservoir block of 100 m x 100 m x 100 m. A natural fracture network of 20 penny-shaped fractures is stochastically generated in the domain using the approach described in Chapter 4. Poisson's distribution, log-normal distribution and Fisher von Mises distribution are used for defining fracture location, size and orientation data, respectively. The input parameters for fracture generation are listed in Table 6.2. This domain is meshed into 68,921 nodes and 64,000 brick elements with a uniform element size of 2.5 m x 2.5 m x 2.5 m. The geometry and mesh of this model are shown in Figure 6.1.

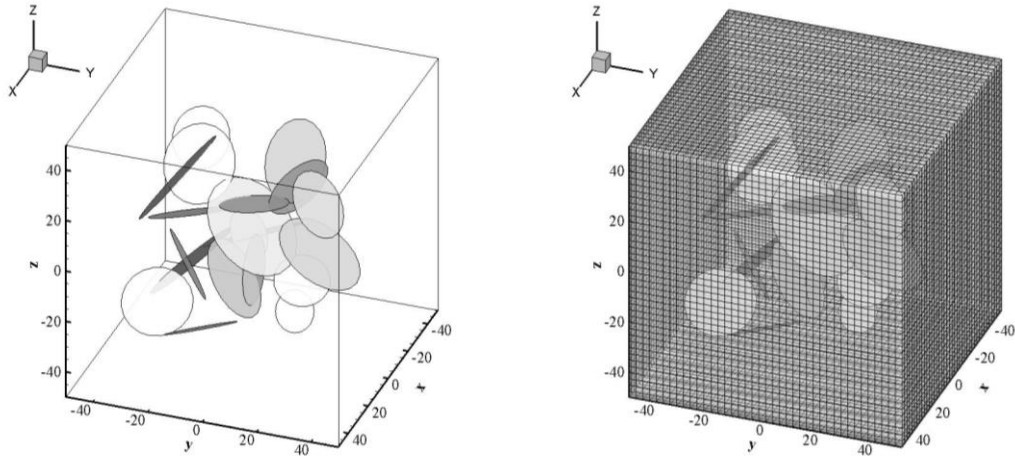


Figure 6.1. Simulation domain contains 20 stochastic fractures (left); A uniform mesh with 64,000 elements (right).

Table 6.1 Fracture network generation inputs

Number of Fractures	20
Mean of Fracture Radii (Log EX)	2.5
Standard Deviation of Fracture Radii (Log SD)	0.3
Size-aperture Coefficient	4.0E-5
Fisher von Mises Orientation Parameter	2.8

The injection well is considered to be located at the center of this model, with an injection interval of 20 m in the middle (from -10 m to 10 m). Considering the scale ratio of the simulation domain and the well radius, the injection interval is represented by injection elements in the vertical direction. A constant injection rate of  $0.001 \text{ m}^3/\text{s}$  is specified at the injection wellbore. The top boundary of this domain is set to be an unconstrained free boundary, while zero normal displacements are applied for the bottom and lateral boundaries. All side boundaries are assumed to be no flow.

Assuming the reservoir is located at a depth of 2 km, and it is under a strike-slip faulting regime. The vertical stress is 45 MPa ( $S_v$ , z direction), the maximum horizontal stress is 50 MPa in the E-W direction ( $S_{Hmax}$ , x direction), and the minimum horizontal stress is 30 MPa in the N-S direction ( $S_{Hmin}$ , y direction). The initial pore pressure is assumed to be 20 MPa. The initial reservoir temperature is 170 °C and the temperature of the injected fluid is 20 °C. The properties of reservoir rock and fractures are selected to represent a typical fractured EGS (Wang and Ghassemi 2013; Doonechaly et al. 2016; Ucar et al. 2016), and are summarized in Table 6.2.

Table 6.2 Reservoir, fracture and fluid properties

Rock Properties	
Young's Modulus	10 GPa
Drained Poisson's Ratio	0.22
Undrained Poisson's Ratio	0.46
Biot's Coefficient	0.97
Matrix Permeability	1E-17 m <sup>2</sup>
Rock Porosity	0.2
Rock Density	2400 kg/m <sup>3</sup>
Thermal diffusivity	1.6E-6 m <sup>2</sup> /s
Thermal Expansion Coefficient of Solid	1.8E-5 K <sup>-1</sup>
Fracture Properties	
Basic Friction Angle	30°
Shear Dilatation Angle	2°
90% Closure Stress	20 MPa
Characteristic Slip Distance	2E-5 m
Direct Effect Parameter	0.011
Evolution Effect Parameter	0.020
Reference Sliding Velocity	1E-12 m/s
Mode I Fracture Toughness	2.0 MPa·m <sup>0.5</sup>
Fluid Properties	
Fluid Density	1000 kg/m <sup>3</sup>
Fluid viscosity	3E-4 Pa·s
Fluid Bulk Modulus	2.235 GPa
Fluid Compressibility	4.475E-5 Pa <sup>-1</sup>

Heat Capacity of Fluid	4200 J/(kg·K)
Thermal Expansion Coefficient of Fluid	3.0E-4 K <sup>-1</sup>
Stress State	
Maximum Horizontal Stress	50 MPa
Minimum Horizontal Stress	30 MPa
Vertical Stress	45 MPa
Initial and Boundary Conditions	
Initial Pore Pressure	20 MPa
Initial Reservoir Temperature	170 °C
Injection Rate	0.001 m <sup>3</sup> /s
Injecting Fluid Temperature	20 °C

### 6.1.2 Simulation Results

An injection duration of 9 hours is simulated, and the response of the fractured reservoir to injection is analyzed, in terms of spatial distribution of pressure and temperature changes, permeability evolution and injection induced micro-seismicity.

In this model, the propagation of natural fractures is considered, and its effects on the simulation results are evaluated. Initially, only 8 out of 20 fractures are connected to the injection flow path, as shown in Figure 6.2 (left). After 6 hours of injection, 1 fracture starts to propagate. Since the propagated fracture is still in an isolated status, no new fractures are added to the existing flow path. As fluid is continued to be injected, this fracture continues to propagate and coalesces with a nearby fracture at the time of 8 hours. The second fracture propagation occurs after injection for 9 hours. After fracture propagations, 6 more fractures get connected to the flow path and the connectivity of the fracture network is improved. As a consequence, the fluid flow within the fractured system and the stimulation outcome are affected, as will be discussed below.

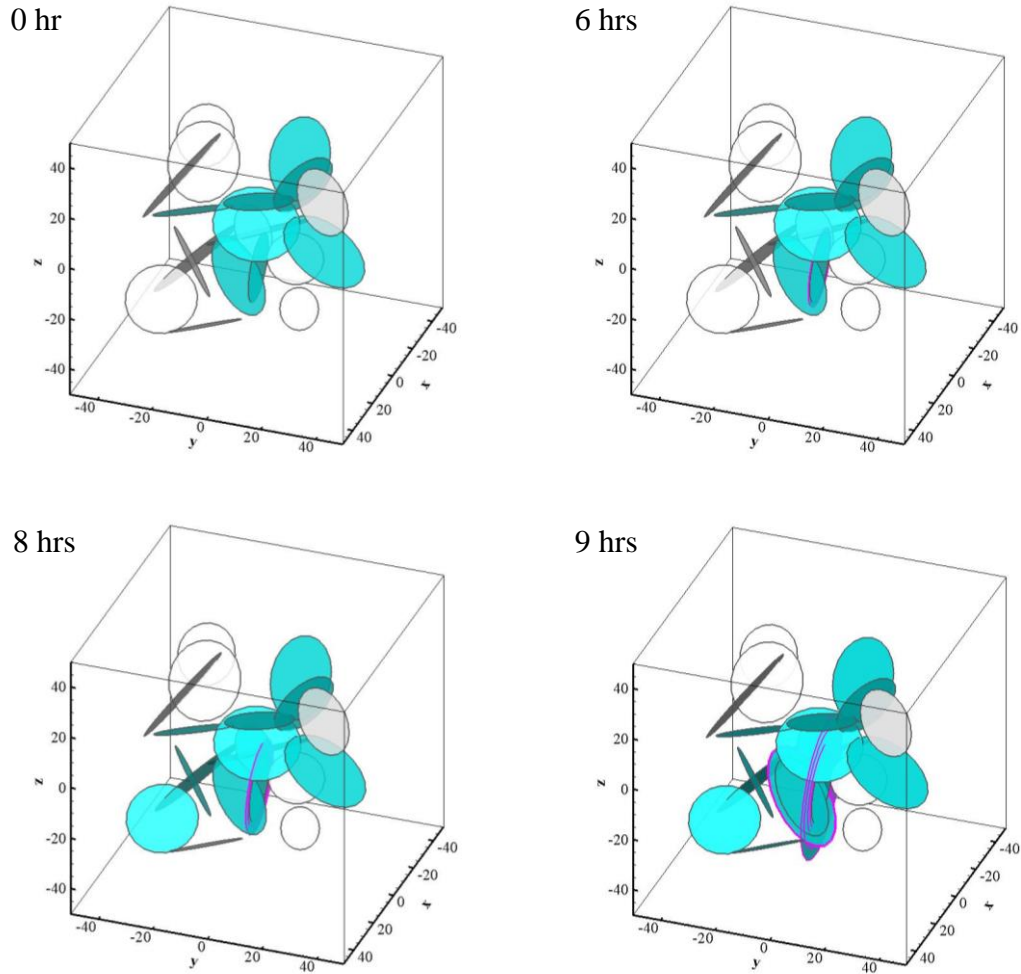


Figure 6.2. Comparison of fracture network connectivity before (top left) and after fracture propagations (after 6, 8 and 9 hours injection). The interconnected fractures on the injection flow path are shown in green. The isolated fractures are shown in grey. The edges of the propagated fractures are shown in pink.

The evolution of pore pressure distribution during the injection (at 1 hr, 4 hrs, 7 hrs, and 9 hrs) is shown in Figure 6.3. The results show that the pore pressure in the reservoir is elevated as injection continues. It can also be seen that the pore pressure development is controlled by the fracture network. The injection fluid mostly pressurizes the interconnected fractures other than the rock

matrix, which is reasonable, since the permeability of the fractures ( $3\text{E-}12\text{ m}^2$  to  $2\text{E-}10\text{ m}^2$ ) is several orders of magnitude higher than that of the matrix ( $1\text{E-}17\text{ m}^2$ ).

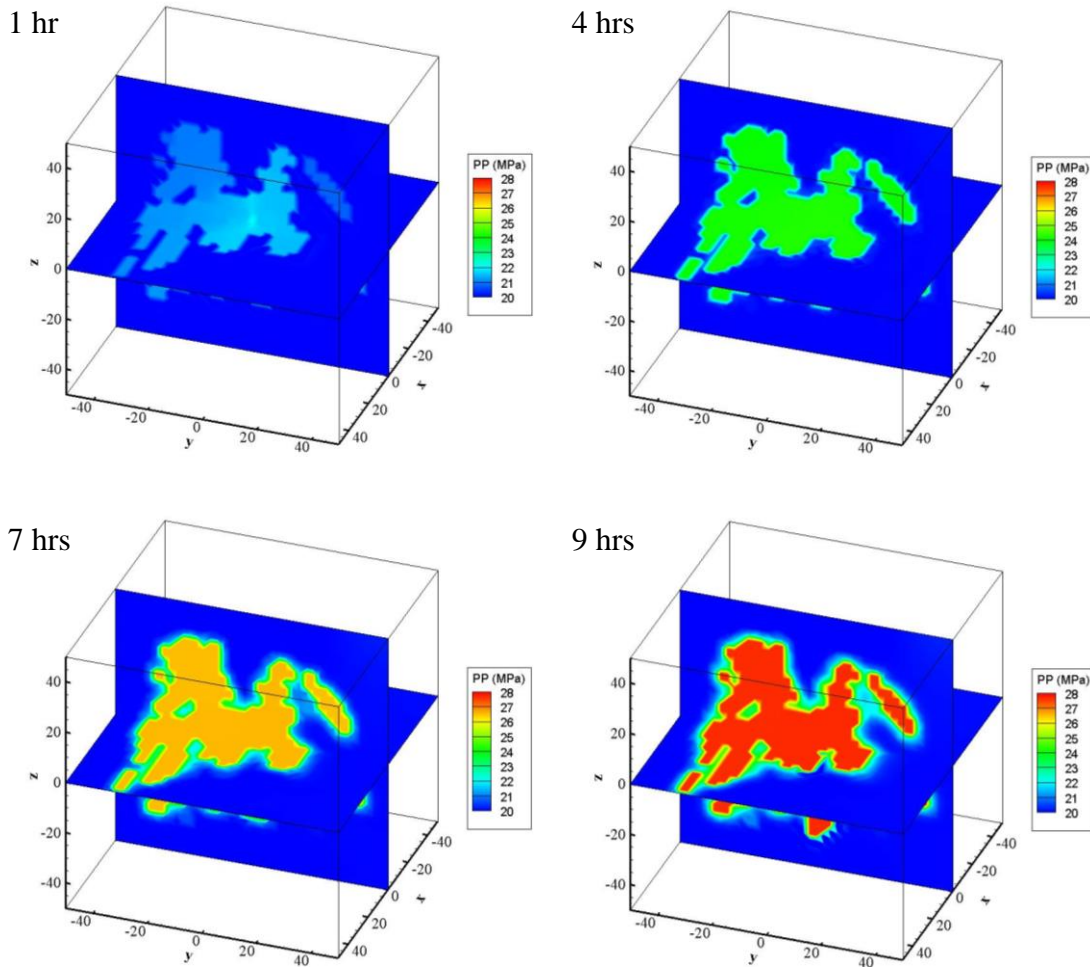


Figure 6.3. Pore pressure development within the reservoir at different injection time (central slice  $x=0$  and central slice  $z=0$  are shown).

The pore pressure evolutions on individual fractures are shown in Figure 6.4. Significant pore pressure increase is observed on the interconnected fractures, while there is less pore pressure increase on isolated fractures. The connectivity of the fracture network plays an essential role in fluid flow and pore pressure development.

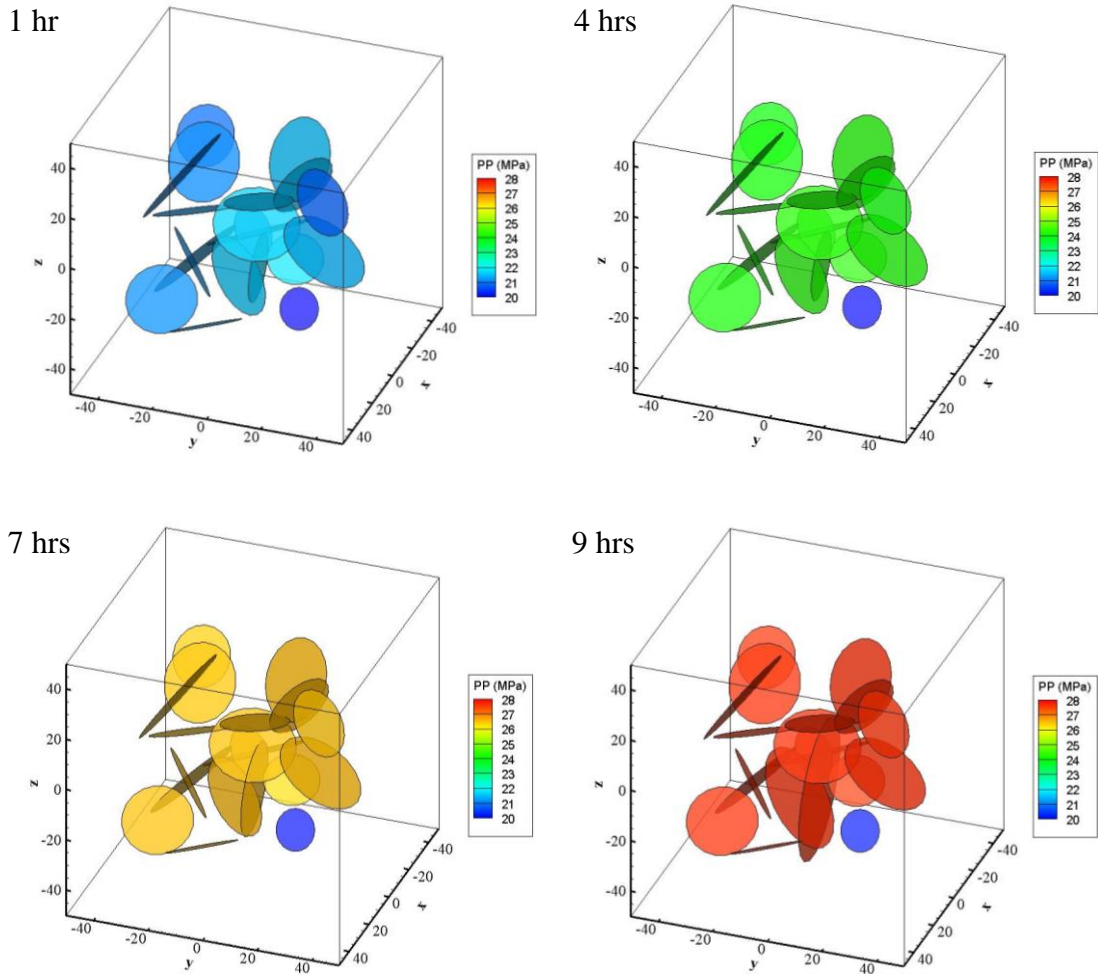


Figure 6.4. Pore pressure development within the fracture network at different injection time.

The local 2D pore pressure distribution on individual fracture planes are also recorded. Figure 6.5 shows an example of pressure development on a fracture plane after 1 hour and 6 hours of injection, respectively. This fracture is located in the center of this domain, with a center point at (0, 0, 0.5). Initially it has 3 intersections with the neighboring fractures. After 1 hour of injection, the pressure on this fracture surface is in the range of 21.0 MPa to 21.1 MPa, and its distribution is controlled by the relative strengths of the intersection line sources. After 6 hours of injection, this fracture has a new intersection with other fractures as a result of fracture propagation, and the pressure



within this fracture is further increased to 25.44 MPa. It should be noted that this fracture has reached a steady state, resulting a nearly uniform local pressure distribution, as shown in the right figure in Figure 6.5.

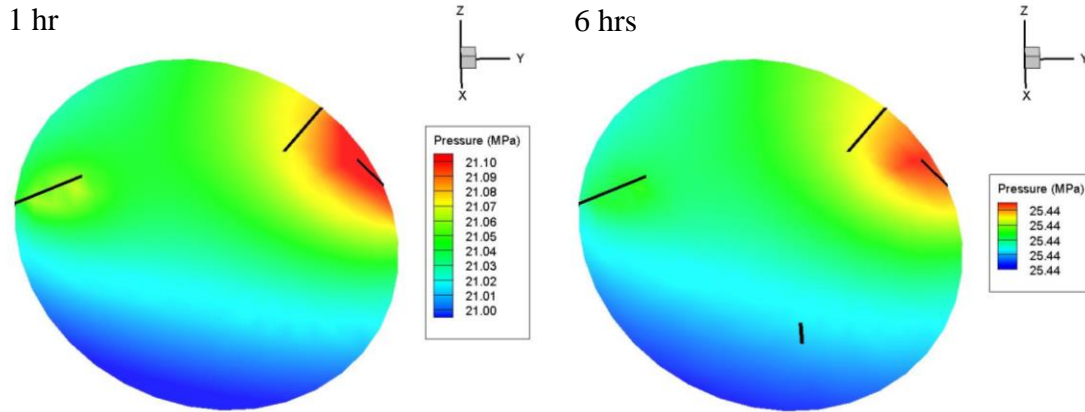


Figure 6.5. Example of 2D pore pressure development on a fracture plane at different injection time. The center point of this fracture is located at (0, 0, 0.5).

Figure 6.6 shows the evolution of temperature distribution within the fracture network. The results show that heat transfer is confined within the interconnected fracture network. Cooling occurs on early on the fractures that have direct connections with the injection well interval. As injection continues, the temperature front diffuses further into the fracture network and causes cooling on a few more fractures. After 9 hours of cold water injection, the average temperature of all fractures is reduced to 104 °C. No temperature change is observed on the isolated fractures, which again suggests that the heat transfer within the fractured rock is dominated by the convective heat transfer via fracture flow.

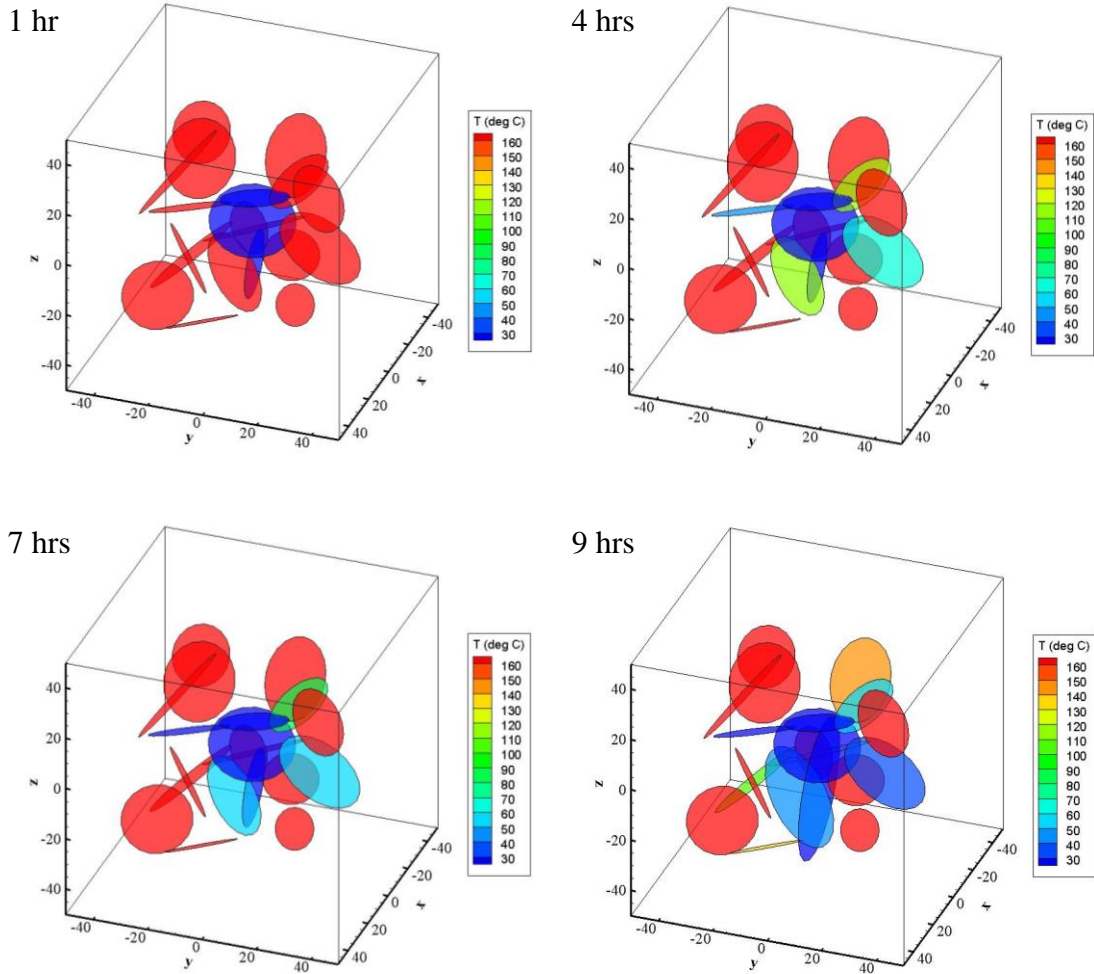


Figure 6.6. Temperature development within the fracture network at different injection time.

In this simulation, both shear slippages and opening events are observed on fractures. Figure 6.7 shows the slipped and opened fractures at different injection time. After 1 hour of injection, the pressure and stress changes are not sufficient to cause the fractures to slip in shear or mechanically open. After injecting for 4 hours, 5 fractures slip and 1 fracture opens. As injection continues, more slippage events occur. In the end of the 9 hours of injection, 12 fractures slip and 2 fracture open.

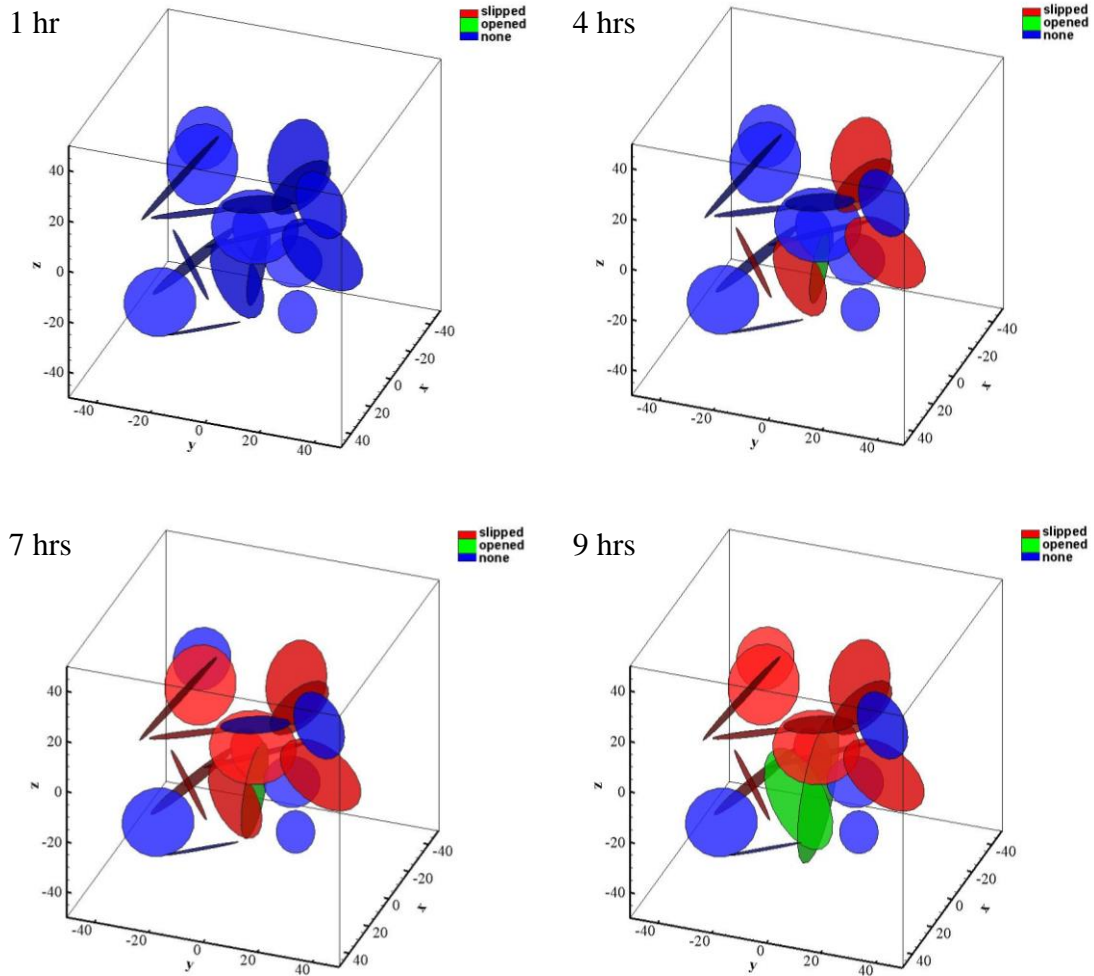


Figure 6.7. Fracture status at different injection time. Slipped fractures are shown in red, and opened fractures are shown in green. The fractures shown in blue do not have status change.

During injection, fracture deformation could lead to an increase in fracture aperture and consequently enhances the permeability. The evolution of fracture permeability is shown in Figure 6.8. Significant permeability enhancement can be seen on most of the fractures. After 9 hours of injection, the maximum fracture permeability enhancement is approximately three-fold.

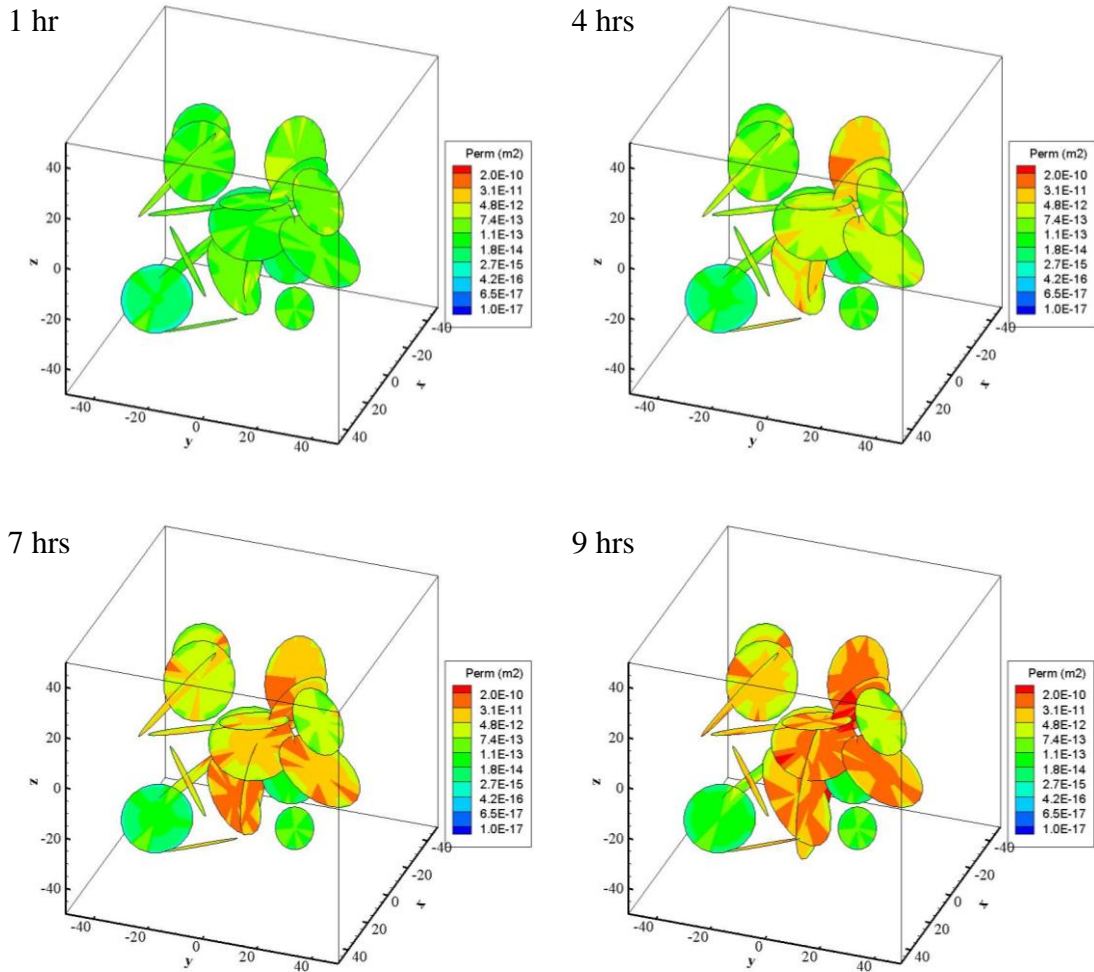


Figure 6.8. Permeability development within the fracture network at different injection time.

Figure 6.9 shows the permeability improvement in terms of equivalent permeability of finite elements at different injection time. It can be seen that the presence of natural fractures provides a good source of permeability in the fractured medium with low permeable rock matrix. After injection, the overall equivalent permeability of the fractured medium is improved.

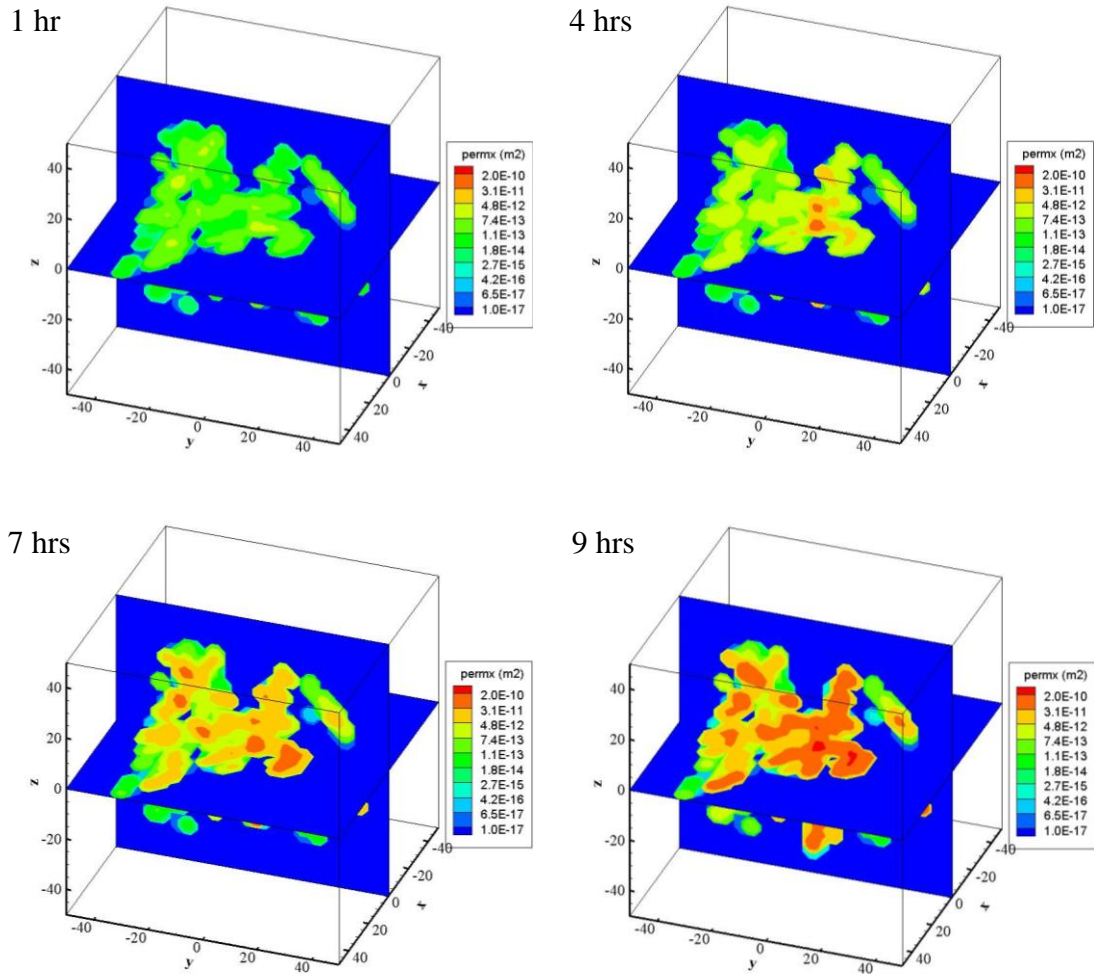


Figure 6.9. Equivalent permeability development within the reservoir at different injection time (central slice  $x=0$  and central slice  $z=0$  are shown).

Shear slippage induced microseismic events are also recorded during the simulation. As shown in Figure 6.10, a few microseismic events occurred near the injection interval at the early stage of injection. As injection continues, more fractures slipped in shear and generated widely distributed microseismic events. After 9 hours of injection, a total of 12 microseismic events were generated. The stimulated zone indicated by microseismicity cloud has a similar shape as the pore pressure elevated zone.

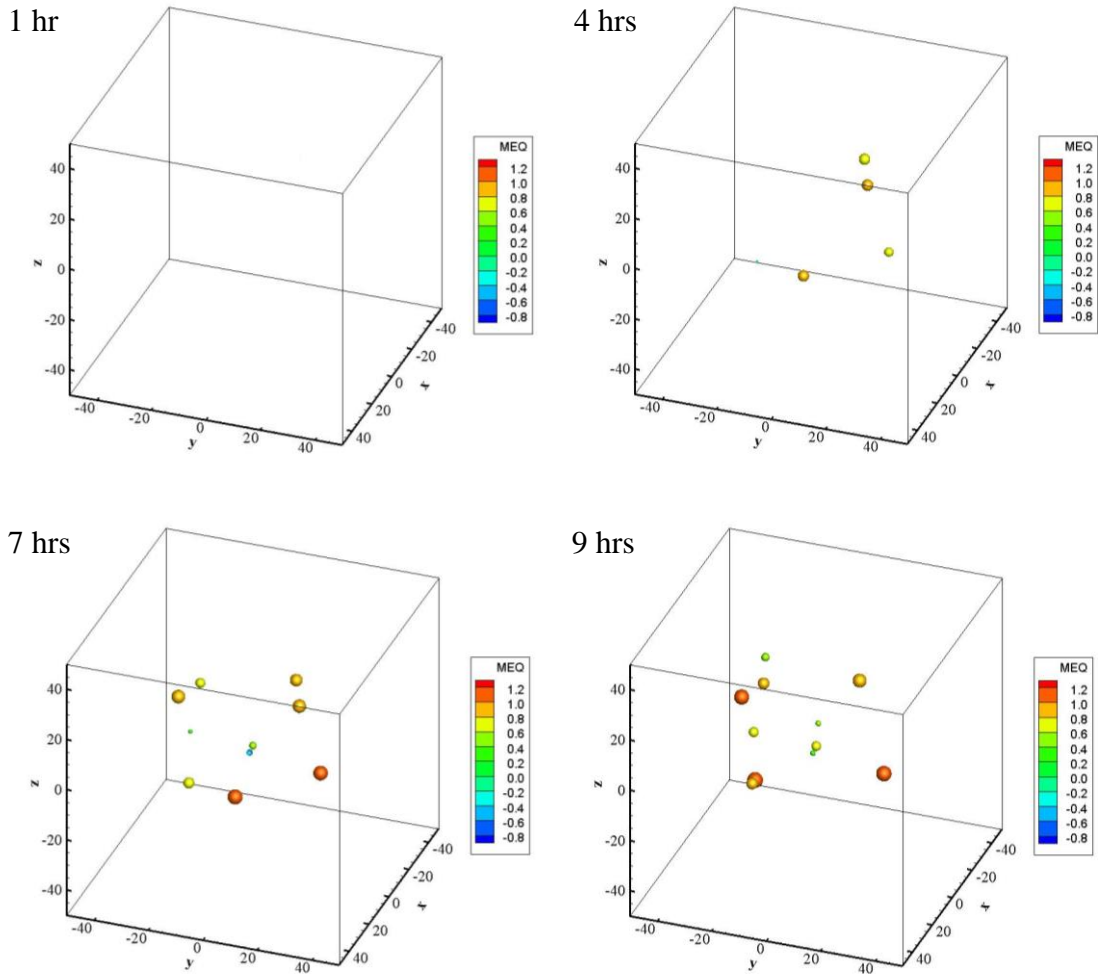


Figure 6.10. Injection induced microseismicity within the reservoir at different injection time.

It can also be seen from Figure 6.10 that the magnitudes of microseismic events are not strongly related to the distance from the slipped fracture to the injection source. It is reasonable since seismic moments depend on both slip displacement and fracture geometry (Eqn. (4.61)), which are influenced by a number of parameters, such as the pore pressure and stress alterations, fracture orientation and fracture size. This simulation was also performed using different time step controls and the same results are produced.

### 6.1.3 Discussion

In this study, three types of the geomechanical response of fractures are considered: fracture opening, shear slippage, and fracture propagation. To examine the contribution of each mechanism to the stimulation outcome, we plot the average fracture aperture profile (Figure 6.11) and the average equivalent permeability profile (Figure 6.12) against the history of these events.

It can be seen from Figure 6.11 that the average aperture of all fractures is increased from 0.16 mm to 0.66 mm after injection, with an increase of 4 times. When injection begins, the temperature of the 3 fractures that intersecting the injection wellbore was immediately set to be 20 °C, which is the same as the injection fluid temperature. This cooling effect induces significant tensile stress, causes these fractures to open and significantly increases their apertures. As injection continues, shear slippages occur on some fractures and induce dilation in apertures. When propagation criteria are met, fractures propagate. After propagation, the connectivity of the entire fracture network could be improved, which contributes to further pressurization in the fracture network and benefits the stimulation outcome. The enhancement in fracture aperture and permeability is a result of the combined contributions from opening, shear slippage, and propagation.

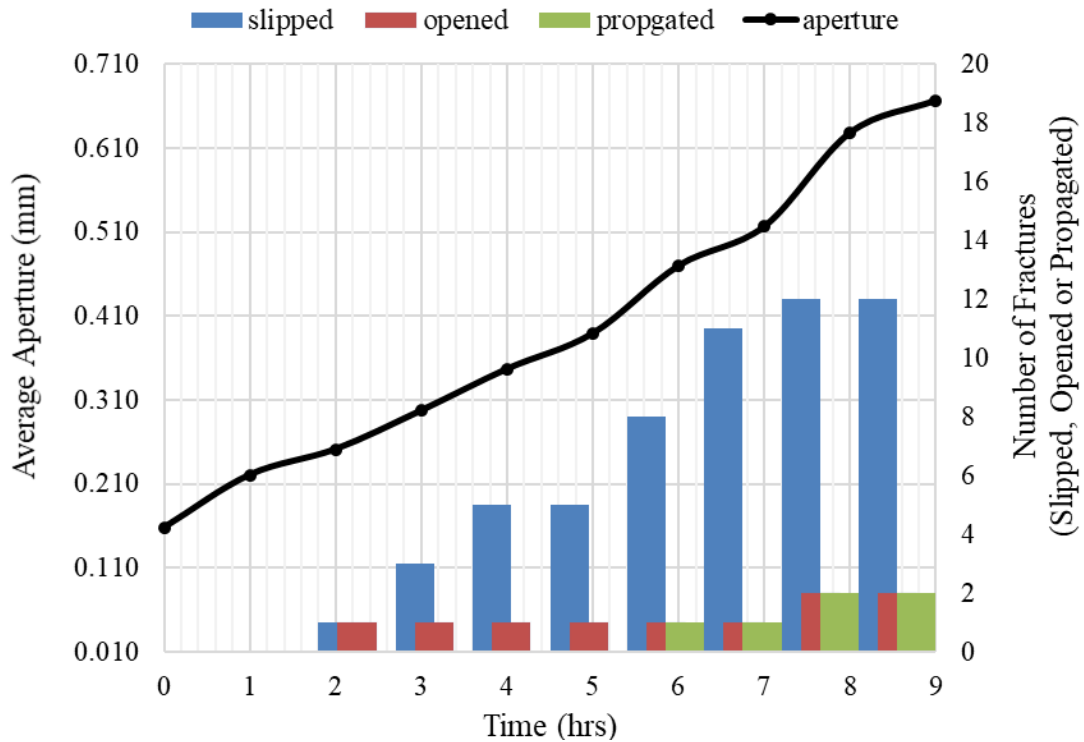


Figure 6.11. Average fracture aperture profile and the corresponding fracture opening, shear slippage and propagation events.

A similar response is found on the average permeability. As shown in Figure 6.12, after 9 hours of injection, due to the combined contributions of fracture opening, shear dilation and propagation, the average permeability is increased from  $4.6\text{E-}16 \text{ m}^2$  to  $2.3\text{E-}14 \text{ m}^2$ , with an enhancement of approximately two folds.



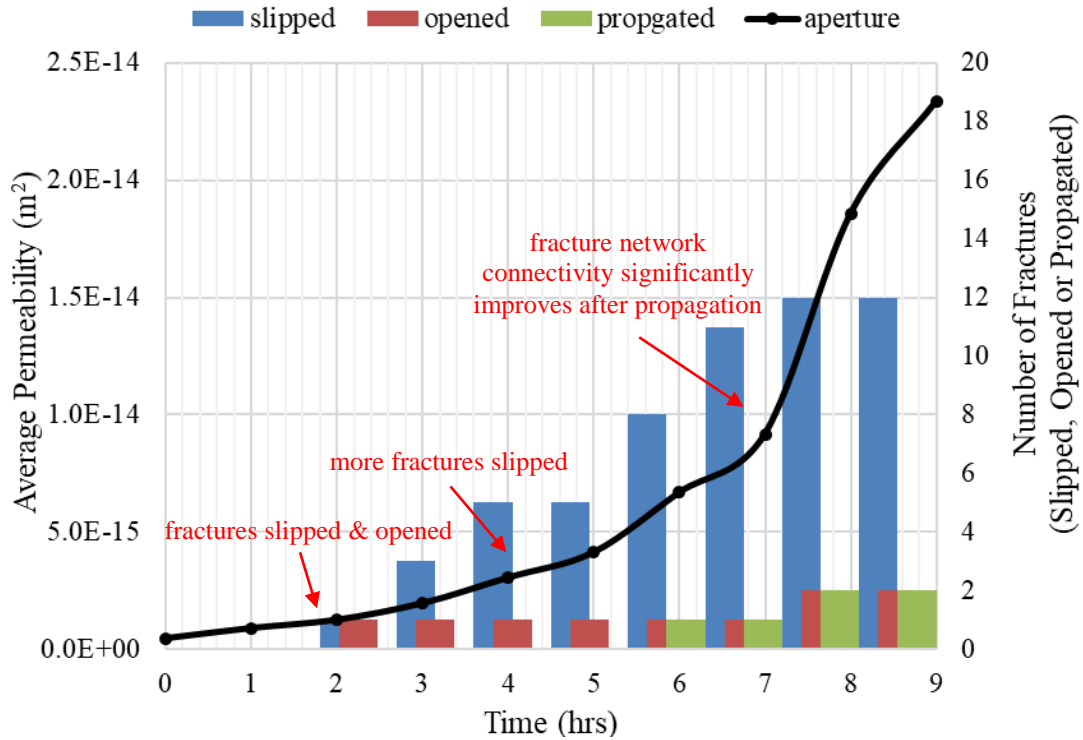


Figure 6.12. Average permeability profile and the corresponding fracture opening, shear slippage and propagation events.

In order to better understand the contributions on permeability enhancement from different mechanisms, we carried out three additional experiments for comparison: (1) isothermal case, without considering thermal effects; (2) shear dilation only case, without considering fracture propagation; and (3) constant friction case, without considering Rate-and-state friction effects. The case present earlier is referred to as the base case. In the comparison cases, all other settings are the same as the base case, and the same input parameters are used. The simulation results in terms of average fracture aperture and average permeability are shown in Figure 6.13 and Figure 6.14, respectively.

Comparing the results in Figure 6.13 and Figure 6.14 clearly demonstrates that the stimulation outcomes are significantly influenced by thermal effects. When the difference between the

injection temperature and the reservoir temperature is ignored, the enhancement in fracture aperture and permeability will be greatly underestimated. The inclusion of fracture propagation predicts higher permeability since the propagated fractures could increase the fracture network connectivity, which in turn result contributing higher permeability enhancement. When the rate-and-state friction (RSF) model is included, higher shear displacement (Eqn. (4.48)) and higher dilated fracture aperture (Eqn. (4.49)) are obtained. Consequently, the predicted permeability is higher than the constant friction case.

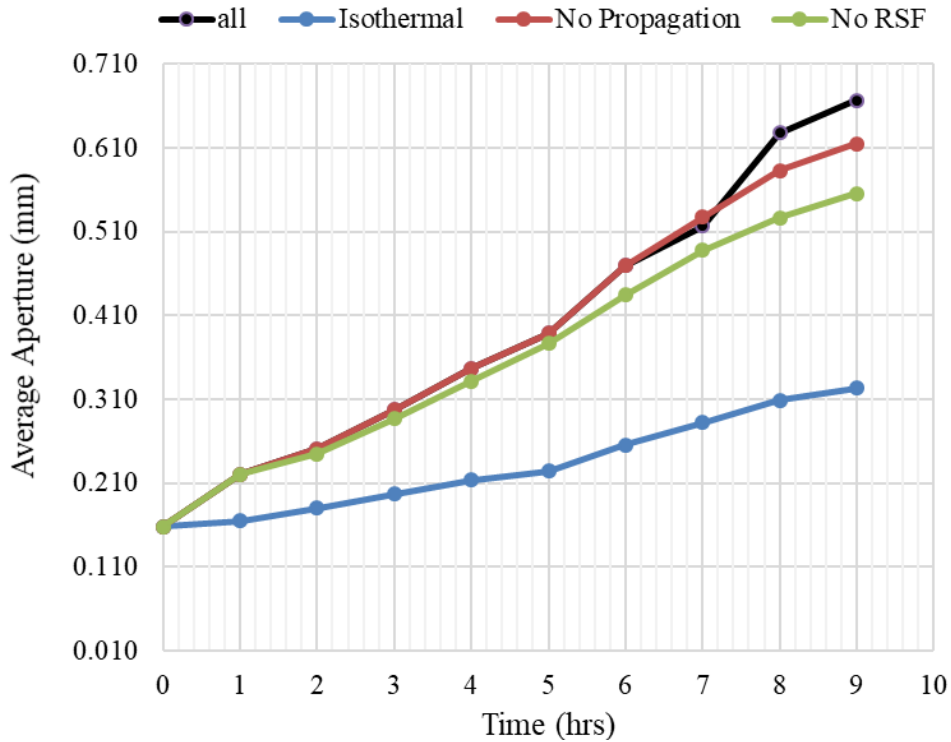


Figure 6.13. Comparison of average fracture aperture profiles predicted from different cases.

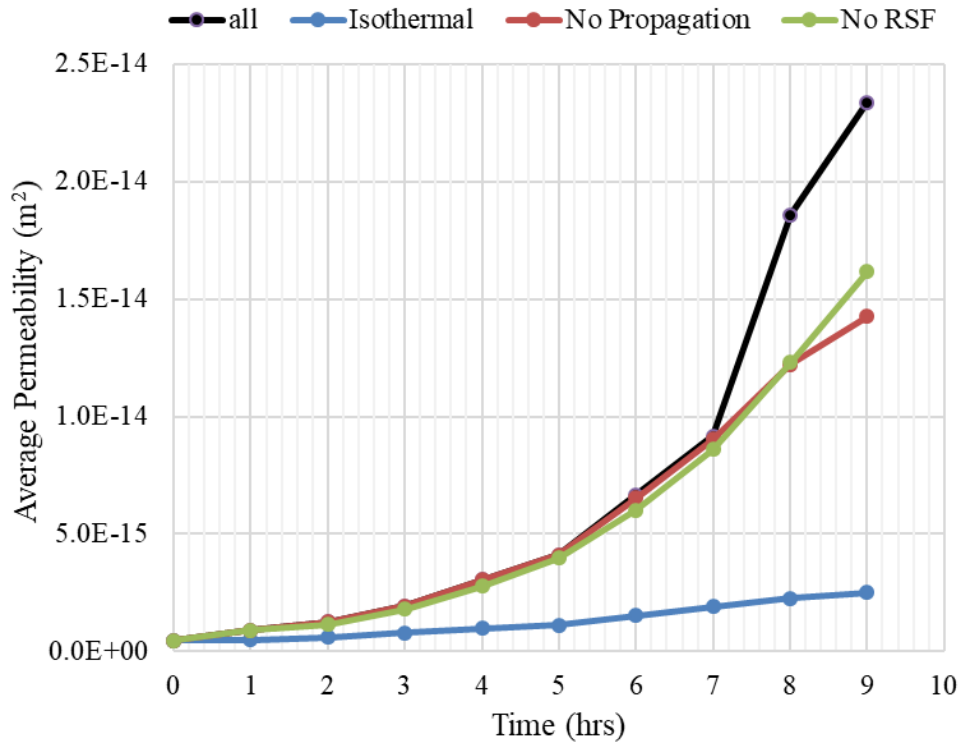


Figure 6.14. Comparison of average permeability profiles predicted from different cases.

The selection of the friction model also influences the induced microseismicity. As shown in Figure 6.15, after 9 hours of injection, a total of 12 microseismic events are predicted by the RSF model, and 82% of these events have a seismic magnitude between 0.6 to 1.1. The results from the constant friction model show 11 microseismic events, and 83% of their magnitudes are in the range from 0.1 to 0.9. This comparison demonstrates that the RSF model would predict more microseismic events as well as higher seismic magnitudes than the constant friction model. In this simulation, a velocity weakening friction law (RSF parameter  $a < b$ ) is assumed. When unstable slip event occurs, the shear strength of a fracture (Eqn. (4.45)) is reduced, which could generate higher excess shear stress and hence larger shear displacement (Eqn. (4.48)), compared to the constant friction model. As a result, the seismic moment (Eqn. (4.61)) and magnitude (Eqn. (4.62)) of a shear slippage induced microseismic event are larger.

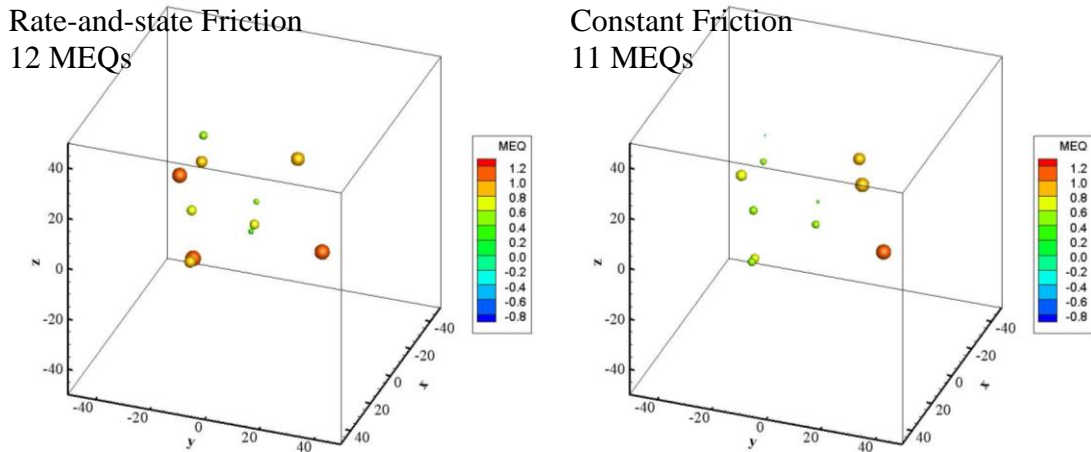


Figure 6.15. Comparison of the injection induced microseismic clouds estimated from RSF model (left) and constant friction model (right), after 9 hours of injection.

#### 6.1.4 Case Summary

This simulation example shows that the presence of a natural fracture network has a significant impact on the stimulation outcome in a fractured reservoir. Fluid flow and heat transfer within the reservoir are mostly controlled by the fracture network. Results also show that fracture could dilate, open, slip and propagate due to injection induced stress variations. During the injection process, increase in fracture aperture is observed, and it has a direct impact on reservoir permeability enhancement. From the simulation results, we have also seen the increases in fracture aperture and permeability result from the combined contributions of fracture opening, shear slippage, and propagation.

Thermal effects play an important role in the stimulation process, especially when the opening of fractures due to cooling is considered. Ignoring the temperature difference between the injection fluid and the reservoir will cause a dramatic error in estimating the permeability development in fractured reservoirs.

The friction model should also be selected appropriately for evaluating injection induced shear slippage and the associated microseismicity, as it describes the fundamental frictional characteristics of a fracture.

Fractures may propagate under certain injection conditions. The propagation of fractures also has a contribution to the stimulation outcomes, by improving the connectivity of the fracture network.

The inclusion of a fracture propagation model along with the shear slippage model provides a better approach for analyzing the permeability enhancement mechanism in fractured reservoirs.

The proposed model is shown to be capable of analyzing the dynamic response of a complex naturally fractured reservoir subject to injection, and it provides a powerful numerical tool for evaluating reservoir performance and stimulation outcome.

## **6.2 Sensitivity Analysis**

In this study, we are interested in the key parameters controlling the response of naturally fractured reservoirs to fluid injection. After carrying out the small scale fracture network simulation, we conducted a sensitivity analysis on a fractured reservoir with a large scale fracture network, to investigate the effects of different parameters (e.g., number of fractures, fracture size and orientation, stress orientation, stress regime, differential stress, fluid viscosity, injection scheme) on the overall permeability enhancement and injection induced microseismicity results.

### **6.2.1 Model Setup**

The same reservoir domain as in Section 6.1 is used, which is a block of 500 m x 500 m x 300 m. It is uniformly discretized into 75,000 brick elements. A large stochastic natural fracture network of 1000 penny-shaped fractures is generated using the parameters listed in Table 6.3.

Table 6.3 Fracture generation inputs

Number of Fractures	1000
Mean of Fracture Radii (Log EX)	2.3
Standard Deviation of Fracture Radii (Log SD)	0.6
Size-aperture Coefficient	4.0E-5
Fisher von Mises Orientation Parameter	2.8

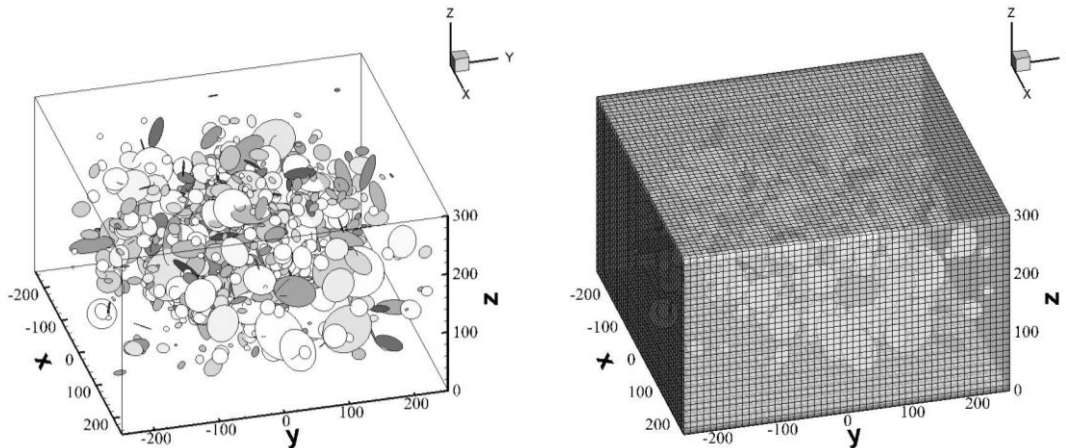


Figure 6.16. Simulation domain contains 1000 stochastic fractures (left); A uniform mesh with 75,000 elements (right).

The fracture network geometry and the domain mesh are illustrated in Figure 6.16. It should be noted that fracture parameters are dependent on geological conditions and are more likely to be different in different stress regimes. However, the same set of fracture network is used in the sensitivity study for the purpose of comparison, except in the cases for evaluating the effects of fracture network properties, such as fracture number, size, and orientation, where different fracture networks are generated.

In this sensitivity study, a constant injection pressure of 25 MPa is applied, and the injection is assumed to be under an isothermal condition, which means the temperature of the injected fluid is

the same as reservoir temperature. Exceptions are in the cases for evaluating the effects of injection rate and injection temperature, in which different values of injection rate are applied, and various temperature differences between injecting fluid and reservoir are considered, respectively. All other properties are the same as the previous simulation in Section 6.1. An injection duration of 72 hours is simulated. The results of this sensitivity study are presented as below.

### 6.2.2 Effect of Fracture Density

Fracture network plays an important role in governing the response of a fractured reservoir to injection. To start with, we performed sensitivity studies on various fracture network properties, including statistical parameters controlling stochastic fracture distribution (fracture density, size, and orientation) and a mechanical parameter controlling the shear dilation response (fracture dilation angle).

To study the effect of fracture density on reservoir permeability enhancement and induced seismicity during the injection process, three sets of fracture networks are generated with a different total number of fractures, nfrac: 500, 750 and 1000.

The corresponding evolutions of the average permeability of the entire reservoir block (Eqn. (4.16)) during the 72 hours of injection are plotted in Figure 6.17. It is evident that the permeability enhancement increases with the increased number of fractures. In the three cases studied with a total of 500, 750 and 1000 fractures, the permeability is increased by 1.6, 2.3 and 3.3 times, respectively. We also notice that the initial permeability also increases with the increased fracture number. It is increased from  $1.55\text{E-}16 \text{ m}^2$  to  $3.13\text{E-}16 \text{ m}^2$  when the number of fractures varied from 500 to 1000. It is because the average reservoir directional permeability is calculated from the sum of elemental permeability (Eqn. (4.15)). The increased number of fractures contributes to achieving more elemental permeability in each direction, and hence in the overall reservoir block.

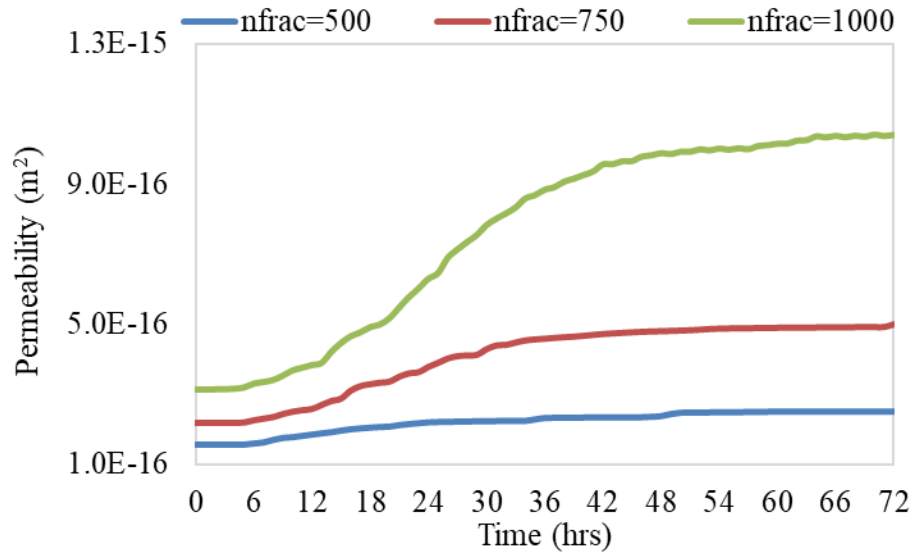


Figure 6.17. Comparison of permeability enhancement during 72 hrs of injection for the cases of different fracture number.

Figure 6.18 shows the comparisons of induced microseismicity at the end of the 72 hours of injection and the corresponding pore pressure distribution within the fracture networks containing a different number of fractures. We could see from the figure that the injection induced microseismicity (left panels in Figure 6.18) is also sensitive to the number of fractures within the simulated reservoir domain. The number of microseismic events increases as increasing the total number of fractures. There are two main reasons for this response. First, as the total number of fractures increases, the number of fractures that are favorably oriented for slip is increased. Second, the increase in fracture number not only improves the initial reservoir permeability, but also contributes to the improvement of fracture network connectivity, which in turn results in a broader diffusion of fluid flow and elevated pore pressure (see right panels in Figure 6.18), and cause more fractures to slip and dilate. Therefore, the case with a larger fracture number has seen more microseismic events and a much more significant permeability enhancement.



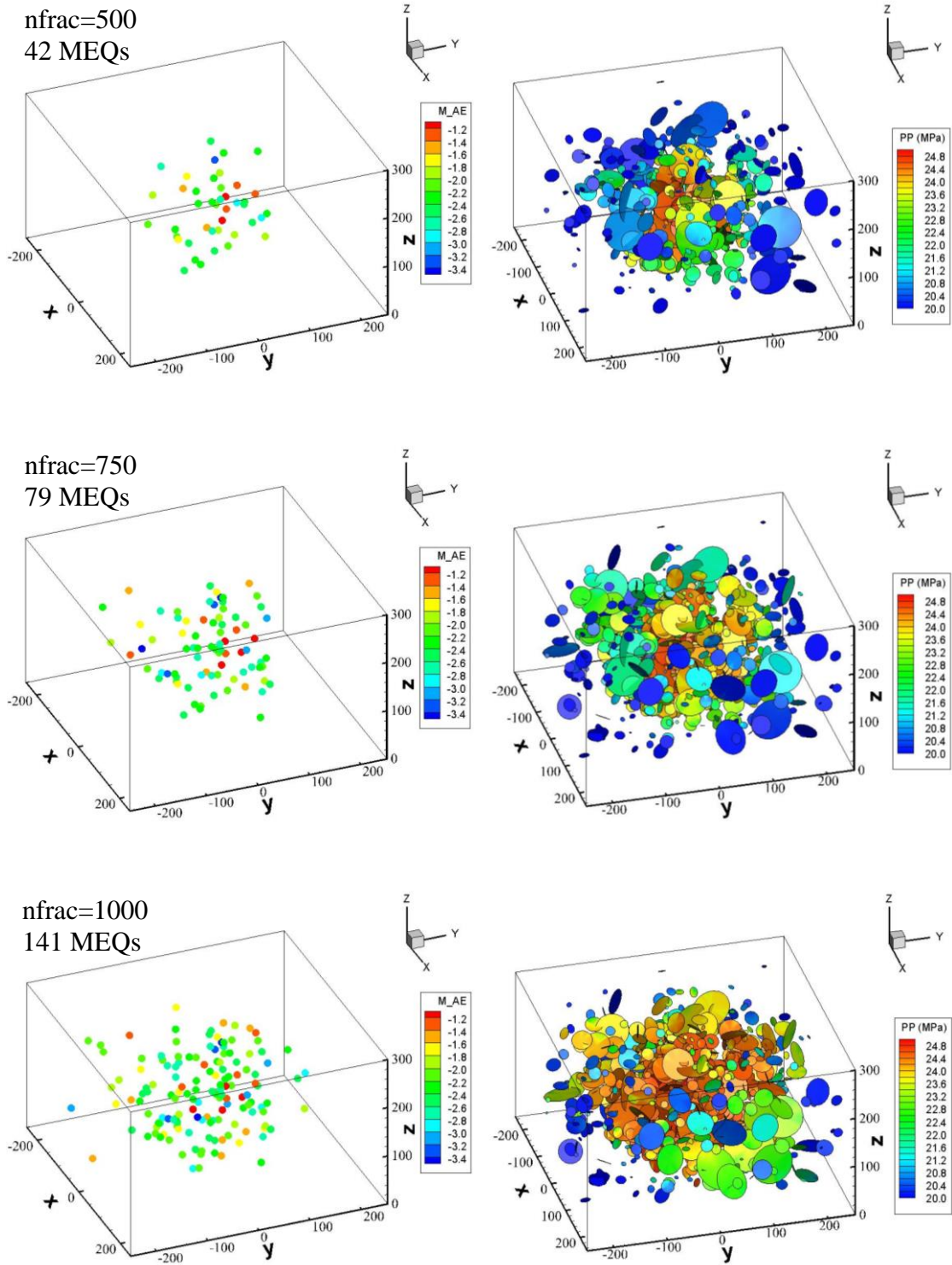


Figure 6.18. Comparison of microseismic events and pore pressure distribution in fracture network after 72 hrs of injection for the cases of different fracture number.

### 6.2.3 Effect of the Initial Fracture Size

To investigate the effect of fracture size on overall permeability enhancement, three different values of the mean ( $\mu$ ) of log values of fracture radii are specified in stochastic fracture network generation: 2.1, 2.3 and 2.5, which corresponds to a mean fracture radius of 8 m, 10 m and 12 m, respectively. The other input variable in the log-normal distribution of fracture size, the standard deviation ( $\sigma$ ) of  $\ln r$ , is set to a constant value of 0.6 in this series of studies.

Results are presented in Figure 6.19, which shows that when the mean fracture radius varies from 8 m to 12 m, the average reservoir permeability at the end of the injection increases from  $4.4\text{E-}16$   $\text{m}^2$  to  $2.2\text{E-}15$   $\text{m}^2$  revealing that larger fractures contribute more permeability enhancement during injection. It is evident from Eqn. (4.48) that larger fracture radius reduces shear stiffness and increases shear displacement. According to Eqn. (4.49), a higher stimulated aperture would be induced by shear dilation. Therefore, as a result, the enhancement of the overall reservoir permeability is improved. In addition, we also notice that the increase in fracture size also results in a higher initial reservoir permeability, which is similar to the effect of increasing fracture number. When the radii of fractures embedded in the fractured medium are enlarged, there will be more elements intersected by the fractures, which means higher elemental permeability, and hence higher average permeability of the fractured block.

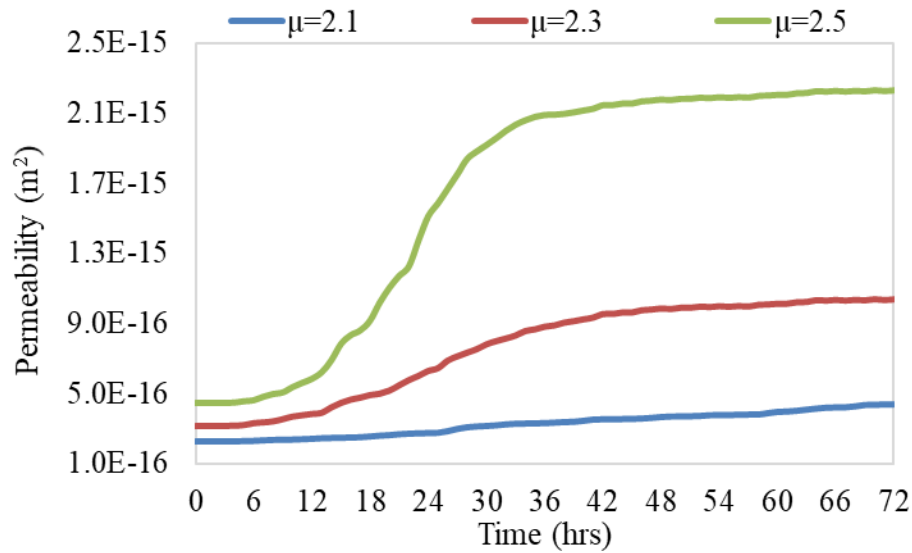


Figure 6.19. Comparison of permeability enhancement during 72 hrs of injection for the cases of different fracture size.

Similar to the effect of increasing fracture number, as the fracture size increases, the fracture network connectivity is improved, and consequently, the fluid flow diffusion and pressure increase within the reservoir domain are promoted. In Case 1, when the mean fracture radius is small, the flow has not yet diffused to the regions far from the injection well after 72 hours of injection. In contrary, a broader spatial distribution of fluid flow diffusion and pore pressure increase are observed in Case 3, in which the largest fracture size is assumed. Therefore, the fractures in Case 3 are exposed more pressure increase, have a larger tendency to slip and induce more microseismic events, consequently more permeability enhancement.

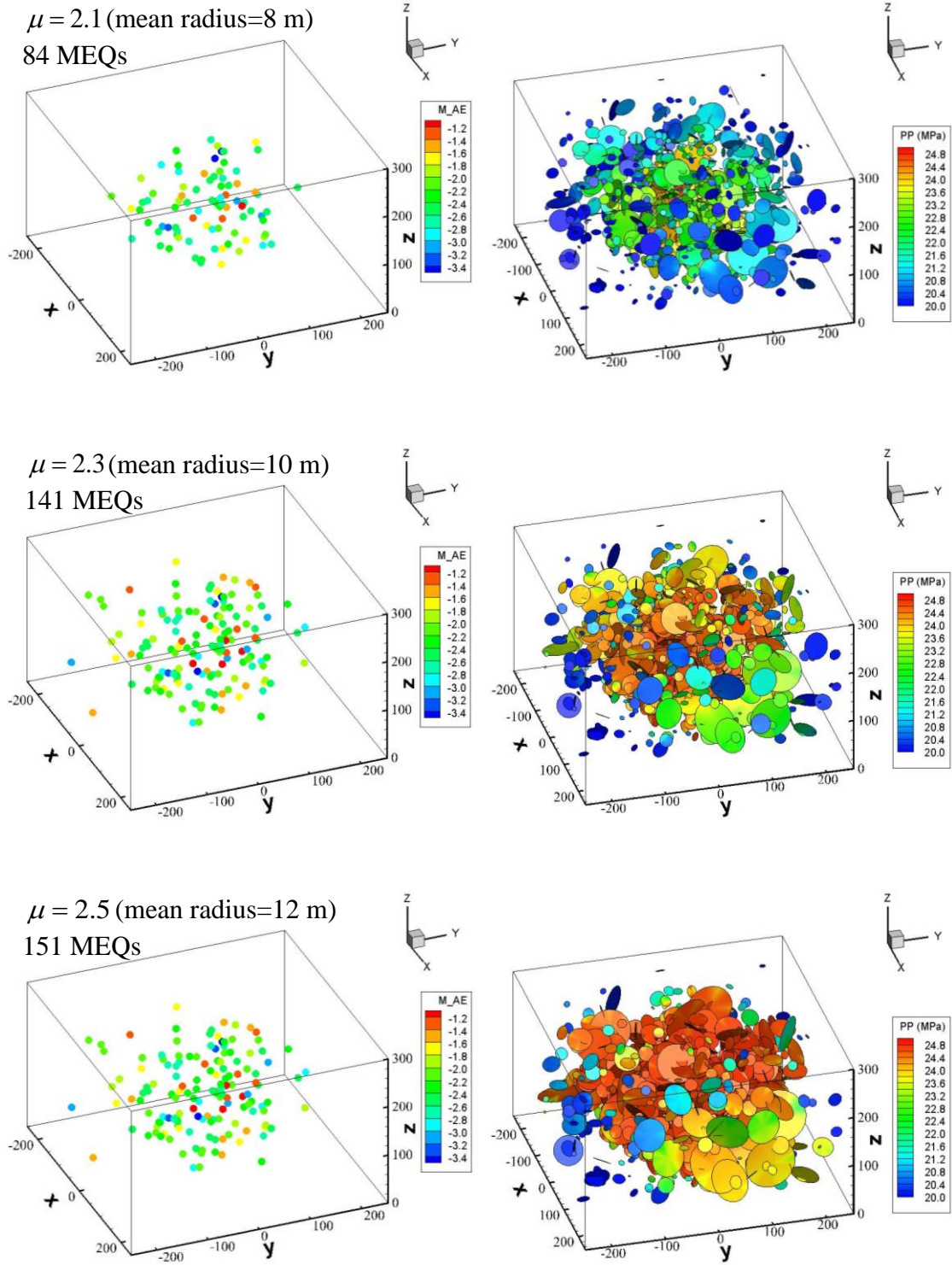


Figure 6.20. Comparison of microseismic events after 72 hrs of injection for the cases of different mean fracture radius value.

#### 6.2.4 Effect of Fracture Orientation

Fracture orientation has a direct impact on determining the stresses acting on a fracture and hence the potential of fracture shear slippage. In order to investigate the effect of fracture orientation on the injection response of fractured reservoirs, we generated three stochastic fracture networks with a different distribution of fracture orientations using different Fisher coefficient value: (1)  $\kappa=1.8$ ; (2)  $\kappa=2.8$ ; and (3)  $\kappa=5.0$ . As mentioned earlier in Chapter 4.2, the Fisher coefficient measures the dispersion in fracture orientations. In Case 3, the higher Fisher coefficient generates fractures having a higher concentration around the mean direction.

Figure 6.21 and Figure 6.22 shows the comparison of permeability enhancement and induced microseismic clouds in the three cases, respectively.

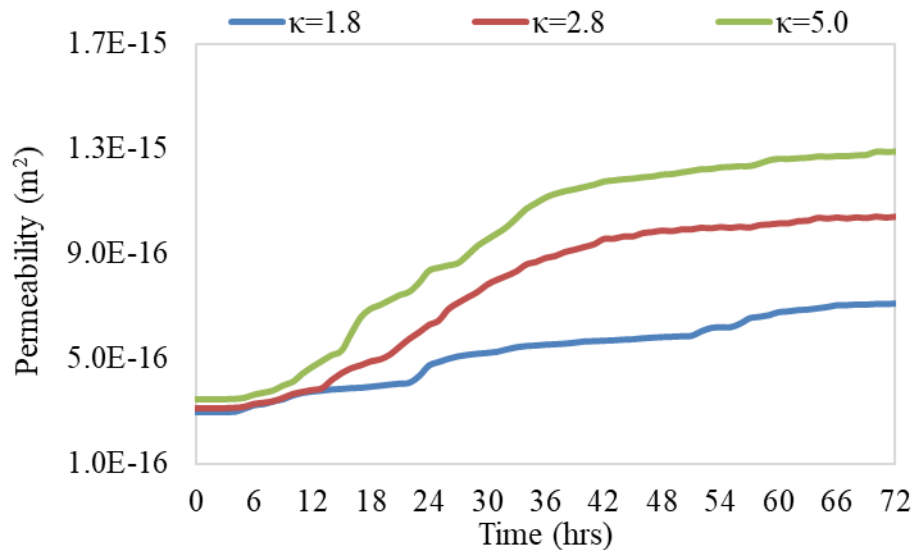


Figure 6.21. Comparison of permeability enhancement during 72 hrs of injection for the cases of different fracture orientation distribution.

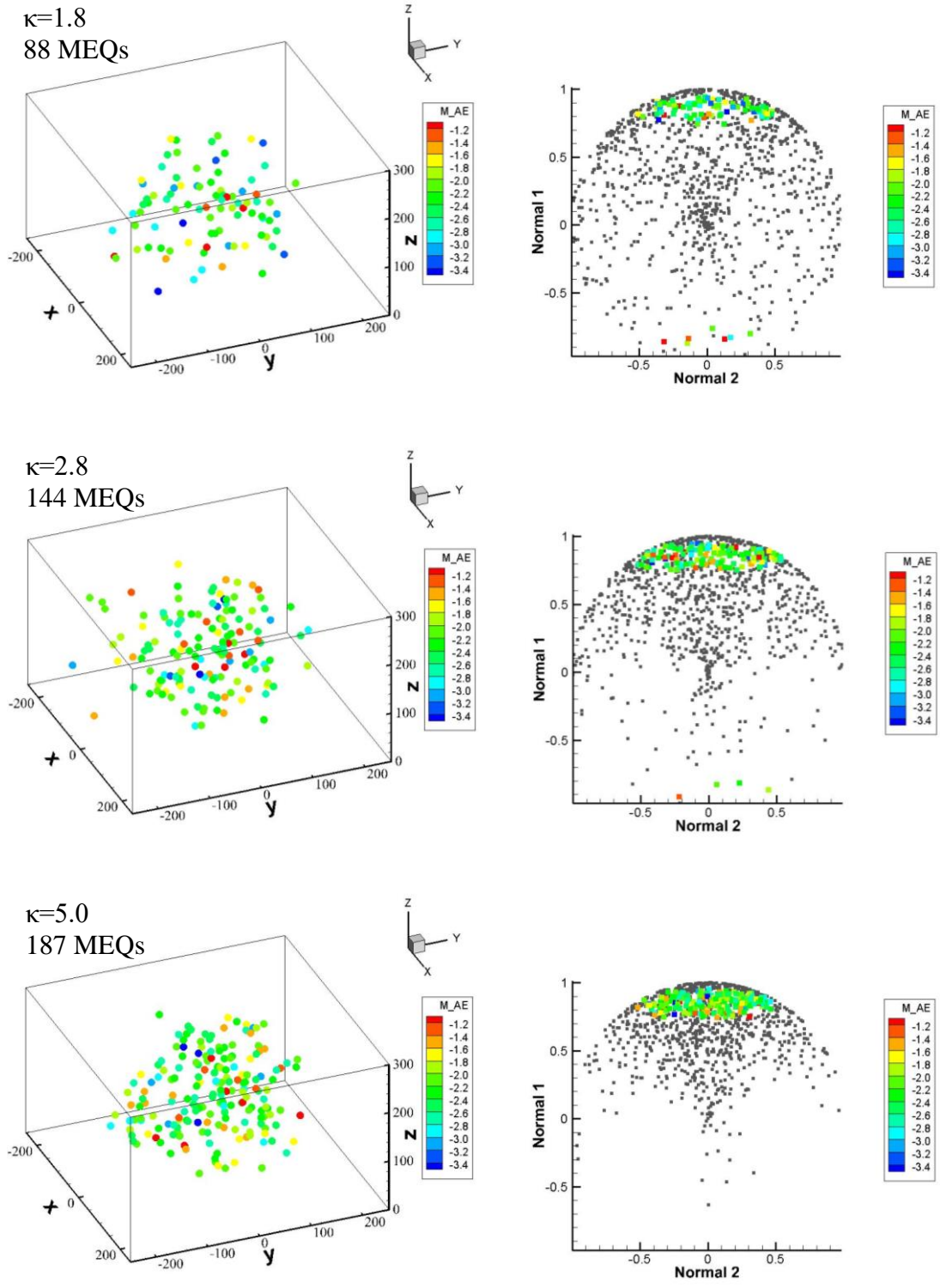


Figure 6.22. Comparison of microseismic events after 72 hrs of injection for the cases of different fracture orientation distribution parameter.

The role of fracture orientations is evident. For the settings in this series of study, both the enhancement in reservoir permeability and the number of seismic events increase with increasing Fisher coefficient, which means the fracture network with a highly concentrated orientation distribution is favorable for shear stimulation. It is because in this study the mean orientation of the stochastic fractures is assumed to coincide with the direction of the maximum principal stress, which is a favorable orientation for shear slippage as a result of a relatively small pore pressure perturbation. Case 3 has more fractures aligned in this direction (right panels in Figure 6.22), and hence is more likely to have the greatest number of slipped events and result in a higher stimulated permeability.

#### 6.2.5 Effect of Fracture Dilation Angle

Besides the distribution characteristics of natural fractures, the mechanical properties of fractures such as dilation angle also have an influence on the injection induced shear slippages and the associated permeability enhancement. For studying the effect of fracture shear dilation angle on the response of the fractured reservoir subject to injection, 3 sets of models were simulated with different dilation angle,  $\phi_{dil}$ : 2°, 3° and 4°. These are the typical values found in hot dry rock stimulation sites, representing smooth, fairly smooth and fairly smooth fracture surfaces, respectively (Willis-Richards et al. 1996).

It can be observed from Figure 6.23 that the permeability enhancements are higher in the models with a higher dilation angle. In the cases studied here, for increasing the shear dilation angle from 2° to 4°, the corresponding average reservoir permeability after 72 hours of injection increases from 1.04E-15 m<sup>2</sup> to 2.82E-15 m<sup>2</sup>.

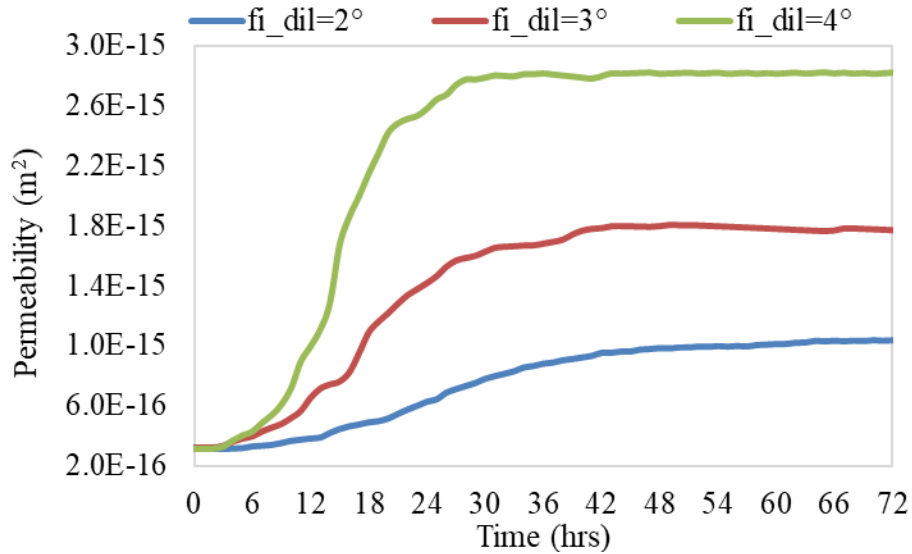


Figure 6.23. Comparison of permeability enhancement during 72 hrs of injection for the cases of different fracture dilation angle.

The results of the induced microseismic events are plotted in Figure 6.24. It can be seen from this figure that both the number of the seismic events and the distribution pattern are similar in these three cases. In the cases studied here, changing the value of fracture dilation angle has little influence on the occurrence of injection induced shear slippage and the associated microseismicity. The difference in the permeability enhancements in Figure 6.23 could be explained as a result of the higher contribution of dilation in fractures with a higher value of dilation angle. It is evident that the increased shear dilation angle directly increases the effective shear dilation angle (Eqn. (4.46)). Although there is a decrease in the shear displacement (Eqn. (4.45) and (4.48)) due to the increased effective shear dilation angle, the resulting overall effect on the dilated aperture due to shear slippage (Eqn. (4.49)) is positive, hence the overall permeability is enhanced.



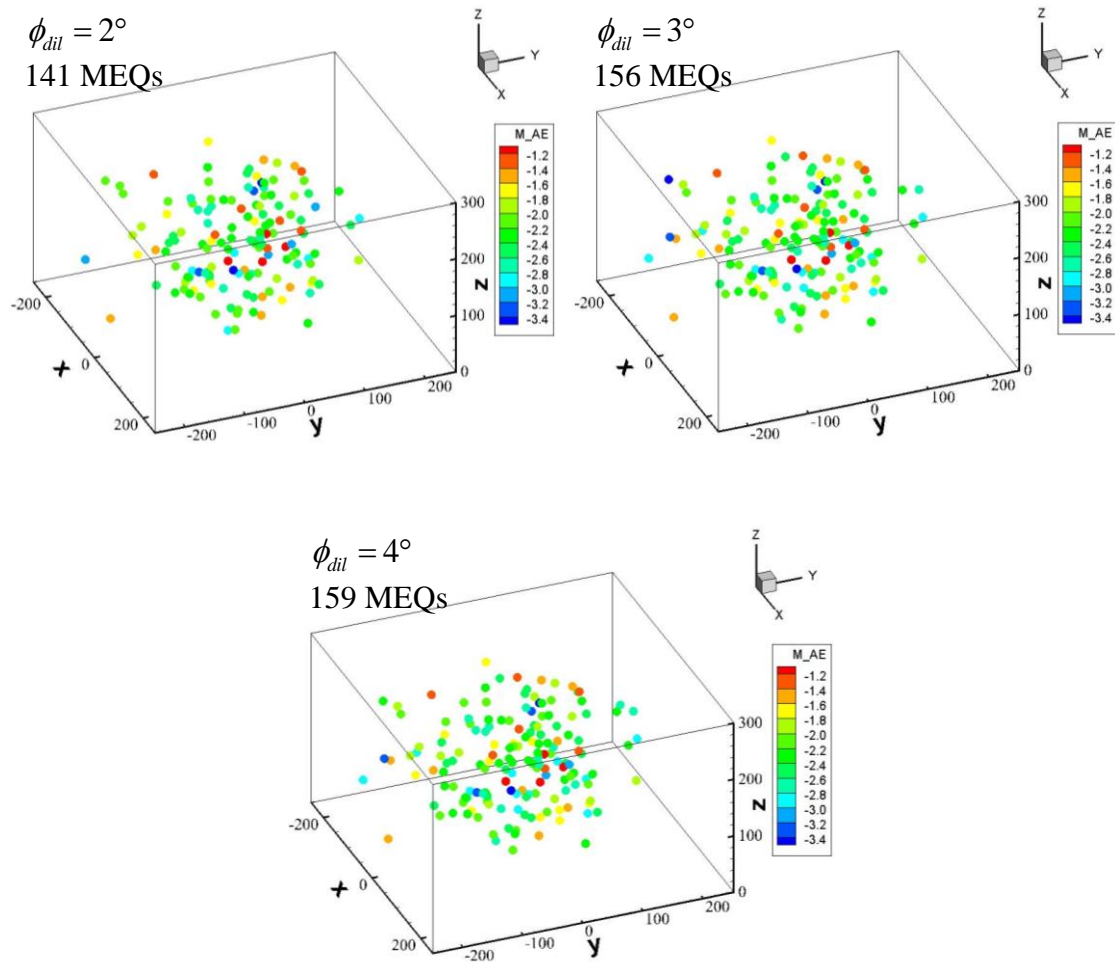


Figure 6.24. Comparison of microseismic events after 72 hrs of injection for the cases of different differential stress.

### 6.2.6 Effect of the Rock Matrix Permeability

To evaluate the effect of matrix permeability, three simulations are conducted using same properties except from the matrix permeability values: 0.005 mD ( $5E-18 \text{ m}^2$ ), 0.05 mD ( $5E-17 \text{ m}^2$ ) and 0.5 mD ( $5E-16 \text{ m}^2$ ).

The equivalent permeability is the sum of the matrix permeability and the fracture permeability. As expected, Figure 6.25 shows that in all three cases, the average reservoir permeability at the initial stage is higher than the matrix permeability. It confirms the presence of natural fractures does contribute to the overall reservoir permeability. The average reservoir permeability in Case 3 is much higher than in the other two cases since it has a higher matrix permeability (0.5 mD). During injection, fractures dilate as a result of pore pressure and stress changes. As shown in Figure 6.26, fracture dilation behavior is sensitive to matrix permeability. Cases 1 with the lowest matrix permeability (0.005 mD) results in the most significant increase in the average fracture aperture. The contribution of the dilated apertures to reservoir permeability enhancement could also be seen in Figure 6.25. After 72 hours of injection, the average reservoir permeability in Case 1, 2 and 3 is increased by 6.0, 3.2 and 1.8 times, respectively.

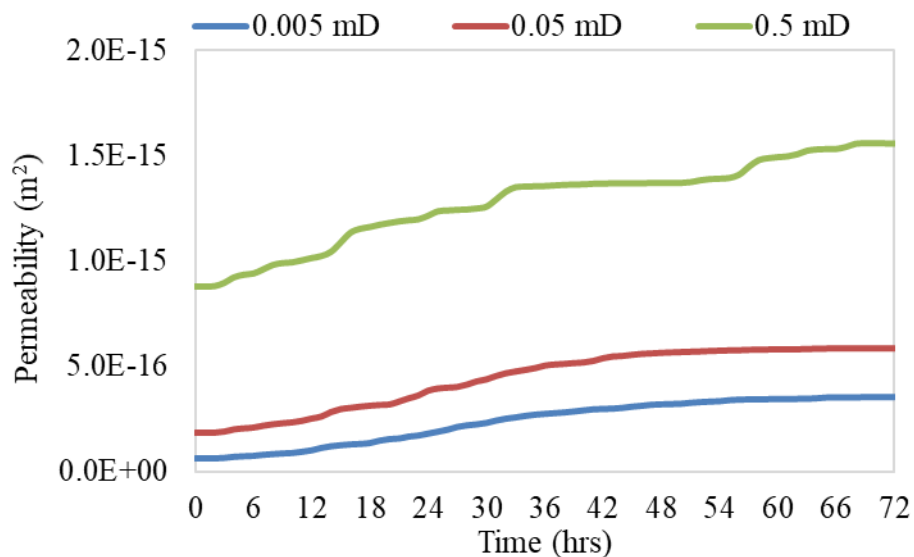


Figure 6.25. Comparison of permeability enhancement during 72 hrs of injection for the cases of different matrix permeability.

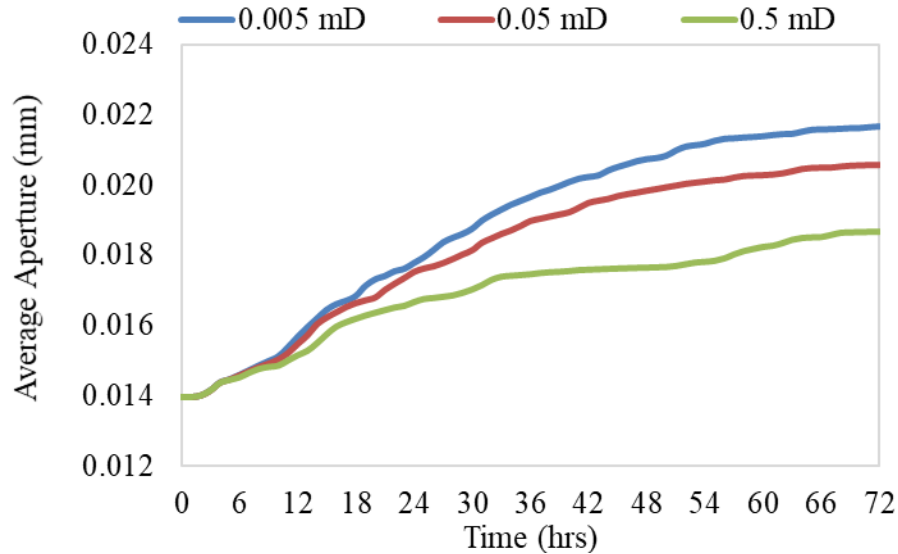


Figure 6.26. Comparison of average fracture aperture increase during 72 hrs of injection for the cases of different matrix permeability.

The resulting microseismic events also depend on the matrix permeability, as shown in Figure 6.27. As matrix permeability decreases, the number of induced microseismic events increases, which is consistent with the observations in fracture aperture and permeability evolution. It is because the low matrix permeability prevents the diffusion of fluid flow into the matrix and provides higher pressure increases in the fractures (Figure 6.27), which consequently results in more aperture increase and more permeability enhancement. Results of these simulations show that fracture slippage and consequently permeability of the fractured rock is significantly affected by the permeability of the rock matrix. Permeability enhancement attributed to the mechanism of fracture shear dilation is more significant in low permeable reservoirs.

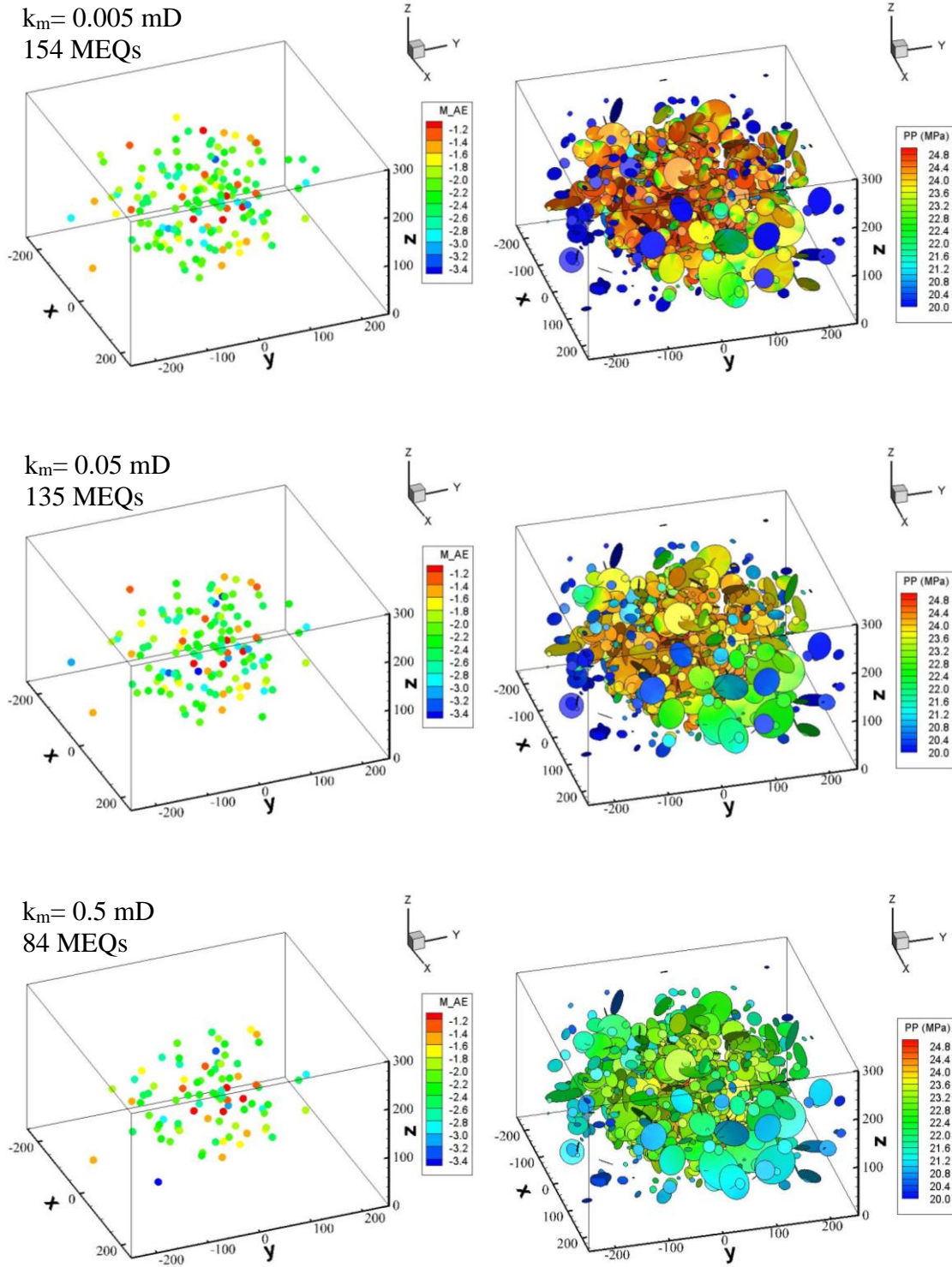


Figure 6.27. Comparison of microseismic events and pore pressure distribution in fracture network after 72 hrs of injection for the cases of different matrix permeability.

### 6.2.6 Effect of the In-situ Stress Orientation

The stresses acting on a fracture depends on its direction relative to the in-situ principal stresses as well as the magnitudes of these principal stresses. Therefore, it is important to investigate the effects of various in-situ stress conditions on the resulting induced microseismicity and permeability evolution during the injection process.

The first parameter investigated is the stress orientation. For the assumed normal faulting regime ( $S_v=50$  MPa,  $S_{Hmax}=40$  MPa and  $S_{Hmin}=35$  MPa), two cases are examined: (1) the orientation of the maximum horizontal stress  $S_{Hmax}$  is in the N-S direction; (2) the orientation of the maximum horizontal stress  $S_{Hmax}$  is in the E-W direction.

Figure 6.28 illustrates the evolution of the average permeability of the entire reservoir block. Comparing the permeability curves in Figure 6.28, it can be seen that the permeability enhancement is significantly higher for the case when  $S_{Hmax}$  is in the N-S direction compared to the case with  $S_{Hmax}$  in the E-W direction. We also notice that there is a discrepancy in the average permeability in these two cases at the beginning of the injection ( $t=0$ ). It is because, for a given fracture, the initial fracture aperture  $a_0$  at zero effective stress is assumed to be proportional to fracture size (Eqn. (4.3)), and is the same in both cases. In this work, stress-dependent permeability model is used. When the same fracture network is subjected into different stress conditions, the initial in-situ aperture of the fractures (Eqn. (4.50)) varies, which resulting different values of initial permeability in the two cases.

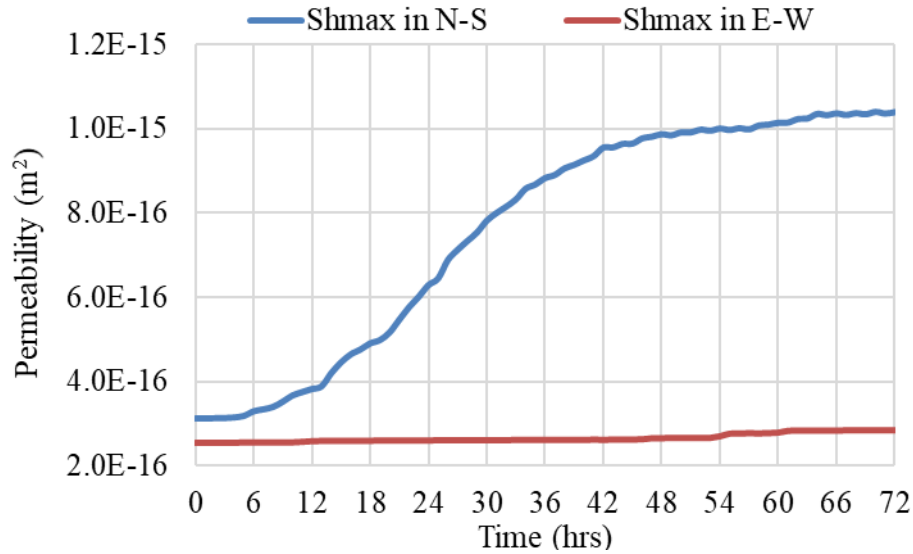


Figure 6.28. Comparison of permeability enhancement during 72 hrs of injection for the cases of different maximum horizontal stress azimuth.

During simulation, the injection induced microseismic events are also recorded. As shown in Figure 6.29, when  $S_{Hmax}$  is in the N-S direction, a total of 141 MEQs occur after 72 hours of injection, while only 4 MEQs are induced when  $S_{Hmax}$  is rotated 90° to the E-W direction. This significant difference in MEQs explains the difference observed in the permeability evolution curves. In Case 1, where  $S_{Hmax}$  is in the N-S direction, more fractures slip in shear as a result of injection induced pressure and stress changes. Therefore, the permeability enhancement caused by shear dilation is much more significant.

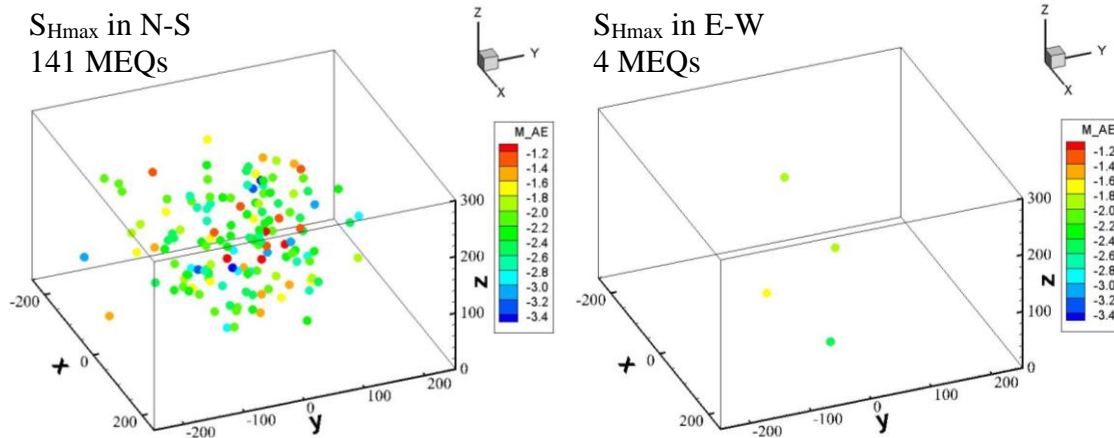


Figure 6.29. Comparison of microseismic events after 72 hrs of injection for the cases of different maximum horizontal stress azimuth.

Figure 6.30 shows the orientations of the slipped fractures after 72 hours of injection in both cases. The grey points represent the normal directions of all fractures in the domain, while colored points represent the slipped fractures and the color contour shows the magnitude of shear slippage induced microseismic events. It can be seen from this figure that in both cases, shear slippage occurs on the fractures whose normal orientations fall into a certain range with respect to the maximum horizontal stress. The fractures oriented close to the maximum horizontal stress direction are favorable to slip, and have greater contributions to the enhancement of permeability. In case 1, as there are more fractures generated align with its maximum horizontal stress direction, it could have more fractures to slip and dilate, inducing more microseismic events and significantly improving the overall permeability. The less number of microseismicity and less permeability enhancement observed in case 2 can be explained by the lack of optimally orientated fractures with respect to the stress orientation in this case.

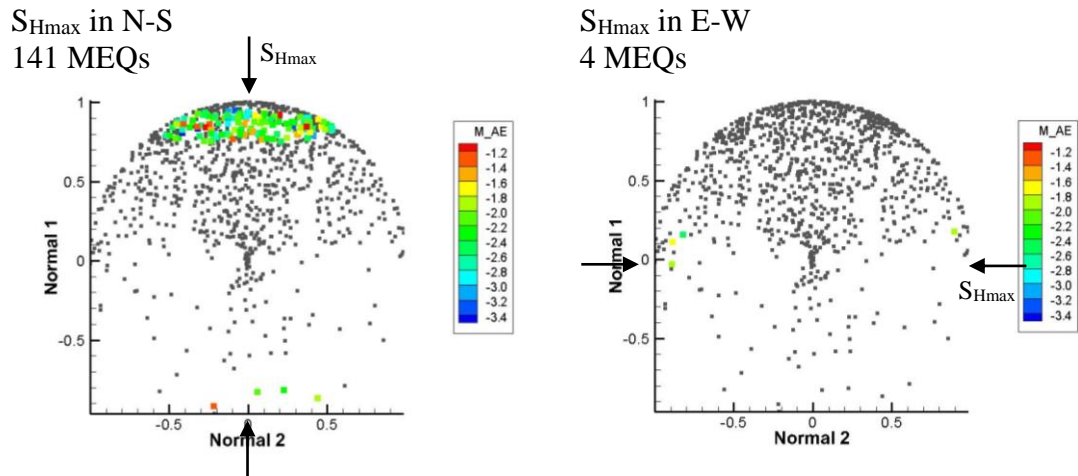


Figure 6.30. Comparison of orientations of slipped fractures after 72 hrs of injection for the cases of different maximum horizontal stress azimuth.

### 6.2.7 Effect of the Stress Regime

The effect of stress regime on injection induced shear slip of fractures and permeability enhancement is also investigated. Three different far-field stress regimes are tested: (1) normal faulting ( $S_v=50$  MPa,  $S_{Hmax}=45$  MPa,  $S_{hmin}=30$  MPa), with vertical stress as the maximum in-situ stress component; (2) strike-slip faulting ( $S_{Hmax}=50$  MPa,  $S_v =45$  MPa,  $S_{hmin}=30$  MPa), with horizontal stresses as the maximum and minimum in-situ stresses; and (3) reverse faulting ( $S_{Hmax}=50$  MPa,  $S_{hmin} =45$  MPa,  $S_v =30$  MPa), with vertical stress as the minimum in-situ stress component. In all three cases, the magnitude of the maximum shear stress is identical, and the maximum and minimum horizontal stresses  $S_{Hmax}$  and  $S_{hmin}$  are set in the N-S direction and in the E-W direction, respectively.

The comparison of permeability enhancements is shown in Figure 6.31. Similar trends are observed in the models under normal faulting and strike-slip faulting regimes, which have more significant improvements in average reservoir permeability compared to the model in reverse



faulting. For most of the fractures present in this series of models, the normal faulting and strike-slip faulting stress conditions tend to generate a lower effective normal stress on them, which reduces their shear strength and increases the possibility of shear slippage. We also note there is a variation in the initial permeability of the reservoir under different stress regimes. This is because the initial aperture of fractures is calculated based on their orientation relative to the in-situ principal stresses. For this given stochastically generated fracture network, several large fractures that are governing the average reservoir permeability tend to have a lower normal stress and a larger initial in-situ aperture under the reverse stress condition. Hence, the average initial permeability is higher in the reverse faulting regime compared to the other two regimes.

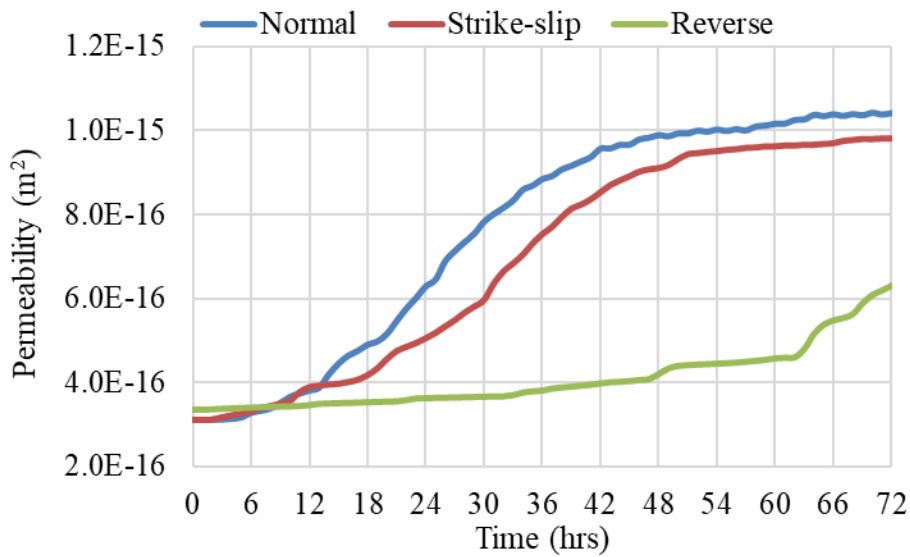


Figure 6.31. Comparison of permeability enhancement during 72 hrs of injection for the cases of different stress regime.

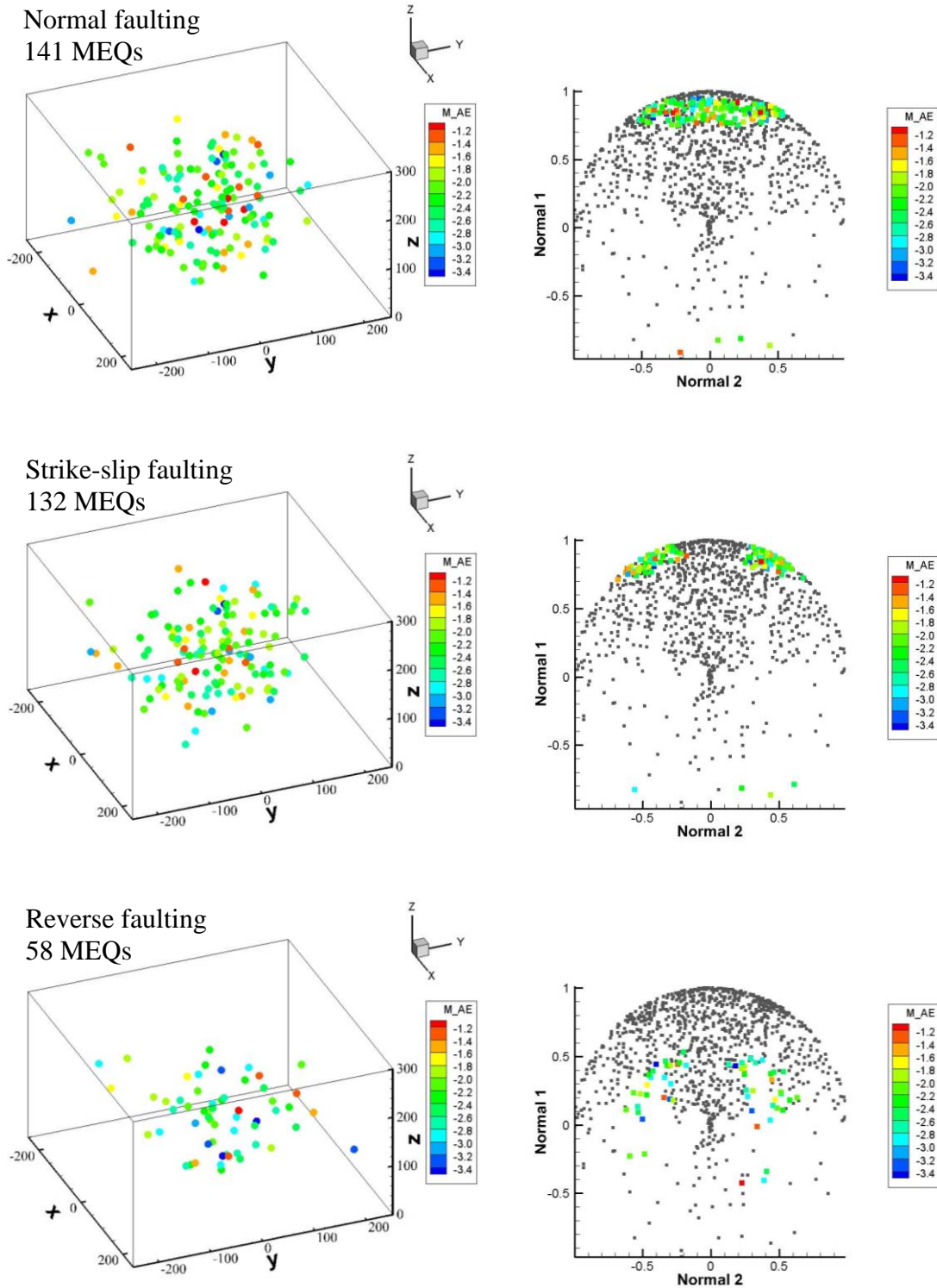


Figure 6.32. Comparison of microseismic events and orientations of slipped fractures after 72 hrs of injection for the cases of different differential stress.

As expected, the comparison of induced microseismicity in Figure 6.32 also shows sensitivity to the in-situ stress regime. When the same set of fractures is subjected to different stress regime, the slipped fractures show different orientations. These observations again demonstrate the important role of fracture orientation with respect to the in-situ stresses in the fracture shear behavior. For the given fracture network, normal faulting and strike-slip faulting are more favorable for creating shear slippage on fractures. We also note that in all three stress regimes, the distributions of the resulting microseismic events are quite scattered, without showing a preferred growth direction. It may be due to the fact that we ignore the dependence of fracture distribution parameters on geological conditions and in-situ stress fields.

#### 6.2.8 Effect of Differential Stress

A series of simulations are also conducted for various differential stresses to investigate their effects on the response of fractured reservoirs to fluid injection. For the assumed normal faulting regime, different magnitudes of the differential stress ( $dS$ ) between the maximum principal stress ( $S_v$ ) and the minimum principal stress ( $S_{hmin}$ ) are applied, by keeping  $S_{hmin}$  fixed at 30 MPa and changing the values of  $S_v$ . Three cases are studied: (1)  $S_v=53$  MPa and  $dS=23$  MPa; (2)  $S_v=50$  MPa and  $dS=20$  MPa; and (3)  $S_v=47$  MPa and  $dS=17$  MPa.

The resulting permeability evolutions are illustrated in Figure 6.33. In Case 3, after 72 hours of injection, the average permeability in the reservoir block is significantly increased from  $3.15E-16$  m<sup>2</sup> to  $3.36E-16$  m<sup>2</sup>, which is increased by 7%. Significant permeability enhancements are observed in Case 1 and Case 2. When the differential stress is increased to 20 MPa in Case 2, the average reservoir permeability is increased by 3.3 times, increased from  $3.13E-16$  m<sup>2</sup> to  $1.04E-15$  m<sup>2</sup>. A much more significant permeability enhancement is observed in Case 1, as the differential stress is further increased to 23 MPa, where the average permeability was increased by 5.3 times, from

3.20E-16 m<sup>2</sup> to 1.70E-15 m<sup>2</sup>. It can also be seen from Figure 6.33 that in Case 1 and Case 2, after a certain duration of injection, the rate of permeability increase slows down, and the reservoir permeability tends to reach a plateau value, which is reasonable for the assumed constant injection pressure boundary. As injection continues, the entire reservoir reaches equilibrium in pressure, therefore, no further enhancement in permeability will develop. We also note that the equilibrium state is reached earlier in Case 1, at about 24 hours of injection. It is due to the faster fluid diffusion in the reservoir as a result of significant permeability enhancement occurred in the early stage of the injection process.

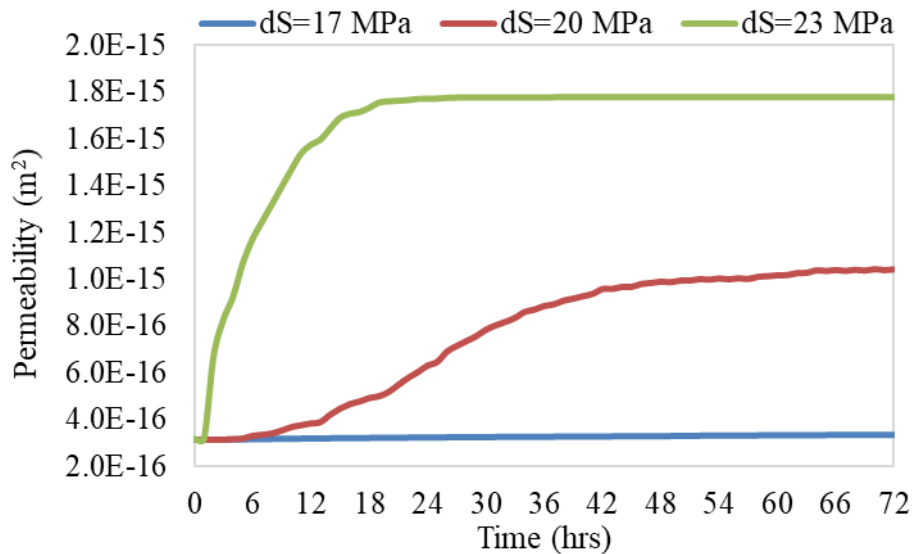


Figure 6.33. Comparison of permeability enhancement during 72 hrs of injection for the cases of different deviatoric stress between the vertical and the minimum horizontal stresses ( $dS = S_v - S_{hmin}$ ).

The response of induced microseismicity is also sensitive to the differential stress change, as shown in Figure 6.34. The results indicate that higher differential stress has the highest propensity to promote slip, dilate and increase permeability. After 72 hours of injection, Case 1 and Case 2

predicted a total of 254 and 141 microseismic events, respectively. Only 1 fracture slipped and generated 1 microseismic event in Case 3.

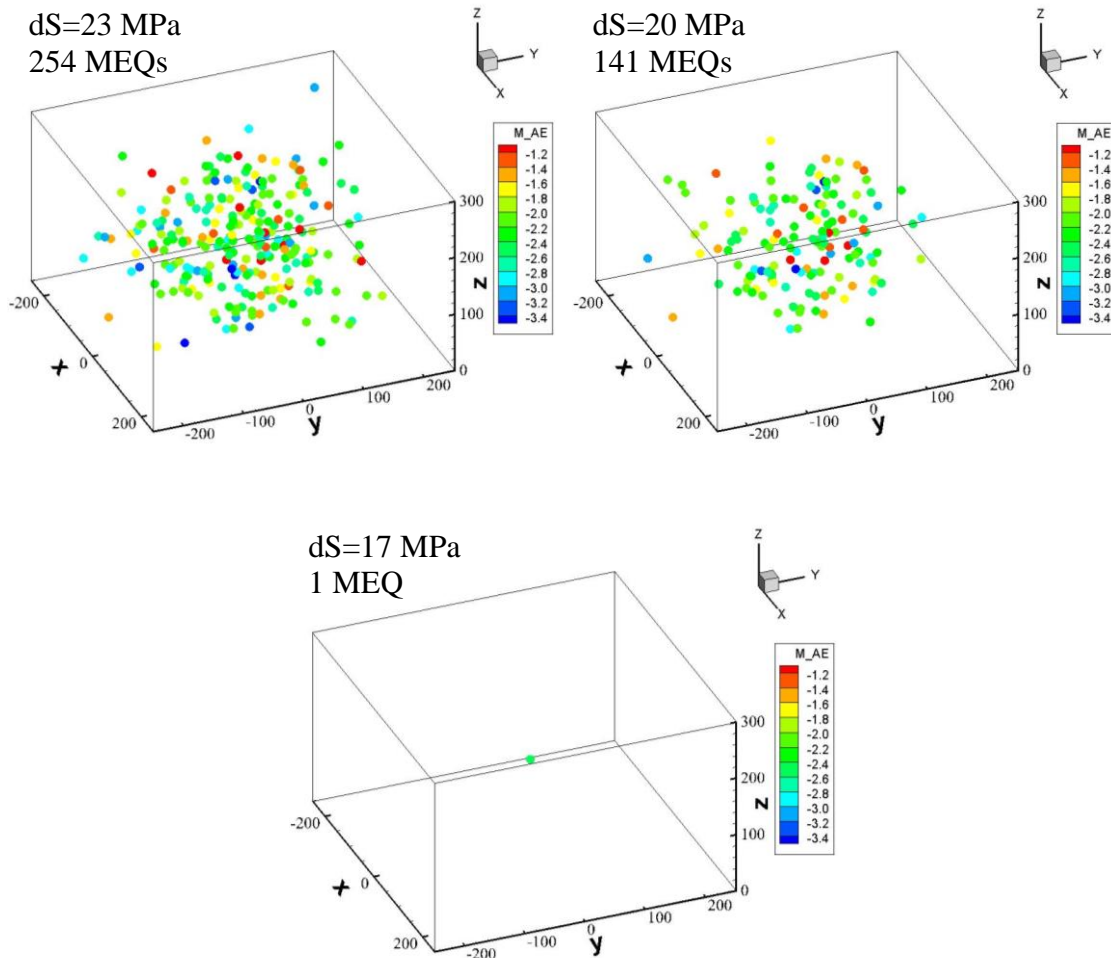


Figure 6.34. Comparison of microseismic events after 72 hrs of injection for the cases of different differential stress between the vertical and the minimum horizontal stresses (top left:  $dS=23$  MPa; top right:  $dS=20$  MPa; bottom:  $dS=17$  MPa).

The various response of the fractured reservoir to different differential stresses could be schematically explained with the aid of a Mohr diagram. In Figure 6.35, the Mohr circles defined by the difference between the maximum and minimum principal stresses in these three cases

studied are plotted, to show the states of initial stresses (colored semi-circles) in relation to the shear failure line (black straight line). As shown in this figure, keeping the minimum principal stress unchanged, as differential stress increases with increasing the magnitude of the maximum principal stress, the diameter of the Mohr circle is enlarged. Hence it is more likely to have shear slippages on fractures. In Case 3 ( $dS=23$  MPa), the Mohr circle at the initial state already touches the failure line, and shear flip could occur on the critically stressed fractures. As injection starts, more fractures would slip, dilate and increase permeability as a result of injection induced perturbations in the pressure and stress field. Therefore, significant permeability enhancement and more microseismic events are expected for the cases with higher differential stress.

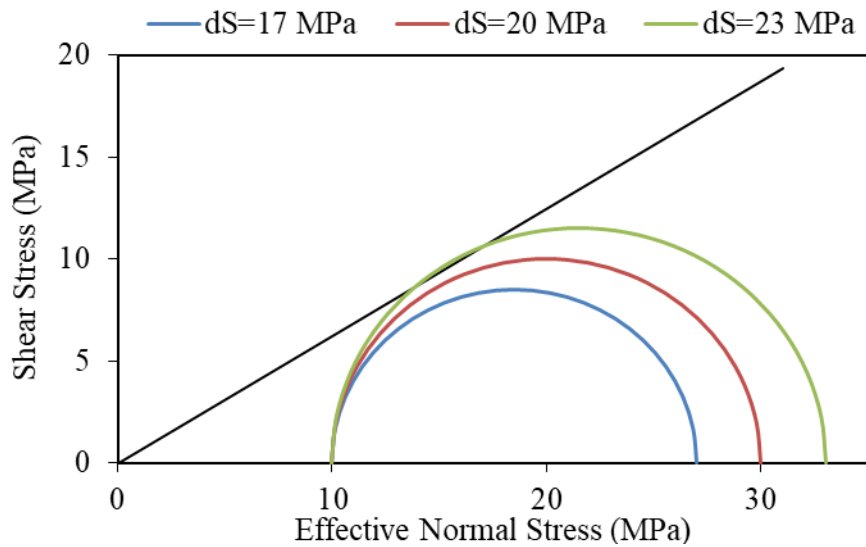


Figure 6.35. Mohr diagram representation of different initial stress states.

We also examined the cases that having the same value of differential stress, but different magnitudes of the initial maximum and minimum principal stresses. For the assumed normal faulting regime, three cases were designed: (1)  $S_v=53$  MPa and  $S_{hmin}=33$  MPa; (2)  $S_v=50$  MPa and

$S_{hmin}=30$  MPa; and (3)  $S_v=47$  MPa and  $S_{hmin}=27$  MPa. The differential stress,  $dS$ , is identical in these cases, with a value of 20 MPa.

The resulting permeability evolution curves and microseismicity clouds are plotted in Figure 6.36 and Figure 6.37, respectively, which show significant sensitivity to the principal stress magnitudes. Case 3 with the lowest initial principal stresses has a permeability increase from  $7.9E-16$  m<sup>2</sup> to  $4.3E-15$  m<sup>2</sup> (increased by 5.5 times). In contrast, the permeability increase in Case 1 where the highest initial principal stresses were applied is from  $2.40E-16$  m<sup>2</sup> to  $2.46E-16$  m<sup>2</sup> (only increased by 2%). The difference in the initial average reservoir permeability is also attributed to the different initial principal stresses. The lower the applied in-situ compressive stresses, the higher the stress-dependent fracture aperture, hence the higher the permeability.

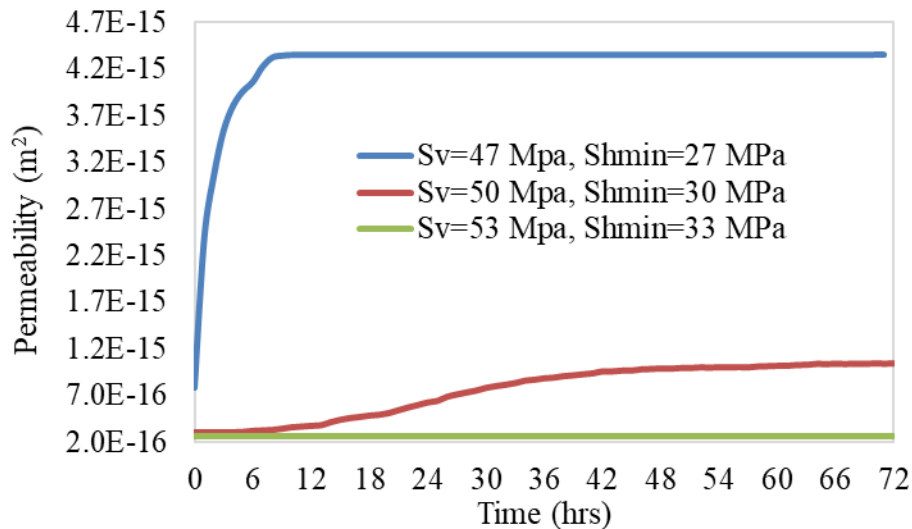


Figure 6.36. Comparison of permeability enhancement during 72 hrs of injection for the cases of different stress magnitudes.

The resulting microseismic events are also significantly affected by the different stress magnitudes applied in the reservoir, as shown in Figure 6.37. After 72 hours of injection, no microseismic

events is observed in Case 1, the case with the highest initial principal stresses, which means fractures within the reservoir domain do not slip under such stress condition. As the initial stress magnitudes reduce, the number of slipped events is increased. A total of 141 events is observed in Case 2. The number is dramatically increased to 470 in Case 3.

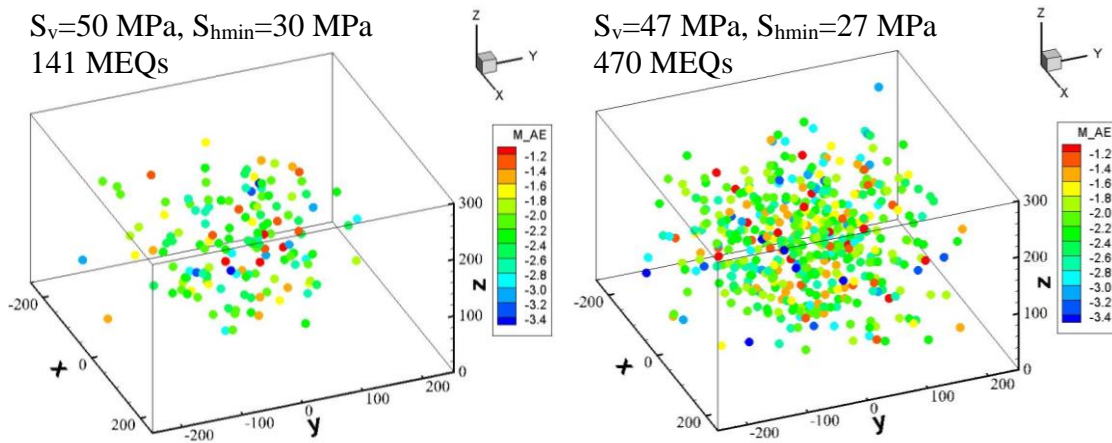


Figure 6.37. Comparison of microseismic events after 72 hrs of injection for the cases of different stress magnitudes (left:  $S_v=50$  MPa and  $S_{hmin}=30$  MPa; right:  $S_v=47$  MPa and  $S_{hmin}=27$  MPa). No microseismic events in Case 1 ( $S_v=53$  MPa and  $S_{hmin}=33$  MPa).

The various responses in the induced microseismicity could also be explained using a Mohr diagram. When the maximum and minimum principal stresses are increased by the same amount, the differential stress is unaffected. Therefore, the Mohr circle remains the same diameter and only shifts to the right, which means moving away from the failure envelope. As shown in Figure 6.38, the Mohr circle at the initial stress state in Case 3 ( $S_v=47$  MPa and  $S_{hmin}=27$  MPa) already touches the failure line, suggesting fractures oriented at specific directions could slip under the initial in-situ condition. It explains the dramatic enhancement in reservoir permeability at the early stage of injection. As the initial stresses continually increase, the Mohr circles in Case 2 and Case 1



move to the right, farther away from the failure line. After the same period of injection, Case 2 observed less slipped events compared to Case 3. None of the fractures slipped under the stress condition in Case 1, where the highest initial stresses were applied.

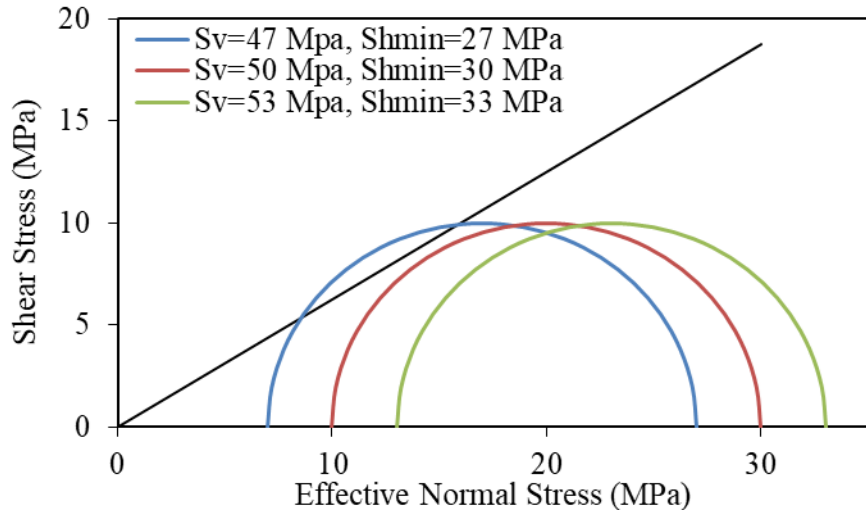


Figure 6.38. Mohr diagram representation of different initial stress magnitudes.

### 6.2.9 Effect of Fluid Viscosity

The properties of injecting fluid are important parameters to consider during the injection operation. Among them, the viscosity is probably the most important property as it directly governs the fluid flow (Eqn. (4.11)) within the reservoir and controls reservoir pressure change. We also conducted three injection simulations using different values of fluid viscosity  $\mu_f$ :  $1.6E-4$  Pa·s,  $3.0E-4$  Pa·s, and  $1.0E-3$  Pa·s, which corresponds to the water viscosity at  $170$  °C,  $100$  °C and  $20$  °C.

Comparison of the resulting permeability resolutions is shown in Figure 6.39. It can be seen that after 72 hours of injection, the case with the highest fluid viscosity has the minimum increase in reservoir permeability. In the cases with lower viscosity, much significant permeability

enhancements are observed. These results suggest that a low viscous fluid is more favorable for enhancing the permeability in naturally fractured reservoirs via shear stimulation.

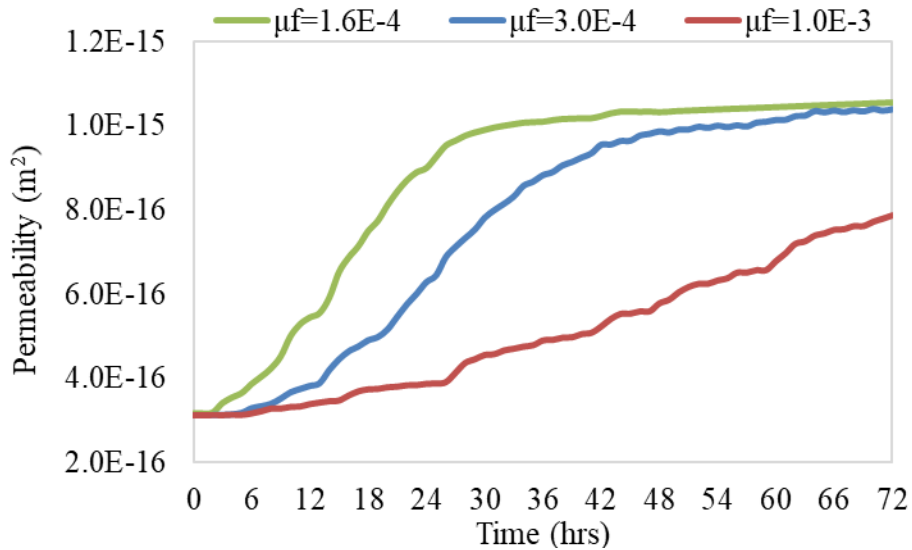


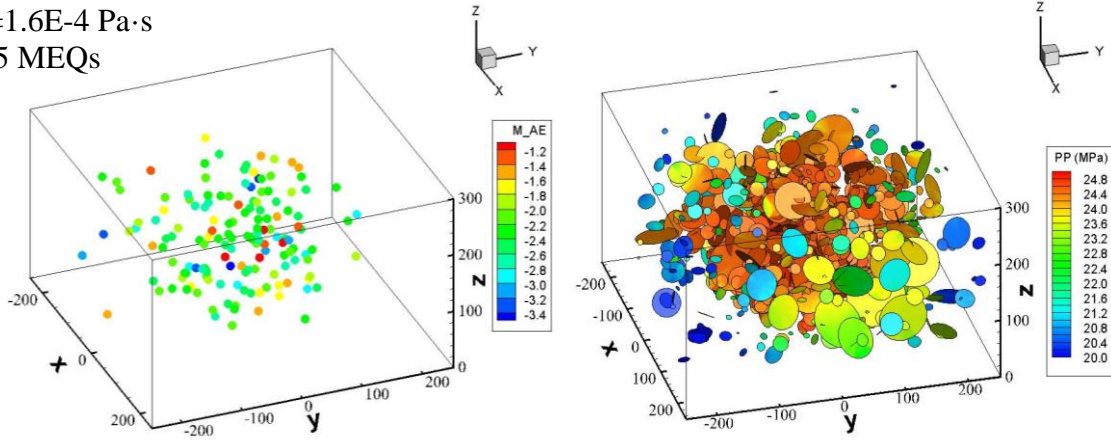
Figure 6.39. Comparison of permeability enhancement during 72 hrs of injection for the cases of different fluid viscosities.

Figure 6.40 shows the induced microseismicity after 72 hours of injection in each case and their corresponding pore pressure distributions. We could see from the figure that the induced microseismicity is also sensitive to fluid viscosity. The case with a lower fluid viscosity results in more microseismic events and has a broader distribution of the seismic cloud. This response could be explained by the difference in the pore pressure evolution processes. As a result of reducing fluid viscosity, the hydraulic conductivity is increased, which increases the diffusion speed of elevated pressure caused by injection. Consequently, the faster pressure disturbance within the fracture network tends to cause more fractures to slip in shear and dilate, inducing more seismic events and greatly enhancing reservoir permeability. In Case 1, when a low viscosity ( $1.6E-4$  Pa·s) fluid is injected, the rapid fluid diffusion causes a much more significant disturbance of pore

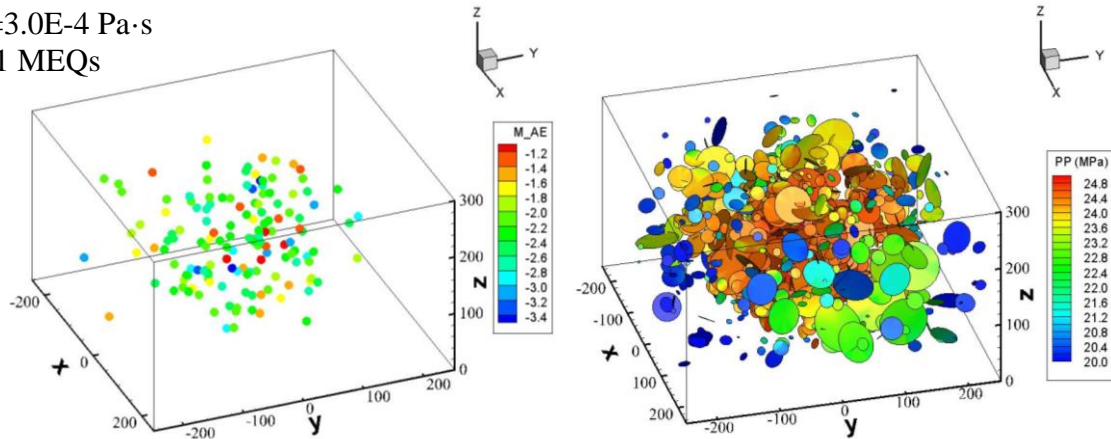
pressure within the fracture network, and it induces more slipped events. Also, due to the fast diffusion, the pressure within the reservoir quickly reached the near equilibrium state after 40 hours of injection. Beyond which, there is no significant increase in reservoir permeability, as shown in the permeability curve of Case 1 in Figure 6.39.

In conventional hydraulic fracturing aimed at creating new fractures, high viscous fluid/gel is usually preferred to reduce fluid leak-off into the formation (e.g., Hossain 2001), and to carry proppants that required to keep the induced hydraulic fracture open. On the contrary, the results from these sensitivity studies suggest that a low viscous fluid has positive effects on shear stimulation of natural fractures by promoting fluid and pressure diffusion in the fracture network. In addition, due to the roughness of sliding fracture surfaces, no proppants is required during the shear dilation process. Therefore, the use of a low viscous fluid is suitable for shear stimulation.

$\mu_f=1.6E-4 \text{ Pa}\cdot\text{s}$   
145 MEQs



$\mu_f=3.0E-4 \text{ Pa}\cdot\text{s}$   
141 MEQs



$\mu_f=1.0E-3 \text{ Pa}\cdot\text{s}$   
87 MEQs

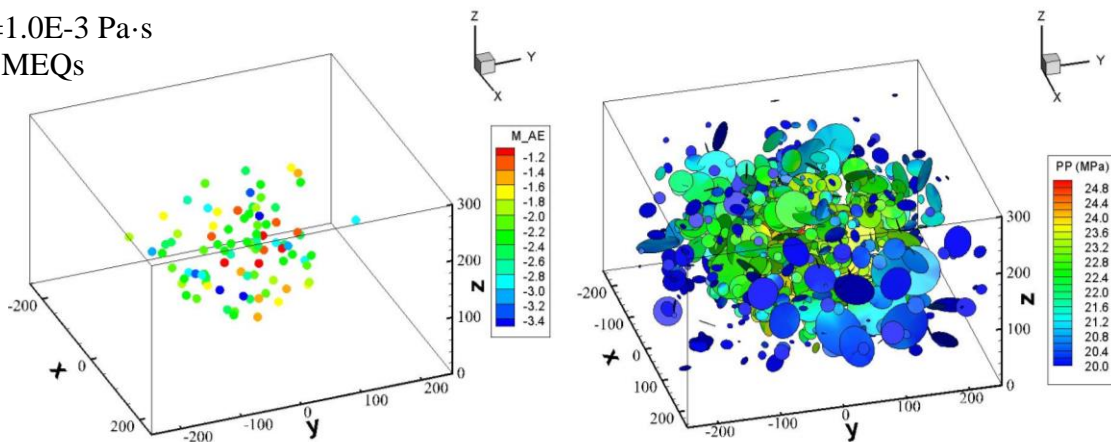


Figure 6.40. Comparison of microseismic events and pore pressure distribution in fracture network after 72 hrs of injection for the cases of different fluid viscosities.

### 6.2.10 Effect of Injection Rate

The operational factors such as injection rate and volume are also important parameters to consider for stimulation designs. To investigate how the injection rate will affect the injection outcome, different value of injection rate is fixed at the wellbore, instead of a constant injection pressure in the previous studies. The stress condition is the same as in the base case, i.e.,  $S_v$  is 45 MPa and  $S_{Hmax}$  and  $S_{hmin}$  is 50 MPa and 30 MPa, respectively. Three injection rates,  $Q_{inj}$ , are examined: 0.025 m<sup>3</sup>/s, 0.050 m<sup>3</sup>/s and 0.075 m<sup>3</sup>/s. The same injection duration of 72 hours was simulated.

Figure 6.41 shows the evolutions of average reservoir permeability against the injection time. It is clear from the figure that in all three cases, the overall permeability is greatly improved as a result of the injection. At the same injection time, a larger volume of fluid will be injected in the case of a higher injection rate, and the reservoir permeability enhancement is higher.

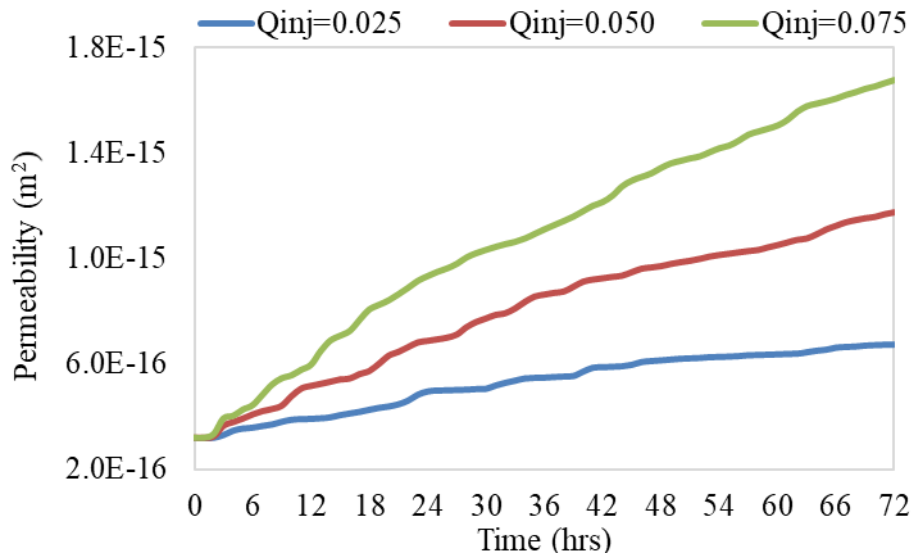


Figure 6.41. Comparison of permeability enhancement during 72 hrs of injection for the cases of different injection rate.

The evolution of average reservoir permeability is also plotted against the injected volume in Figure 6.42. It shows that the permeability is continually improved as more volume of fluid is injected into the fractured reservoir. When injecting the same amount of fluid under different injection rate, much more significant permeability enhancement is observed in the case of a higher injection rate.

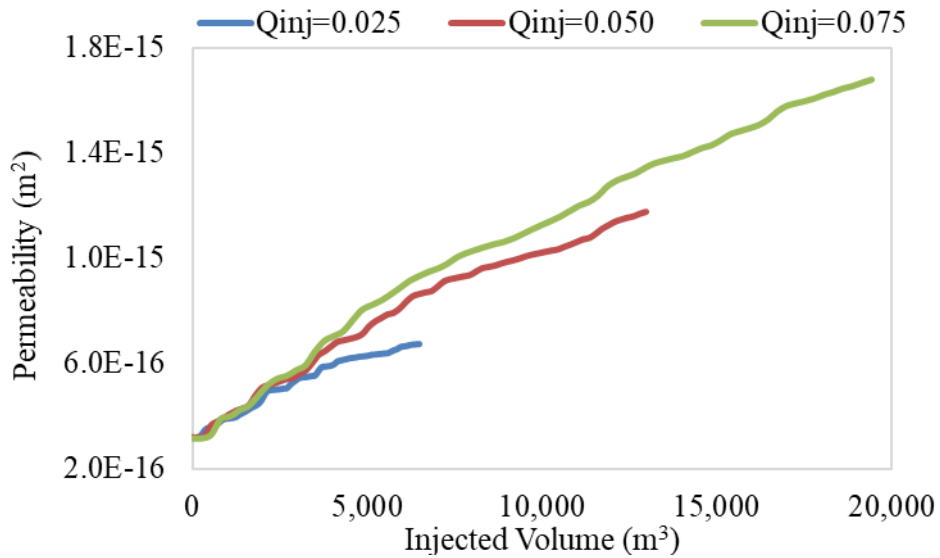


Figure 6.42. Comparison of permeability enhancement against injected volume for the cases of different injection rate.

Figure 6.43 shows the comparisons of injection induced microseismicity and the pore pressure distribution after injecting the same volume of fluid, 6480 m<sup>3</sup>, in the three cases. The corresponding injection time is 72 hours for Case 1 (Q<sub>inj</sub>=0.025 m<sup>3</sup>/s), 36 hours for Case 2 (Q<sub>inj</sub>=0.050 m<sup>3</sup>/s), and 24 hours for Case 3 (Q<sub>inj</sub>=0.075 m<sup>3</sup>/s). The results suggest that both the number and the maximum magnitude of induced microseismic events could be increased by injecting the same volume during a short time, i.e., increasing injection rate.

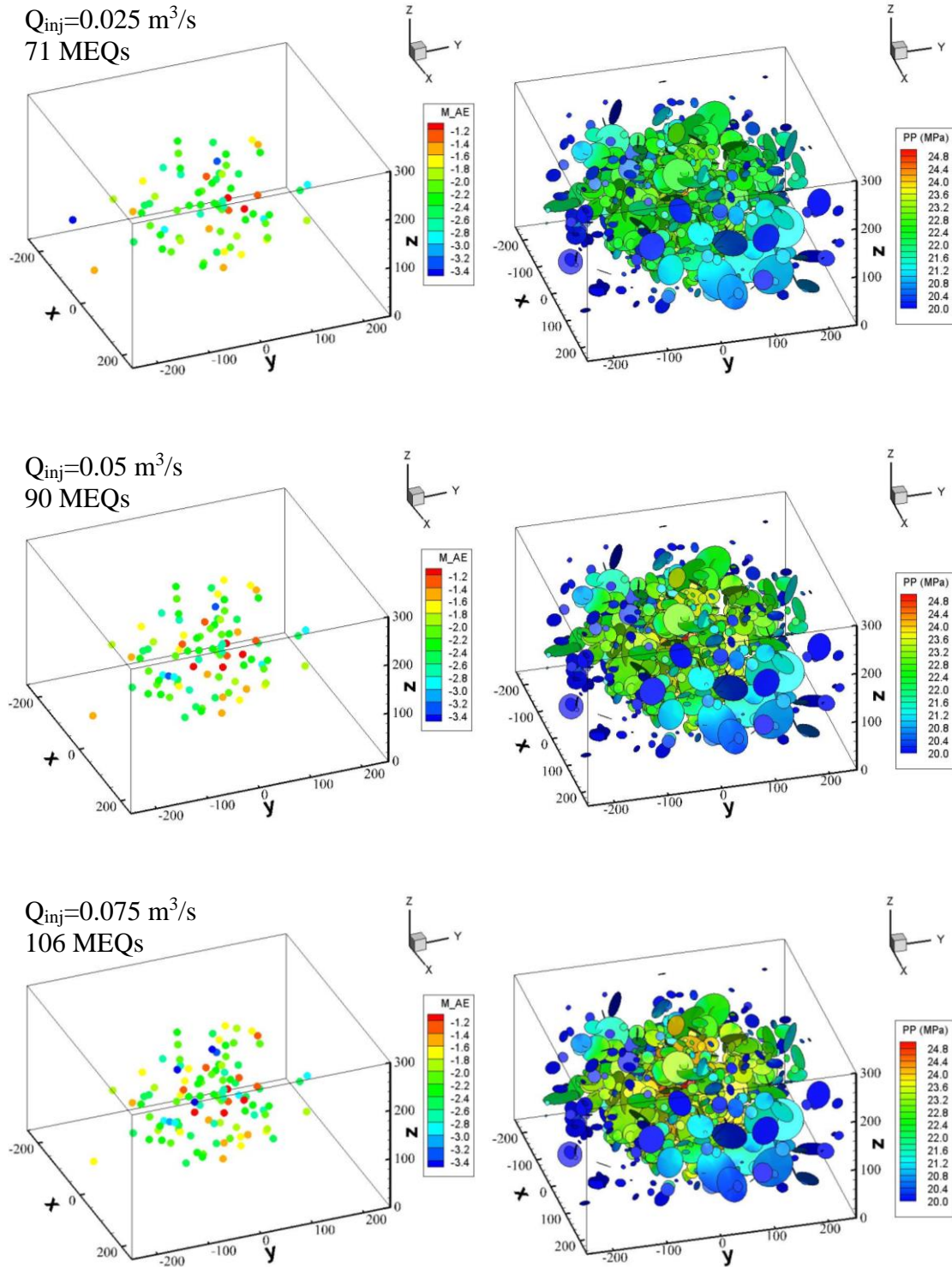


Figure 6.43. Comparison of microseismic events and pore pressure distribution in fracture network after injecting the same volume of fluid ( $6480 \text{ m}^3$ ) using different injection rate.

Comparing the pore pressure distributions (right panels in Figure 6.43), we could see that an increase in the injection rate leads to higher pressure build up. As the higher pressure translates into lower effective normal stresses acting on fractures, it in turn promotes the possibility of fracture slippages. Therefore, a relatively high injection rate is favorable for enhancing reservoir permeability via the mechanism of fracture shear stimulation.

We also examined the effects of injection rate under different stress differentials. We consider a low rate of  $0.075 \text{ m}^3/\text{s}$  and a high rate of  $0.15 \text{ m}^3/\text{s}$ , and two differential stresses between the maximum and minimum horizontal stresses ( $dS = S_{H_{\max}} - S_{H_{\min}}$ ) with a magnitude of 1 MPa and 15 MPa, respectively. The same vertical stress and the minimum horizontal stress are assumed in this series of studies, with a value of 30 MPa. Using different combinations of the two parameters, four cases are simulated: (1)  $dS=1 \text{ MPa}$  and  $Q_{\text{inj}}=0.075 \text{ m}^3/\text{s}$ ; (2)  $dS=1 \text{ MPa}$  and  $Q_{\text{inj}}=0.15 \text{ m}^3/\text{s}$ ; (3)  $dS=15 \text{ MPa}$  and  $Q_{\text{inj}}=0.075 \text{ m}^3/\text{s}$ ; and (4)  $dS=15 \text{ MPa}$  and  $Q_{\text{inj}}=0.15 \text{ m}^3/\text{s}$ . The total injection volume is kept the same as  $19,400 \text{ m}^3$ , and the injection duration for the low injection rate case and the high injection rate case is set to be 72 hours and 36 hours, respectively. In all four simulations, the injection pressure is below the minimum principal stress.

The comparison of overall reservoir permeability enhancements is plotted against the injected volume in Figure 6.44. In the cases with a higher differential stress of 15 MPa, the reservoir permeability is increased from  $5.4\text{E-}16 \text{ m}^2$  to  $3.1\text{E-}15 \text{ m}^2$  and  $2.4\text{E-}15 \text{ m}^2$  for the high and low injection rate, respectively, corresponding to an increase of 5.8 times and 4.5 times. However, in the cases with a low differential stress of 1 MPa, the average reservoir permeability is only increased by 2.2 times and 1.9 times for the high and low injection rate, respectively. The results indicate that injecting fluid at a relatively high rate always leads to a higher permeability enhancement. In the cases with a higher differential stress, the enhancement in the average



reservoir permeability is much more significant. Comparing the results from Case 2 (low  $dS$  and high  $Q_{inj}$ ) and Case 3 (high  $dS$  and low  $Q_{inj}$ ), it suggests that for this given fracture network, when the differential stress is high, reservoir stimulation via shear dilation could be effectively accomplished by injecting water even at a reasonably low injection rate. The results are also dependent on the fracture network geometry and whether propagation is allowed or not.

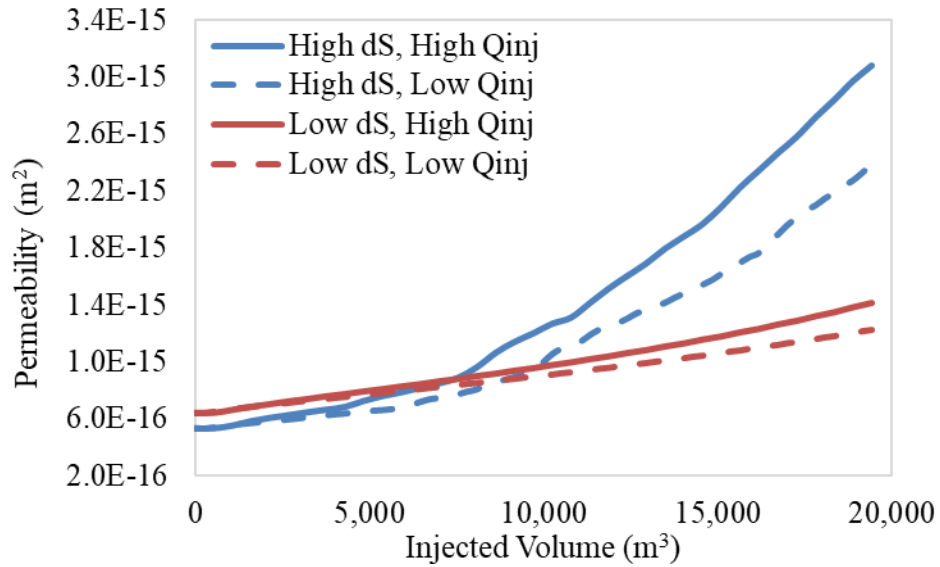


Figure 6.44. Comparison of permeability enhancement against injected volume for the cases of different injection rate and different stress differential: low injection rate of 0.075 m<sup>3</sup>/s (dashed lines) and high injection rate of 0.15 m<sup>3</sup>/s (solid lines), low differential stress of 1 MPa (red colored) and high differential stress of 15 MPa (blue colored).

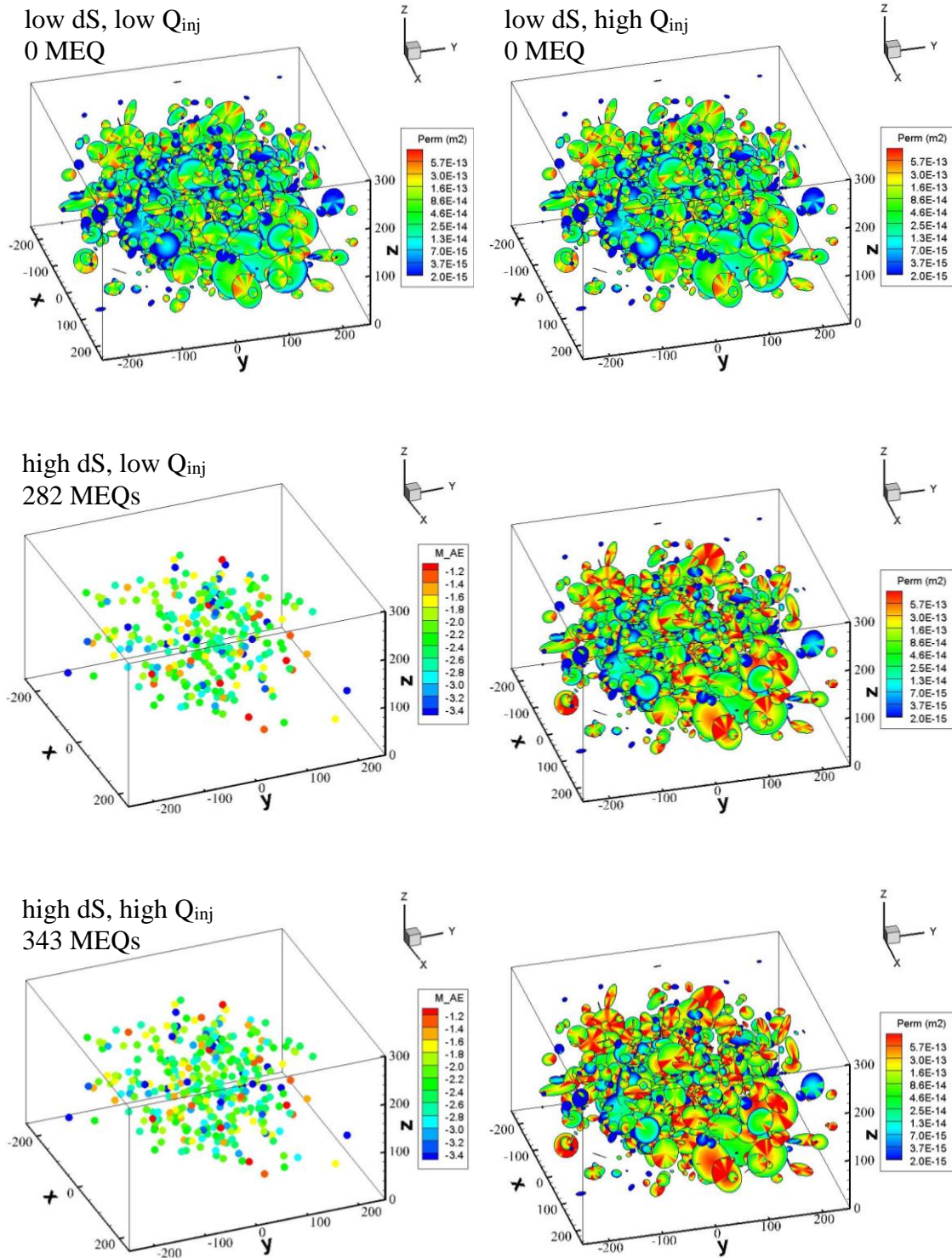


Figure 6.45. Comparison of microseismic events and the average reservoir permeability after injecting the same volume ( $19400 \text{ m}^3$ ) of fluid for the cases of different injection rate (low injection

rate of 0.075 m<sup>3</sup>/s and high injection rate of 0.15 m<sup>3</sup>/s) and different horizontal stress differential (low differential stress of 1 MPa and high differential stress of 15 MPa).

Figure 6.45 compares the average reservoir permeability and the microseismic events generated from different injection rate and differential stress combinations. It is evident that as expected, after injecting the same volume of fluid, a higher injection rate in a highly differential stress field promotes more fractures to slip in shear and induce microseismicity in the reservoir. In the cases which having a low differential stress of 1 MPa, none of the fractures slip in shear and therefore, no microseismic event is induced. The permeability enhancement in the low differential stress cases is attributed to the dilation of fracture aperture caused by fracture normal deformation during the injection process.

#### 6.2.11 Effect of Injection Temperature

In the above sensitivity studies, the injections are assumed under isothermal conditions. However, as described in Chapter 6.1, the thermal effect also plays an important role in governing the response of fractured reservoirs to injection and is worthy evaluations. In the simulations present in this section, the temperature of the injection fluid is fixed at 50 °C. Different values of initial reservoir temperature are assumed: 50 °C, 100 °C and 170 °C. The corresponding temperature difference is 0 °C, 50 °C and 120 °C, respectively.

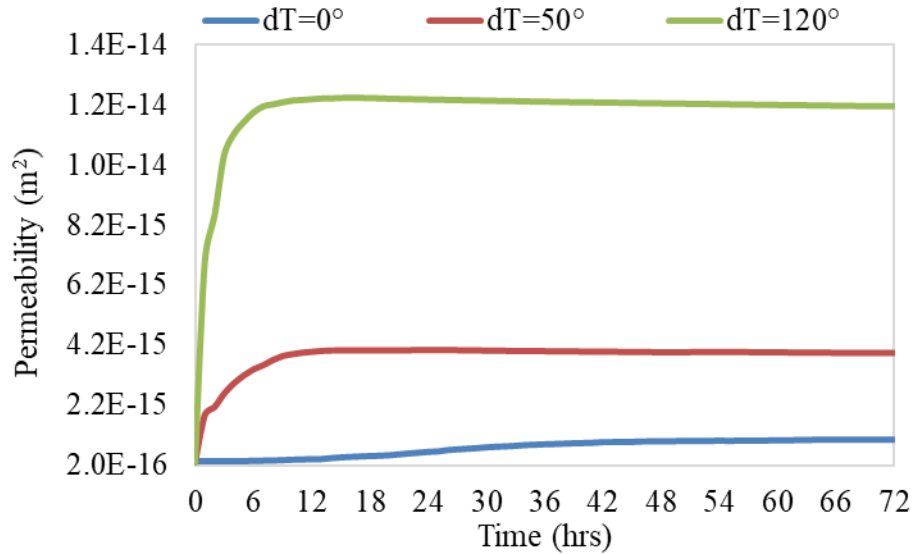


Figure 6.46. Comparison of permeability enhancement during 72 hrs of injection for the cases of different injection temperature difference.

The comparison of average reservoir permeability evolutions is illustrated in Figure 6.46. In the isothermal case, the average reservoir permeability is increased 3.3 times, from  $3.13\text{E-}16 \text{ m}^2$  to  $1.04\text{E-}15 \text{ m}^2$ . In Case 2, when the temperature difference between the injection fluid and the reservoir is  $50 \text{ }^\circ\text{C}$ , after 72 hours of cold water injection, the permeability is significantly increased to  $3.92\text{E-}15 \text{ m}^2$ , which is increased by 12.8 times. The enhancement of permeability is much more significant in Case 3, where the temperature difference is further increased to  $120 \text{ }^\circ\text{C}$ . After the cold fluid is injected for 72 hours, the average permeability in the reservoir block is increased by 39.8 times, to a value of  $1.22\text{E-}14 \text{ m}^2$ . In this study, many fracture clusters are directly connected with the injection well, allowing heat transfer via the fractures. We assume the temperature on the fractures that intersecting with the wellbore is immediately reduced to the same temperature as the injected fluid. The large temperature difference on these fractures ( $50 \text{ }^\circ\text{C}$  in Case 2, and  $120 \text{ }^\circ\text{C}$  in Case 3) would generate significant high tensile stresses and cause them to mechanically open,

which contributes to the sharp increments in the average permeability at the very early stage of injection. For a fracture network with poor connectivity and limited access to the injection source, the heat transfer would be insignificant, therefore, the thermal effects on the injection outcome are expected to be minimal.

Figure 6.47 shows the microseismic events and temperature drawdown induced by fluid injection under different thermal conditions. As expected, the isothermal case results in the least number of seismic events. In the two thermal cases, cooling is observed on the fractures near the injection well. Case 3 has more thermally impacted fractures with a highest temperature reduction of 120 °C, and results in the maximum number of seismic events. The results show that the higher the temperature difference between the injection fluid and the reservoir, the more the injection induced slipped events. The thermal effects due to cooling could induce tensile thermal stress on fracture surfaces, promote fracture shear slippage and consequently induce microseismicity and improve reservoir permeability.

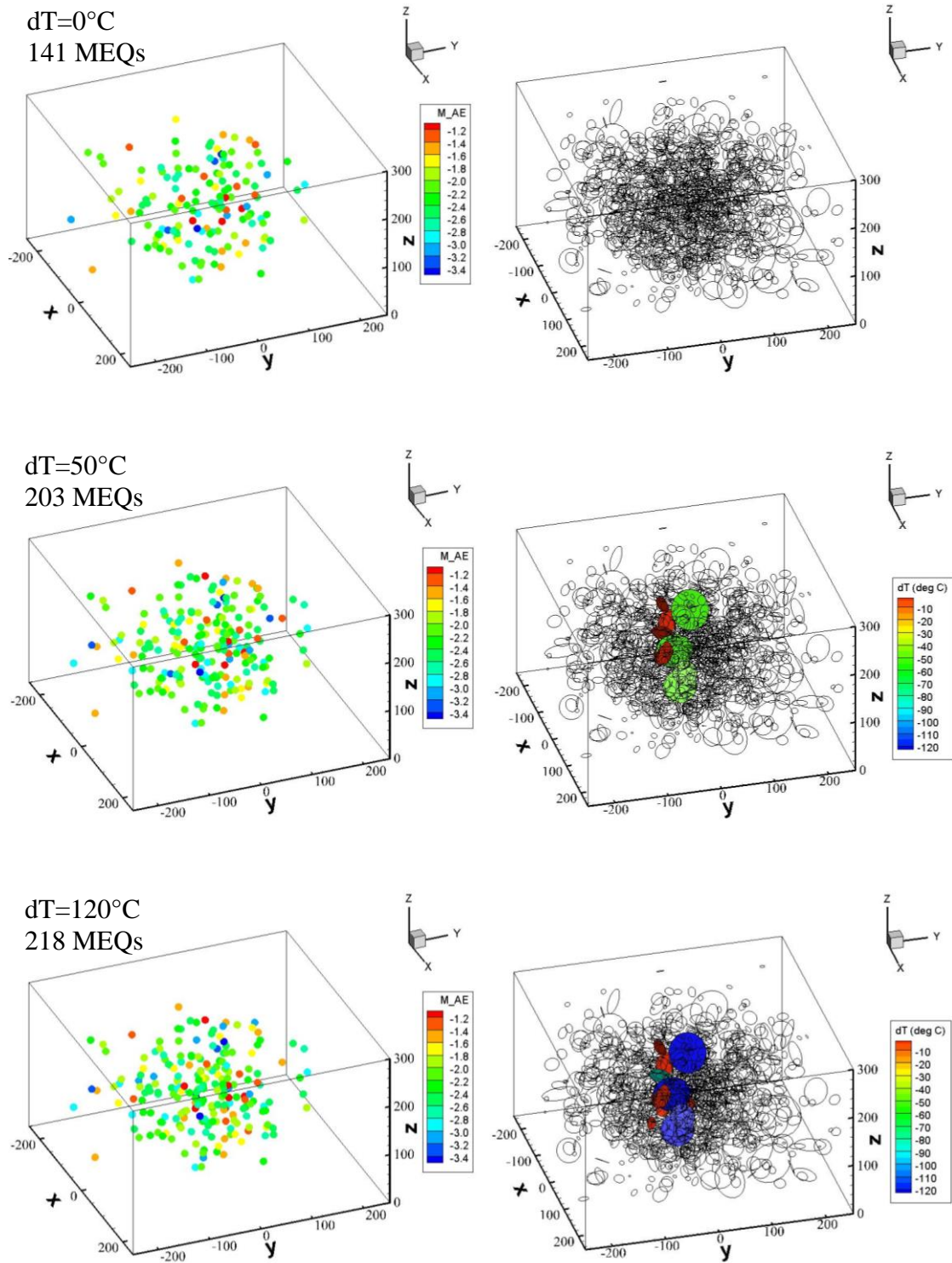


Figure 6.47. Comparison of microseismic events (left) and temperature drawdown (right) in fracture network after 72 hrs of injection for the cases of different temperature difference. For

better visualizations, in the right panels, the temperature drawdowns are only shown on the thermal affected fractures.

#### 6.2.12 Summary

The developed numerical model is used to investigate the effects of various parameters on the overall reservoir permeability enhancement and induced microseismicity in a naturally fractured reservoir subject to fluid injection. Based on the results of case studies, the following conclusions can be drawn:

The distribution of fractures within the natural fracture network has a significant effect on the injection response. Higher fracture density and larger fractures not only contribute to higher initial permeability, but also contribute to more slipped events and result in higher permeability enhancement. The orientation of natural fractures plays an important role in determining the stresses on the fractures and the slip potential. Therefore, it has major control over the injection response of fractured reservoirs. Besides the distribution parameters of the fracture network, the mechanical properties of fractures could also affect the results. Increasing fracture shear dilation angle would enlarge the dilated apertures caused by shear slippage, hence has positive effects on permeability enhancement by the mechanism of fracture shear slippage.

The results also reveal the important role of in-situ stress conditions acting in the reservoir. For a given natural fracture network, the stress regime, the orientation of the stresses, and the magnitude of the differential stress between the maximum and minimum principal stresses govern not only the relative direction of the fractures with respect to the in-situ stresses, but also the magnitudes of the stresses acting on fracture planes. When a natural fracture is favorably oriented with respect to the principal stresses, the fracture would have the greatest propensity to slip, dilate and increase

reservoir permeability. Higher differential stress and lower in-situ stress magnitudes are favorable for fracture shear slippage and the associated permeability enhancement.

The response of a fractured rock is also sensitive to the permeability of its matrix. When the rock matrix permeability is low, fluid flow diffusion into the matrix is prevented, providing higher pressures within the fracture network, and consequently promoting fracture slippage and dilation.

The operational parameters such as fluid viscosity, injection rate and injection volume control the fluid diffusion and pressure change within the reservoir, hence, are also important factors affecting the injection outcomes. In contrary to a high viscous fluid which is usually preferred for creating new fractures by hydraulic fracturing, an injecting fluid with low viscosity shows favorable for induce shear slippage on fractures. Moreover, since no proppants is required in shear dilation of natural fractures, the use of low viscous fluid for shear stimulation is suitable.

As injection volume increases, higher pressure buildup within the reservoir would lead to a greater increase in fracture aperture and cause fractures to slip in shear and dilate, hence improving permeability. Injecting the same volume of fluid at a high rate would cause larger perturbation in the pore pressure field, promote shear slippage on fractures, and induce more microseismic events with higher seismic magnitudes.

The temperature difference between the injected fluid and the reservoir is also a crucial factor in controlling the injection outcomes. Cooling on fracture surface induces thermal stress in tension, which is beneficial for fracture dilation and permeability enhancement. When a large amount of tensile thermal stress is induced, fractures may be mechanically open, significantly improving the overall reservoir permeability.

The results from these sensitivity studies suggest that the response of naturally fractured reservoirs to fluid injection is a complex process controlled by many factors, including the properties of



natural fractures, in-situ stress conditions, rock matrix permeability, the properties of injecting fluid, injection scheme and injection temperature. All of these factors should be carefully evaluated during the design phase of an injection operation to optimize its performance.

## 7. Model Applications

The developed model has applications in many diverse engineering fields. In this chapter, we present an application on simulating the stimulation response of an enhanced geothermal system and an application on simulating the wastewater disposal and the potential of induced seismicity.

### 7.1 Newberry EGS Stimulation

#### 7.1.1 Background

The Newberry Volcano EGS Demonstration project is designed to demonstrate cutting-edge research for Enhanced Geothermal System (EGS) development and to improve the feasibility and viability of EGS technologies and applications. The project site is located in the high temperature and low permeability volcanic formations in Central Oregon, on the northwest flank of the Newberry Volcano (AltaRock 2014).

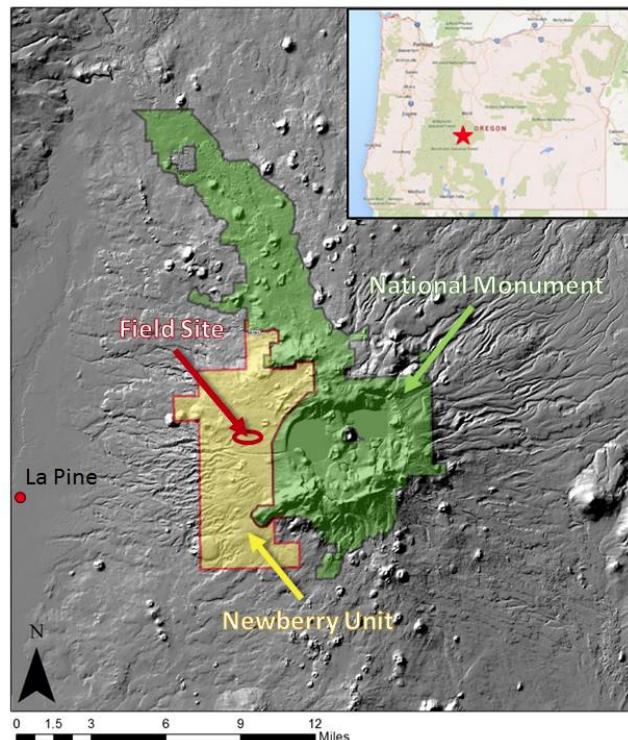


Figure 7.1. Location map of the Newberry EGS Demonstration site (taken from Alta Rock 2014).

The Demonstration project has been executed in multiple phases. Phase 1 of the Demonstration began on May 2010 involved hydrological testing and stimulation planning. In the fall of 2012, Phase 2.1 of the demonstration, stimulation of Well NWG 55-29 was initiated. The first stimulation injected a total of 41,639 m<sup>3</sup> (11 million gallons) of water at a maximum wellhead pressure (WHP) of 16.9 MPa (2450 psi). However, casing leaking was observed. After casing repair, Phase 2.2 stimulation began in September 2014 and terminated in November 2014. During the stimulation, 9,464 m<sup>3</sup> (2.5 million gallons) of water were injected at a maximum wellhead pressure of 19.7 MPa (2850 psi) (AltaRock 2014).

In this study, we use the proposed coupled thermo-poroelastic finite element model to simulate the Phase 2.2 stimulation. The first round of injection began on September 23, 2014 and ended on October 15, followed by a fall-off test. On November 11, the second round injection started, and lasted for 10 days until November 21.

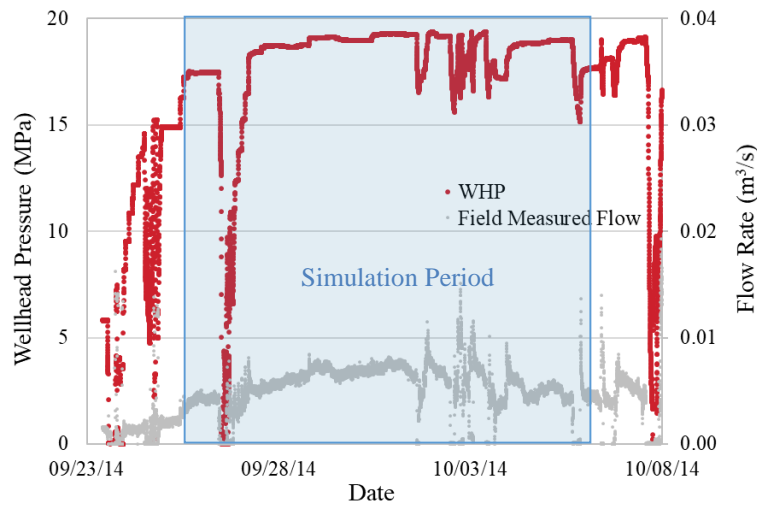


Figure 7.2. Wellhead pressure and flow rate profiles of Newberry EGS Phase 2.2 stimulation from September 23 to October 8, 2014. Data from AltaRock (2014).

Our target simulation period is from September 26, 20:00 to October 7, 10:00, a total of 254 hours, such that the noisy data due to leaks, equipment repairs and thermal zonal isolation material (TZIM) treatments is not included. The 254 hours includes a step-rate test and the initial part of Round 1 stimulation. The detailed injection profile is illustrated in Figure 7.2.

### 7.1.2 Model Setup

The simulation domain used to represent the Newberry EGS is 2000 m in the N-S direction (x-axis), 3000 m in the E-W direction (y-axis), and 2200 m in the vertical direction (z-axis). The injection well NWG 55-29 is assumed to be located in the center of the domain. Cold water is injected from two open sections: from 1896 m to 2228 m and from 2492 m to 3066 m. The model geometry and injection intervals are shown in Figure 7.3 (left). The grey line represents the wellbore, and the red portions represent the open intervals. Considering the scale ratio of the simulation domain and the well radius, the open intervals are represented by vertical injection elements as a line source. The injection pressure of each injection element is specified based on a known wellhead pressure and a hydrostatic pressure calculated at the middle of each injection element. For the specific flowing conditions within the wellbore and the fluid properties assumed in this model, the wellbore frictional pressure drop is less than 0.02 MPa, which is negligible compared to other pressure terms. Therefore, it is not considered in this current model. The injection rate of the line source is calculated as part of the simulation output.

The domain is discretized into 55,924 8-nodes brick elements with 60,480 nodes (Figure 7.3, right). To investigate the near wellbore response, finer gridding is used in this area. The model consists of three layers, representing three main geological formations of the Newberry reservoir: John Day (1300 m to 2400 m), Intruded John Day (2400 m to 3400 m) and Intruded John Day base (3400 m to 3500 m) (AltaRock 2014).

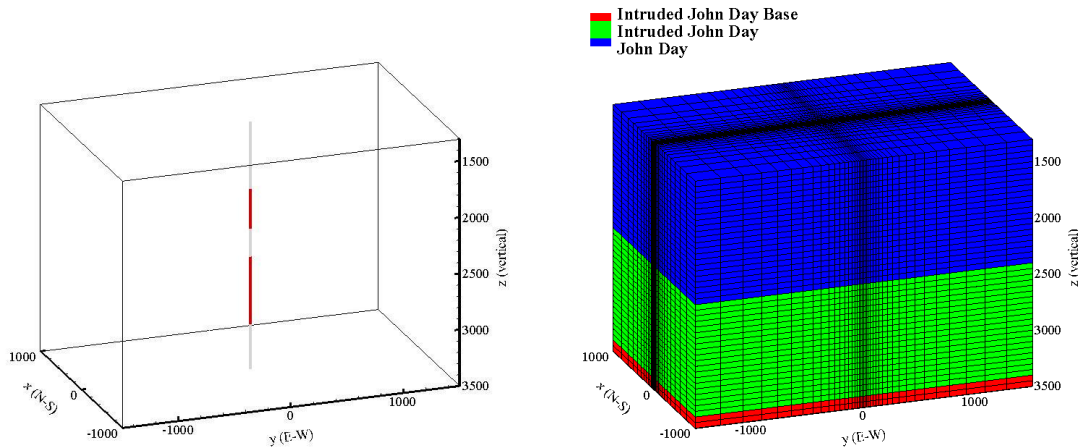


Figure 7.3. Left: The simulation domain is 2000 m in N-S (x-direction), 3000 m in E-W (y-direction), and 2200 m in vertical (z-direction). The wellbore is located in the center (grey line), which has two open intervals (red lines). Right: The domain consisting of three geological formations is discretized into 55,924 elements.

The pore pressure and temperature are prescribed at the top and bottom boundaries, whereas the side boundaries are assumed closed for fluid flow. Zero normal displacement is imposed for the lateral and bottom boundaries. The top of the domain is modeled as an unconstrained “free” boundary. The initial conditions are taken from earlier analyses of the pre-stimulation steady-state conditions at Newberry (Cladouhos et al. 2011; AltaRock 2014 and Sonnenthal et al. 2015). The initial temperature distribution follows a high gradient of 100 °C/km, with a maximum temperature of about 365 °C at the bottom of the domain. Initial pore pressure is assumed to be slightly lower than hydrostatic, with a linear gradient of 8.3 MPa/km. Pre-stimulation analysis on the stress field suggests a normal faulting regime in the Newberry site (Cladouhos et al. 2011). The maximum principal stress is vertical, with a lithostatic gradient of 24.1 MPa/km (1.07 psi/ft). The

intermediate principal stress is oriented in the N-S direction ( $S_{Hmax}$ , x direction) with a gradient of 23.5 MPa/km (1.04 psi/ft). The minimum principal stress is oriented in the E-W direction ( $S_{Hmin}$ , y direction) with a gradient of 14.9 MPa/km (0.66 psi/ft).

Table 7.1 Reservoir properties used in model

Young's Modulus	15 GPa
Drained Poisson's Ratio	0.22
Undrained Poisson's Ratio	0.46
Biot's Coefficient	0.97
Fluid Viscosity	$3 \times 10^{-4}$ Pa·s
Thermal Expansion Coefficient of Solid	$1.8 \times 10^{-5}$ K <sup>-1</sup>
Thermal Expansion Coefficient of Fluid	$3.0 \times 10^{-4}$ K <sup>-1</sup>
Thermal Diffusivity	$1.6 \times 10^{-6}$ m <sup>2</sup> /s
Maximum Horizontal Stress	23.5 MPa/km
Minimum Horizontal Stress	14.9 MPa/km
Vertical Stress	24.1 MPa/km
Fluid Pressure	8.3 MPa/km
Permeability of John Day ( $k_x, k_y, k_z$ )	$1 \times 10^{-17}, 5 \times 10^{-18}, 1 \times 10^{-17}$ m <sup>2</sup>
Permeability of Intruded John Day ( $k_x, k_y, k_z$ )	$1 \times 10^{-17}, 5 \times 10^{-18}, 1 \times 10^{-17}$ m <sup>2</sup>
Permeability of Intruded John Day Base ( $k_x, k_y, k_z$ )	$1 \times 10^{-18}, 1 \times 10^{-18}, 1 \times 10^{-18}$ m <sup>2</sup>

The mechanical properties were taken from the laboratory measurements on Newberry tuff samples (Li et al. 2012 and Wang et al. 2016). Thermal and hydrological properties follow those used in previous studies (AltaRock 2014; Sonnenthal et al. 2015). Homogeneous distributions of parameters are used in this current study, except for permeability. Since the Newberry site features a NS-striking fracture system (Sonnenthal et al. 2015), anisotropic initial permeability is assumed in the fractured zone, i.e., John Day and the Intruded John Day formations: higher values ( $1 \times 10^{-17}$  m<sup>2</sup>) in the x-direction and vertical direction compared to the y-direction ( $5 \times 10^{-18}$  m<sup>2</sup>). Permeability of the lowest 100 m in the Intruded John Day base formation is set to be  $1 \times 10^{-18}$  m<sup>2</sup> in all directions. To represent the fractured zone located in the Newberry EGS site, a natural fracture network is generated and introduced into the reservoir domain. The fractures are assumed to be penny-shaped,

and are specified by location, size and orientation. In this study, both the borehole televiewer (BHTV) and micro-earthquake (MEQ) data are used as basis for fracture generation. Two sets of fractures are generated: 351 fractures detected by BHTV and 399 fractures ascertained from the MEQ events detected during the Phase 2.2 stimulation (AltaRock 2014). The orientation and depth of fractures imaged in the wellbore are used to describe the 351 fractures intersecting with the wellbore. The other 399 fractures are assumed to distribute within 400 m from the wellbore and at a depth between 2000 m and 3000 m, as suggested by the MEQ cloud distributions. Further, we assume the orientations of the 399 fractures from MEQs based on fault plane directions calculated from seismic moment tensor results (AltaRock 2014).

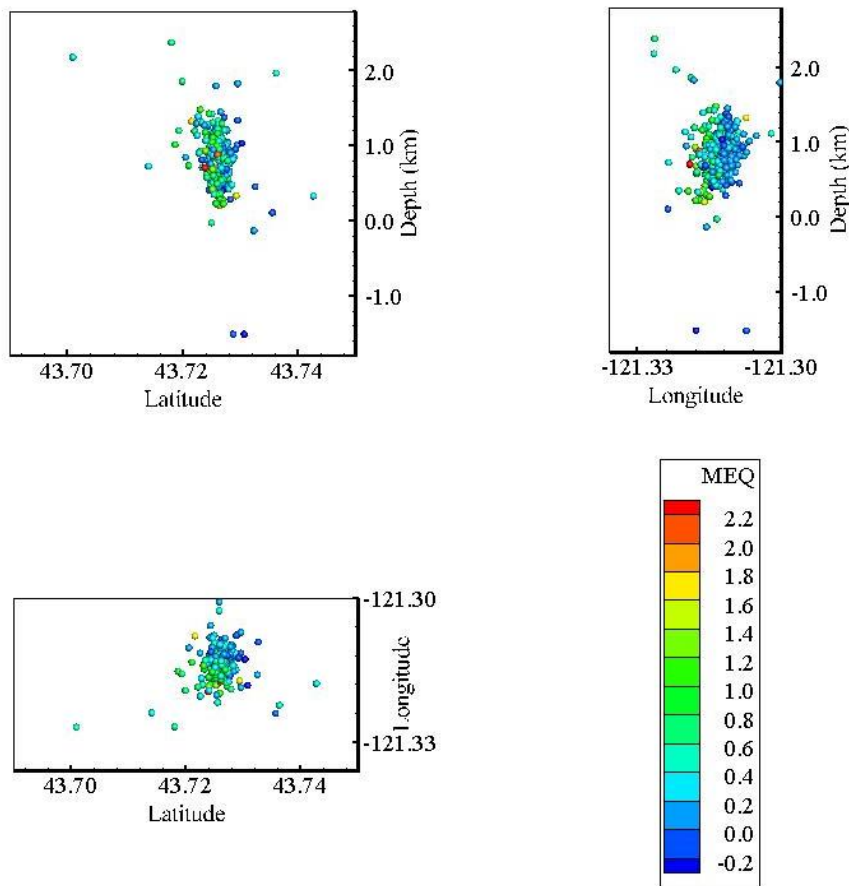


Figure 7.4. Location maps of MEQs detected during Phase 2.2 stimulation. The seismic cloud plots within 400 m from the wellbore and at a depth between 2000 m and 3000 m.

Figure 7.5 shows the histograms of the dip directions and dip angles of the 750 fractures. There are two primary sets of fractures both with a wide dispersion: east-dipping fractures with an average dip direction of  $110^\circ$  and west-dipping fractures with an average dip direction of  $280^\circ$ , and most fractures have a dip angle between  $40^\circ$  to  $70^\circ$ , which also agree with the fracture orientations estimated from Geomechanics-Based Stochastic Analysis of Mircoseismicity (GBSAM) (Lu and Ghassemi 2017).

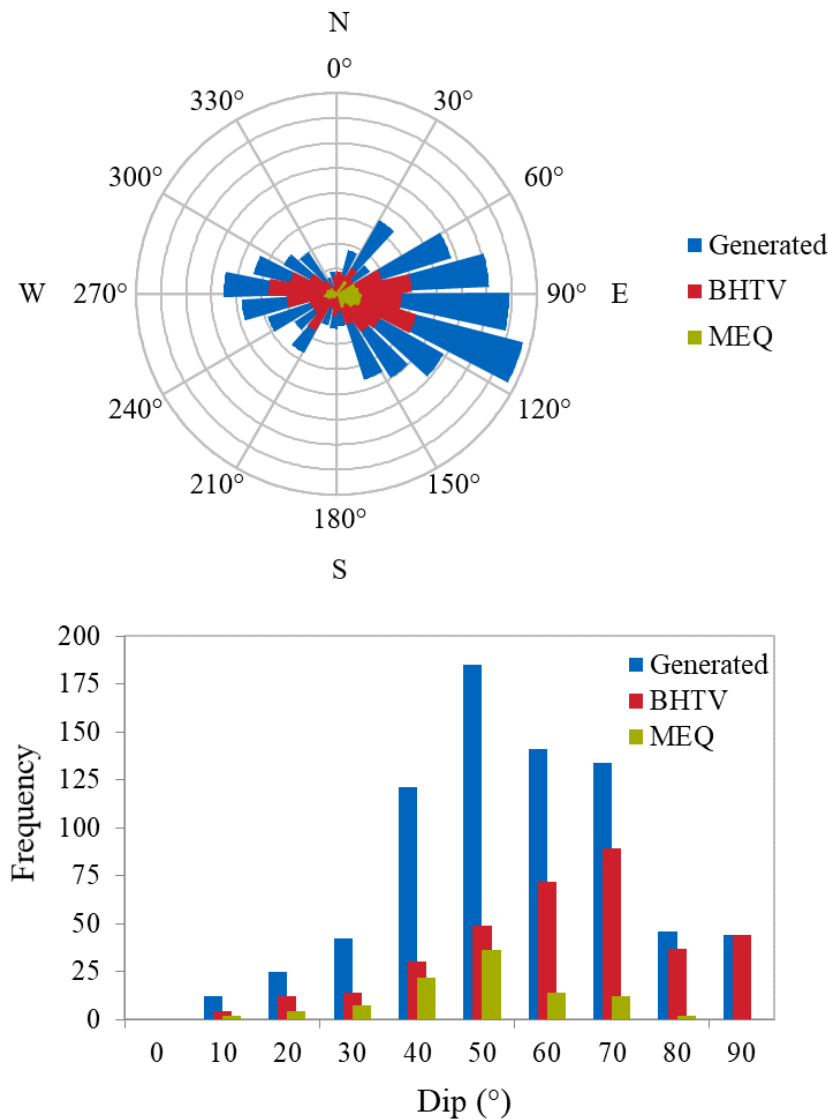


Figure 7.5. Rose diagram of dip directions (top) and histogram of dip angles (bottom) of generated fractures, and obtained from BHTV and MEQ data.



Since it is difficult to determine the fracture size from wellbore data, Log-normal distribution is used for fracture size generation. Fracture radii are assumed to range from 10 m to 200 m, which align with previous studies (Cladouhos et al. 2011). The initial apertures of the fractures are assumed to be proportional to radius, which could be calculated using Eqn. (4.3). The coefficient  $\beta$  is assumed to be 0.0004 and the exponent  $n$  is set to be 0.5, which are adopted from the typical values for a hot dry rock system (Tezuka and Watanabe 2000). The aperture of fractures is assumed to be stress-dependent. At each time step, stresses on the fracture surfaces are calculated to update aperture and permeability. The fracture network of 750 penny-shaped fractures is shown in Figure 7.6.

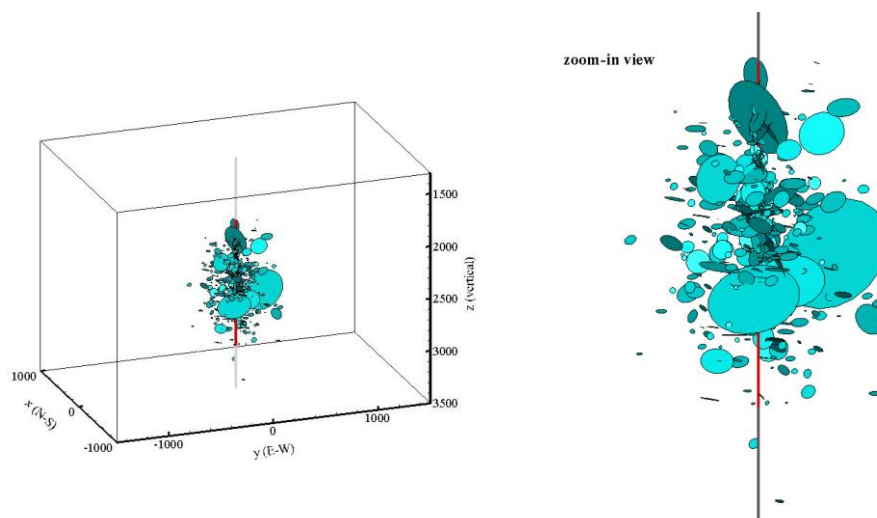


Figure 7.6. Fracture network in the simulation domain. A total of 750 fractures are generated and introduced to the simulation domain.

The slip on natural fractures is a highly complex process involving many factors, such as fracture geometry, stress condition and constitutive friction law. Among them, constitutive friction law is a particularly important one, since it is an internal factor representing the material characteristic of a fracture. Constant friction and rate-and-state friction (RSF) are the most commonly used

friction laws. Friction experiments (Fang et al. 2016) on drilling cuttings from well NWG 55-29 suggested that the rate-strengthening/weakening parameter at the base of the open injection interval is nearly zero, which means the rate and state effects are negligible. Therefore, a constant friction approach is suitable for this modeling.

Table 7.2 Fracture parameters used in model

Number of Fractures	750
Fracture Radius	10-200 m
Fracture Size (Log SD)	2.63
Fracture Size (Log EX)	0.79
Size-aperture Coefficient	$4 \times 10^{-4}$
Basic Friction Angle	0.459
Shear Dilatation Angle	0.035
90% Closure Stress	20 MPa

### 7.1.3 Simulation Results

In this study, we follow the injection WHP profile from September 26, 20:00 to October 7, 10:00. Cold water is injected from the openhole sections by using WHP boundary control. The injection water temperature at depth is assumed to be the same as the surface temperature (25 °C), with the heat transmission in the wellbore neglected. It should be noted that this temperature is lower than the actual water temperature at the injection interval, therefore, the cooling effect will be overestimated by using this assumption. However, for the short injection period we modeled, the cooling effect is confined to the near wellbore region, and it would not significantly affect the overall modeling results.

The WHP profile and the resulting injection rate profile are plotted in Figure 7.7. In each stage, as the WHP increases, a significant increase in flow rate is observed, following by a decline to lower rates. Other authors (Cladouhos et al. 2015) interpreted the flow spikes as the compression of water due to the pressure increase in the wellbore and the formation. However, considering the small

change in water compressibility under the injection conditions, likely the water compression alone is not sufficient to cause such high temporary flows. One could explain this behavior in terms of the fracture network response. When increasing the injection pressure, it is likely that some fractures opened due to the elevated pressure, and the increase in fracture volume is reflected in a higher injection rate. If there is insufficient energy to further increase the pressure within the fractures, no further increase in the fracture volume would occur, which may correspond to the rate declines.

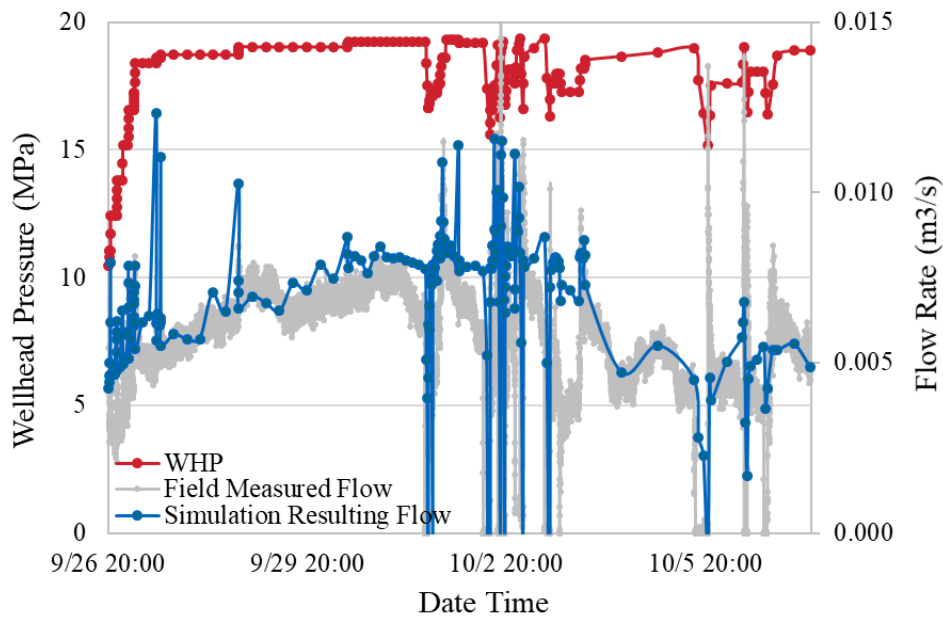


Figure 7.7. Wellhead pressure and injection rate profiles. As the WHP increases, a simultaneously significant increase in flow rate is observed and following by a decline to lower rates. The flow spikes may due to fracture volume increase as a result of fracture opening. When there is no sufficient injection pressure to promote further opening, the flow required for fracture volume increase vanishes, resulting in a decline in flow rate. The resulting flow rates generally agree with the field measured values.

Figure 7.7 also shows the comparison between the simulation resulting flow rate and the flow rate measured at the field. It should be pointed out that many attempts are made to best fit the actual injection rates. Since the distribution of fractures has a major control on reservoir behavior and it is difficult to accurately quantify the distribution from the available data, a trial and error process has been used. The simulation is firstly run with a fracture network model generated from an initial guess on fracture distribution. If the resulting injection rate is lower than the field measured rate, the orientation and size of some fractures are adjusted to create a better connected fracture network which allows more fluid to be injected into the reservoir. If the resulting rate is higher than the actual value, some of the fractures are disconnected from the main flow path. The fractures for adjustment are selected based on their contributions to the network connectivity, hence, fluid flow. We start by adjusting the large fractures located on or near the flow path, by rotating them, increasing or decreasing their radius, to improve or diminish the overall connectivity of the fracture network. During this process, the properties of the isolated small fractures which have negligible contributions to the flow behavior are adjusted accordingly, such that the overall statistical distribution of fracture network properties, such as fracture number, size, and orientation, is not affected. After each adjustment, the resulting flow rate is compared with the field observed data. This adjusting process is repeated until an acceptable match is reached. The fracture network after adjusting is shown in Figure 7.3. The resulting flow rates generally agree with the field measured values, though the match is not exact in details. Future adjustments on the model inputs are required to capture the sensitive changes in flow rate.

Pore pressure distributions within the reservoir after 3 hours injection and after 254 hours injection are shown in Figure 7.8. It can be seen that pore pressure development is mostly controlled by the

fracture network connectivity. Injection fluid mainly pressurizes the fractures that intersect the wellbore, and the interconnected fractures.

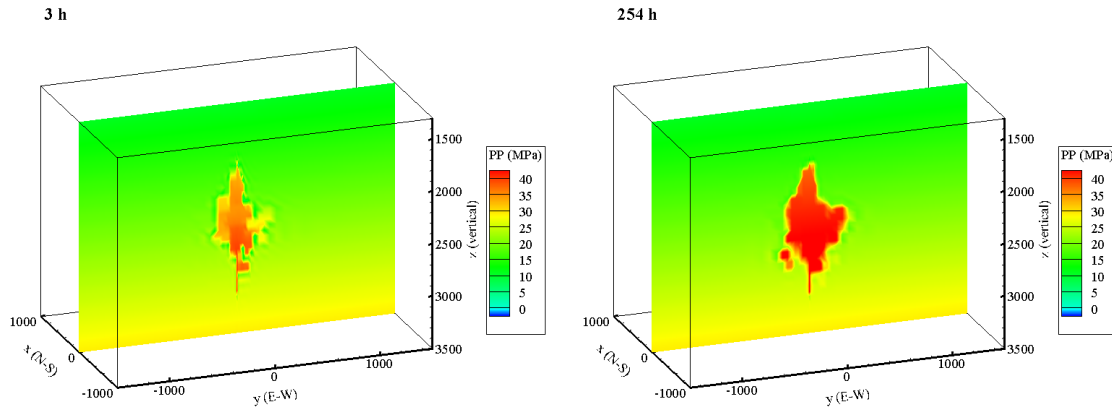


Figure 7.8. Pore pressure evolution after 3 hrs injection (left) and 254 hrs injection (right) shows that pore pressure development is mostly controlled by the fracture network connectivity.

During injection, fractures could dilate and have an increased aperture. As a result, the permeability of fractures could also be increased, since it is critically dependent on the third power of fracture apertures. Figure 7.9 shows the evolution of the geometric averaged fracture permeability after 3 hours and 254 hours of injection, respectively. During injection most fractures show permeability improvement which contributes to the overall reservoir permeability enhancement.

Figure 7.10 shows the simulated injection induced MEQ events after 3 hours and 254 hours injection, respectively. At the beginning of the initial step-rate test, only a few MEQs occurred adjacent to the wellbore. As injection continued, more MEQ events were located in a broader

diffusion space. After the 254 hours of short period injection, a total of 39 MEQs was observed in the near wellbore area.

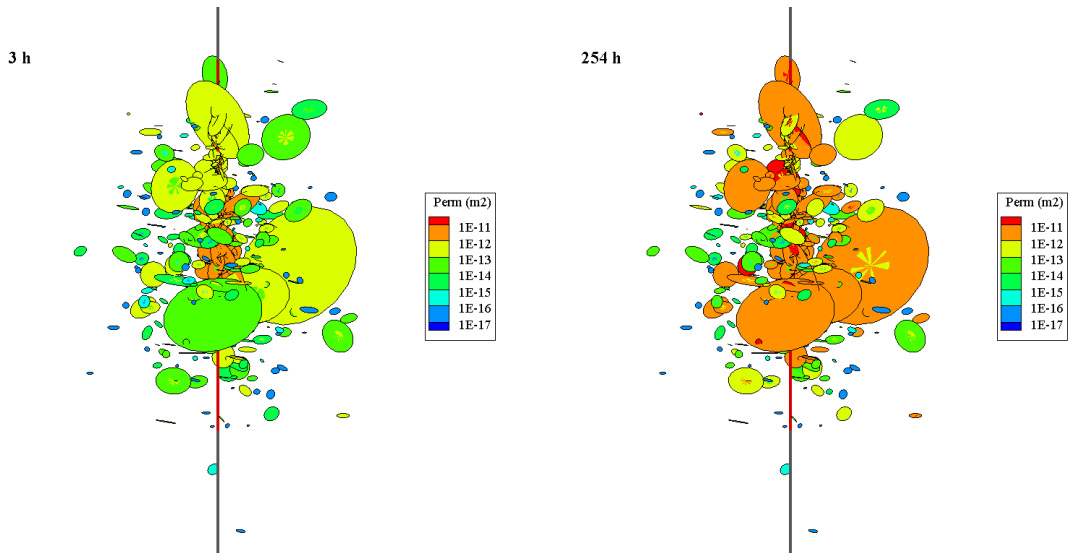


Figure 7.9. Fracture permeability evolution after 3 hrs injection (left) and 254 hrs injection (right) shows the permeability of most of the fractures is improved during injection.

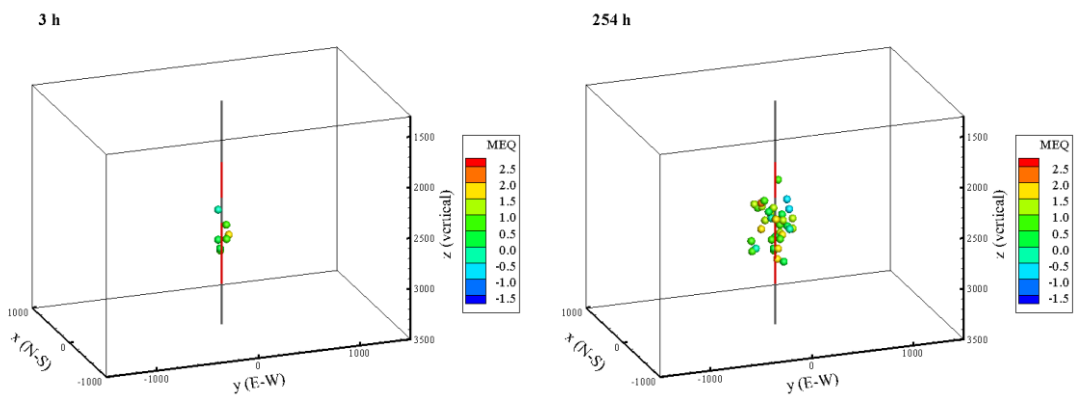


Figure 7.10. Injection induced MEQs evolution after 3 hrs injection (left) and 254 hrs injection (right) shows that MEQ events were induced as injection continued.

Three planar views of the MEQ locations are shown in Figure 7.11. It can be seen that most events are located near the openhole sections, within 200 m from the wellbore, and between the depths of 2000 m and 3000 m. It confirms that the near wellbore area has been successfully stimulated by water injection. Our simulation results are in good agreement with the field observations, even though we obtained fewer MEQ numbers due to the short simulation period ended on October 7. If the injection continues, more MEQs are expected to occur. It should be mentioned that our model assumes only one MEQ event is generated per fracture per slip while in reality a fracture could slip multiple times during stimulation and generate repeated MEQs. Therefore, our model could underestimate the total number of MEQs, which contributes to the discrepancy in the simulated and field observed MEQ numbers. It should also be mentioned that the lower magnitudes of the modeled MEQs compared to the field observed MEQs might be attributed to smaller fracture size distribution in the model. Since seismic moment is proportional to the area of a slipped fracture (Eqn. (4.63)), fracture size could be the limit of a seismic moment, hence, the magnitude of an induced MEQ. Further data mining in model input parameters is required to improve the match with the field data, since many parameters are difficult to quantify and each of them has large uncertainties.

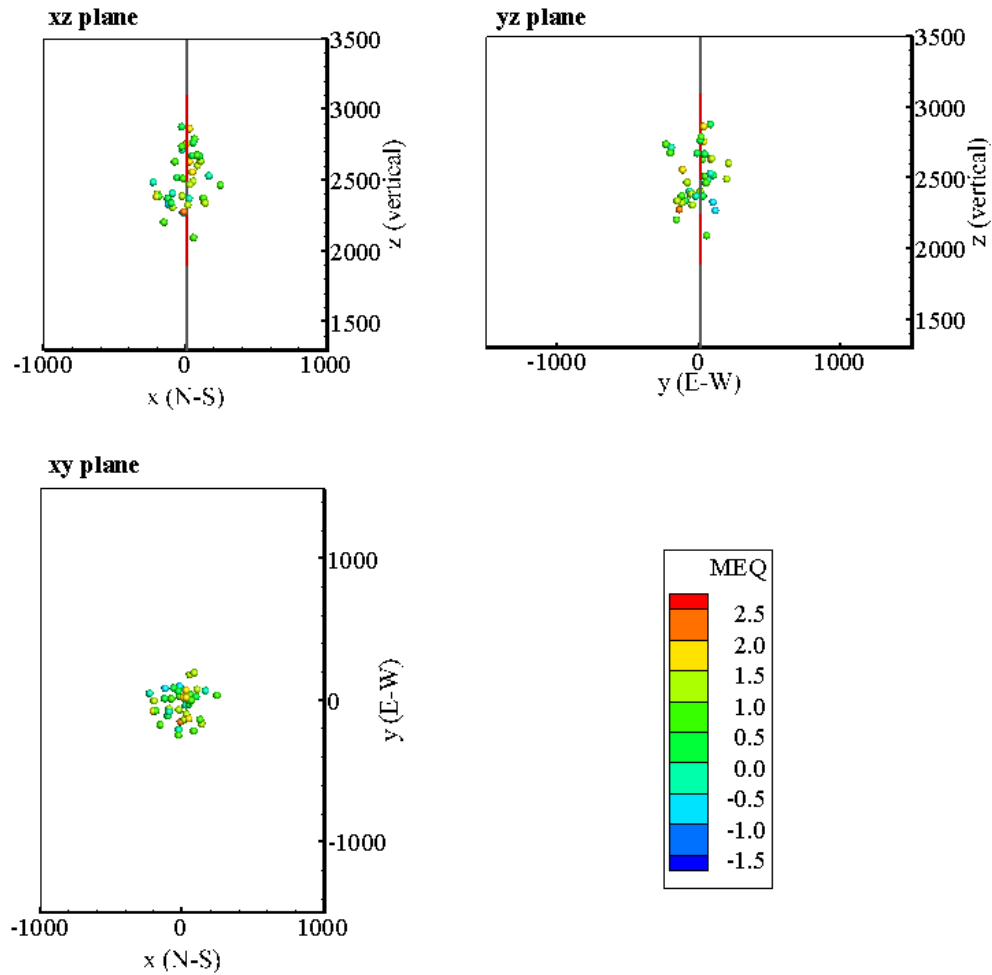


Figure 7.11. Location maps of 39 MEQs obtained in the preliminary simulation (from September 28 to October 7). The plane views show that the induced MEQs locate within 200 m radius from the wellbore, and are close to the depths of the injection intervals, which are in good agreement with the field observations.

The normal directions of the slipped fractures and the magnitudes of their corresponding MEQs after 254 hours of injection are plotted in Figure 7.12. As shown in the figure, the normals of slipped fractures fall into a certain range which indicates the significant influence of fracture orientation on the occurrence of fracture shear slippage and induced MEQs.



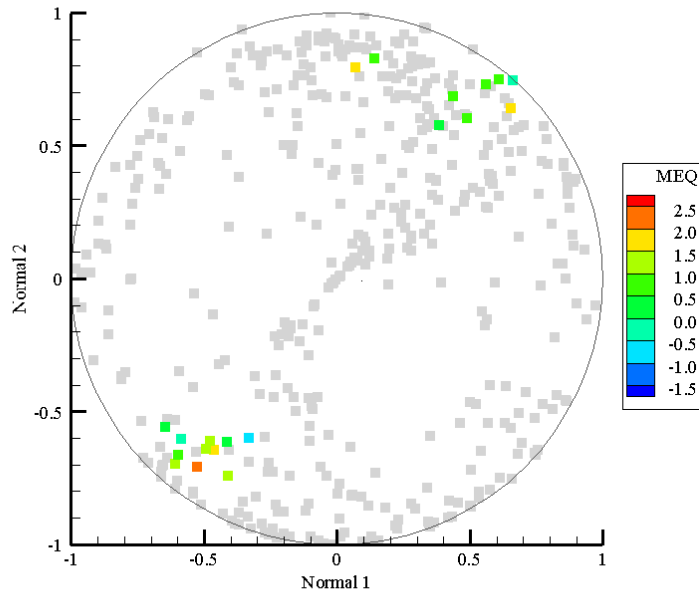


Figure 7.12. Normals to the fracture planes and the MEQ magnitudes of the slipped fractures (colored squares) after 254 hours injection. The fractures that did not slip are shown as blank squares.

During the simulation, the temperature change only occurred in the area near the injection wellbore. It is due to the low thermal conductivity and the short simulated time. As water was injected, the fractures directly connected with the injection intervals were cooled down, while the other fractures remain at their initial temperature following the temperature gradient in depth.

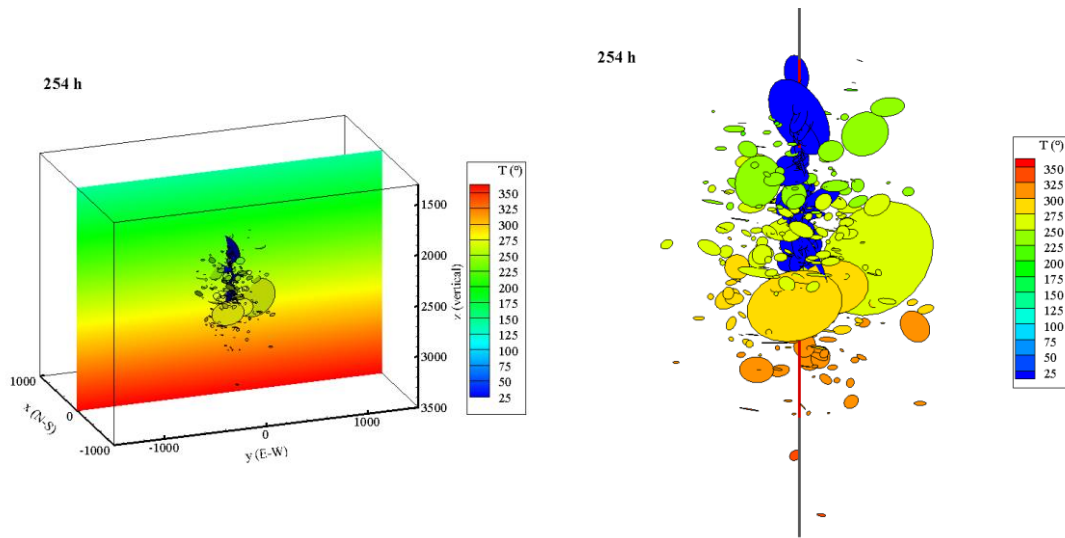


Figure 7.13. Left: distribution of temperature after 254 hours injection. Right: zoom in view of temperature distribution on fractures. Only the temperature of fractures around the injection well is reduced.

In this case, we also observed the rotation of the stress tensor and changes in stress regime around the injection well caused by water injection. At the beginning of this simulation, the stress regime in Newberry was understood to be one of normal faulting ( $S_v > S_{Hmax} > S_{hmin}$ ) with the maximum principal stress and the intermediate principal stresses being nearly equal ( $S_{Hmax} = 0.97S_v$ ) (AltaRock 2014). After injection, the maximum principal stress near the injection well rotated from vertical toward the horizontal direction and resulted in a strike-slip regime, as shown in Figure 7.14. The magnitude of the in-situ stress was also altered by injection. As pore pressure in the vicinity of the injection well is increased, excess compressive stress is generated due to poroelastic effects. In contrast, thermal induced stress due to cooling is tensile, which means a reduction from the in-situ compressive stress. The total stress is a combination of the contributions from both poroelastic and thermoelastic induced stresses (e.g., Ghassemi and Zhou, 2011; Rawal and Ghassemi, 2014).

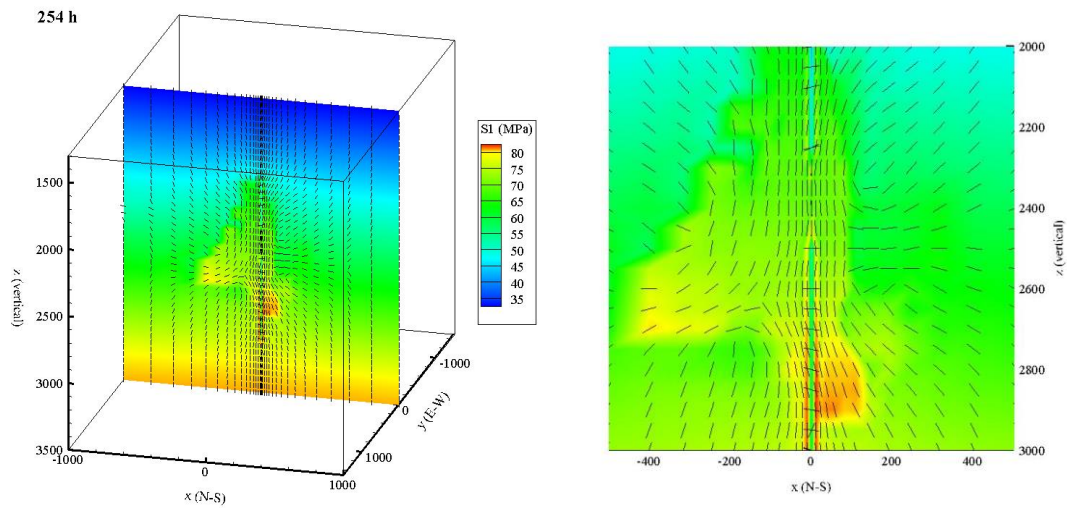


Figure 7.14. Distribution of the maximum principal stress and its vector after 254 hours injection (left: central slice in x-z plane; right: zoom in view of the area near injection intervals). The maximum principal stress near the injection well rotated from vertical toward the horizontal direction and resulted in a strike-slip regime.

Figure 7.15 is an example of the stress profile along a line in the x-z plane central slice ( $y=0$  m) at the middle depth of the injection interval ( $z=2500$  m). Due to the presence of the randomly distributed fractures and the varied injection pressure history, variations are seen in the stress profile. In the near wellbore region (from  $-500$  m to  $500$  m), excess compressive stresses due to pore fluid diffusion are observed, while at the wellbore, there is a reduction in the compressive stresses caused by cooling. Since in the simulation period, the temperature variation does not propagate a great distance, the reduction is only seen close to the wellbore. In this figure, two stress rotation regions are also seen, where the maximum horizontal stress ( $S_{Hmax}$ ) exceeds the vertical stress ( $S_v$ ), which means the maximum principal stress rotates  $90^\circ$  (e.g., Gao and Ghassemi, 2017; Kumar and Ghassemi, 2018).

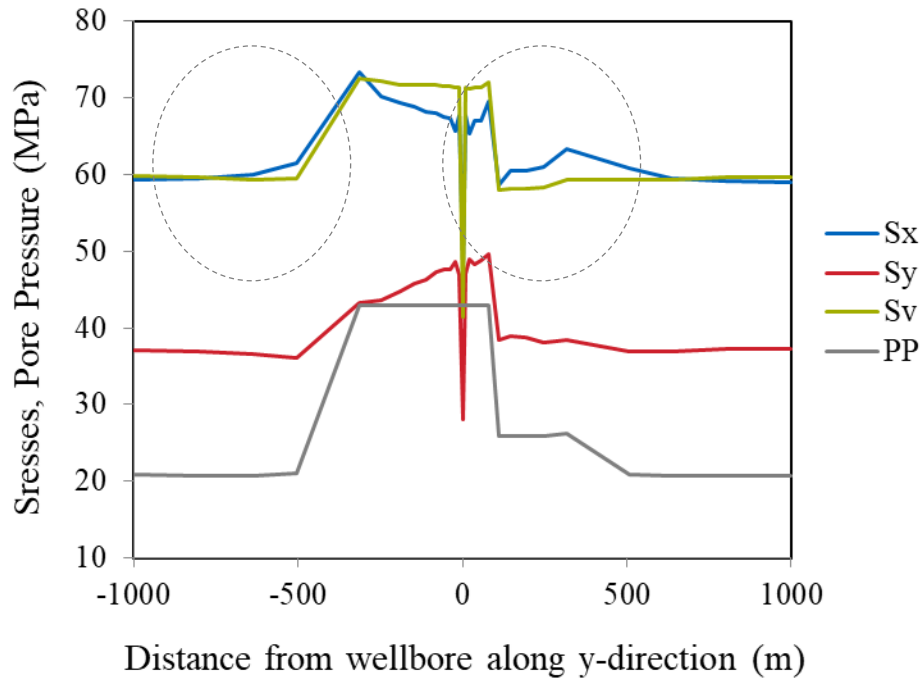


Figure 7.15. Stress profile along a line in the x-z plane central slice ( $y=0$  m) at the middle depth of the injection interval ( $z=2500$  m) after 254 hours injection. It shows two stress rotation regions (in grey dashed lines) where the maximum principal stress rotates from the initial vertical direction towards horizontal. Excess compressive stresses in the vicinity of injection well (-500 m to 500 m) is due to poroelastic stress induced by pore pressure increase. The compressive stress reduction at the wellbore is due to cooling induced tensile stress.

The operator of the Newberry EGS Stimulation project observed a discrepancy between the stress model derived during the stimulation and the model based on pre-stimulation data. The stress model derived from the stimulation seismic data shows horizontal compression and relatively weaker vertical stress, which is inconsistent with the local and regional stress field suggesting a vertical maximum principal stress (AltaRock 2014). After evaluating the contributions of four likely source of native stress (tectonic stress, local topographic stress, magmatic stress and

subduction zone stress) to the total stress field, they suggested that the most likely explanation for the discrepancy may be due to fluid injection and additional modeling of this phenomenon is required. Our modeling results successfully confirm that fluid injection could significantly modify the stress field adjacent to the well, in addition to merely raising pore fluid pressures. This reaffirms the need for investigating the effects of potential stress regime change under different stimulation scenarios on the long term production from the EGS reservoirs. Our numerical model provides an effective tool for predicting and evaluating the stimulation response of naturally fractured geothermal reservoirs.

#### 7.1.4 Summary

The simulation results of the Newberry EGS Phase 2.2 stimulation show good agreements with field observations. Increase in fracture permeability is captured, together with the injection induced microseismic events observed in the near wellbore area, which confirms that this stimulation successfully improved the hydraulic conductivities of the reservoir. A history matching of the injection rate was performed. Our modeling results suggest that the flow spikes occurred as the injection pressure increases in each stage may be due to fracture volume increase as a result of fracture opening. As stated in AltaRock's report for Phase 2.2 report, Newberry EGS demonstration, seismicity data "suggests that the fluid injection, with a wellhead pressure of about 20 MPa, is significantly modifying the stress field in addition to simply raising pore pressure fluid pressures". It was suggested that additional modeling of this phenomenon would be required to ascertain whether the stress field inferred from the seismicity is related to pore pressure perturbations. Our numerical simulations clearly show that the injection has indeed caused a rotation in the stress tensor around the injection well. The stress regime changes from the initial normal faulting to a strike-slip regime, which explains the discrepancy between the pre-stimulation stress model and

the stress model derived during the stimulation. Our simulation results confirm that fluid injection could not only raise pore fluid pressure, but also alter the stress field. It is of great importance to evaluate the potential stress change under different stimulation scenarios, since it could have significant effects on the long term production from the EGS reservoir. This model is useful in analyzing the behavior of naturally fractured reservoirs and could be used for evaluating future stimulation plans.

## **7.2 Oklahoma Wastewater Injection**

This section provides an application of the developed numerical model to the problem of wastewater injection. The wastewater injection in central Oklahoma was simulated and the response of the fault systems within the injection area was analyzed.

### **7.2.1 Background**

In the past several years, the central United States has seen a rapid increase in seismicity rates, as shown in Figure 7.16. In Oklahoma, increased seismic activity has been observed since 2009. The increased seismic activity is generally attributed to the disposal of wastewater coproduced along with oil and gas productions (e.g., Keranen et al. 2013; McGarr 2014; Walsh and Zoback 2015; Chen et al. 2017; Hincks et al. 2018). It can be seen from Figure 7.17 that the trend of the occurrence of earthquakes in Oklahoma correlates well with large volumes of wastewater disposal.

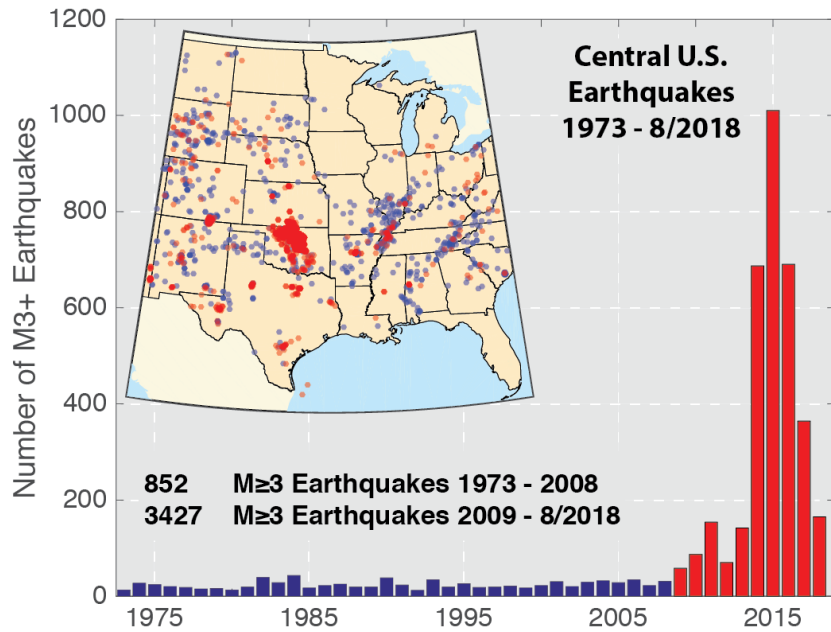


Figure 7.16. Increasing rate of earthquakes in the central United States beginning in 2009 (Rubinstein 2018).

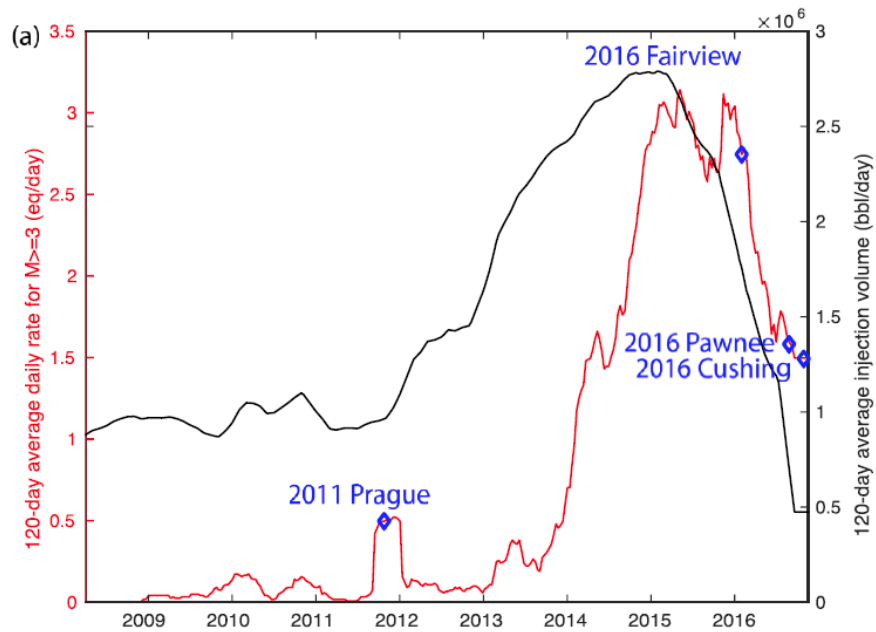


Figure 7.17. Relationship between wastewater injection and seismic activity in Oklahoma from 2008 to 2017 (Chen et al. 2017).

In Oklahoma, most of the wastewater (more than 50%) is injected via deep saltwater disposal wells (SWD) into the commonly under-pressured and relative permeable Arbuckle Group sedimentary rocks (Murray 2015), which lies directly on top of the Precambrian crystalline basement where most seismic events occurred (McNamara et al. 2015). These seismic events have been explained to be associated with slip on nearby faults due to active wastewater disposal in the vicinity (e.g., Keranen et al. 2013; Sumy et al. 2014; McGarr 2014). The mechanism of injection induced seismicity is generally explained by the classic Mohr-Coulomb failure criteria. When water is injected into a deep formation which has hydraulic communications with a nearby fault, the increased pore pressure could be transmitted to the fault zone and reduce the effective normal stress acting on the fault, thereby reducing the fault strength, inducing slip and seismicity.

The most significant earthquake sequences in Oklahoma include the 2011 Prague earthquake and the 2016 Pawnee earthquake. In November 2011, three large damaging earthquakes (>5.0 Mw) occurred near the town of Prague, Oklahoma, including a foreshock of Mw 5.0 on November 5, a main shock of Mw 5.7 on November 6 and an aftershock of Mw 5.0 on November 8 (Sumy et al. 2014). The Mw 5.7 main shock was the largest recorded earthquake in Oklahoma history, and this record was surpassed by the 2016 Pawnee earthquake occurred on September 3, 2016. The 2016 Mw 5.8 Pawnee earthquake was also the most powerful earthquake in the central and eastern United States over the past 70 years (Yeck et al. 2017). The Mw 5.0 and greater large earthquakes also include the 2016 Mw 5.1 Fairview earthquake occurred on February 13 and the 2016 Mw 5.0 Cushing earthquake occurred on November 7.

As large injection related earthquakes would lead to significant seismic risks including building damages and people injuries, public concern about wastewater disposal is growing. It is of great importance to improve the current understanding of the interactions between wastewater injection



and induced seismicity. However, despite numerous studies have been carried out focusing on this topic in recent years, most of these studies rely on several simplifying assumptions. The fluid flow is commonly solved analytically using a 2D radial flow model (e.g., Norbeck 2016), without considering the heterogeneity in the lithologic properties and the variations in the stress field (e.g., Walsh et al. 2017). The interaction between multiple injection wells and the detailed real injection history are ignored, and the pore pressure change is simplified calculated by linearly superposing each well (e.g. Walsh et al. 2017). Furthermore, many of the existing models do not have the capability to predict the seismic magnitude of the potentially induced earthquakes (e.g., Carrell 2014; Walsh and Zoback 2016) and do not account for the dynamic friction evolution during a seismic event (e.g. Walsh et al. 2017).

The objective of this study is to develop a robust numerical model that could integrate the fully coupled reservoir fluid flow model with a geomechanical model for natural fracture network and an earthquake simulation model within a rate-and-state friction framework for simulating the response of central Oklahoma fault systems to water injection. We are also trying to identify the possible correlations between fluid injection and the induced earthquakes and seeking to optimize fluid injection strategy to reduce the risk of slip on nearby faults.

### 7.2.2 Study Area

The study area selected for modeling wastewater injection into the central Oklahoma subsurface is located in the northeast Oklahoma, extents northern Pottawatomie County, eastern and southern Lincoln County. Selection of this area is based on the increased seismicity in this area and the increased SWD injection volumes in the 2000 to 2011 timeframe. This area is approximately 20 km by 20 km, encompassed approximately 400 square kilometers (shown by the yellow rectangle

in Figure 7.18). The latitudes range from 35.41°N to 35.59°N, and the longitudes range from 96.93°W to 96.69°W.

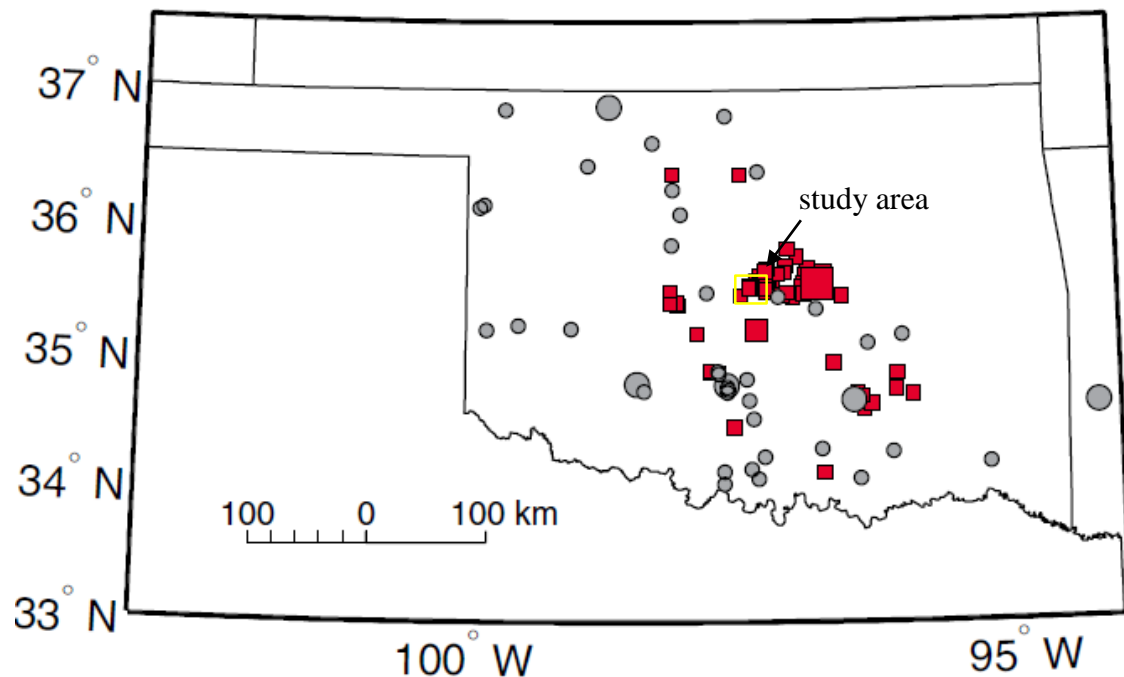


Figure 7.18. Location of the study area (shown in the yellow box). Oklahoma  $M_L \geq 3$  seismic events from the USGS PDE catalog. Events from 1975 to 2008 are shown by grey circles, and events from 2009 to 2011 are shown by red squares. Marker size indicates seismic magnitude. (modified from Llenos and Michael 2013).

Within this selected study area, two major fault systems present: the Wilzetta fault zone (WFZ) and the Meeker-Prague fault (MPF). The Wilzetta fault zone is a relatively long, narrow zone of high angle normal, strike-slip, and reverse faults (Dycus 2013). The Wilzetta fault is a complex Pennsylvanian-age fault system about 124 miles in length (Keranen et al. 2013), which includes a prominent structure feature of the Cherokee Platform and a member of a series of sub-parallel subsurface faults in the region (Dycus 2013). The Wilzetta fault is a vertical or near vertical fault, with a main trace trending approximately N25°-30°E. In some cases, it is truncated by a series of

faults trending  $\sim N55^{\circ}-60^{\circ}E$  (Dycus 2013). The Meeker-Prague fault extends for about 10.8 miles and strikes approximately  $N55^{\circ}E$ . It obliquely intersects the main trace of the Wilzetta fault. The included angle between these two faults is approximately  $30^{\circ}$  (Dycus 2013).

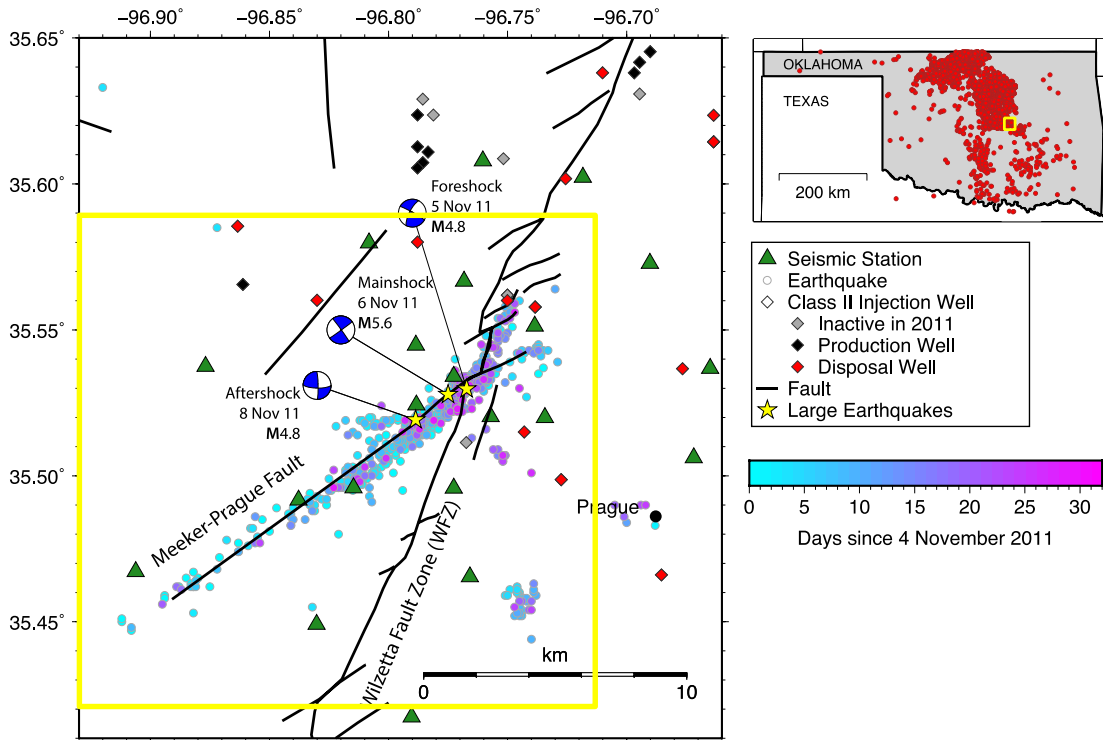


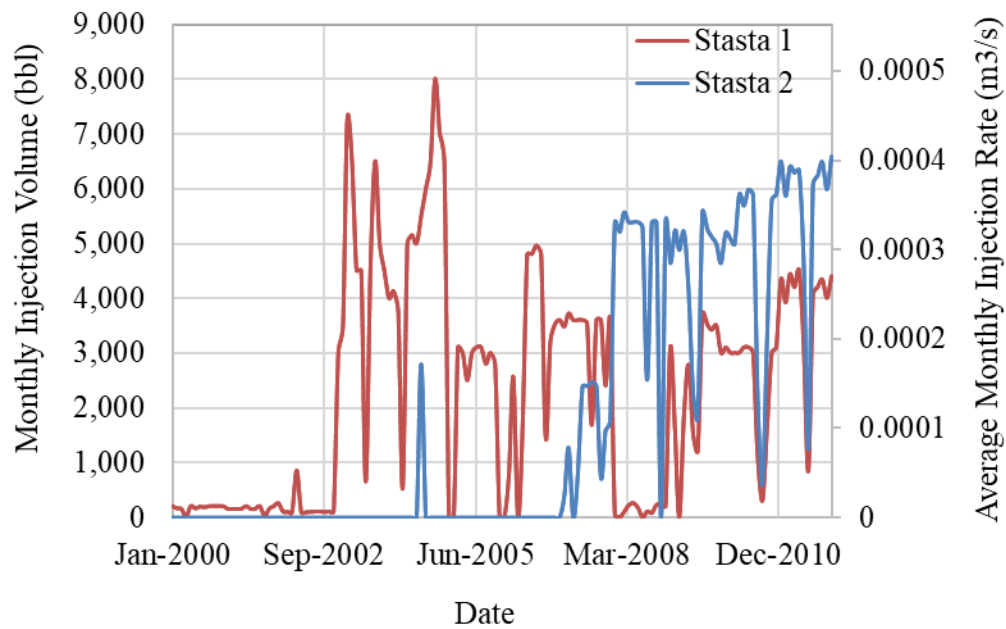
Figure 7.19. Two major fault systems within the study area: the WFZ trending  $\sim N25-30^{\circ}E$  and the MPF trending  $\sim N55^{\circ}E$  (modified from McMahon et al. 2016).

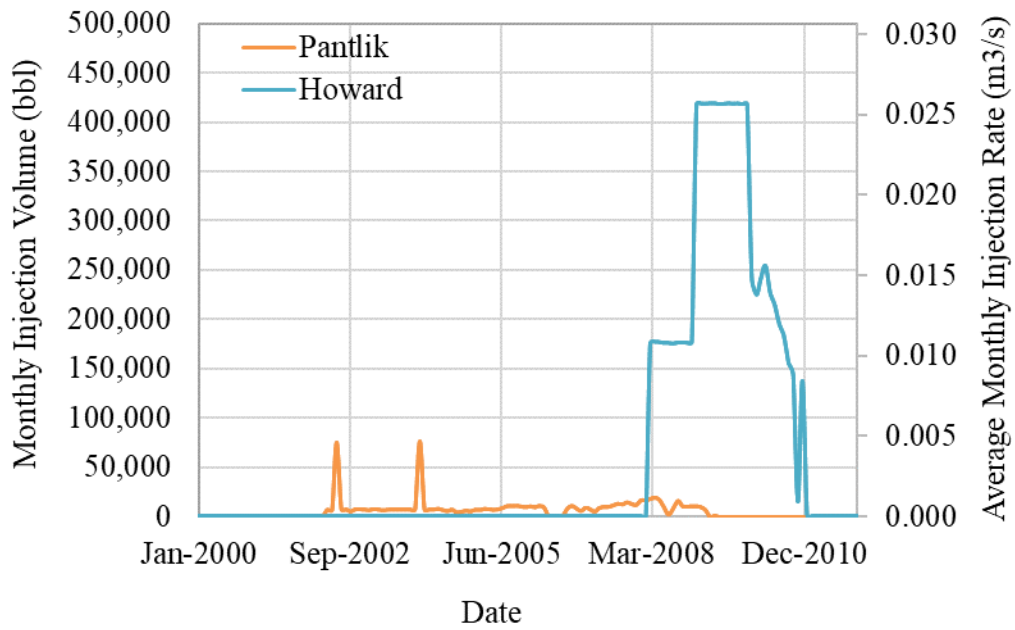
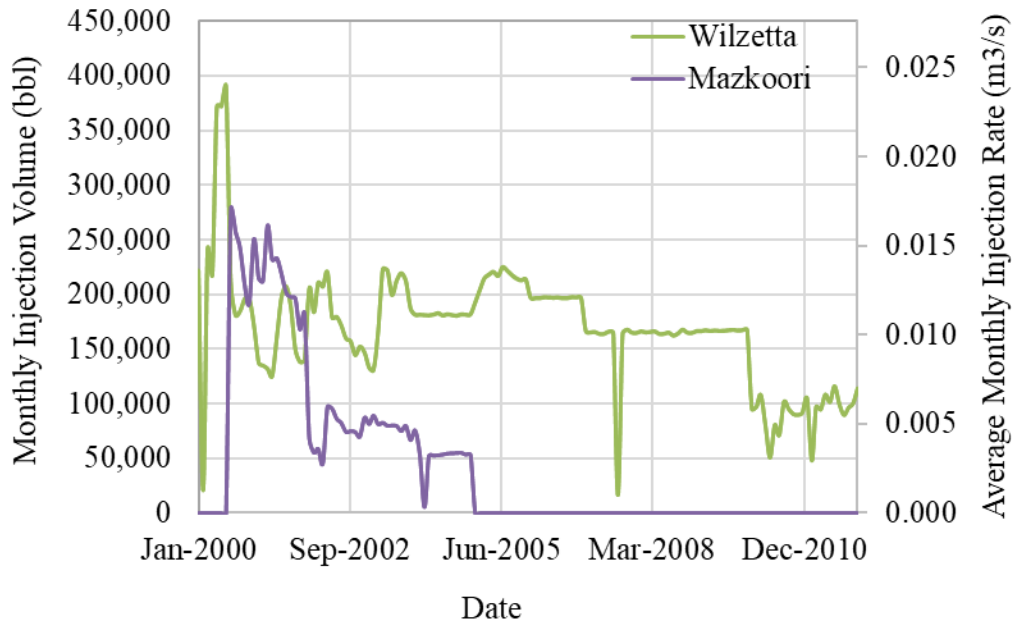
Between 2000 and 2011, there are eight active SWD wells injecting large volumes of wastewater into this area: Stasta 1, Stasta 2, Wilzetta, Mazkoori, Pantlik, Turner, Jesse and Howard. Well information such as location, injection volume, and duration of injection are obtained from the reported data by Oklahoma Geological Survey (OGS) (<http://www.ou.edu/ogs/data>) and Oklahoma Corporation Commission database (<http://www.occeweb.com/og/ogdatafiles2.htm>). Figure 7.20 summarizes the monthly reported injected volumes recorded in well reports. For each

well, the monthly average injection rate is calculated. The average injection rate varies in these wells, and the highest rate is approximately 0.036 m<sup>3</sup>/s (600,000 bbl/month).

Table 7.3 Overview of the SWD injection wells

Well Name	Latitude	Longitude	Injection Start Year	2000-2011 Total Injection Volume (10 <sup>6</sup> m <sup>3</sup> )
Stasta 1	35.560	-96.750	1993	0.052
Stasta 2	35.562	-96.750	1993	0.058
Pantlik	35.501	-96.725	2009	0.138
Wilzetta	35.558	-96.738	1999	3.850
Mazkoori	35.541	-96.751	2000	0.986
Jesse	35.426	-96.701	2003	2.326
Turner	35.442	-96.726	2004	2.568
Howard	35.421	-96.754	2008	1.435





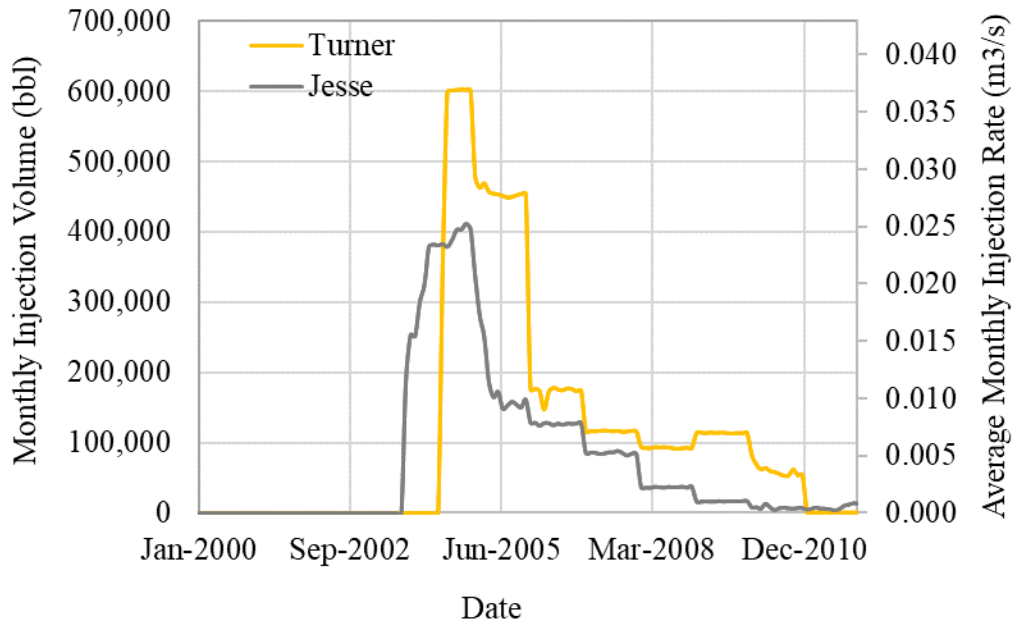


Figure 7.20. Injection profiles of the 8 SWD wells between 2000 to 2011. Monthly injection volume data from Oklahoma Corporation Commission (OCC) database. Monthly average injection rate is calculated accordingly.

### 7.2.3 Model Setup

This study aims to build a conceptual numerical model for evaluating the effect of water injection on pore pressure and stress changes within the central Oklahoma region and its consequential influence on the potential of the induced seismicity.

The dimension of this model is approximately 20 km x 20 km x 1 km. It extends from 708222.5 m to 728400.7 m (96.93°W to 96.69°W) in the E-W (x direction), from 46332.98 m to 65976.26 m (35.41°N to 35.59°N) in the N-S (y direction), and from 2000 m to 3000 m in the vertical direction. As shown in Figure 7.21, the model domain consists of two layers: the Arbuckle Group sedimentary rocks (2000 m to 2600 m) and the Precambrian crystalline basement (2600 m to 2800 m). The domain is discretized into 400,000 brick elements using a uniform element size of 100 m

x 100 m x 126 m. The input parameters of this model are taken from previous geological and geomechanical studies on this area, and are listed in Table 7.4.

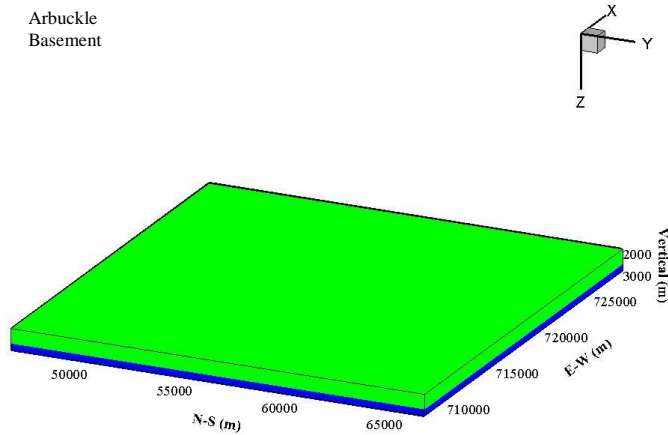


Figure 7.21. Numerical model consists of two layers: the Arbuckle group (2000 m to 2600 m, shown in green) and the basement (2600 m to 3000 m, shown in blue).

Table 7.4 Input parameters in the model

Rock Properties	
Young's Modulus	65 GPa
Drained Poisson's Ratio	0.22
Undrained Poisson's Ratio	0.46
Biot's Coefficient	0.97
Horizontal Permeability of Arbuckle	1E-12 m <sup>2</sup>
Vertical Permeability of Arbuckle	5E-13 m <sup>2</sup>
Permeability of Basement	1E-18 m <sup>2</sup>
Porosity of Arbuckle	0.15
Porosity of Basement	0.10
Rock Density	2550 kg/m <sup>3</sup>
Fracture Properties	
Number of Fractures	510
Fracture Radius	0 m ~ 400 m

Mean of Fracture Radii (Log EX)	4.8
Standard Deviation of Fracture Radii (Log SD)	0.4
Size-aperture Coefficient	0.0004
Basic Friction Angle	0.61
Shear Dilatation Angle	0.0353
90% Closure Stress	20 MPa
Characteristic Slip Distance	2E-5 m
Direct Effect Parameter	0.011
Evolution Effect Parameter	0.015
Reference Sliding Velocity	1E-12 m/s
Fluid Properties	
Fluid Density	1000 kg/m <sup>3</sup>
Fluid viscosity	3E-4 Pa·s
Fluid Bulk Modulus	2.235 GPa
Fluid Compressibility	4.475E-5 Pa <sup>-1</sup>
Stress State	
Maximum Horizontal Stress	79 MPa
Minimum Horizontal Stress	39 MPa
Vertical Stress	65 MPa
Initial and Boundary Conditions	
Initial Pore Pressure	24.2 MPa
Injection Rate	follows well history

The Arbuckle Group is the primary target of wastewater disposal in Oklahoma. According to OCC, from 2009 to 2014, the Arbuckle zone SWD volumes comprised 51% to 68% of the statewide total volume (Morgan and Murray 2015). Since wastewater injection is practically intensive within the Arbuckle group in comparison with other formations, only the Arbuckle group is considered in this model, and the presence of other overburden formation layers is considered only through their contributions to the vertical stress.

Subsurface geology data show that the Arbuckle group has a formation top located between 1800 m to 2200 m depth from the subsurface (Keranen et al. 2013), and has a variable thickness of 600



m to 2750 m (Faith et al. 2010). A uniform thickness of the modeled Arbuckle layer is set to be 600 m, based on an estimated average thickness of 1900 ft (579 m) from the “WFZ Basement” cross-section study (Dycus 2013). This selection of layer thickness is consistent with the previous studies (Barbour et al. 2017). The reported permeability of the Arbuckle group has a wide range from 0.1 mD to 17000 mD, and the mean large-scale permeability measured from drill-stem tests is 797 mD ( $7.91 \times 10^{-13} \text{ m}^2$ ) (Carrell 2014). Previous studies also indicate that Arbuckle is highly heterogeneous and anisotropic (Carrell 2014; Morgan and Murray 2015). In this conceptual model, we assume the horizontal permeability is  $1 \times 10^{-12} \text{ m}^2$  (10 mD), and the anisotropy ratio of the vertical permeability to horizontal permeability is 0.5, which has been suggested as a textbook anisotropy ratio for the Arbuckle formation (Domenico and Schwartz 1990; Carrell 2014). The reported Arbuckle porosity ranges from 3% to 40% with a representative mean value of 15% (Rahi and Halihan 2009; Carrell 2014). The rock mechanical properties of the Arbuckle layer rocks are taken from the geomechanical characterization on outcrop samples (Yu and Ghassemi 2017), as summarized in Table 7.4.

Below the Arbuckle group is the igneous Precambrian age basement rock, which is the location of the majority of earthquakes in north-central Oklahoma. The thickness of the basement ranges from about 2600 m to more than 3500 m (Devegowda 2016). Recent seismicity occurred in the basement is mostly confined to a depth between 2000 m to 5000 m depth (Dycus 2013). However, in order to reduce the numerical cost, the basement to a depth of 3000 m is included in our current model. The basement matrix has a very low permeability on the order of  $10^{-15} \sim 10^{-18} \text{ m}^2$  and a low porosity of 10% ~ 15% (Morgan et al. 2015). In this model, the permeability and porosity for the basement matrix is set to be  $10^{-18} \text{ m}^2$  and 10%, respectively. Same rock mechanical properties as in the Arbuckle group are used for the basement layer.

To represent the highly faulted and fractured nature of this region, a natural fracture network is generated based on fault characterization data. We assume all fractures are in the basement, and no fractures in the Arbuckle formation (Devegowda 2016). Due to the lack of detailed fracture distribution data such as fracture density, size, location and orientation, the following assumptions are made: (1) the fractures are penny-shaped; (2) fracture centers are located along the fault traces and stochastically distributed within the fault line; (3) fracture depth varies within the entire thickness of the basement layer, from 2600 m to 3000 m; (4) the orientations of these fractures follow the fault trends ( $\pm 5^\circ$ ); (5) fracture length ranges between 0 to 400 m, which is estimated from the magnitudes of the 110 best quality events recorded in 2011 (Holland 2015) using a well-known empirical earthquake magnitude-scaling relationship (Wells and Coppersmith 1994), i.e.,  $\log(\text{length}) = -2.44 + 0.59\text{Mag}$ . A total of 510 fractures are generated, as shown in Figure 7.22. Though this fracture network may not reflect the actual fractured conditions in the subsurface, it allows us to evaluate the injection response at different locations on the fault systems efficiently. In this conceptual model, a rate-and-state friction model is used for describing friction evolution. The RSF frictional properties of the fractures are taken from previous studies on the frictional faulting response in Oklahoma earthquake sequence (Norbeck and Horne 2016). The direct effect parameter and the evolution effect parameter are prescribed to be 0.011 and 0.015, respectively. The reference sliding velocity is assumed to be 1E-12 m/s, and the characteristic slip distance is assumed to be 2E-5 m.

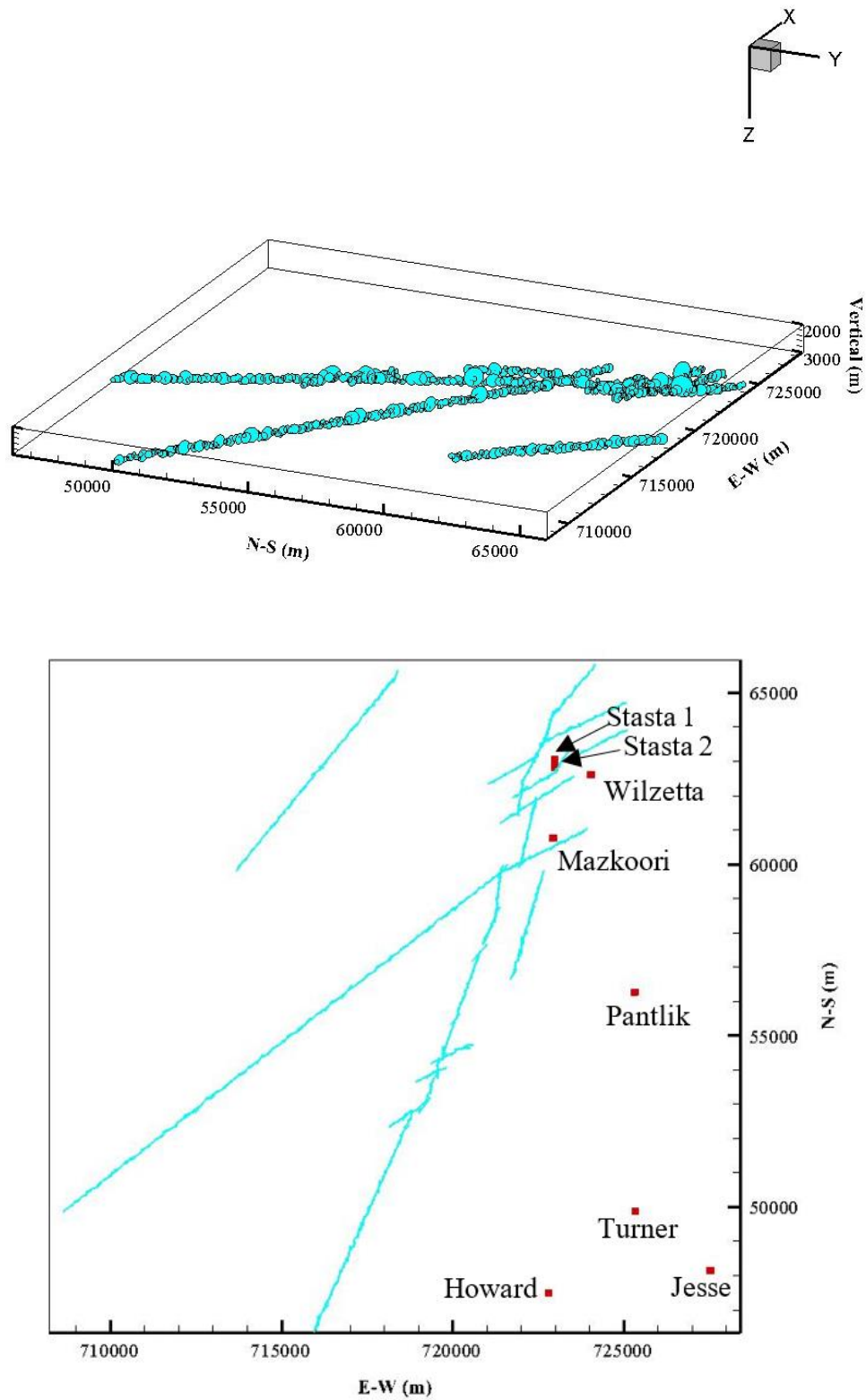


Figure 7.22. Fracture network modeled in the basement: 3D view (top) and 2D view (bottom). The injection wells are shown in red squares.

The regional stress state in central Oklahoma is characterized primarily by strike-slip, with the maximum horizontal stress oriented approximately N85°E (Alt and Zoback 2014). Under this condition, the vertical stress represents the intermediate principal stress. The stress gradients of the maximum ( $S_{Hmax}$ ) and the minimum horizontal stresses ( $S_{Hmin}$ ) are estimated to be 30 MPa/km and 15 MPa/km, respectively, and the vertical stress ( $S_v$ ) gradient is estimated to be 25 MPa/km (Norbeck et al. 2016). The Arbuckle group is predominantly underpressured (Carrell 2014; Morgan and Murray 2015), and has an equivalent fluid pressure gradient less than the hydrostatic gradient for saltwater (0.465 psi/ft or 10.3 MPa/km), which is assumed to be 9.3 MPa/km. Considering the low thermal conductivity of the rock matrix and the small convective heat transfer within the matrix via fluid flow through pores, temperature front would not propagate a long distance from the injection wells to reach the faults that located a few kilometers away. Therefore, thermal effects are currently ignored in this large size model to keep the numerical cost at a manageable level.

On the top boundary of this model, which is the upper surface of the Arbuckle layer, the load from the weight of the overburden formations is applied. The side boundaries are modeled as no flow boundary. Gravity is also considered by applying a gravitational load to the entire model. Zero normal displacement is applied on the bottom and side boundaries, and an unconstrained free boundary is assumed for the top. After applying the initial and boundary conditions, an initialization step is performed to ensure the model is in equilibrium before injection is modeled. This initialization results in a vertical compaction less than 1 m at the top surface, which is negligible compared to the model thickness of 1000 m and is discarded.

The injection wells in the selected study area are modeled as vertical line source, and the injection interval on each well is assumed throughout the entire thickness of the Arbuckle (from 2000 m to

2600 m). The 12 years injection history between 2000 and 2011 is followed by specifying the average monthly injection rate on individual wells.

We simulate the 12 years water injection into the central Oklahoma region, monitor the changes of the pore pressure and stress fields in the domain, and evaluate the possibility of induced seismicity. It should be noted that due to the simplifications used in this conceptual model, the objective of this study is to better understand the response of the fault systems to injection, rather than to match the observations in the field. Both model setup and input data are subject to further revision and improvements.

#### 7.2.4 Results

To illustrate the perturbations in the pore pressure and stress fields caused by fluid injection, the simulation results are plotted for two selected depths, i.e., at the middle depth of the Arbuckle formation (2300 m) and at the middle depth of the basement (2800 m), and for four selected time steps, at the end of 2002, 2005, 2008 and 2011, i.e., after 3 years, 6 years, 9 years, and 12 years of injection.

Figure 7.23 shows the evolution of pore pressure within the Arbuckle formation (at the depth of 2300 m) during the 12 years. It is evident that fluid injection into this permeable formation increases the pore pressure in the area near the injection wells. It can also be seen from the figure that the distribution of the elevated pore pressure is dominated by the relative strength of the active injection sources. During the 12 years of injection, the maximum pressure increase at this depth is about 1.3 MPa, from the initial pore pressure of 21.4 MPa to 22.7 MPa.

The evolution of pore pressure within the basement is plotted in Figure 7.24, which shows that the fracture network in the basement is also pressurized as a result of fluid injection into the Arbuckle formation. It indicates that the fluid could migrate from the Arbuckle downwards into the basement

via the existing faults. As injection continues, higher pressure buildup is observed. After the 12 years of injection, the maximum pressure buildup within the fractures is approximately 1.0 MPa, with the pressure increased from the initial value of 26.1 MPa to 27.1 MPa. Slight pressure buildup is also observed near the well locations, which is due to the downward fluid migration from the injection wells into the basement rock matrix.

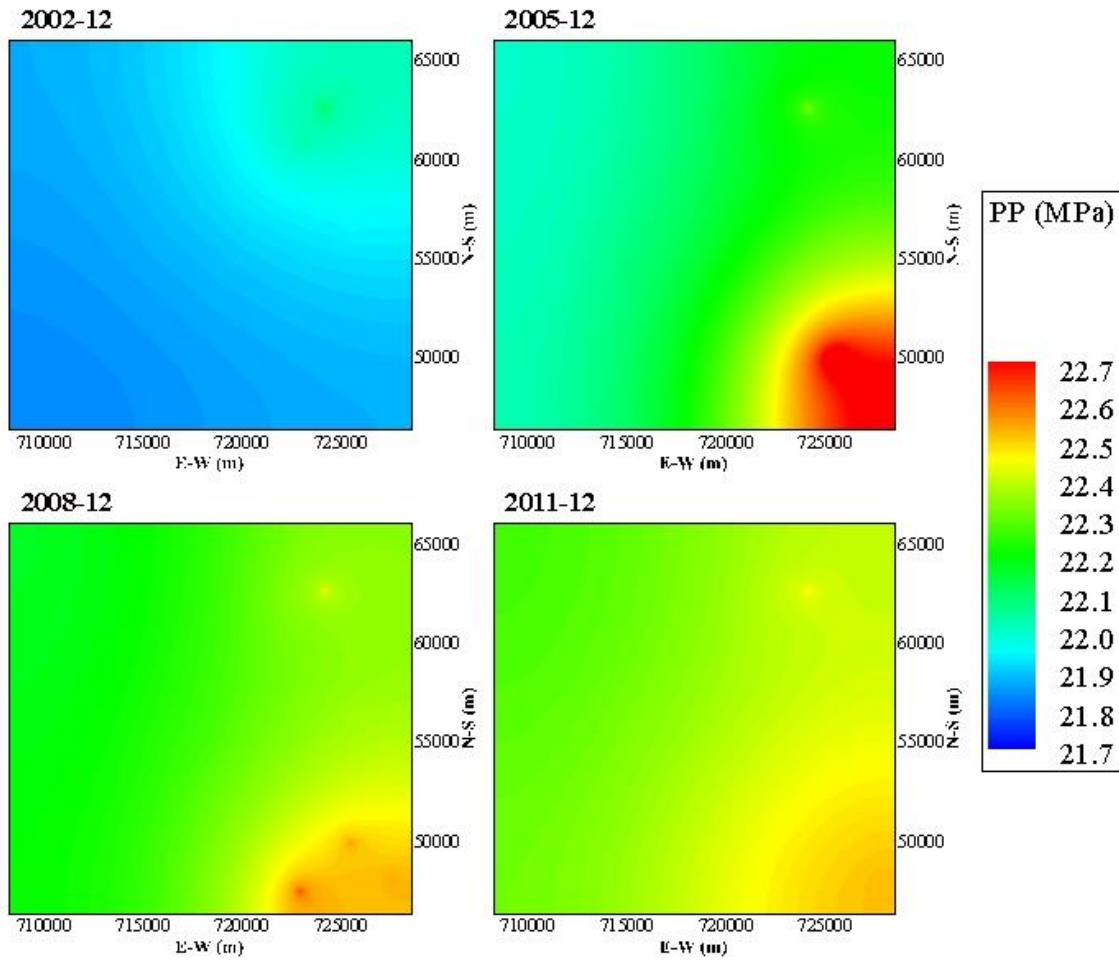


Figure 7.23. Pore pressure evolution at the middle depth of the Arbuckle formation (2D view, central slice:  $z=2300$  m).

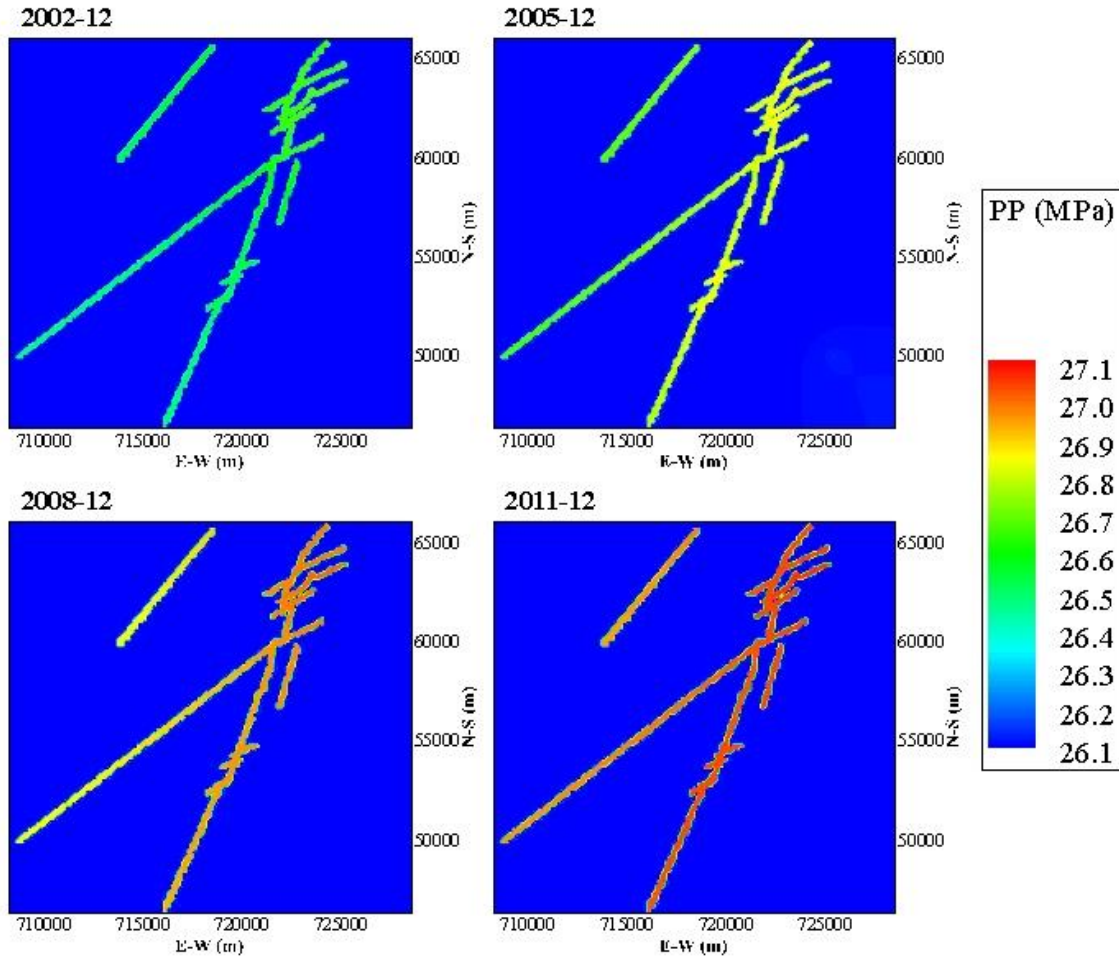


Figure 7.24. Pore pressure evolution at the middle depth of the basement (2D view, central slice:  $z=2800$  m).

In addition to changes in the pore pressure field, fluid injection also induces changes in the stress field. The total stress changes in the  $x$  (E-W) and  $y$  (N-S) directions within the Arbuckle formation at the middle depth of 2300 m and in the basement at the middle depth of 2800 m are shown in Figure 7.25. During injection, an increase in the compressive total stress is observed, which is due to the poroelastic coupling effects caused by pore pressure increase.

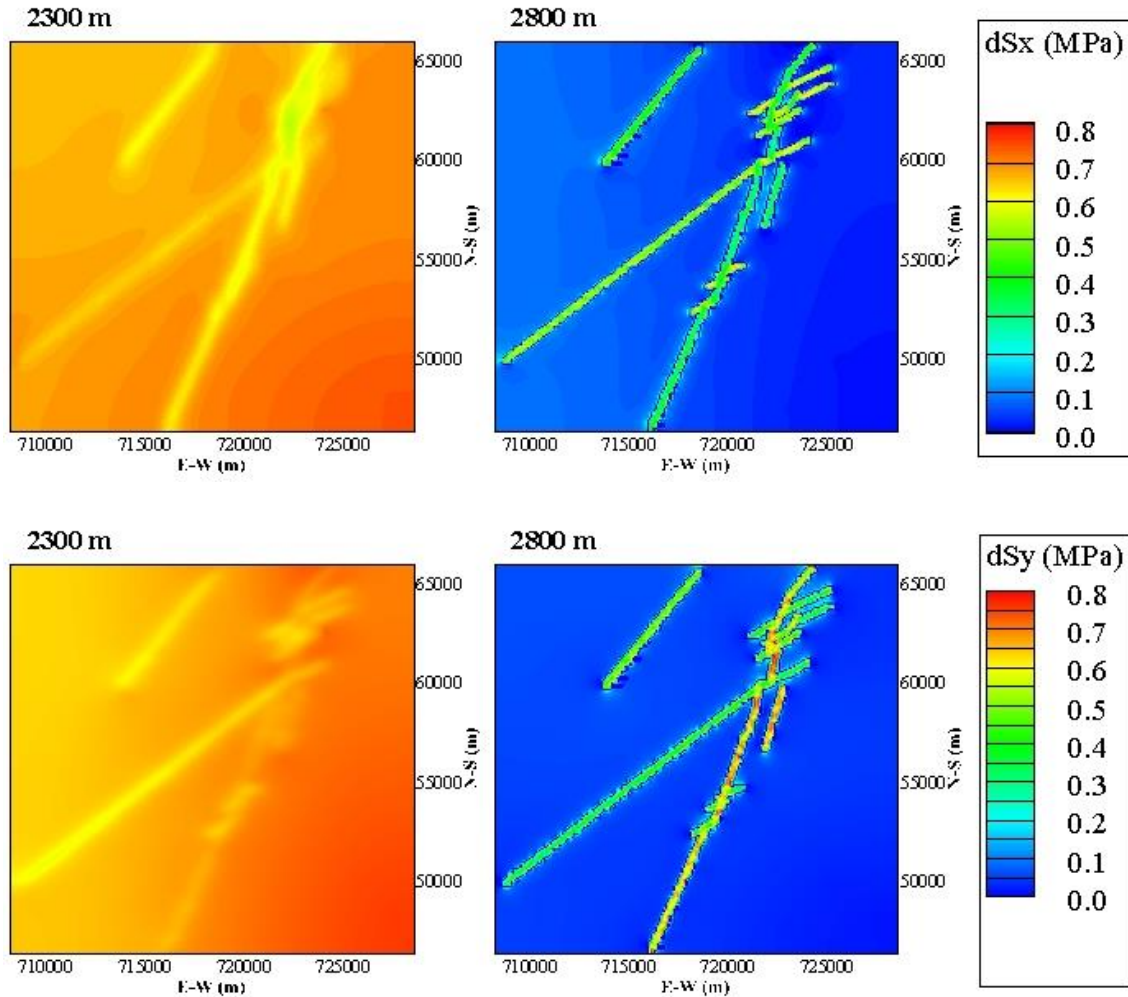


Figure 7.25. Change of the total stress after 12 years of injection at the middle depth of the Arbuckle formation (central slice:  $z=2300$  m) and at the middle depth of the basement (central slice:  $z=2800$  m). Top: total stress in the x direction ( $S_x$ ); bottom: total stress in the y direction ( $S_y$ ).

The changes in the effective stresses within the Arbuckle formation and the basement are shown in Figure 7.26, respectively. As expected, a reduction of the effective stresses components is observed in the areas affected by elevated pore pressure. It is clear from the definition of effective



stress that it is equal to the total stress minus the pore pressure. Due to the fact that during injection pore pressure is increasing more than the total stress, which leads to reducing the effective stress.

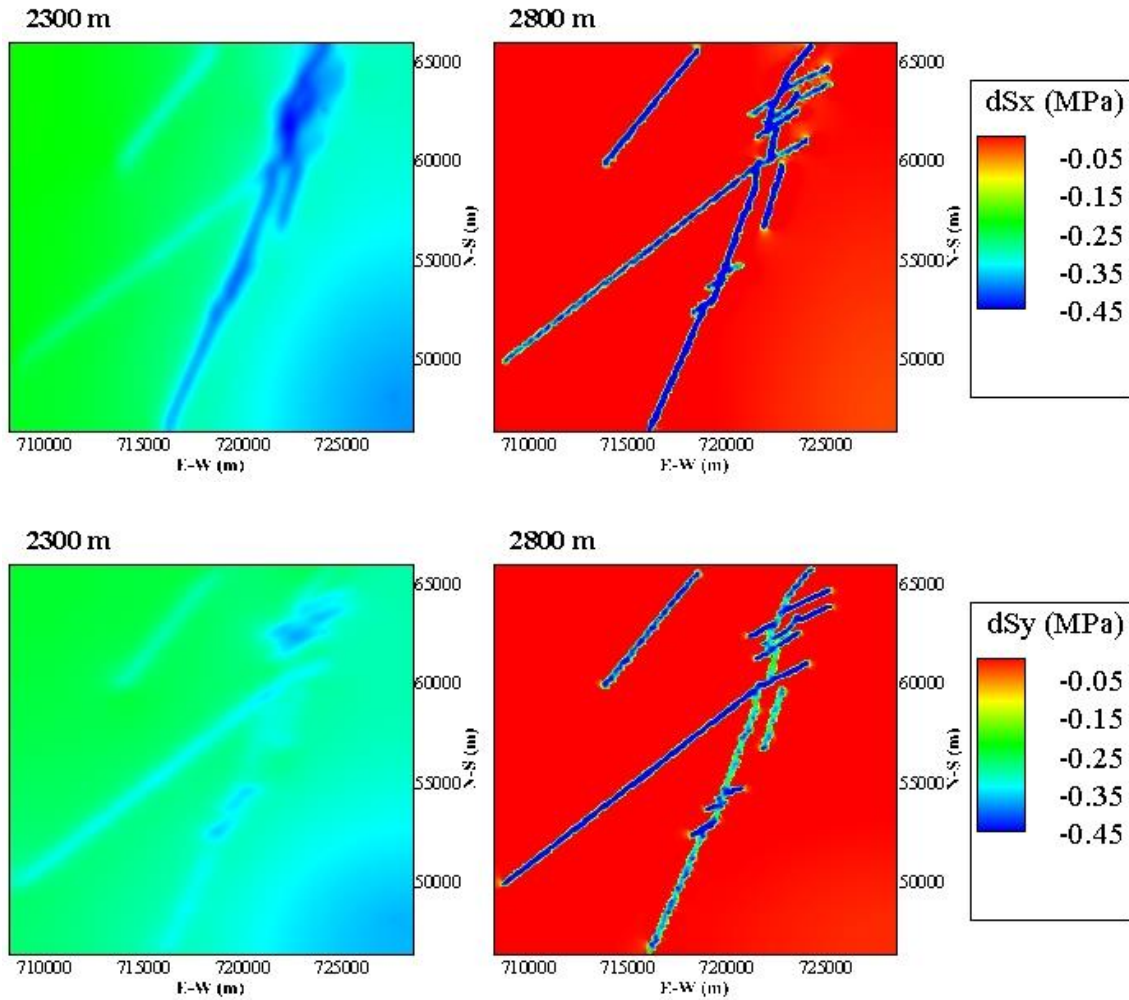


Figure 7.26. Change of the effective stress after 12 years of injection at the middle depth of the Arbuckle formation (central slice:  $z=2300$  m) and at the middle depth of the basement (central slice:  $z=2800$  m). Top: total stress in the x direction ( $S_x$ ); bottom: total stress in the y direction ( $S_y$ ).

The average pore pressure on a fracture could be approximated by averaging the elemental values of all elements intersected by the fracture. The 12 years evolution of pore pressure within the

fracture network is plotted in Figure 7.27. It clearly shows that as fluid injection continues, excess pressure is gradually built up in the fracture network, and higher pressure buildup occurs on fractures near the high volume injection wells. After 12 years of injection, the maximum pressure increase on fractures is about 1.0 MPa.

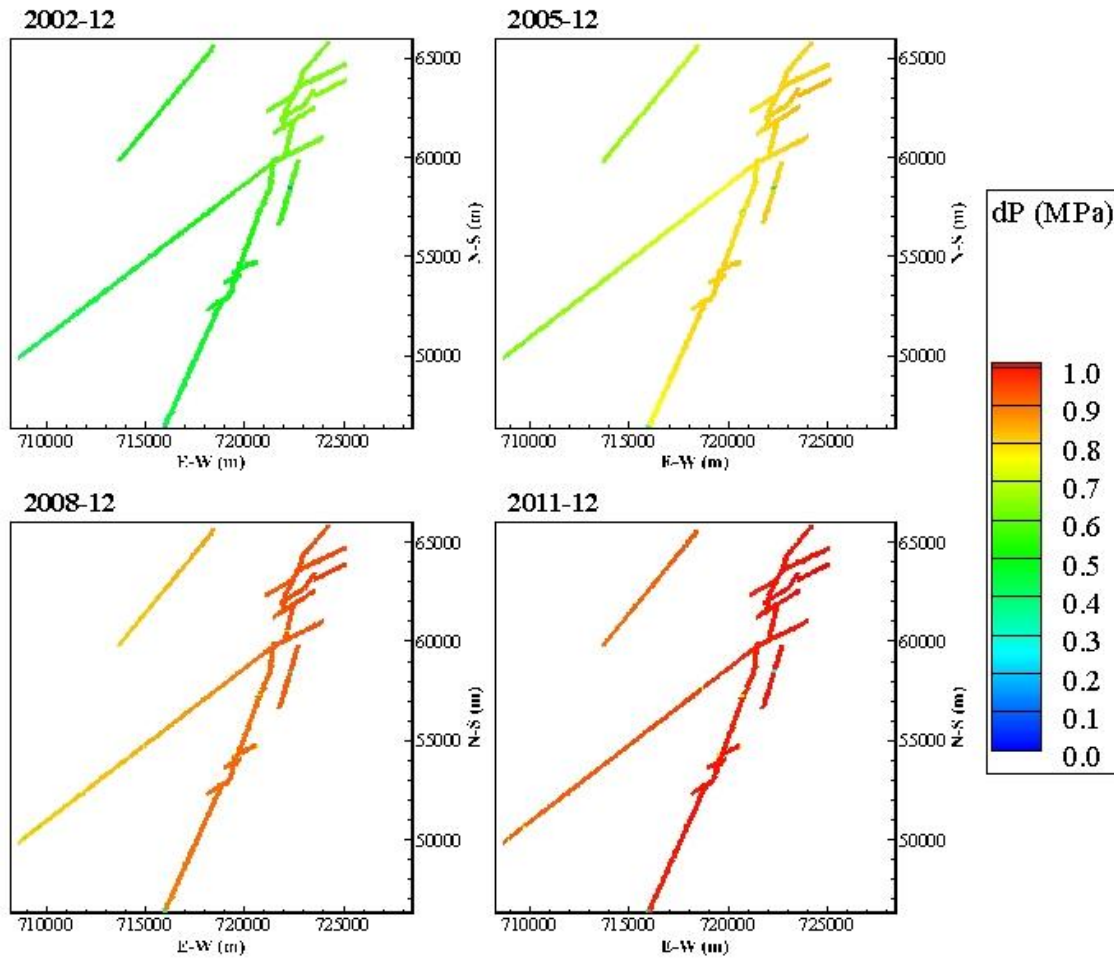


Figure 7.27. Pore pressure evolution within the fracture network (2D view). The injection wells are shown in red squares.

In this study, the frictional response of fractures is modeled within a RSF framework. Since a velocity weakening RSF model is assumed, during the injection process, reductions in friction coefficient are captured on a few fractures. As shown in Figure 7.28, after 12 years of injection,

the maximum reduction in friction coefficient is about 0.05. In addition to the poroelastic effects caused by injection, the weakening of fracture frictions also contributes to the slips and the associated seismicity.

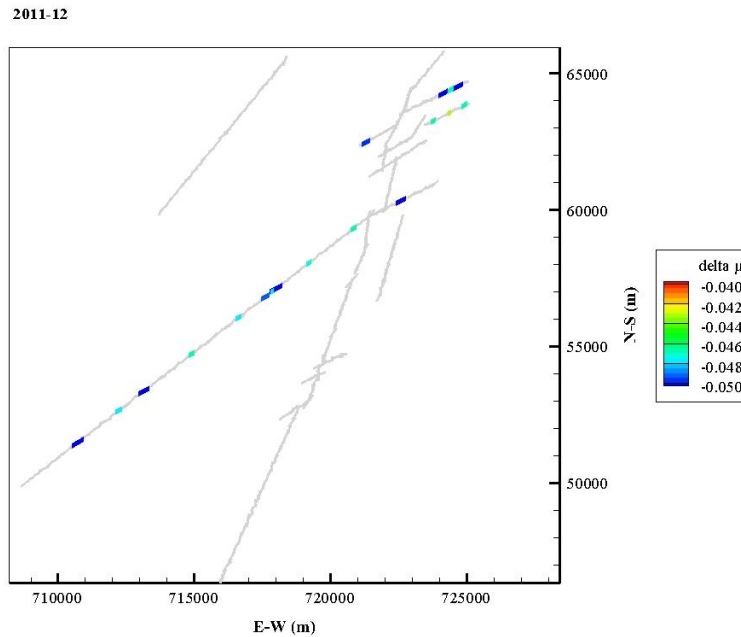


Figure 7.28. Friction coefficient reduction of fractures (2D view). A maximum reduction of 0.05 is observed on fractures.

Induced seismicity is recorded during this simulation, as illustrated in Figure 7.29. The seismic events are plotted using the colored spheres, with the colors and sizes indicating the magnitude of seismic events. After 3 years of injection, no seismic event is observed. As injection continues, at the end of 2005, 3 events occur near three high volume injection wells, Stasta 1, Stasta 2 and Wilzetta. After 9 years of injection, 15 seismic events occur. After 12 years of injection, a total of 18 seismic events is induced with a maximum event magnitude of 3.02. It could also be seen that seismic events could be induced by high volume injection wells as far as more than 10 km away.

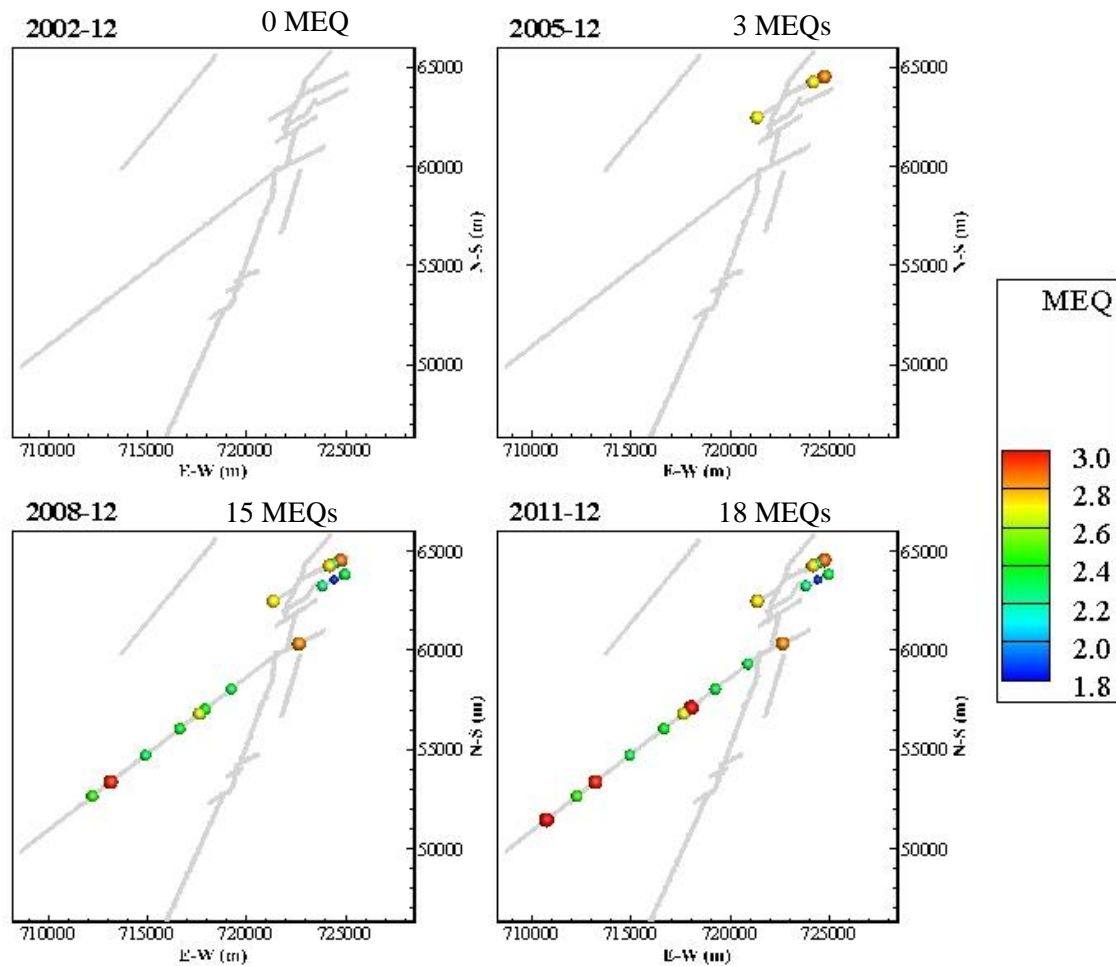


Figure 7.29. Distribution of the induced microseismic events (2D view). Most MEQs occur on the N55°E Meeker-Prague fault.

The predicted seismic events are in good agreements with the earthquake records in Oklahoma, which also shows a sudden increase in seismicity since 2008. It is also obvious from this figure that the predicted locations of induced seismicity are consistent with the field observations of MEQ distribution (Figure 7.19). Most MEQs occur on the Meeker-Prague fault striking N55°E, which is a major fault system with an orientation favorable to slip. As discussed in the previous chapter, the orientation of a fracture plays an important role in the determining the stresses acting on the fracture, and hence the occurrence of shear slippage and the induced seismicity. Even though the

Wilzetta fault is located closer to the injection wells, its orientation relative to the stress field is less favorable for shear slippage as a result of a small pore pressure perturbation.

The number of the predicted seismic events is several orders of magnitude less than the field observed number. As mentioned earlier, due to the lack of fracture distribution data, the objective of this conceptual model is to understand the mechanisms associated with water injection, rather than to exactly match the field observations. We also notice that the maximum magnitude of the simulation resulting MEQs is approximately  $M_w$  3.0, which is lower compared to the  $M_w$  5.7 Prague earthquake occurred on November 6, 2011. It may be due to the limit of fracture size assumed in this conceptual model. As seismic moment is proportional to the area of a slipped fracture, for a certain amount of slip displacement, the size of the fracture could be the limit of the seismic moment and magnitude. In the field, larger surface areas are available for rupture and generating larger earthquakes. For the  $M_w$  5.0 earthquake occurred on November 5, 2011, the estimated rupture size is 2.8 km long by 2.9 km deep. The estimated rupture size for the  $M_w$  5.7 earthquake on November 6 is estimated as large as 8.3 km long by 5.4 km deep (Norbeck and Horne 2016). These estimated rupture size are much larger than the fractures size used in this conceptual model. Future studies on fracture characterization are essential for refining the selection of the model inputs and hence improving the accuracy of seismic prediction.

#### 7.2.5 Discussions

To investigate the impacts of operational parameters on the potential of induced seismicity and to seek possible injection optimization strategies, we perform a series of numerical tests by varying the injection volume, injection rate and injection depth. We narrow down the study area to a small area with a size of 4 km by 4 km, and consider a single injection well. The geometry of the small area is shown in Figure 7.30. A total of 59 fractures present within this area, distributed along the

N55°E Meeker-Prague fault and the N30°E Wilzetta fault traces. Same as the large scale simulation presented in the previous section, two geological layers are modeled: the Arbuckle group from 2000 m to 2600 m, and the crystalline basement from 2600 m to 3000 m. All fractures are assumed within the basement. The model inputs are the same as listed in Table 7.4, except the injection parameters varied in the testing cases.

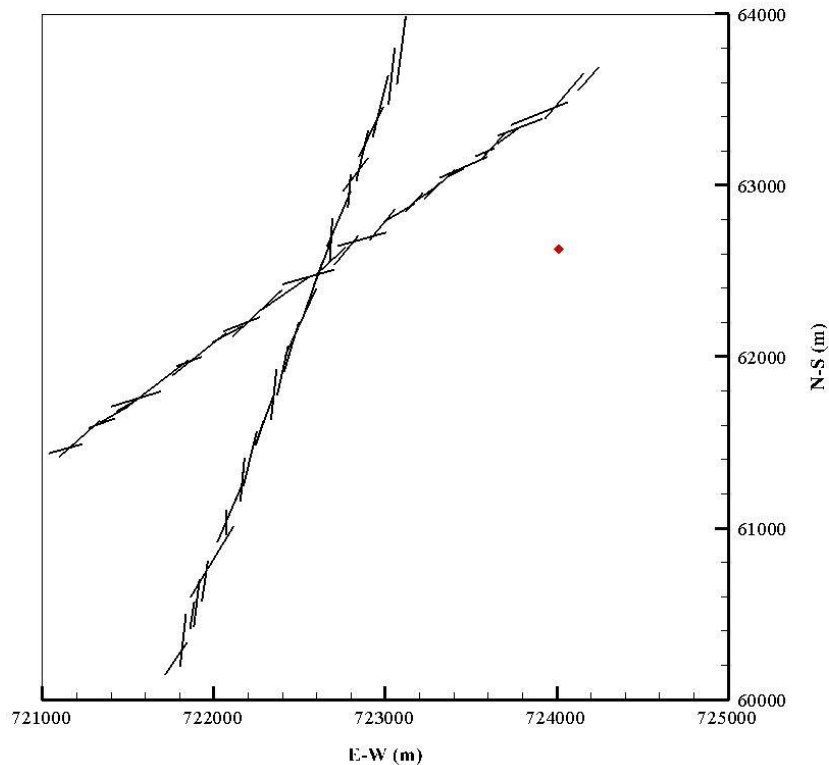


Figure 7.30. 2D view of the fracture network within the selected small area (4 km x 4 km). The injection well is shown in red square.

In the first series of tests, we consider a constant injection rate scheme, and run the model using three different values for injection rate:  $0.015 \text{ m}^3/\text{s}$ ,  $0.010 \text{ m}^3/\text{s}$  and  $0.005 \text{ m}^3/\text{s}$ , which corresponds to a monthly injection volume of approximately 240,000 bbl, 160,000 bbl and 80,000 bbl, respectively. The choice of the injection rates is based on the representative rates in two high

volume injection wells located in the vicinity of the faults, the Wilzetta well and the Mazkoori well. Figure 7.31 is example of the pore pressure distribution within the fracture network after injecting for 1 year using a constant rate of  $0.015 \text{ m}^3/\text{s}$ , along with the associated induced seismic events. As a result of injection into the permeable Arbuckle layer, the fractures in the basement are also pressurized. The resulting seismic events are distributed along the favorably oriented Meeker-Prague fault striking  $\text{N}55^\circ\text{E}$ , which is consistent with results of the large scale simulation.

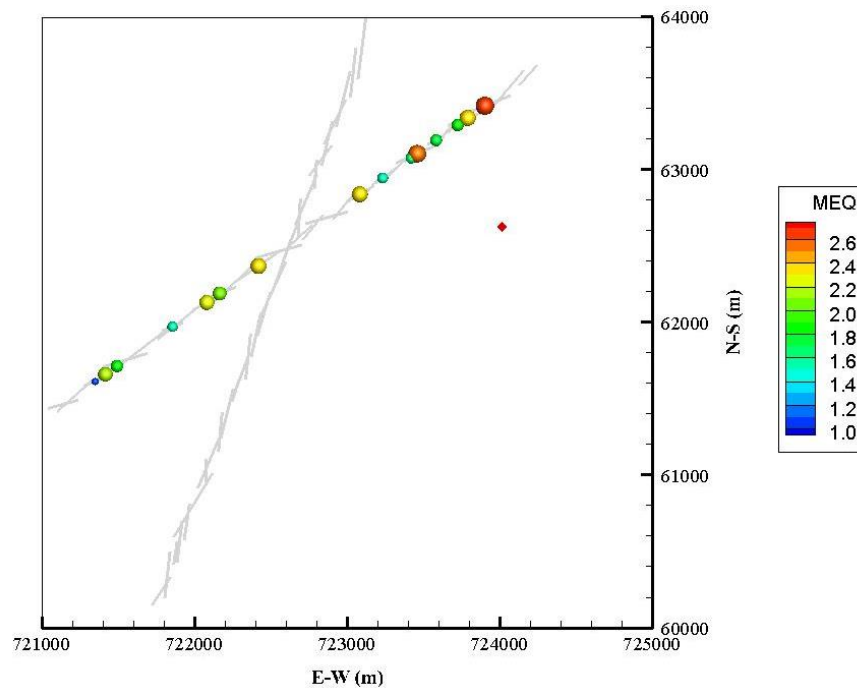


Figure 7.31. Induced seismic events within the small area after 1 year of injection using a constant injection rate of  $0.015 \text{ m}^3/\text{s}$ . The injection well is shown in red square. The seismic events are shown in circles.

The maximum expected size of earthquakes (maximum magnitude or seismic moment) is an important parameter in assessing seismic hazard and risk. Analysis of numerous case histories of fluid injection induced earthquake sequences has indicated that the maximum seismic moment or magnitude for a specified injection activity might in relation to the volume of injected fluid

(McGarr 2014). In Figure 7.32, the maximum seismic moment in each testing case is plotted as a function of the cumulative injection volume. A similar increasing trend in the maximum seismic moment is seen in these cases. As more fluid is injected, the maximum seismic moment increases. This observation suggest that we could cap the injection volume to migrate the size of the potentially seismic events that may be induced during wastewater disposal operations.

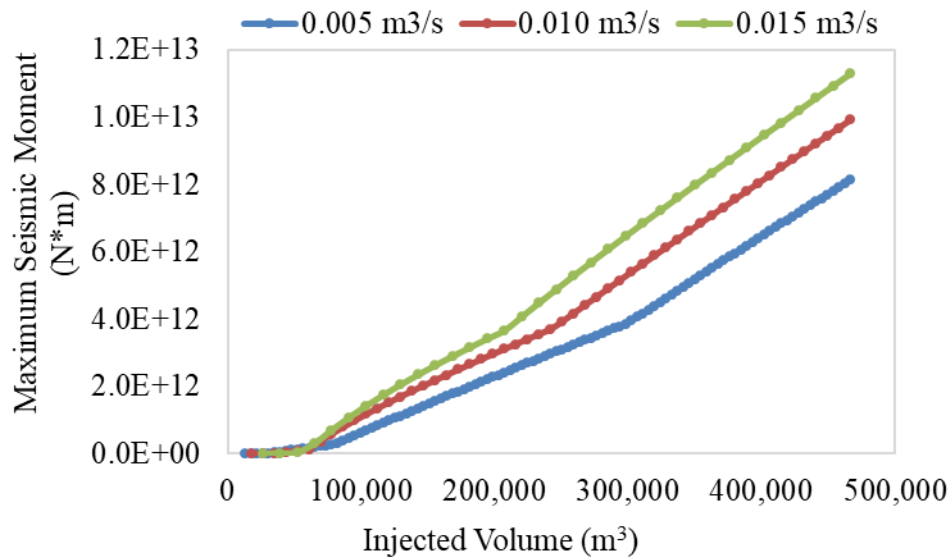


Figure 7.32. Maximum seismic moment as a function of cumulative injection volume in the cases of different injection rate.

The influence of injection rate on the maximum seismic moment could also be seen in Figure 7.32. For a given injected volume, the case injecting at the lowest rate of 0.005 m³/s predicts the lowest value of the maximum seismic moment or magnitude. The lower injection rate allows the fluid to distribute more evenly throughout the fracture network, resulting a lower pressure difference between the highest and the lowest pressure value. Consequently, the possibility of shear slippage is reduced. Therefore, injecting the same amount of fluid at a lower rate over a longer time could



serve a strategy to reduce the size of the induced seismic events, hence, minimize the potential seismic hazard and risks.

We also varied the injection depth in the testing cases. In the basic case, the injection interval is set throughout the Arbuckle layer, from 2000 m to 2600 m. In the comparing case, the injection depth is reduced to 2300 m, which is at 300 m above the top surface of the basement. Thus, water is injected into the upper Arbuckle layer only. A constant injection rate of  $0.015 \text{ m}^3/\text{s}$  is applied on the well for 1 year. Figure 7.33 shows the comparison of the maximum seismic moment of the induced seismic events observed in the two cases. It is evident that the injection depth relative to the basement is strongly correlates with seismic moment release. After 1 year of injection, the basic case with an injection depth of 2600 m induces a maximum seismic moment of  $1.1\text{E}13 \text{ N}\cdot\text{m}$ , corresponding to a seismic magnitude of 0.002. When the injection depth is reduced by 300 m, the maximum seismic moment is reduced by a factor of 1.43, resulting a value of  $7.9\text{E}12 \text{ N}\cdot\text{m}$ , which corresponds to a smaller maximum seismic magnitude of -0.1. When the injection well depth is reduced, the diffusion of fluid and pressure within the Arbuckle layer in the vertical direction is restricted. As a consequence, the elevated pore pressure transmitted into the basement fractures is reduced, minimizing the possibility of slippage.

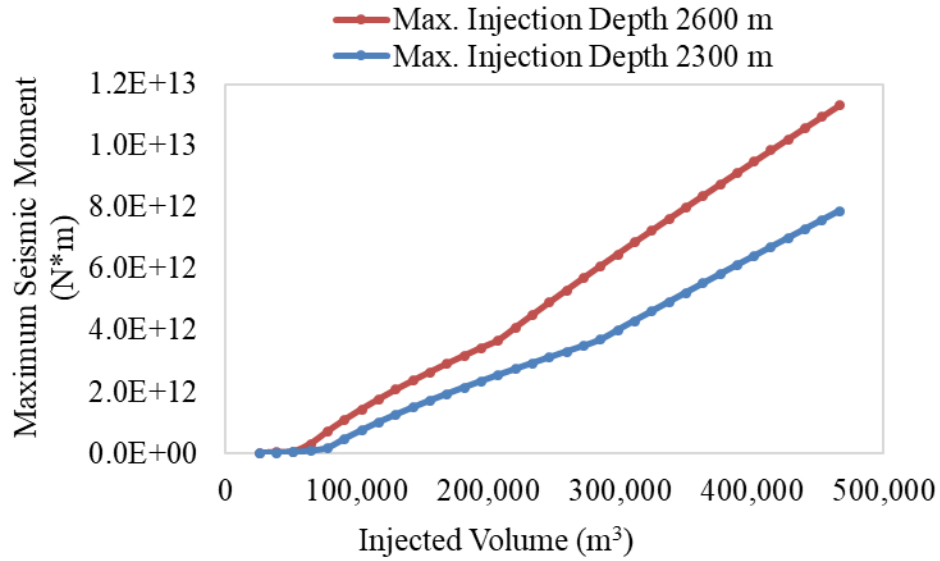


Figure 7.33. Maximum seismic moment as a function of cumulative injection volume in the cases of different injection depth.

These numerical tests suggest that for a given site with known hydrogeological conditions and fault configuration, the injection scheme governs the spatial and temporal perturbation of excess pore pressure, consequently, fault stability and the potential of induced seismicity. During wastewater disposal operations, the injection parameters, such as injection volume, rate and injection well depth, should be carefully selected. Capping the total injection volume, reducing injection rate, and restricting injection depth relative to the basement are possible injection strategies to effectively minimize the seismic hazards and risks.

### 7.2.6 Summary

This study utilized a 12 years injection history of wastewater injection into central Oklahoma to develop a better understating of the response of the existing fault systems and the potential of

induced seismicity. A conceptual model considering the poroelastic coupling behavior during injection and shear slippage induced seismicity is developed.

Simulation results show that the injected fluid increases pore pressure within the target Arbuckle layer and migrates into the deeper crystalline basement rocks via natural fractures along the faults. Under the assumed condition, the pressure increase in the fractures after 12 years of injection is up to 1.0 MPa. This small pressure change is sufficient to promote slippage on favorably oriented fractures and induce seismicity. The predicted seismicity is primarily occurred along the Meeker-Prague fault striking N55°E, which is consistent with the distribution of the field observed seismic events between 2000 to 2011.

This study also carried out numerical tests to explore the correlations between key well operational parameters and induced seismicity. The results suggest that the magnitude of the maximum seismic event could be minimized by limiting the total injected volume, reducing the injection rate and restricting the injection depth relative to the basement.

Despite the uncertainty in input parameters, this conceptual model provides valuable understanding of the process of induced seismicity in the faulted wastewater disposal region. It could be served as an initial assessment tool for evaluating the potential of injection induced seismicity prior to detailed studies. It could also be used to evaluate the effectiveness of seismic hazard mitigation strategies.

## **8. Summary**

### **8.1 Conclusions**

This dissertation presents a numerical model for simulating the response of naturally fractured reservoirs to fluid injection. A fully coupled thermo-poroelastic model is utilized to simulate the coupling between rock deformation, fluid flow and heat transfer in the porous rock medium during injection process. A discrete stochastic fracture network model is implanted into the thermo-poroelastic model using an equivalent continuum approximation. The integration of these two models is achieved by linking the permeability change with the stress dependent fracture deformation and fracture network growth. Not only fracture aperture changes due to opening and shear dilation is accounted in updating the equivalent permeability, but also fracture network geometry change due to fracture propagation. The potential of injection induced seismicity is also modeled, providing a real-time distribution of both the locations and magnitudes of the seismic events. In addition, a heat transfer model for heat flow within a fracture network is developed by considering both the convection via fracture flow and the conduction between the fluid within fractures and the adjacent rock mass. The local pressure distribution on individual fractures is also solved using an analytical approach. This numerical model has been verified against analytical solutions and numerical results in the literature.

The model is applied to several numerical examples for evaluating the response of naturally fractured reservoirs to fluid injection, with different modeling emphasis. The results show that:

The developed model is capable of predicting different aspects of reservoir response to fluid injection. It is useful for predicting the changes in the pore pressure, temperature and stress fields within the reservoir, evaluating fracture network deformation and the associated permeability enhancement, and understanding the injection induced microseismicity.

Natural fracture network plays an important role in the injection outcome as it governs the fluid and heat flow within the fractured system, the development of pore pressure field and the occurrence of induced microseismicity. Results also show that the enhancement of permeability is attributed to the combined contributions of fracture opening, shear slippage and propagation.

The injection response of a naturally fractured reservoir is a highly complex process affected by many parameters, including the properties of natural fractures, in-situ stress conditions, the properties of rock matrix, the properties of injecting fluid, injection scheme and injection temperature. A careful evaluation of these parameters is essential for injection optimization.

Simulation of the Newberry EGS stimulation project is carried out using a stochastic fracture network generated based on field data. The simulated injection profile and the induced microseismic events are in good agreements with the field observations. The simulation results also show that fluid injection could not only increase pore pressure but also change the in-situ stress. The perturbation and rotation of the stress field is observed near the injection well, which helps to explain the discrepancy between the pre-stimulation stress model and the stress model derived from stimulation seismic data.

Results from Oklahoma wastewater injection simulation indicate that the presence of fractures and faults permit the downward fluid migration from the Arbuckle injection target into the deeper crystalline basement, causing shear slippage of favorably oriented fractures and inducing seismicity. To minimize the potential hazards and risks of induced seismicity during wastewater injection operations, well operational parameters should be carefully selected. The possible injection strategies induced capping the total injection volume, reducing injection rate, and restricting injection depth relative to the basement.

The integrated model developed in this study has shown to be capable of predicting the complex behavior of naturally fractured reservoirs during fluid injection process. It is a powerful tool for planning and optimizing the injection process in naturally fractured reservoirs.

## **8.2 Contributions**

The contributions of this dissertation are summarized as below:

1. This research develops a step-by-step workflow to incorporate a stochastic discrete fracture network into a 3D fully coupled thermo-poroelastic finite element model for simulating the behavior of naturally fractured reservoirs. The detailed integration procedure of these two models is presented.
2. The geomechanical model for simulating the deformation behavior of a natural fracture network is improved by considering the propagation of natural fractures simultaneously with shear dilation. It has a capability of capturing the permeability enhancement due to the improvement of fracture network connectivity as a result of fracture growth.
3. As fracture aperture is assumed to be stress dependent in this work, fracture could deform during injection process. The model for heat transfer within a fracture network is improved by considering the change in thermal energy retained by the fluid within the fractures caused by fracture volume change.
4. An analytical approach is used for estimating the local 2D pressure distribution on individual fracture planes. It utilizes the fracture network pressure distribution results and the intersection information between fractures, and provides a computational efficient estimation.

5. The model for injection induced seismicity is improved by the inclusion of a rate-and-state friction model (RSF), which has an advantage of capturing the friction evolution on a fracture/fault as a function of sliding velocity and its past sliding history.

6. The developed FORTRAN code is part of the Reservoir Geomechanics and Seismicity Research (RGSR) Group's in-house code, GeoFrac-Stim. Each of the developed sub-models is implemented as an optional module. This code is also compatible with various modules, such as rock heterogeneity model, continuum damage model, providing flexibility in representing different aspects of rock and fracture behavior.

7. The developed numerical model has been applied to various verification problems and engineering problems, which confirm the capability of this model as well as provide important insights into the behavior of naturally fractured reservoirs.

### **8.3 Recommendations**

The following areas are recommended for future studies:

1. It is challenging to generate a realistic 3D natural fracture network model for representing complex natural fractures presenting in the underground. Further efforts on fracture characterization are required to obtain accurate fracture distribution parameters with respect to fracture density, size and orientation. Furthermore, since the fracture network is generated from a stochastic approach, Monte-Carlo tests are required to verify the reproducibility in stochastic simulation, and to examine the influence of random data set on the simulation results.

2. Future models might also include the mechanical coupling between fracture deformation and finite element displacement by considering the induced stress and elemental strain in rock matrix due to fracture deformation.

3. Advanced fracture propagation model might be included to improve the capability of accurately identifying and predicting the growth of natural fractures.
4. Including wellbore heat transmission to determine the temperature change between the surface and the injection interval is essential for more accurately modeling the thermal effects caused by cold fluid injection operations.
5. Conditional statistical distributions of rock matrix and natural fracture properties should also be incorporated to represent the inherently heterogeneity of fractured rocks. In addition, since fluid properties, such as density and viscosity, are pressure and temperature dependent, the dynamic fluid property changes should be considered when modeling the behavior of the deep underground reservoirs during injection/extraction process.
6. Enhancement of the computational efficiency is important, especially for large scale fractured reservoir simulations. High performance computing technique, such as parallel computing, would be beneficial.



## References

- Aboustit, B.L., Advani, S.H., Lee, J.K. and Sandhu, R.S., 1982. Finite element evaluations of thermo-elastic consolidation. In Proceedings of the 23rd U.S. Symposium on Rock Mechanics (USRMS), Berkeley, California, 25-27 August.
- Ahmed, T., 2010. Reservoir Engineering Handbook. Gulf Professional Publishing.
- Aliguer Piferrer, I. et al., 2015. Numerical stress initialization in geomechanics via the FEM and a two-step procedure. In COMPLAS XIII: proceedings of the XIII International Conference on Computational Plasticity: fundamentals and applications: 667-676.
- Alt, R.C. and Zoback, M.D., 2014. Development of a detailed stress map of Oklahoma for avoidance of potentially active faults when siting wastewater injection wells. In AGU Fall Meeting Abstracts.
- AltaRock, 2014. Phase 2.2 report, Newberry EGS demonstration.
- Altman, J.B., 2010. Poroelastic effects in reservoir modelling. Ph.D. dissertation, Karlsruher Instituts für Technologie.
- Ampuero, J.P. and Rubin, A.M., 2008. Earthquake nucleation on rate and state faults—aging and slip laws. *Journal of Geophysical Research: Solid Earth*, 113(B1).
- Baecher, G.B., Lanney, N.A. and Einstein, H.H., 1977. Statistical description of rock properties and sampling. In Proceedings of the 18th U.S. Symposium on Rock Mechanics (USRMS), Golden, Colorado, 22-24 June.
- Biot, M.A., 1941. General theory of three-dimensional consolidation. *Journal of applied physics*, 12(2): 155-164.
- Bonnet, E., Bour, O., Odling, N.E., Davy, P., Main, I., Cowie, P. and Berkowitz, B., 2001. Scaling of fracture systems in geological media. *Reviews of geophysics*, 39(3): 347-383.

Boulton, G., Chan, T., Christiansson, R., Ericsson, L.O., Hartikainen, J., Jensen, M.R., Stanchell, F.W. and Wallroth, T., 2004. Thermo-hydro-mechanical (THM) impacts of glaciation and implications for deep geologic disposal of nuclear waste. In Elsevier Geo-Engineering Book Series, 2: 299-304.

Bourke, P.J., 1987. Channeling of flow through fractures in rock (No. AERE-R--12305). UKAEA Atomic Energy Research Establishment.

Breede, K., Dzebisashvili, K., Liu, X. and Falcone, G., 2013. A systematic review of enhanced (or engineered) geothermal systems: past, present and future. *Geothermal Energy*, 1(1): 4.

Bruel, D. and Cacas, M.C., 1992. Numerical modelling technique. *Geothermal Energy in Europe: the Soultz Hot Dry Rock Project*, 267.

Bruel, D., 2002. Impact of induced thermal stresses during circulation tests in an engineered fractured geothermal reservoir: example of the Soultz-sous-Forets European hot fractured rock geothermal project, Rhine Graben, France. *Oil & Gas Science and Technology*, 57(5): 459-470.

Cacas M.C., Ledoux, E., De Marsily, G., and Tillie, B., 1990. Modeling fracture flow with a stochastic discrete fracture network: calibration and validation 1. The flow model. *Water Resources Research*, 26(3): 479-489.

Carrell, J., 2014. Field-scale hydrogeologic modeling of water injection into the Arbuckle zone of the midcontinent. M.S. thesis, University of Oklahoma.

Carrera, J., Heredia, J., Vomvoris, S. and Hufschmied, P., 1990. Modeling of flow on a small fractured monzonitic gneiss block. *Hydrogeology of Low Permeability Environments*, 2: 115-167.

Chan, T., Christiansson, R., Boulton, G.S., Ericsson, L.O., Hartikainen, J., Jensen, M.R., Ivars, D.M., Stanchell, F.W., Vistrand, P. and Wallroth, T., 2005. DECOVALEX III BMT3/BENCHPAR WP4: The thermo-hydro-mechanical responses to a glacial cycle and their

potential implications for deep geological disposal of nuclear fuel waste in a fractured crystalline rock mass. *International Journal of Rock Mechanics and Mining Sciences*, 42(5-6): 805-827.

Chen, G. and Ewy, R.T., 2005. Thermoporoelastic effect on wellbore stability. *SPE Journal*, 10(02): 121-129.

Chen, X., Nakata, N., Pennington, C., Haffener, J., Chang, J.C., He, X., Zhan, Z., Ni, S. and Walter, J.I., 2017. The Pawnee earthquake as a result of the interplay among injection, faults and foreshocks. *Scientific reports*, 7(1): 4945.

Cheng, A.H.D., 2016. *Poroelasticity*. Heidelberg, Germany: Springer International.

Cheng, Q. and Ghassemi, A., 2016. Numerical modeling of Newberry EGS stimulation. In *Proceedings of the 50st U.S. Rock Mechanics/Geomechanics Symposium*, Houston, Texas, 26-29 June.

Cheng, Q. and Ghassemi, A., 2017. Numerical modeling of fluid flow, heat transfer and induced microseismicity in three dimensional fracture networks. In *Proceedings of the 51st U.S. Rock Mechanics/Geomechanics Symposium*, San Francisco, California, 25-28 June.

Cheng, Q., Wang, X. and Ghassemi, A., 2018. Numerical Simulation of Reservoir Stimulation with Reference to the Newberry EGS. *Geothermics*. (under production)

Cladouhos, T.T., Clyne, M., Nichols, M., Petty, S., Osborn, W.L., and Nofziger, L., 2011. Newberry Volcano EGS demonstration stimulation modeling. *GRC Transactions*, 35: 317-322.

Cladouhos, T.T., Petty, S., Swyer, M.W., Uddenberg, M.E., Grasso, K., Nordin, Y., 2016. Results from Newberry Volcano EGS Demonstration, 2010–2014. *Geothermics*, 63: 44–61.

Crank, J. and Nicolson, P., 1947, January. A practical method for numerical evaluation of solutions of partial differential equations of the heat-conduction type. In *Mathematical Proceedings of the Cambridge Philosophical Society*, 43(1): 50-67. Cambridge University Press.

Delaney, P. T., 1982. Rapid intrusion of magma into wet rock: ground water flow due to pressure increases. *Journal of Geophysical Research*, 87: 7739–7756.

Dershowitz, W.S. and Einstein, H.H., 1988. Characterizing rock joint geometry with joint system models. *Rock mechanics and rock engineering*, 21(1): 21-51.

Dershowitz, W.S., 1984. Rock joint systems. Ph.D. dissertation, Massachusetts Institute of Technology.

Devegowda, D., 2016. Modeling pore pressure variations and potential for induced seismicity adjacent to water disposal wells. Final report of RPSEA Project 12122-91: 4D integrated study using geology, geophysics, reservoir modeling & rock mechanics to develop assessment models for potential induced seismicity risk.

Dieterich, J.H., 1979. Modeling of rock friction: 1. experimental results and constitutive equations. *Journal of Geophysical Research: Solid Earth*, 84(B5): 2161-2168.

Dieterich, J.H., 1992. Earthquake nucleation on faults with rate-and state-dependent strength. *Tectonophysics*, 211(1-4): 115-134.

Dieterich, J.H., 2007. Applications of rate-and state-dependent friction to models of fault slip and earthquake occurrence.

Dycus, M., 2013. Structural Characterization of the Wilzetta Fault Zone: Lincoln, Pottawatomie, and Creek Counties, Oklahoma. M.S.thesis, University of Tulsa.

Erdogan, F. and Sih, G.C., 1963. On the crack extension in plates under plane loading and transverse shear. *Journal of Basic Engineering*, 85(4): 519-525.

Fang, Y., Hartog, S., Elsworth, D., Marone, C., Cladouhos, T., 2016. Anomalous distribution of microearthquakes in the Newberry Geothermal Reservoir: mechanisms and implications. *Geothermics*, 63: 62-73.

Farmahini-Farahani, M. and Ghassemi, A., 2016. Simulation of micro-seismicity in response to injection/production in large-scale fracture networks using the fast multipole displacement discontinuity method (FMDDM). *Engineering Analysis with Boundary Elements*, 71: 179-189.

Finlayson, B.A., 2013. *The method of weighted residuals and variational principles*, 73. SIAM.

Fisher, R.A., 1953. Dispersion on a sphere. *Proceedings of the Royal Society of London Series A*, 217(1130): 295-305.

Fredrich, J.T. and Fossum, A.F., 2002. Large-scale three-dimensional geomechanical modeling of reservoirs: examples from California and the deepwater Gulf of Mexico. *Oil & Gas Science and Technology*, 57(5): 423-431.

Freeman, T.T., Chalaturnyk, R.J. and Bogdanov, I.I., 2008. Fully coupled thermo-hydro-mechanical modeling by COMSOL Multiphysics, with applications in reservoir geomechanical characterization. In *COMSOL Conf.*

Gale, J.E., 1987. Comparison of coupled fracture deformation and fluid flow models with direct measurements of fracture pore structure and stress-flow properties. In *Proceedings of the 28th U.S. Symposium on Rock Mechanics (USRMS)*, Tucson, Arizona, 29 June-1 July.

Gao, Q. and Ghassemi, A., 2017. Pore pressure and stress distributions around a hydraulic Fracture in heterogeneous rock. *Rock Mechanics and Rock Engineering*, 50(12): 3157-3173.

Gentier, S., Billiaux, D. and Van Vliet, L., 1989. Laboratory testing of the voids of a fracture. *Rock mechanics and rock engineering*, 22(2): 149-157.

Ghassemi, A. and Diek, A., 2003. Linear chemo-poroelasticity for swelling shales: theory and application. *Journal of Petroleum Science and Engineering*, 38(3-4): 199-212.

Ghassemi, A. and Zhang, Q., 2004. A transient fictitious stress boundary element method for porothermoelastic media. *Engineering analysis with boundary elements*, 28(11): 1363-1373.

- Ghassemi, A. and Zhou, X., 2011. A three-dimensional thermo-poroelastic model for fracture response to injection/extraction in enhanced geothermal systems. *Geothermics*, 40(1): 39-49.
- Ghassemi, A., Tao, Q. and Diek, A., 2009. Influence of coupled chemo-poro-thermoelastic processes on pore pressure and stress distributions around a wellbore in swelling shale. *Journal of petroleum science and Engineering*, 67(1-2): 57-64.
- Ghassemi, A., Tarasovs, S. and H.-D. Cheng, A., 2003. An integral equation solution for three-dimensional heat extraction from planar fracture in hot dry rock. *International Journal for Numerical and Analytical Methods in Geomechanics*, 27(12): 989-1004.
- Gholizadeh Doonechaly, N., Abdel Azim, R.R. and Rahman, S.S., 2016. A study of permeability changes due to cold fluid circulation in fractured geothermal reservoirs. *Groundwater*, 54(3): 325-335.
- Goodarzi, S., Settari, A., Zoback, M. and Keith, D.W., 2013. Thermal effects on shear fracturing and injectivity during CO<sub>2</sub> storage. In *Proceedings of the ISRM International Conference for Effective and Sustainable Hydraulic Fracturing*, Brisbane, Australia, 20-22 May.
- Hakami, E. and Barton, N., 1990. Aperture measurements and flow experiments using transparent replicas of rock joints. *Rock Joints*: 383-390.
- Hammond, L. and Grzebieta, R., 2000. The requirement for hydrostatic initialisation in LS-DYNA/USA finite element models. *Shock and Vibration*, 7(2): 57-65.
- Hanks, T.C. and Kanamori, H., 1979. A moment magnitude scale. *Journal of Geophysical Research: Solid Earth*, 84(B5): 2348-2350.
- Heidug, W.K. and Wong, S.W., 1996. Hydration swelling of water-absorbing rocks: a constitutive model. *International journal for numerical and analytical methods in geomechanics*, 20(6): 403-430.

Hemami, B. and Ghassemi, A., 2018. A study of basement structures in central Oklahoma with reference to seismicity. In Proceedings of the 52nd U.S. Rock Mechanics/Geomechanics Symposium, Seattle, Washington, 17-20 June.

Hicks, T.W., Pine, R.J., Willis-Richards, J., Xu, S., Jupe, A.J. and Rodrigues, N.E.V., 1996. A hydro-thermo-mechanical numerical model for HDR geothermal reservoir evaluation. International Journal of Rock Mechanics and Mining Sciences & Geomechanics Abstracts, 33(5): 499-511.

Hincks, T., Aspinall, W., Cooke, R. and Gernon, T., 2018. Oklahoma's induced seismicity strongly linked to wastewater injection depth. Science, 359(6381): 1251-1255.

Holland, A. A., 2015. Preliminary fault map of Oklahoma: Oklahoma Geological Survey Open File Report, v. OF3-2015.

Holzbecher, E., 2017. Analytical solution for the steady poroelastic state under influence of gravity. In Proceedings of the 2017 COMSOL Conference, Rotterdam, 18-20 October.

Hossain, M. M., 2001. Reservoir stimulation by hydraulic fracturing: complexities and remedies with reference to initiation and propagation of induced and natural fractures. Ph.D. dissertation, University of New South Wales.

Hou, Z., Gou, Y., Taron, J., Gorke, U.J. and Kolditz, O., 2012. Thermo-hydro-mechanical modeling of carbon dioxide injection for enhanced gas-recovery (CO<sub>2</sub>-EGR): a benchmarking study for code comparison. Environmental Earth Sciences, 67(2): 549-561.

Hristopulos, D.T. and Christakos, G., 1999. Renormalization group analysis of permeability upscaling. Stochastic Environmental Research and Risk Assessment, 13(1-2): 131-160.

Huang, K., Cheng, Q., Ghassemi, A. and Bauer, S., 2018. Coupled thermo-poromechanical modeling and evaluation of shear slip in fractured rock. Geothermics. (under revision).

Huang, K., Zhang, Z. and Ghassemi, A., 2013. Modeling three-dimensional hydraulic fracture propagation using virtual multidimensional internal bonds. *International Journal for Numerical and Analytical Methods in Geomechanics*, 37(13): 2021-2038.

Hudson, J.A. and Ladson, J.A.H.A., 1980. Printed circuits for studying rock mass permeability. *International Journal of Rock Mechanics and Mining Science*, 17(5).

Hutton, D.V., 2003. *Fundamentals of finite element analysis*. New York: McGraw-hill.

Ida, Y., 1972. Cohesive force across the tip of a longitudinal - shear crack and Griffith's specific surface energy. *Journal of Geophysical Research*, 77(20): 3796-3805.

Jaeger, J.C., Cook, N.G.W., and Zimmerman, R.W., 2007. *Fundamentals of rock mechanics*. 4th edition. Blackwell Publishing.

Jing, Z., Willis-Richards, J., Watanabe, K. and Hashida, T., 2000. A three-dimensional stochastic rock mechanics model of engineered geothermal systems in fractured crystalline rock. *Journal of Geophysical Research: Solid Earth*, 105(B10): 23663-23679.

Kamali, A. and Ghassemi, A., 2018. Analysis of injection-induced shear slip and fracture propagation in geothermal reservoir stimulation. *Geothermics*, 76: 93-105.

Kazemi, H., 1969. Pressure transient analysis of naturally fractured reservoirs with uniform fracture distribution. *Society of petroleum engineers Journal*, 9(04): 451-462.

Kazemi, H., Merrill Jr, L.S., Porterfield, K.L. and Zeman, P.R., 1976. Numerical simulation of water-oil flow in naturally fractured reservoirs. *Society of Petroleum Engineers Journal*, 16(06): 317-326.

Keranen, K.M., Savage, H.M., Abers, G.A. and Cochran, E.S., 2013. Potentially induced earthquakes in Oklahoma, USA: Links between wastewater injection and the 2011 Mw 5.7 earthquake sequence. *Geology*, 41(6): 699-702.



Klimczak, C., Schultz, R.A., Parashar, R. and Reeves, D.M., 2010. Cubic law with aperture-length correlation: implications for network scale fluid flow. *Hydrogeology Journal*, 18(4): 851-862.

Koh, J., Roshan, H. and Rahman, S.S., 2011. A numerical study on the long term thermo-poroelastic effects of cold water injection into naturally fractured geothermal reservoirs. *Computers and Geotechnics*, 38(5): 669-682.

Kolditz, O. and Clauser, C., 1998. Numerical simulation of flow and heat transfer in fractured crystalline rocks: application to the hot dry rock site in Rosemanowes (UK). *Geothermics*, 27(1): 1-23.

Kolditz, O., 1995. Modelling flow and heat transfer in fractured rocks: conceptual model of a 3-D deterministic fracture network. *Geothermics*, 24(3): 451-470.

Kumar, D. and Ghassemi, A., 2015. 3D simulation of multiple fracture propagation from horizontal wells. In *Proceedings of the 49th U.S. Rock Mechanics/Geomechanics Symposium*, San Francisco, California, 28 June-1 July.

Kumar, D., 2018. Personal communications.

Kurashige, M., 1989. A thermoelastic theory of fluid-filled porous materials. *International Journal of Solids and Structures*, 25(9): 1039-1052.

La Pointe, P.R., Eiben, T., Dershowitz, W. and Wadleigh, E., 1997. Compartmentalization analysis using discrete fracture network models (No. CONF-970317-1). BDM Oklahoma, Inc., Bartlesville, Oklahoma.

Lapusta, N., 2001. Elastodynamic analysis of sliding with rate and state friction. Ph.D. dissertation, Harvard University.

Laubach, S., Marrett, R. and Olson, J., 2000. New directions in fracture characterization. *The Leading Edge*, 19(7): 704-711.

Lee, J., Choi, S.U. and Cho, W., 1999. A comparative study of dual-porosity model and discrete fracture network model. *KSCE Journal of Civil Engineering*, 3(2): 171-180.

Lee, S.H. and Ghassemi, A., 2010. Thermo-poroelastic analysis of injection-induced rock deformation and damage evolution. In *Proceedings of the 35st Workshop on Geothermal Reservoir Engineering*, Stanford University, Stanford, California, 1-3 February.

Lee, S.H., 2011. Thermo-poroelastic modeling of reservoir stimulation and microseismicity using finite element method with damage mechanics. Ph.D. dissertation, Texas A&M University.

Li, X., Cui, L. and Roegiers, J.C., 1998. Thermoporoelastic analyses of inclined boreholes. In *Proceedings of the SPE/ISRM Rock Mechanics in Petroleum Engineering*, Trondheim, Norway, 8-10 July.

Li, Y., Wong, J., and Ghassemi, A., 2012. Mechanical properties of intact and jointed welded tuff from Newberry volcano. In *Proceedings of the 37th workshop on geothermal reservoir engineering*, Stanford University, Stanford, California, 30 January-1 February.

Llenos, A.L. and Michael, A.J., 2013. Modeling earthquake rate changes in Oklahoma and Arkansas: Possible signatures of induced seismicity. *Bulletin of the Seismological Society of America*, 103(5): 2850-2861.

Long, J.C.S., 1983. Investigation of equivalent porous medium permeability in networks of discontinuous fractures (No. LBL-16259). Lawrence Berkeley Lab., CA (USA).

Long, J.C.S., Remer, J.S., Wilson, C.R. and Witherspoon, P.A., 1982. Porous media equivalents for networks of discontinuous fractures. *Water Resources Research*, 18(3): 645-658.

Lu, J., Ghassemi, A., 2017. Geomechanics-based stochastic analysis of microseismicity for analysis of fractured reservoir stimulation. In *Proceedings of the 42nd workshop on geothermal reservoir engineering*, Stanford University, Stanford, California, 13-15 February.

- Marín, E., 2010. Characteristic dimensions for heat transfer. *Latin-American Journal of Physics Education*, 4(1): 56-60.
- Massiot, C., Townend, J., McNamara, D.D. and Nicol, A., 2015. Fracture width and spacing distributions from borehole televiewer logs and cores in the Rotokawa Geothermal Field, New Zealand. In *World Geothermal Congress 2015*. International Geothermal Association.
- McGarr, A., 2014. Maximum magnitude earthquakes induced by fluid injection. *Journal of Geophysical Research: solid earth*, 119(2): 1008-1019.
- McGarr, A., Spottiswoode, S.M., Gay, N.C. and Ortlepp, W.D., 1979. Observations relevant to seismic driving stress, stress drop, and efficiency. *Journal of Geophysical Research: Solid Earth*, 84(B5): 2251-2261.
- McKenna, S.A. and Reeves, P.C., 2006. Fractured continuum approach to stochastic permeability modeling.
- McMahon, B.K., 1971. A statistical method for the design of rock slopes. In *Proceedings of the 1st Australia–New Zealand Conference on Geomechanics*. Melbourne, 314-321.
- McMahon, N.D., Aster, R.C., Yeck, W.L., McNamara, D.E. and Benz, H.M., 2017. Spatiotemporal evolution of the 2011 Prague, Oklahoma, aftershock sequence revealed using subspace detection and relocation. *Geophysical Research Letters*, 44(14): 7149-7158.
- McNamara, D.E., Benz, H.M., Herrmann, R.B., Bergman, E.A., Earle, P., Holland, A., Baldwin, R. and Gassner, A., 2015. Earthquake hypocenters and focal mechanisms in central Oklahoma reveal a complex system of reactivated subsurface strike-slip faulting. *Geophysical Research Letters*, 42(8): 2742-2749.
- McTigue, D.F., 1986. Thermoelastic response of fluid-saturated porous rock. *Journal of Geophysical Research: Solid Earth*, 91(B9): 9533-9542.

- Min, K.B., Rutqvist, J., Tsang, C.F. and Jing, L., 2004. Stress-dependent permeability of fractured rock masses: a numerical study. *International Journal of Rock Mechanics and Mining Sciences*, 41(7): 1191-1210.
- Min, K.S., Huang, K. and Ghassemi, A., 2011. A study of numerical simulations of mixed-mode fracture propagation in rock. In *Proceedings of the 36th Workshop on Geothermal Reservoir Engineering*, Stanford University, Stanford, California, January 31-February 2.
- Mody, F.K. and Hale, A.H., 1993. Borehole-stability model to couple the mechanics and chemistry of drilling-fluid/shale interactions. *Journal of Petroleum Technology*, 45(11): 1-093.
- Morgan, B.C. and Murray, K.E., 2015. Characterizing small-scale permeability of the Arbuckle Group, Oklahoma. Oklahoma Geology Survey. Open-File Rept. OF2-2015: 1-12.
- National Research Council, 1996. *Rock Fractures and Fluid Flow: Contemporary Understanding and Applications*. National Academies Press.
- Noorishad, J., Tsang, C.F. and Witherspoon, P.A., 1984. Coupled thermal-hydraulic-mechanical phenomena in saturated fractured porous rocks: Numerical approach. *Journal of Geophysical Research: Solid Earth*, 89(B12): 10365-10373.
- Norbeck, J.H. and Horne, R.N., 2016. Evidence for a transient hydromechanical and frictional faulting response during the 2011 Mw 5.6 Prague, Oklahoma earthquake sequence. *Journal of Geophysical Research: Solid Earth*, 121(12): 8688-8705.
- Norbeck, J.H., 2016. Hydromechanical and frictional faulting behavior of fluid-injection-induced earthquakes. Ph.D. dissertation, Stanford University.
- Norbeck, J.H., McClure, M.W., Lo, J.W. and Horne, R.N., 2016. An embedded fracture modeling framework for simulation of hydraulic fracturing and shear stimulation. *Computational Geosciences*, 20(1): 1-18.

Oda, M., 1986. An equivalent continuum model for coupled stress and fluid flow analysis in jointed rock masses. *Water resources research*, 22(13): 1845-1856.

Oreskes, N., Shrader-Frechette, K. and Belitz, K., 1994. Verification, validation, and confirmation of numerical models in the earth sciences. *Science*, 263(5147): 641-646.

Palciauskas, V.V. and Domenico, P.A., 1982. Characterization of drained and undrained response of thermally loaded repository rocks. *Water Resources Research*, 18(2): 281-290.

Palmer, A.C. and Rice, J.R., 1973. The growth of slip surfaces in the progressive failure of over-consolidated clay. *Proceedings of the Royal Society of London A*, 332(1591): 527-548.

Patton, F.D., 1966. Multiple modes of shear failure in rock. In *Proceedings of the 1st Congress of International Society of Rock Mechanics*, Lisbon, Portugal, 25 September-1 October, 1: 509-513.

Pennington, C., Chen, X., Abercrombie, R.E., McMahon, N.D. and Aster, R.C., 2016. Seismological analysis of induced earthquakes in central Oklahoma, comparing a large seismogenic fault with M5 earthquakes and small faults lacking M4 events. *AGU Fall Meeting Abstracts*.

Pepper, D.W. and Heinrich, J.C., 2017. *The finite element method: basic concepts and applications with MATLAB, MAPLE, and COMSOL*. CRC Press.

Pine, R.J. and Batchelor, A.S., 1984. Downward migration of shearing in jointed rock during hydraulic injections. *International Journal of Rock Mechanics and Mining Sciences & Geomechanics Abstracts*, 21(5): 249-263.

Raghavan, R. and Chin, L.Y., 2004. Productivity changes in reservoirs with stress-dependent permeability. *SPE Reservoir Evaluation & Engineering*, 7(04): 308-315.

Rahi, K. and Halihan, T., 2009. Estimating selected hydraulic parameters of the Arbuckle-Simpson aquifer from the analysis of naturally-induced stresses: Oklahoma Water Resources Board, Arbuckle-Simpson Aquifer Special Study, 48.

Rahman, M.K., Hossain, M.M. and Rahman, S.S., 2002. A shear-dilation-based model for evaluation of hydraulically stimulated naturally fractured reservoirs. *International Journal for Numerical and Analytical Methods in Geomechanics*, 26(5): 469-497.

Rawal, A., and Ghassemi, A. 2014. A reactive poro-thermoelastic analysis of cold water injection in enhanced geothermal reservoir. *Geothermics*, 50: 10-23.

Rice, J.R. and Cleary, M.P., 1976. Some basic stress diffusion solutions for fluid-saturated elastic porous media with compressible constituents. *Reviews of Geophysics*, 14(2): 227-241.

Rice, J.R., 1968. A path independent integral and the approximate analysis of strain concentration by notches and cracks. *Journal of applied mechanics*, 35(2): 379-386.

Rodemann H., 1982. Analytical model calculations on heat exchange in a fracture. In *Urach Geothermal Project*. Stuttgart, 351–353.

Rowe, C.D. and Griffith, W.A., 2015. Do faults preserve a record of seismic slip: A second opinion. *Journal of Structural Geology*, 78: 1-26.

Rubinstein, J., 2018. Induced earthquakes. USGS online webpage. Accessed 12 September 2018, <https://earthquake.usgs.gov/research/induced/overview.php>.

Ruina, A., 1983. Slip instability and state variable friction laws. *Journal of Geophysical Research: Solid Earth*, 88(B12): 10359-10370.

Rutqvist, J., Wu, Y.S., Tsang, C.F. and Bodvarsson, G., 2002. A modeling approach for analysis of coupled multiphase fluid flow, heat transfer, and deformation in fractured porous rock. *International Journal of Rock Mechanics and Mining Sciences*, 39(4): 429-442.

- Safari, M.R. and Ghassemi, A., 2011. 3D analysis of huff and puff and injection tests in geothermal reservoirs. In Proceedings of the 36st Workshop on Geothermal Reservoir Engineering, Stanford University, Stanford, California, January 31-February 2.
- Safari, R. and Ghassemi, A., 2015. 3D thermo-poroelastic analysis of fracture network deformation and induced micro-seismicity in enhanced geothermal systems. *Geothermics*, 58: 1-14.
- Samuelson, J., Elsworth, D. and Marone, C., 2011. Influence of dilatancy on the frictional constitutive behavior of a saturated fault zone under a variety of drainage conditions. *Journal of Geophysical Research: Solid Earth*, 116(B10).
- Schwartz, F.W. and Domenico, P.A., 1990. *Physical and chemical hydrogeology*. John Wiley.
- Segall, P., Rubin, A.M., Bradley, A.M. and Rice, J.R., 2010. Dilatant strengthening as a mechanism for slow slip events. *Journal of Geophysical Research: Solid Earth*, 115(B12).
- Sesetty, V. and Ghassemi, A., 2017. Simulation of hydraulic fracture clusters considering viscosity and toughness dominated propagation. In Proceedings of the 51st US Rock Mechanics/Geomechanics Symposium, San Francisco, California, 25-28 June.
- Sesetty, V. and Ghassemi, A., 2018. Hydraulic fracture propagation in naturally fractured anisotropic shale. In Proceedings of the 52nd U.S. Rock Mechanics/Geomechanics Symposium, Seattle, Washington, 17-20 June.
- Smith, I.M., Griffiths, D.V. and Margetts, L., 2013. *Programming the finite element method*. John Wiley & Sons.
- Sneddon, I.N., 1946. The distribution of stress in the neighbourhood of a crack in an elastic solid. *Proceedings of the Royal Society of London A*, 187(1009): 229-260.

- Snow, D.T., 1970. The frequency and apertures of fractures in rock. In *International journal of Rock mechanics and Mining sciences & Geomechanics Abstracts*, 7(1): 23-40.
- Sonnenthal, E.L., Smith, J.T., Cladouhos, T., Kim, J. and Yang, L., 2015. Thermal-hydrological-mechanical-chemical modeling of the 2014 EGS stimulation experiment at Newberry volcano, Oregon. In *Proceedings of the 40th Workshop on Geothermal Reservoir Engineering*, Stanford University, Stanford, California, 26-28 January.
- Sumy, D.F., Cochran, E.S., Keranen, K.M., Wei, M. and Abers, G.A., 2014. Observations of static Coulomb stress triggering of the November 2011 M5.7 Oklahoma earthquake sequence. *Journal of Geophysical Research: Solid Earth*, 119(3): 1904-1923.
- Terzaghi, K., 1923. Die Berechnung der Durchlässigkeit des Tonen aus dem Verlauf der hydromechanischen Spannungserscheinungen. *Sitzungsber. Akad. Wiss.(Wien). Math.-Naturwiss. Kl., Abt. Iia*, 132: 125-138.
- Tezuka, K. and Watanabe, K., 2000. Fracture network modeling of Hijiori hot dry rock reservoir by deterministic and stochastic crack network simulator (D/SC). In *Proceedings of the World Geothermal Congress, Kyushu Tohoku, Japan, 28 May-10 June*: 3933-3938.
- Tezuka, K., Tamagawa, T. and Watanabe, K., 2005. Numerical simulation of hydraulic shearing in fractured reservoir. In *Proceedings of the World Geothermal Congress, Antalya, Turkey, 24-29 April*.
- Ucar, E., Berre, I. and Keilegavlen, E., 2016. Modelling of the shear dilation based hydraulic stimulation in Enhanced Geothermal Systems considering fractures in different scales. In *Proceedings of the European Geothermal Congress, Strasbourg, France, 19-24 September*.
- Valko, P. and Economides, M.J., 1995. *Hydraulic fracture mechanics*. New York: Wiley.



Vermilye, J.M. and Scholz, C.H., 1995. Relation between vein length and aperture. *Journal of Structural Geology*, 17(3): 423-434.

Vilarrasa, V., Olivella, S., Carrera, J. and Rutqvist, J., 2014. Long term impacts of cold CO<sub>2</sub> injection on the caprock integrity. *International Journal of Greenhouse Gas Control*, 24: 1-13.

Walsh III, F.R. and Zoback, M.D., 2016. Probabilistic assessment of potential fault slip related to injection-induced earthquakes: application to north-central Oklahoma, USA. *Geology*, 44(12): 991-994.

Walsh, F. R., Zoback, M. D., Pais, D., Weingarten, M., and Tyrrell, T., 2017. FSP 1.0: A program for probabilistic estimation of fault slip potential resulting from fluid injection, user guide from the Stanford center for induced and triggered seismicity.

Walsh, F.R. and Zoback, M.D., 2015. Oklahoma's recent earthquakes and saltwater disposal. *Science Advances*, 1(5): p.e1500195.

Wang, J., Jung, W., Li, Y. and Ghassemi, A., 2016. Geomechanical characterization on Newberry tuff. *Geothermics*. EGS special issue.

Wang, X. and Ghassemi, A., 2011. A three-dimensional stochastic fracture network model for geothermal reservoir stimulation. In *Proceedings of the 36th Workshop on Geothermal Reservoir Engineering*, Stanford University, Stanford, California, January 31-February 2.

Wang, X. and Ghassemi, A., 2012. A 3D thermal-poroelastic model for geothermal reservoir stimulation. In *Proceedings of the 37th Workshop on Geothermal Reservoir Engineering*, Stanford University, Stanford, California, January 30-February 1.

Wang, X. and Ghassemi, A., 2013. A three dimensional thermal-poroelastic model for natural fractured geothermal reservoir stimulation. *GRC Transactions*, 37: 871-878.

Wang, X., 2014. Three-dimensional FEM modeling of geothermal reservoir stimulation using stochastic fracture networks and continuum damage mechanics. Ph.D. dissertation, University of Oklahoma.

Warpinski, N.R., Wolhart, S.L. and Wright, C.A., 2004. Analysis and prediction of microseismicity induced by hydraulic fracturing. *SPE Journal*, 9(01): 24-33.

Warren, J.E. and Root, P. J., 1963. The behavior of naturally fractured reservoirs. *SPE Journal*, 3(3): 245-255.

Watanabe, N., Zehner, B., Wang, W., McDermott, C.I., Taniguchi, T. and Kolditz, O., 2011. Numerical analysis and visualization of uncertainty effects in thermo-hydro-mechanical coupled processes in a hot-dry-rock geothermal reservoir. In *Proceedings of the 7th International Conference on Calibration and Reliability in Groundwater Modelling: Managing Groundwater and the Environment, ModelCARE 2009*.

Wells, D.L. and Coppersmith, K.J., 1994. New empirical relationships among magnitude, rupture length, rupture width, rupture area, and surface displacement. *Bulletin of the seismological Society of America*, 84(4): 974-1002.

White, M.D. et al., 2016. Benchmark problems of the geothermal technologies office code comparison study (No. PNNL-26016). Pacific Northwest National Lab.(PNNL), Richland, WA (United States).

Willis-Richards, J., Watanabe, K. and Takahashi, H., 1996. Progress toward a stochastic rock mechanics model of engineered geothermal systems. *Journal of Geophysical Research: Solid Earth*, 101(B8): 17481-17496.

Xu, C. and Dowd, P., 2010. A new computer code for discrete fracture network modelling. *Computers & Geosciences*, 36(3): 292-301.

Ye, Z. and Ghassemi, A., 2018. Experimental study on injection-induced fracture propagation and coalescence for EGS stimulation. In Proceedings of the 43rd Workshop on Geothermal Reservoir Engineering, Stanford University, Stanford, California, 12-14 February.

Ye, Z. and Ghassemi, A., 2018. Injection - induced shear slip and permeability enhancement in granite fractures. *Journal of Geophysical Research*, doi: 10.1029/2018JB016045.

Ye, Z., Janis, M. and Ghassemi, A., 2017. Laboratory investigation of permeability evolution in shear stimulation of granite fractures for EGS. In Proceedings of the 41st GRC Annual Meeting & GEA GeoExpo, Salt Lake City, Utah, 1-4 October.

Ye, Z., Sesetty, V. and Ghassemi, A., 2018. Experimental and numerical investigation of shear stimulation and permeability evolution in shales. In Proceedings of the SPE Hydraulic Fracturing Technology Conference and Exhibition, the Woodlands, Texas, 23-25 January.

Yeck, W.L., Hayes, G.P., McNamara, D.E., Rubinstein, J.L., Barnhart, W.D., Earle, P.S. and Benz, H.M., 2017. Oklahoma experiences largest earthquake during ongoing regional wastewater injection hazard mitigation efforts. *Geophysical Research Letters*, 44(2): 711-717.

Yin, S., Towler, B.F., Dusseault, M.B. and Rothenburg, L., 2009. Numerical experiments on oil sands shear dilation and permeability enhancement in a multiphase thermoporoelastoplasticity framework. *Journal of Petroleum Science and Engineering*, 69(3-4): 219-226.

Yow, J.L. and Hunt, J.R., 2002. Coupled processes in rock mass performance with emphasis on nuclear waste isolation. *International journal of rock mechanics and mining sciences*, 39(2): 143-150.

Yu, W. and Ghassemi, A., 2017. Laboratory Geomechanical Characterization of the Arbuckle Group in Oklahoma. In Proceedings of the 51st US Rock Mechanics/Geomechanics Symposium, San Francisco, California, 25-28 June.

Zhou, X. and Ghassemi, A., 2009. Finite element analysis of coupled chemo-poro-thermo-mechanical effects around a wellbore in swelling shale. *International Journal of Rock Mechanics and Mining Sciences*, 46(4): 769-778.

## Appendix A: Algorithms for determining fracture network connectivity

The determination of the connectivity of a fracture network requires an algorithm to determine the intersections between fractures and an algorithm to search for conductive flow path assembled by interconnected fractures and to exclude isolated fractures.

### A.1 Detecting intersections between fractures

The first step is to determine if two fractures intersect with each other. The implicit functions of two fracture planes can be written as:

$$n_{x1}x + n_{y1}y + n_{z1}z + d_1 = 0 \quad (\text{A.1})$$

$$n_{x2}x + n_{y2}y + n_{z2}z + d_2 = 0 \quad (\text{A.2})$$

Where  $d_1 = -(n_{x1}x_{c1} + n_{y1}y_{c1} + n_{z1}z_{c1})$  and  $d_2 = -(n_{x2}x_{c2} + n_{y2}y_{c2} + n_{z2}z_{c2})$ ; n and c are the normal and center of a fracture.

There are three possible relative locations of the two fracture planes in three dimensional space:

1. Two fracture planes are parallel ( $n_1 \cdot n_2 = \pm 1$  and  $d > 0$ )

If two fracture planes have same or opposite normal, and the distance between these two planes is not equal to zero, they are parallel. Fractures locating on parallel planes will never intersect, and there will be no intersection in this case.

2. Two fracture planes are co-planar ( $n_1 \cdot n_2 = \pm 1$  and  $d = 0$ )

If two fracture planes have same or opposite normal, and the distance between these two planes is zero, they are the same plane. In this case, the 3D intersection problem is reduced to a planar problem. The intersection problem can be solved by comparing the distance between two fracture centers to the sum of their radius. There will be 1 intersection point if  $d = r_1 + r_2$  or  $d = |r_1 - r_2|$ ; 2

intersection points if  $d < r_1 + r_2$ . The solution to this planar intersection problem is very common, and is not discussed here.

3. Two fracture planes are non-parallel and non-coplanar ( $n_1 \cdot n_2 \neq \pm 1$ )

If two fracture planes are non-parallel and non-coplanar, they will intersect. In this case, the intersection line of these two planes are identified, then this problem reduces to finding the intersection points of this intersection line and a circle. Finally, the intersection between two fractures are determined based on the relative locations of the intersection points by calculating the line segment overlapping.

The intersection line between these two planes is:

$$x = x_0 + ft \tag{A.3}$$

$$y = y_0 + gt \tag{A.4}$$

$$z = z_0 + ht \tag{A.5}$$

Where the parameter coefficients f, g, h and the point is given by:

$$f = y_{c1}z_{c2} - y_{c2}z_{c1} \tag{A.6}$$

$$g = z_{c1}x_{c2} - z_{c2}x_{c1} \tag{A.7}$$

$$h = x_{c1}y_{c2} - x_{c2}y_{c1} \tag{A.8}$$

$$x_0 = (g(d_1z_{c2} - d_2z_{c1}) - h(d_1y_{c2} - d_2y_{c1})) / (f^2 + g^2 + h^2) \tag{A.9}$$

$$y_0 = -(f(d_1z_{c2} - d_2z_{c1}) + h(d_2x_{c1} - d_1x_{c2})) / (f^2 + g^2 + h^2) \tag{A.10}$$

$$z_0 = (f(d_1y_{c2} - d_2y_{c1}) + g(d_2x_{c1} - d_1x_{c2})) / (f^2 + g^2 + h^2) \tag{A.11}$$

Next, the intersection points between a line and a circle in 3D space are determined as follows:

The fracture circle equation written using its center and radius is:

$$(x - x_c)^2 + (y - y_c)^2 + (z - z_c)^2 = r^2 \quad (\text{A.12})$$

The parametric form of the line is:

$$x = x_1 + Ft \quad (\text{A.13})$$

$$y = y_1 + Gt \quad (\text{A.14})$$

$$z = z_1 + Kt \quad (\text{A.15})$$

There could be 0, 1, or 2 intersection points between a line and a circle. Here, only the 2 intersection points case is described, since the 0 intersection points case means no intersection and the 1 intersection points case can be treated as a special case of the 2 intersection points case.

The coordinates of the two intersection points can be calculated as:

$$\begin{aligned} \text{root} = r^2 (F^2 + G^2 + K^2) - & \left[ (F(y_c - y_1) - G(x_c - x_1))^2 \right. \\ & \left. + (G(z_c - z_1) - K(y_c - y_1))^2 + (K(x_c - x_1) - F(z_c - z_1))^2 \right] \end{aligned} \quad (\text{A.16})$$

$$t = \frac{[F(x_c - x_1) + G(y_c - y_1) + K(z_c - z_1)] \pm \sqrt{\text{root}}}{F^2 + G^2 + K^2} \quad (\text{A.17})$$

$$x = x_1 + Ft \quad (\text{A.18})$$

$$y = y_1 + Gt \quad (\text{A.19})$$

$$z = z_1 + Kt \quad (\text{A.20})$$

After finding the 4 intersection points (2 points for each fracture), the next step is to solve an overlapping problem of line segments to obtain the intersection line of two fractures. There are seven possible relative locations of four end points of two line segments:

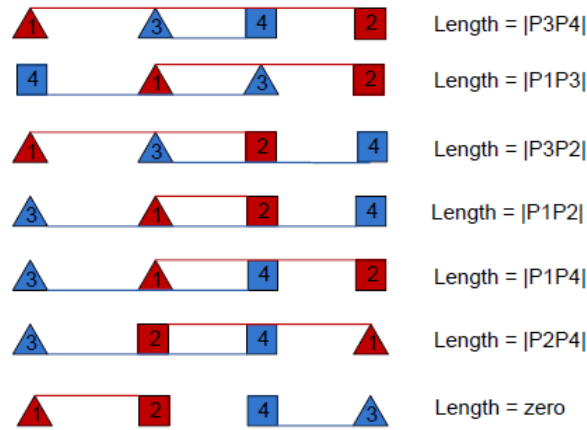


Figure A.1. Possible relative locations for line segment overlapping (Wang 2013).

The relative position of these four points are determined by calculating the value of four angles: angle 132, angle 142, angle 314, and angle 324. Knowing the two intersection points, the length of the intersection line could be obtained. Repeat the same searching procedure for all fracture pairs, we can obtain the local connectivity of the fractures. The flow channel between two intersecting fractures is formed by connecting the fracture centers with the mid-point of fracture intersections, as shown in Figure 4.17.

### A.2 Searching for interconnected flow path

To determine the interconnected flow path within a fracture network, a searching algorithm is developed. The searching process starts from a fracture or a set of fractures defined as the fluid entering fractures. In this work, since we are interested in the conductive fracture flow path from the injection well, the fractures that have intersections with the wellbore are selected to be the entry fractures. For each of the entry fractures, the local connectivity is checked and the fractures intersecting them are added to the flow path. For each of the newly added fractures, we check their local connectivity and add the fractures that have intersections with them to the flow path. This



process is repeated until no new fractures are added. A fracture could intersect with multiple fractures, and may have been accounted in the flow path searched in the previous steps. Therefore, a deduplication step is used to remove the redundant fractures. Finally, the fractures within the network can be classified as “connected” or “isolated” fractures, based on their belonging to the flow path. The detailed searching algorithm is illustrated in Figure A.2.

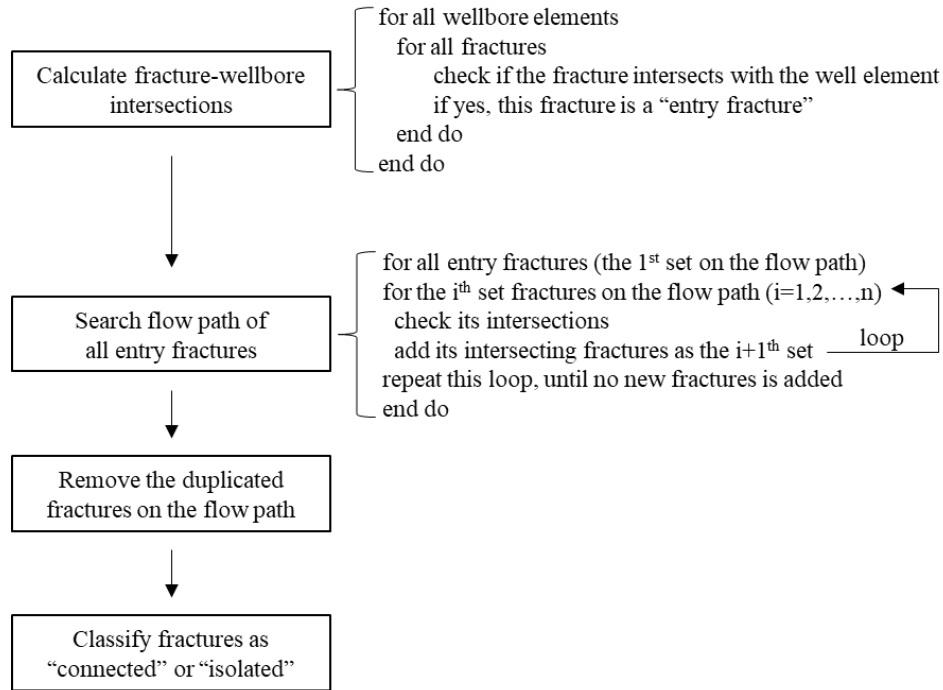


Figure A.2. Algorithm for searching for the connected fracture flow path.

## Appendix B: Potentials of radial and non-radial line intersections and their images

The analytical solution in each fracture plane is based on the assumption that each fracture intersection acts like a source or sink (Long 1983). The procedure to find the expressions for the potentials of radial and non-radial line intersections and their images described as follows.

As shown in Figure 4.14, a radial source has a radial segment image. The equation of the line on which the segment lies can be given as:

$$Ax + By = C \quad (\text{A.21})$$

Written in radial coordinates, the equation becomes:

$$A r \cos \theta + B r \sin \theta = C \quad (\text{A.22})$$

Where  $x = r \cos \theta$ ,  $y = r \sin \theta$  and  $r = \frac{C}{A \cos \theta + B \sin \theta}$ .

When the line segment is radial,  $C = 0$ , the equation of the image segment is:

$$\theta = \tan^{-1}(-A/B) \quad (\text{A.23})$$

The two endpoints of the image segment are given by  $r = a^2 / g_1$  and  $r = a^2 / g_2$ .

When the line segment is non-radial,  $C \neq 0$ , the equation of the image arc is:

$$R = \frac{a^2}{r} = \frac{a^2}{C} (A \cos \theta + B \sin \theta) \quad (\text{A.24})$$

Written in the Cartesian coordinates:

$$\left( x - \frac{a^2 A}{2C} \right)^2 + \left( y - \frac{a^2 B}{2C} \right)^2 = \frac{a^4}{4C^2} (A^2 + B^2) \quad (\text{A.25})$$

It is the equation of a circle centered at  $\left( \frac{a^2 A}{2C}, \frac{a^2 B}{2C} \right)$ ,  $C \neq 0$  with radius  $\frac{a^2}{2C} \sqrt{A^2 + B^2}$ . It always passes through the origin.

For a non-radial line intersection, a local arbitrary X, Y coordinate system can be established for each fracture disc. For calculation convenience, x, y and x', y' coordinates are generated, as shown in Figure A.3. The origin of the x', y' coordinates is located at one end point of the non-radial intersection, and the y' axis lies on the intersection.

Point O is the center of this fracture, and Point P is an arbitrary point on this plane. All the equations for potential distribution must be referred to X, Y coordinates before they are added up to obtain the total potential on this disc.

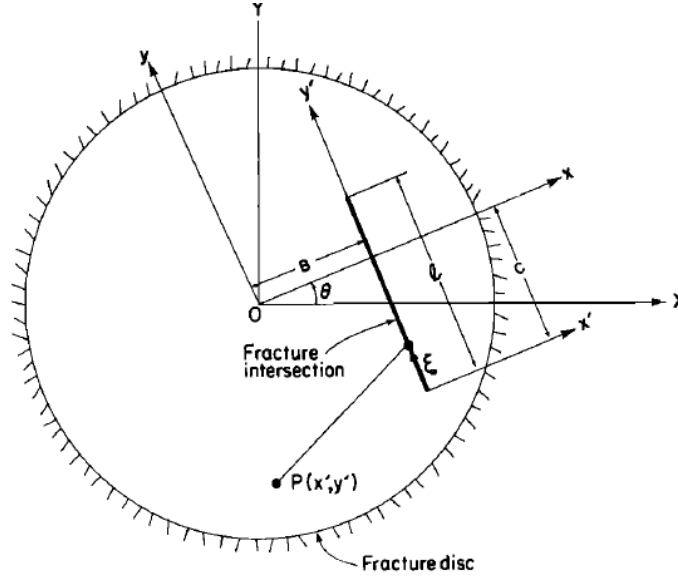


Figure A.3. Non-radial line source (Long 1983).

The fundamental solution of the Laplace equation for the potential due to a point source in an infinite plane is:

$$\phi = Kbh = -\frac{Q}{2\pi} \ln(r) \quad (\text{A.26})$$

Assume such point sources are distributed over a line segment in the fracture plane, and the potential due to the line source is given by:

$$\phi_{iN}^k = -\frac{Q}{2\pi l} \int_0^l \ln(r_p(\xi)) d\xi \quad (\text{A.27})$$

The potential due to the image is similar:

$$\phi_{it}^k = -\frac{Q}{2\pi l} \int_{s_1}^{s_2} \frac{d\xi}{dS} \ln(r_p(s)) ds \quad (\text{A.28})$$

Eqn. (A.27) can be written as:

$$\phi_{iN}^k = -\frac{Q}{2\pi l_i} \int_0^{l_i} \frac{1}{2} \ln \left[ x'^2 + (y' - \xi)^2 \right] d\xi \quad (\text{A.29})$$

It can also be re-written as:

$$\phi_{iN}^k = -\frac{Q}{4\pi l_i} \left\{ (\xi - y') \ln \left[ x'^2 + (y' - \xi)^2 \right] - 2\xi + 2|x'| \tan^{-1} \left( \frac{\xi - y'}{|x'|} \right) \right\}_0^{l_i} \quad (\text{A.30})$$

It has to be translated to x, y coordinates and then rotate to X, Y coordinates. Finally, it will result in an expression of the form:

$$\phi_{iN}^k = Q_i f_{iN}^k (X, Y) \quad (\text{A.31})$$

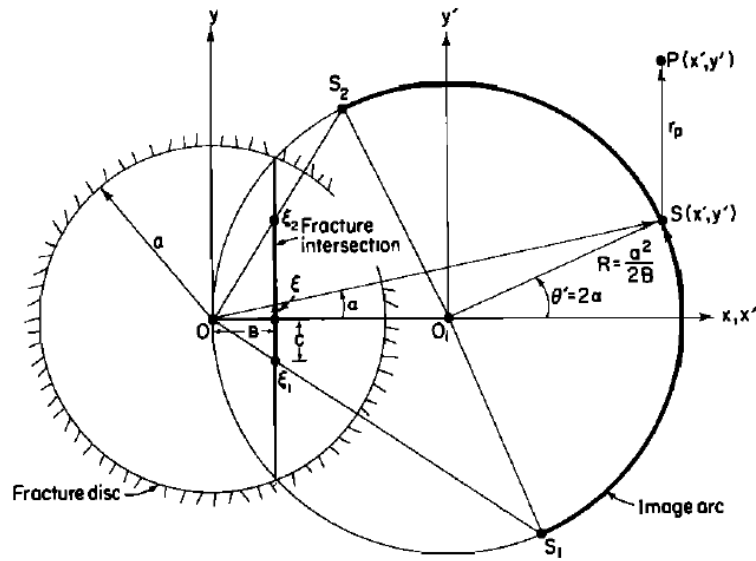


Figure A.4. Non-radial line source image arc (Long 1983).

The image arc of a non-radial source is shown in Figure A.4. The integral for the potential distribution at any point on the plane due to sources on S can be written as:

$$\phi_{iI}^k = -\frac{Q}{2\pi l_i} \int_{S_1}^{S_2} \frac{d\xi}{dS} \ln(r_p(\xi)) ds \quad (\text{A.32})$$

Where  $r_p$  is the distance from a point S on the arc to any point P ( $x'$ ,  $y'$ ) on this plane.

$$r_p^2 = (x' - R \cos \theta')^2 + (y' - R \sin \theta')^2 \quad (\text{A.33})$$

$$\cos \theta' = \cos 2\alpha = 1 - 2 \sin^2 \alpha = 1 - 2 \left( \frac{\xi^2}{\xi^2 + B^2} \right) \quad (\text{A.34})$$

$$\sin \theta' = \sin 2\alpha = 2 \sin \alpha \cos \alpha = \frac{2\xi B}{\xi^2 + B^2} \quad (\text{A.35})$$

Substituting the above equations into Eqn. (A.32), we have:

$$\phi_{il}^k = -\frac{Q_i}{4\pi l_i} \left\{ \int_{\xi_1}^{\xi_2} \ln[\Omega] d\xi - \int_{\xi_1}^{\xi_2} \ln(\xi^2 + B^2) d\xi \right\} \quad (\text{A.36})$$

$$\Omega = \alpha + \beta\xi + \gamma\xi^2 \quad (\text{A.37})$$

$$\alpha = (x'^2 + y'^2 + R^2 - 2Rx')B^2 \quad (\text{A.38})$$

$$\beta = -4Ry'B \quad (\text{A.39})$$

$$\gamma = x'^2 + y'^2 + R^2 + 2Rx' \quad (\text{A.40})$$

Solve for the integral, it can be rewritten as:

$$\phi_{il}^k = -\frac{Q_i}{4\pi l_i} \left\{ \left( \xi + \frac{\beta}{2\gamma} \right) \ln \Omega + \frac{\sqrt{4\alpha\gamma - \beta^2}}{\gamma} \tan^{-1} \left( \frac{2\gamma\xi + \beta}{\sqrt{4\alpha\gamma - \beta^2}} \right) - 2 \left[ \xi \ln(\xi^2 + B^2) + 2B \tan^{-1} \left( \frac{\xi}{B} \right) \right] \right\}_{\xi_1}^{\xi_2} \quad (\text{A.41})$$

Finally, it must be translated to X, Y coordinates and has the form:

$$\phi_{il}^k = Q_i f_{il}^k(X, Y) \quad (\text{A.42})$$

If the intersection is radial, there will be a different form for the potentials. Figure A.5 shows the geometry of a radial line source.

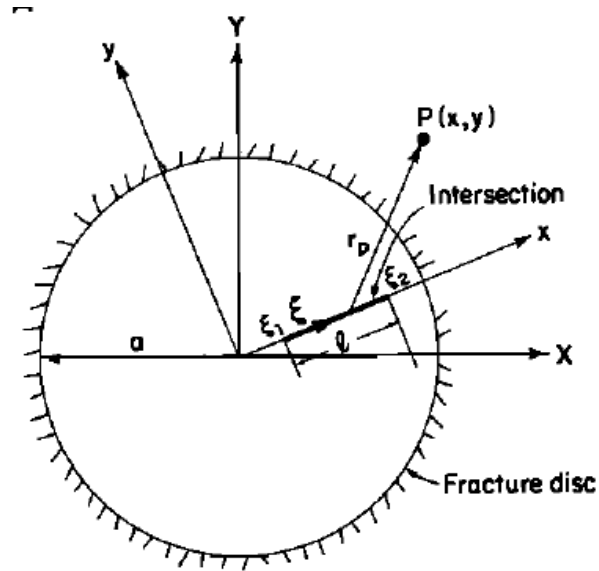


Figure A.5. Radial line source image arc (Long 1983).

The potential due to the radial source is:

$$\phi_{iN}^k = -\frac{Q_i}{4\pi l_i} \int_{\xi_1}^{\xi_2} \frac{1}{2} \ln[(x-\xi)^2 + y^2] d\xi \quad (\text{A.43})$$

Solve for the integral, it can be re-written as:

$$\phi_{iN}^k = -\frac{Q_i}{4\pi l_i} \left\{ (\xi - x) \ln[(x-\xi)^2 + y^2] - 2\xi + 2|y| \tan^{-1}\left(\frac{\xi - x}{|y|}\right) \right\}_{\xi_1}^{\xi_2} \quad (\text{A.44})$$

The image of a radial source is also a radial line segment, as shown in Figure A.6.

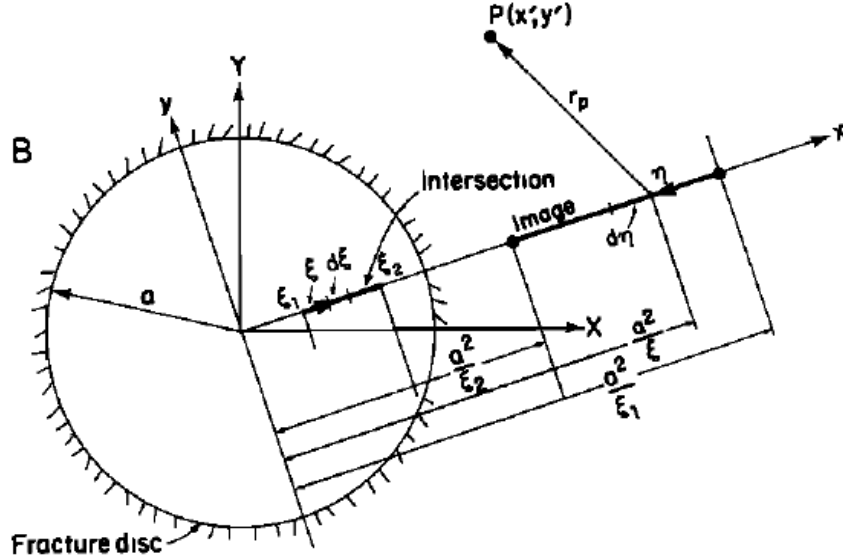


Figure A.6. Radial line source image arc (Long 1983).

The distance from a point on the image to any point P ( $x'$ ,  $y'$ ) is:

$$r_p^2 = \left( x - \frac{a^2}{\xi} \right)^2 + y^2 = \frac{(x^2 + y^2)\xi^2 - 2a^2x\xi + a^4}{\xi^2} \quad (\text{A.45})$$

Similar to the non-radial case, the potential due to the image of a radial source can be written as:

$$\phi_{il}^k = -\frac{Q_i}{4\pi l_i} \int_0^{a^2/\xi_1 - a^2/\xi_2} \frac{d\xi}{l\eta} \ln r_p d\eta = -\frac{Q_i}{4\pi l_i} \left( \int_{\xi_1}^{\xi_2} \ln \Omega d\xi - \int_{\xi_1}^{\xi_2} 2 \ln \xi d\xi \right) \quad (\text{A.46})$$

Where,  $\Omega = \alpha + \beta\xi + \gamma\xi^2$ ;  $\alpha = a^4$ ;  $\beta = -2a^2x$ ;  $\gamma = x^2 + y^2$ .

The integration yields:

$$\phi_{il}^k = -\frac{Q_i}{4\pi l_i} \left\{ \left( \xi + \frac{\beta}{2\gamma} \right) \ln \Omega - 2\xi + \frac{\sqrt{4\alpha\gamma - \beta^2}}{\gamma} \tan^{-1} \left( \frac{2\gamma\xi + \beta}{\sqrt{4\alpha\gamma - \beta^2}} \right) - 2[\xi \ln \xi - \xi] \right\}_{\xi_1}^{\xi_2} \quad (\text{A.47})$$

Finally, apply coordinate transformation, and write all potentials in the X, Y coordinate system.

The potential contribution of the intersection  $i$  and its image on fracture  $k$  is of the form:

$$\phi_i^k = \phi_{iN}^k + \phi_{il}^k = Q_i f_{iN}^k(X, Y) + Q_i f_{il}^k(X, Y) \quad (\text{A.48})$$